# Modeling Basin Dynamics under Changing Climate and LULC on Hydrological Processes in Wabi Shebele River Basin, Ethiopia

Abebe Teklu Toni

Vollständiger Abdruck der von der Fakultät für Bauingenieurwesen und Umweltwissenschaften der Universität der Bundeswehr München zur Erlangung des akademischen Grades eines

Doktor-Ingenieurs (Dr.-Ing.)

genehmigten Dissertation.

Gutachter/Gutachterin

1. Prof. Dr.-Ing. habil. Andreas Malcherek
2. Prof. (Asso.) Dr. Asfaw Kebede Kassa
3. Prof. Raaj Ramsankaran

Die Dissertation wurde am 09. Januar 2024 bei der Universität der Bundeswehr München eingereicht und durch die Fakultät für Bauingenieurwesen und Umweltwis- senschaften am 13. Juni 2024 angenommen. Die mündliche Prüfung fand am 18. Juni 2024 statt.

This page is intentionally left blank.

# Acknowledgements

First, I would like to express my sincere gratitude to my supervisor, Prof. Dr.-Ing. Andreas Malcherek, for his unwavering support and invaluable guidance throughout my research journey. His vast knowledge and insightful advice, extending beyond purely academic topics, proved to be an incredible asset. I am truly grateful for the opportunity to conduct this study under his supervision. The fruitful discussions and interactions that we shared have significantly enriched my experience and contributed immensely to my development.

I would like to express my gratitude to Prof. (Asso.) Asfaw Kebede Kassa, my thesis co-supervisor, for his insightful comments that greatly improved this work. I am also deeply grateful to Prof. Raaj Ramsankaran for reviewing my thesis promptly. His willingness to dedicate time to this task made a significant difference, and I am indebted to him for his invaluable comments. I would like to extend my sincere gratitude to Prof. Thomas Apel for kindly agreeing to chair my thesis examination. Your involvement ensures the integrity and rigor of the process, and I greatly appreciate your commitment.

I would like to express my gratitude to the National Meteorological Authority (NMA) for providing meteorological data and the Ministry of Water and Energy's (MWE) hydrology section for supplying streamflow data. In completing this study, I am grateful for the varied support I received from the Deutscher Akademischer Austauschdienst (DAAD), Ministry of Education (MoE), Institute of Water Management, Faculty of Civil Engineering and Environmental Sciences, Universität der Bundeswehr München (UniBw), and Haramaya University.

I would like to extend my sincere thanks to all the research and laboratory staff at the Institute of Water Management within the Professorship of Hydromechanics and Hydraulic Engineering. Special thanks to Dr.-Ing. Sebastian Müller and Dr.-Ing. Johanna Schmidt for their invaluable support, which helped me navigate many challenges. Dr.-Ing. Sebastian, I am especially grate-

ful for the unforgettable hiking experience in the Alps that you shared with me. I would also like to thank my friend, Dr.-Ing. Yonas Abebe, for his support and for sharing in my frustrations throughout the study period.

Finally, I would like to express my heartfelt thanks to all the members of my family and friends for their unwavering support, love, and affection throughout the study period. Their faith in me played a crucial role in shaping the person I am today. Special gratitude goes to my wife, Sosina Tilahun. Her strength and dedication in caring for our little angel, Hasset Abebe, during my absence have been truly remarkable. I am deeply grateful for her support. Sosina, you are a true blessing in my life, and I love you dearly.

# Contents

# List of Tables

# List of Figures

# Abbreviations and Acronyms

| | |
|---|---|
| ACZ | Agro-Climatic Zone |
| ANN | Artificial Neural Networks |
| CDO | Climate Data Operator |
| CMIP6 | Coupled Model Intercomparison Project Phase 6 |
| DEM | Digital Elevation Model |
| EROS | Earth Resources Observation and Science |
| ETCCDI | Expert Team on Climate Change Detection and Indices |
| FAO | Food and Agriculture Organization |
| GCM | Global Climate Model |
| GDP | Gross Domestic Product |
| GTP | Growth and Transformation Plan |
| HRU | Hydrologic Response Unit |
| IPCC | Intergovernmental Panel on Climate Change |
| ITCZ | Inter-Tropical Convergence Zone |
| KGE | Kling–Gupta Efficiency |
| LULC | Land Use Land Cover |
| LULCC | Land Use Land Cover Change |
| MME | Multi-Model Ensemble |
| MOLUSCE | Methods Of Land Use Change Evaluation |
| MoWIE | Ministry of Water, Irrigation and Electricity |
| NMA | National Meteorological Agency |
| NSE | Nash-Sutcliffe Efficiency |
| OLI | Operational Land Imager |
| PBIAS | Percentage of Bias |
| 95PPU | 95% Prediction Uncertainty |
| QGIS | Quantum Geographic Information System |
| QSWAT | QGIS interface for SWAT model |
| RCM | Regional Climate Model |
| RCPs | Concentration Pathways |
| SCP | Semi-Automatic Classification Plugin |
| SCS-CN | Soil Conservation Service-Curve Number |
| SRTM | Shuttle Radar Topography Mission |
| SSPs | Shared Socioeconomic Pathways |
| SWAT | Soil and Water Assessment Tool |
| TM | Thematic Mapper |
| UTM | Universal Transverse Mercator |
| WSRB | Wabi Shebele River Basin |

This page is intentionally left blank.

# Abstract

Climate change has become a noticeable mega-trend in the 21st century, with widespread adverse effects on the environment and socioeconomic development. In Ethiopia, where over 85% of the population depends on agriculture, the vulnerability to climate change is high. The agrarian sector faces significant threats from shifting weather patterns and long-term climatic variations, impacting the livelihoods of millions in the country. Thus, this study aimed on assessing hydro-climatic trends, climate change, and the potential impacts of future climate change and land use land cover (LULC) dynamics on headwater catchments in the Wabi Shebele River Basin (WSRB) in Ethiopia. Historical hydro-climatic variability and trends were analyzed using the modified MK test and the Sen Slope estimator. Rainfall and maximum temperature exhibited mixed trends, while minimum temperature showed a clear increasing trend, except in the highland part of the basin. Streamflow displayed mixed trends across seasons and gauging stations.

To project future climate change, eight CMIP6 Global Climate Models (GCMs) were employed under four shared socioeconomic pathways (SSPs) scenario. Future climate data were downscaled and bias-corrected, revealing an anticipated increase in mean annual precipitation, maximum and minimum temperatures across various Agro-Climatic Zones (ACZs). Notably, the rate of change in minimum temperature exceeded that of maximum temperature in most ACZs. The research also investigated land use land cover changes using Landsat images and the Semi-Automatic Classification Plugin. Significant transformations were observed over the past 30 years, including the depletion of natural vegetation and an increase in cultivated and built-up areas. Future projections using the Multi-Layer Perceptron Artificial Neural Network (MLP-ANN) model indicated further increases in built-up areas, dense shrubs, grasslands, agricultural land, and barren land, with reductions in water bodies, forestland, and open shrublands.

The SWAT model, a semi-distributed river basin model, was calibrated and validated to simulate hydrological processes. The model effectively captured streamflow pattern within accept-

able ranges. Hydrological responses to climate change and land use land cover alterations in six headwater catchments were predicted using the calibrated model. The results demonstrated that observed changes contributed to increased streamflow, with projected climate changes exerting a greater impact than observed land use land cover changes. The combined impact of climate and land use land cover changes resulted in a substantial increase in streamflow across all studied headwater catchments. Overall, valuable insights into the complex interactions between hydro-climatic variabilities, climate and land use land cover changes, and their cumulative effects on streamflow in the WSRB were provided by this study.

**Keywords**: Climate change, LULC, Headwater catchment, SWAT, GCMs, WSRB

# Kurzfassung

Der Klimawandel ist im 21. Jahrhundert zu einem spürbaren Megatrend geworden, der weitreichende negative Auswirkungen auf die Umwelt und die sozioökonomische Entwicklung hat. In Äthiopien, wo über 85% der Bevölkerung von der Landwirtschaft abhängig sind, ist die Anfälligkeit für den Klimawandel hoch. Der Agrarsektor ist erheblichen Bedrohungen durch wechselnde Wetterbedingungen und langfristige Klimaschwankungen ausgesetzt, die sich auf die Lebensgrundlage von Millionen Menschen im Land auswirken. Daher zielt diese Studie auf die Bewertung hydroklimatischer Trends, des Klimawandels und der möglichen Auswirkungen des zukünftigen Klimawandels und der Dynamik der Landnutzungslandbedeckung (LULC) auf die Quellgebiete im WSRB in Äthiopien ab. Mithilfe des modifizierten MK-Tests und des Sen-Slope- Schätzwertes wurden historische hydroklimatische Variabilität und Trends analysiert. Niederschlag und maximale Temperatur zeigten gemischte Trends, während die minimale Temperatur einen deutlich steigenden Trend zeigte, mit Ausnahme des im Hochlandes des Beckens. Streamflow zeigte über die Jahreszeiten und Messstationen hinweg gemischte Trends.

Um zukünftige Klimaszenarien zu projizieren, wurden acht globale CMIP6-Klimamodelle (GCMs) im Rahmen von vier gemeinsamen sozioökonomischen Pfaden (SSP) verwendet. Zukünftige Klimadaten wurden herunterskaliert und systematische Fehler korrigiert, was einen erwarteten Anstieg des durchschnittlichen Jahresniederschlags sowie der Höchst- und Tiefsttemperaturen in verschiedenen Agrarklimazonen (ACZs) offenbarte. Bemerkenswert ist, dass die Änderungsrate der Mindesttemperatur in den meisten ACZs die der Höchsttemperatur überstieg. Die Forschung untersuchte auch Änderungen der Landnutzung und Landbedeckung mithilfe von Landsat-Bildern und dem Semi-Automatic Classification Plugin. In den letzten 30 Jahren wurden bedeutende Veränderungen beobachtet, darunter der Rückgang der natürlichen Vegetation und eine Zunahme der landwirtschaftlicher und bebauten Flächen. Zukünftige Prognosen unter Verwendung des MLP-ANN-Modells deuten auf eine weitere Zunahme bebauter Flächen, Flächen mit dichtem Buschland, Grasland, landwirtschaftlicher Flächen und unfruchtbarer Flächen hin, mit

einer Verringerung von Gewässern, Wäldern und offenem Buschland.

Das SWAT-Modell, ein Flussgebietsmodell das teilweise hochaufgelöste und teilweise flächengemittelte Daten nutzt, wurde kalibriert und validiert, um hydrologische Prozesse zu simulieren. Das Modell erfasste effektiv die Strömungsdynamik innerhalb akzeptabler Toleranz. Mithilfe des kalibrierten Modells wurden hydrologische Reaktionen auf den Klimawandel und Veränderungen der Landnutzung und Landbedeckung in sechs Quellgebieten vorhergesagt. Die Ergebnisse zeigten, dass beobachtete Veränderungen zu einem erhöhten Wasserfluss beitrugen, wobei prognostizierte Klimaveränderungen größere Auswirkungen hatten als beobachtete Änderungen der Landnutzung und Landbedeckung. Die kombinierten Auswirkungen von Klimaänderungen und Änderungen der Landnutzungslandbedeckung führten zu einem erheblichen Anstieg des Abflusses in allen untersuchten Quellgebieten. Insgesamt liefert diese Studie wertvolle Einblicke in die komplexen Wechselwirkungen zwischen hydroklimatischen Variablen, Landnutzungsänderungen und deren kumulativen Auswirkungen auf den Wasserfluss im WSRB.

# Chapter 1

# Introduction

## 1.1 Background and Justification

Anthropogenic climate change has risen to prominence as a mega-trend in the 21st century because of its far-reaching and adverse impacts on the environment and socioeconomic development across nations, despite variations in the degree of impact. In the past half-century, humans have driven unprecedented and extensive changes in ecosystems, primarily driven by the increasing demand for food, freshwater, timber, fiber, and fuel (Millennium Ecosystem Assessment, 2005). The Intergovernmental Panel on Climate Change report (IPCC, 2014b) warns that the global average temperature likely rise by 1.5 °C to 4.5 °C by 2100, with severe consequences on global resources and water supply. Climate change has already begun to impact food security by increasing temperatures, shifting precipitation patterns, and increasing the frequency of extreme weather events (IPCC, 2019). The IPCC firmly asserts that the lion's share of this temperature rise can be attributed to the increasing concentration of greenhouse gases in the atmosphere, primarily originating from human activities.

Africa's vulnerability to climate change is particularly pronounced for several reasons (Giorgi et al., 2009; IPCC, 2021a). Firstly, many critical sectors in the region, such as agriculture, water management, and public health, rely heavily on climate conditions, making them highly susceptible to climate variability. Additionally, Africa's economies generally possess lower adaptive capacities, exacerbating the challenges posed by climate change. Moreover, the impact of climate change on Africa extends beyond direct temperature and precipitation shifts. It interacts with other environmental stressors like land-use change, desertification, and aerosol emissions, creating complex challenges. These interactions, in turn, threaten agricultural production and food access in numerous African nations, as outlined by (IPCC, 2007), thereby compounding

food security concerns and aggravating malnutrition. Furthermore, climate change and its associated variability introduce additional pressures on water availability and accessibility across the continent. These pressures are expected to be particularly acute in regions like the Horn of Africa (Ayele et al., 2016). In general, Africa faces a multi-faceted and urgent climate challenge that encompasses not only its environmental but also its socio-economic and humanitarian dimensions.

The Eastern Africa region frequently deals with severe precipitation events, which have the potential to result in property and environmental damage, as well as loss of lives (Akinsanola et al., 2021). Meanwhile, in North Eastern Africa (NEAF), the impact of climate change is strikingly apparent, as reported in the Sixth Assessment Report (AR6) (IPCC, 2021b). This is evidenced by a documented reduction in precipitation, the decline of snow and glaciers, the anticipation of more intense rainfall leading to pluvial flooding, and a reduced risk of meteorological drought, particularly in scenarios projecting a 4 °C global warming. These trends emphasize substantial climate-related challenges that the NEAF region is confronting.

Throughout its history, Ethiopia's economic well-being has been closely tied to the availability of rainfall and water resources. This dependence on agriculture remains a fundamental aspect of the country's economic landscape (Amsalu et al., 2006). Notably, more than 85% of Ethiopia's population relies on agrarian activities, rendering them highly vulnerable to the impacts of climate change (Wagino and Amanuel, 2021). Climate change poses a significant threat to this sector, primarily due to shifting weather patterns and long-term climatic variations. The country has experienced periods of economic growth and poverty reduction that coincided with more predictable rainfall and increased public investments in agriculture. Conversely, previous drought episodes have severely constrained economic progress and exacerbated food insecurity. Recent research estimates highlight the potential for climate change and rainfall variability alone to erode Ethiopia's GDP by a range of 0.5% to 2.5% annually. Furthermore, the demand for water in Ethiopia is on an upward trajectory, driven by population growth and economic development. However, this trend contrasts with some countries where water demand is diminishing due to enhanced efficiency in water utilization (IPCC, 2001).

Similarly, Ethiopia is on the brink of a significant demographic transformation, with its population expected to nearly double by 2050. This demographic expansion will inherently intensify the nation's demand for water resources. Ethiopia's forthcoming economic expansion plans are

intricately linked to the enlargement of irrigated agriculture, manufacturing, hydropower, and municipal water supply – all of which hinge on the availability of water resources that can be consistently relied upon (National Planning Commission, 2016). To achieve this, a substantial initiative is underway, involving the development of over 4 million hectares of land through the enhancement of irrigation infrastructure. This ambitious project is set to be led by smallholder farmers during the GTP II period.

In recent years, climate change has triggered far-reaching consequences for human and natural systems (IPCC, 2014a). Among the significant effects of this global phenomenon, there is a growing likelihood of shifts in hydrologic cycles and alterations in the availability of water resources (Abdo et al., 2009; Setegn et al., 2011a). Consequently, any alterations in the spatial and temporal patterns of water resources have profound implications for crucial sectors such as agriculture, industry, and urban development. Climate change stands out as one of the most pressing global challenges of our time, with its far-reaching effects extending to fundamental hydrological processes like precipitation and evapotranspiration. These changes, in turn, carry direct implications for stream flow and groundwater recharge, emphasizing the intricate and substantial impact of climate change on hydrological systems and, by extension, human well-being and the environment.

Numerous studies have highlighted that in addition to climate change, alterations in land use land cover (LULC) are predicted to exert substantial influence on runoff and flooding within catchment areas. This is attributed to the capacity of LULC changes to modify the path of rainfall, thereby impacting the generation of basin runoff by modifying critical components of the water balance, including groundwater recharge, infiltration, interception, and evaporation. LULC changes are known to have notable effects on evapotranspiration, groundwater infiltration, and streamflow. Additionally, they elevate the risk of climate extremes (Dong et al., 2019) and contribute to carbon emissions (Dong et al., 2019; Kim, 2016). The rapid increase in the transformation of natural landscapes into cultivated land, accompanied by the intensified use of these lands, is being witnessed as the global population continues to grow and socio-economic needs expand (Lambin et al., 2003; Meyer and Turner, 1992; Reis, 2008).

When viewed at a global scale, changes in land use land cover have profound impacts on fundamental aspects of Earth's ecological functioning. The ongoing expansion of human-induced al-

terations in land ecology through LULC changes emphasizes the urgency of comprehending and managing these changes in a sustainable and responsible manner. It is essential to recognize that not all these impacts are negative; many of these changes in land use land cover are associated with ongoing improvements in food and fiber production, resource efficiency, and overall wealth and well-being (Lambin et al., 2003)). Understanding the consequences of these land use land cover shifts is a fundamental aspect of sustainable land planning and development (Memarian et al., 2014; Wang et al., 2020). Therefore, data on land use land cover changes are invaluable for informed decision-making in environmental management and future planning. Moreover, anticipating the changes in land use land cover within watersheds and their effects on water resources is a pivotal concern in watershed management and policy (Marshall and Randhir, 2008).

Recent research has explored the combined impact of climate change and land use land cover on hydrological regimes in various regions across the globe. Both climate fluctuations and alterations in land use land cover play significant roles in shaping the hydrological response of watersheds (Dwarakish and Ganasri, 2015). The dynamics of land use change and climate variability stands as a pivotal factor in shaping watershed hydrology, which, in turn, has a profound bearing on the availability of water resources and the sustainability of local ecosystems (Zhang et al., 2016). Of particular importance, water resources in arid and semi-arid regions are notably affected by the combined forces of land use land cover changes (LULC) and climate shifts. This dual impact, emphasizes the critical role of understanding the complex relationship between LULC transformations and climate variations in maintaining water resource equilibrium within these environmentally sensitive areas (Yin et al., 2017).

Thus, quantitative assessments of hydrological implications resulting from changes in climate and land use land cover (LULC) are paramount for addressing sustainable water resource management challenges. These challenges encompass the assurance of adequate water supply for domestic and industrial needs, power generation, and agriculture, while also addressing the demands of future water resource planning, design, management, and preservation of the natural environment. Despite the abundant potential for irrigation and other developmental activities in the Wabi Shebele River basin (WSRB), existing information on the impacts of climate and LULC change on the basin's hydrological processes is limited and fragmented. Researchers and governmental organizations have allocated insufficient attention to the WSRB because of its remote location and paucity of data within the region. Consequently, well-documented studies on

the basin, whether at the national or international level, are scarce.

Therefore, to gain a comprehensive understanding of the historical trends of hydro-climatic variables and the effects of climate and LULC changes on hydrological responses, it is imperative to accurately estimate their impact in the WSRB by selecting appropriate hydrological models. These allow planning appropriate adaptation measures that must be taken ahead of time and give an overall insight to improve sustainable water resource management and improve the livelihood of the society in a region/basin. Moreover, this will give enough room to consider possible future risks in all phases of water resource development projects.

## 1.2 Objectives

**General objective**

The primary objective of this research is to evaluate the influence of climate variabilities and changes, both in historical and future scenarios, on the hydrology of the basin. Simultaneously, it aims to assess the impacts of land use land cover (LULC) dynamics on the hydrological response of headwater catchments within the WSRB in Ethiopia.

**Specific objectives**

- ✦ To analyze the variability and trends in hydro-climatic time series records within the Wabi Shebele River Basin (WSRB);
- ✦ To assess the extent of climate change in WSRB by employing the ensemble mean from eight chosen CMIP6 Global Climate Models (GCMs) across four different Shared Socioeconomic Pathways (SSPs) scenarios;
- ✦ To examine the historical and anticipated changes in land use land cover dynamics in the upstream and central parts of the basin;
- ✦ To evaluate the performance of the SWAT model in simulating hydrological processes within headwater catchments of the basin; and
- ✦ To quantify the potential impacts of climate and LULC changes, and their interaction on streamflow within six headwater catchments in the WSRB.

## 1.3 Outline of the Thesis

This thesis is structured into eight interconnected chapters, with this introductory chapter setting the stage. Each subsequent chapter focuses on a key research theme, offering a thorough analysis that includes an overview, methodology, results, and discussion, followed by the conclusions. Chapter one provides a broad introduction to the thesis, offering essential background information to support the research and outline clearly defined objectives. Chapter two is dedicated to an in-depth review of the relevant literature, covering topics such as hydroclimatic variability and trends, climate change analysis, satellite image-based land use land cover (LULC) classification, and the selection of hydrological models for future climate and LULC change impact modeling. Chapter three provides a comprehensive description of the study area, detailing the topography, climate, basin hydrology, land use, soil, and sources of hydroclimatic data. Chapter four presents the assessment of seasonal and yearly hydro-climatic variabilities and trends within the agroclimatic zones of the study basin. Additionally, streamflow variability and trends are discussed for a selected headwater catchment based on available records. Climate change analysis was also introduced, utilizing the multi-model ensemble mean of eight CMIP6 GCMs. In Chapter Five, the approach to developing land use land cover maps spanning three decades (1990, 2000, 2010, and 2020) is presented. The future LULC map for 2040 was projected based on six explanatory factors using the MLP-ANN projection model. Chapter six focuses on evaluating the performance of the SWAT model through sensitivity, calibration, validation, and uncertainty analyses to model the impact of climate and LULC changes on streamflow. Chapter seven assesses the impact of climate and LULC changes on streamflow in a selected headwater catchment of the Wabi Shebele River Basin during the second, third, and fourth quarters of the 21$^{st}$ century. Finally, chapter eight summarizes the conclusions drawn from the study and provides recommendations for future research and applications.

# Chapter 2

# Basin Dynamics Under Changing Climate and LULC: State of the Art

## 2.1 Hydro-Climatic Trends and Climate Change

### 2.1.1 Historical Hydro-Climatic Variability and Trends

#### Climate variability

The climate variability, includes all forms of climate inconsistency (i.e. deviations from long-term statistics) and can be considered as a natural phenomenon and happens occasionally from time to time. The most common approaches to understand rainfall and temperature variability have been put into application either or a combination of descriptive statistics and various indices. There are several studies done in Ethiopia whether at the national or regional level.

In a study conducted by Elzopy et al. (2021), several key indices, including the Precipitation Concentration Index (PCI), Seasonality Index (SI), Rainfall Anomaly Index (RAI), and Departure Analysis Rainfall (DAR), were employed to gain insights into the long-term climatic patterns of rainfall in Ethiopia. The research findings, based on the analysis of the Coefficient of Variation (CV), led to the conclusion that the variations in both seasonal and annual rainfall in Ethiopia are not notably severe. In addition, Asfaw et al. (2018) conducted a comprehensive examination of climate data in the Woleka sub-basin in north-central Ethiopia, utilizing CV and PCI. Their findings indicated that, in this region, 'Belg' rainfall displays more pronounced inter-annual variability than the 'Kiremt' rainfall pattern.

In the watersheds of Choke Mountain, Ademe et al. (2020) highlighted the applicability of CV,

PCI, and RAI in characterizing rainfall patterns within the agricultural regions of Ethiopia's highlands. Furthermore, this research noted a significant spatiotemporal anomaly in maximum temperature, minimum temperature, and rainfall, with a pronounced trend of warming observed since the 2000s. Similarly, CV, PCI, and Standardized Rainfall Anomaly (SRA) were employed to assess the inter-annual and intra-annual variability in rainfall within the Alwero watershed in western Ethiopia (Alemayehu et al., 2020). The study's findings led to the conclusion that climatic variability and trends in rainfall are notably localized within the country. The application of SRA has helped in understanding the inter-annual rainfall variability within the Omo-Ghibe River Basin, Ethiopia (Degefu and Bewket, 2015). The research findings revealed that regions characterized by bimodal rainfall patterns exhibit notably higher inter-annual variability in rainfall.

In the northern district of the middle WSRB, Bayable et al. (2021) investigated the spatiotemporal variability of rainfall and its correlation with Pacific Ocean Sea Surface Temperatures (SST) in the West Harerge Zone of eastern Ethiopia. They employed satellite-based rainfall data and relied on key metrics such as the CV and SAI. Their research findings revealed significant spatial and temporal variations in rainfall patterns across monthly, seasonal, and annual timeframes. Similarly, in the upper and middle regions of the basin, Harka et al. (2021) investigated the spatiotemporal distribution and variability of rainfall using a combination of the CV, PCI, and SAI, in conjunction with station data. Their investigation highlighted a consistent trend where the majority of rainfall stations experienced high annual rainfall during the Kiremt (wet) season, while the Bega (dry) season exhibited notable variability in rainfall amount.

#### Climatic trends

Statistical methods have become widely adopted for the detection of time-series trends within hydro-meteorological data, encompassing variables like temperature, precipitation, and streamflow. In recent research focused on climate data analysis, both in Ethiopia and worldwide, the prevailing approach often combines the Mann-Kendall (MK) trend test along with Sens's slope estimator (Mann, 1945; Sen, 1968) and the Spearman Rank Correlation Coefficient (Gauthier, 2001). Notably, these techniques offer the advantage of being nonparametric and rank-based, although they necessitate data preprocessing to account for serial correlation and seasonal effects (Gauthier, 2001). Additionally, many researchers have employed indices provided by the World Meteorological Organization's Expert Team on Climate Change Detection and Indices (ETCCDI) for trend analysis (Berhane et al., 2020; Esayas et al., 2018; Teshome and Zhang,

2019). A more recent graphical technique, Innovative Trend Analysis (ITA) Şen (2012), is gaining attention for its ability to detect trends without the need for data preprocessing regarding serial correlation.

In Ethiopia, researchers, both at the national and international levels, have consistently employed the Mann-Kendall (MK) and Sen's slope approach for hydro-climatic trend analysis in various studies (Ademe et al., 2020; Asfaw et al., 2018; Bayable et al., 2021; Degefu and Bewket, 2015; Eshetu, 2020). These investigations have revealed a noteworthy warming trend, with maximum temperatures exhibiting a more substantial increase compared to minimum temperatures, consequently leading to raised average temperatures across all agroecosystems and seasons in the Ethiopian highlands. Moreover, there is an apparent decreasing trend in rainfall Ademe et al. (2020), a result supported by Elzopy et al. (2021) for temperature but with no significant trend noted in seasonal and annual rainfall. Cheung et al. (2008) used the t-test parametric method and regression for annual time- series and found no significant changes in rainfall within an Ethiopian watershed. For the seasonal rainfall the test found significant decreases in June to September rainfall.

When considering regional trend analyses, Asfaw et al. (2018) observed an increase in annual temperatures in the Woleka Sub-basin, North-Central Ethiopia, attributed to rising minimum temperatures and a simultaneous decrease in both the 'Kiremt' season and annual rainfall. In the West Harerge Zone, Eastern Ethiopia, Bayable et al. (2021) noted a decreasing trend in rainfall for most months over the study period (1983-2019), though it wasn't statistically significant. On the other hand, (Degefu and Bewket, 2015) identified an increasing trend in the areal-averaged rainfall series for the bimodal regions of the Omo-Ghibe River Basin, Ethiopia.

When examining climatic extremes, Esayas et al. (2018) found a noticeable trends in climate extremes in Wolaita Zone, Southern Ethiopia. This study reveals a consistent increase in warm extremes, accompanied by a corresponding decrease in cold extremes. In contrast, there was no significant trend observed in rainfall extremes. Further insights from the CMIP5 database, as analyzed by Teshome and Zhang (2019), indicate a general decline in rainfall extremes, encompassing metrics such as annual total precipitation (PRCPTOT), Consecutive Wet Days (CWD), and the number of heavy rainfall days (R10 and R20), alongside a concurrent rise in the frequency of Consecutive Dry Days (CDD). This comprehensive analysis also underscores the presence of

a warming trend in Ethiopia when considering temperature extremes.

#### Hydrological variability and trend

In line with the analysis of climatic time series, the assessment of streamflow variability and trends can also be conducted using the range of techniques mentioned earlier. Tadese et al. (2019), in their study, employed a combination of graphical methods, descriptive statistics (including CV, Kurtosis, and Skewness), and the Mann-Kendall (MK) test. Their findings showed significant streamflow variability during the MAM and JJAS seasons, with an observed upward trend at the majority of monitoring stations in the upper and middle parts of the Awash Basin and a declining trend in the lower part of the basin.

The Mann–Kendall trend test, preceded by the correction of serial correlation, was employed in the study of streamflow variability within the Omo-Ghibe River basin (Degefu and Bewket, 2017). This analysis was conducted alongside the utilization of 14 indices derived from the daily streamflow data collected from 15 gauging stations. The results of the trend test revealed weak and non-systematic patterns of change in the annual, wet (Kiremt) season, and high flow magnitudes. However, a distinct increasing tendency was observed for low-flow magnitudes. In a separate investigation by Degefu et al. (2019), a combination of 10 streamflow indices and the Mann-Kendall test was used to assess the temporal characteristics of streamflow across various watersheds in Ethiopia. The study outcomes indicated a significant trend of increasing changes in mean annual and mean seasonal streamflow magnitudes for streams and rivers situated in the Ethiopian highlands.

### 2.1.2 Future Predicted Climate Change and Impacts

According to IPCC (2007), climate change is defined as a shift in climate conditions attributed either directly or indirectly to human activities. This alteration affects the composition of the global atmosphere and occurs in addition to natural climate variability observed over comparable time periods, which can arise from either natural or human-induced factors. Climate itself can be understood as the ”average” weather conditions prevailing in a specific location or region. It captures typical weather patterns for a given area, relying on long-term averages, often spanning decades or more. For instance, climate change might manifest as alterations in the climate normal, which represent the expected average values for temperature and precipitation. Climate change refers to transformations in the climate state that are apparent through shifts in the mean and/or variability of its properties. These changes typically persist for an extended period of

time, often spanning a decade or more.

#### Climatic models

Climate models serve as the fundamental tools for exploring how the climate system reacts to various forces. They enable us to make predictions about climate patterns over short-term (seasonal to decadal) and long-term (over the next century and beyond) timeframes (Flato et al., 2013). These projections of future climate changes are pivotal not only for enhancing our comprehension of the climate system but also for assessing the potential risks to society and identifying possible actions and strategies for addressing these challenges (O'Neill et al., 2016).

Climate models are mathematical representations of crucial processes within Earth's climate system (IPCC, 2014c). Like any mathematical model of natural phenomena, climate models simplify reality because our understanding of climate physics is not complete, and this simplification is necessary for computational efficiency. However, this simplification introduces inherent uncertainties or random model errors when comparing model-simulated statistical properties, such as mean and variance, to climatological observations. Consequently, using raw model data in impact studies can be limited (Cochard et al., 2018). Climate research employs a wide spectrum of models, ranging from straightforward energy balance models to complex Earth System Models (ESMs) that demand cutting-edge high-performance computing capabilities (Flato et al., 2013).

In the 1960s, scientists embarked on the development of the earliest primitive climate models, which featured basic representations of the atmosphere and ocean. These initial models were often one-dimensional and considerably less complex than their modern counterparts. However, climate modeling has seen substantial progress in recent years, driven by significant advancements in supercomputing technology, computational efficiency, and a deeper understanding of the Earth system. The latest generation of climate and Earth system models, such as those in the CMIP6 initiative, have incorporated numerous enhancements, including more accurate representations of physical, chemical, and biological processes, as well as increased spatial resolution. These improvements have led to more accurate simulations of recent climate conditions, encompassing key climate change indicators and various aspects of the Earth system (IPCC, 2021a).

Climate models can be categorized based on their spatial boundaries into two main types: regional climate models (RCMs) and global climate models (GCMs). RCMs offer higher spatial

resolution compared to GCMs, making them well-suited for simulating climate patterns at a more localized level. They can be integrated within a global model to provide finer-scaled simulations for specific regions. This becomes especially important when considering the impact of local topographical features, like mountains, on local climate changes. GCMs, due to their coarser resolution, may not capture small-scale topographical effects effectively, which highlights the importance of RCMs in providing a more detailed perspective.

Selecting suitable climate variables is a pivotal phase in climate change modeling, depending on the specific goals of the project or research at hand. For many investigations pertaining to climate change impacts and the assessment of water resource availability, historical and future data on precipitation and temperature constitute primary considerations. Precipitation serves as the driving force behind numerous processes that influence water resource availability, functioning as the principal input for the water balance equation. Simultaneously, temperature substantially influences the magnitude of water loss, particularly in tropical and subtropical regions worldwide.

#### Climate Change scenarios

Due to the inherent complexity of the Earth's climate system and our limited understanding of its complexity, precise predictions of climate change remain challenging. As a result, climatologists often rely on climate change scenarios as a valuable tool in their research (IPCC, 2007). These scenarios offer insights into potential future trajectories of key factors driving climate change, including greenhouse gases, chemically reactive gases, aerosols, and land use. Significantly, these scenarios are customized to align with various socioeconomic developments, making them essential inputs for climate model simulations (O'Neill et al., 2016). Furthermore, climate scenarios serve as the foundation for assessing potential climate impacts and identifying strategies for mitigation, along with their associated costs (van Vuuren et al., 2011).

In the year 2000, the Intergovernmental Panel on Climate Change (IPCC) released its Special Report on Emissions Scenarios (SRES), presenting four distinct scenario families designed to encompass a spectrum of potential future conditions (IPCC, 2007). Identified using alphanumeric combinations like A1, A2, B1, and B2, each scenario was crafted through a complex interplay between socioeconomic factors influencing greenhouse gas and aerosol emissions and the projected magnitudes of these emissions over the course of the 21st century. Subsequently, the IPCC Third Assessment Report (TAR) and Fourth Assessment Report (AR4), published in

2001 and 2007 respectively, relied on these SRES scenarios.

In 2013, climate scientists reached a consensus on a fresh set of scenarios, which placed their focus on the anticipated levels of greenhouse gases in the Earth's atmosphere by the year 2100 (IPCC, 2014c). This collective set of scenarios is now widely recognized as the Representative Concentration Pathways, or simply RCPs. Each RCP is a numerical representation of the climate forcing potential, quantified in Watts per square meter, that would arise from greenhouse gases present in the atmosphere by the year 2100 (van Vuuren et al., 2011). These values, along with their associated rate and trajectory of forcing, are crucial components used in configuring climate models, much like their predecessors.

Global atmospheric general circulation models (GCMs) have been developed to simulate the current climate and predict future climatic changes, particularly leading up to the IPCC AR6. In parallel, the energy modeling community has introduced a novel set of emissions scenarios, known as Shared Socioeconomic Pathways" (SSPs), driven by diverse socioeconomic assumptions. These SSP scenarios were selected to drive the climate models for CMIP6. Specifically, a subset of scenarios was selected to provide a spectrum of potential end-of-century climate outcomes. In IPCC AR5, four Representative Concentration Pathways (RCPs) were used to explore various future greenhouse gas emission possibilities. These scenarios, namely RCP2.6, RCP4.5, RCP6.0, and RCP8.5, have updated versions in CMIP6. These revised scenarios are referred to as SSP1-2.6, SSP2-4.5, SSP3-7.0 (newly introduced), and SSP5-8.5, each of which results in 2100 radiative forcing levels comparable to their predecessors in AR5.

#### Downscaling and bias correction of climate model data

GCMs typically possess a relatively coarse spatial resolution, which poses a challenge when applying them to regional ecohydrological studies. Consequently, a process known as downscaling becomes essential to obtain accurate input data for hydrological models (Hesse et al., 2015). Moreover, direct utilization of GCM outputs in impact studies is uncommon due to inherent systematic errors, or biases, present in these models. These biases can arise from factors such as limited spatial resolution, simplified representations of physical and thermodynamic processes, numerical schemes, or incomplete knowledge of climate system intricacies (Navarro-Racines et al., 2015). Therefore, it becomes imperative to downscale and bias-correct the raw outputs from climate models to generate climate projections better suited for impact modeling.

High-resolution projections of the Earth's future climate are of paramount significance in various climate-related studies, encompassing investigations into climate extremes, water resources, agriculture, air quality, and wind power. Several common approaches have been employed to produce such high-resolution projection data, including interpolation, statistical downscaling, dynamical downscaling, and hybrid statistical-dynamical downscaling.

Simultaneously, bias adjustment plays a crucial role by statistically transforming climate model data to mitigate systematic discrepancies when compared to a reference dataset typically derived from observations (Berg et al., 2022). Various methodologies have been proposed to perform these adjustments, ranging from straightforward scaling techniques to more advanced approaches based on multivariate distribution mapping (Maraun, 2016; Teutschbein and Seibert, 2012). Primary adjustment methods include adjustments based on the mean, mean and variance, and quantile values. Notable techniques include linear scaling, local intensity scaling, power transformation, distribution mapping, and quantile mapping (Teutschbein and Seibert, 2012).

#### Climate change impact on basin hydro-climatic

The impacts of climate change on the hydrological cycle in general and on water resources in particular are of high significance due to the fact that all natural and socio/economic system critically depends on water. The direct impact of climate change can be variation and changing pattern of water resources availability and hydrological extreme events such as floods and droughts, with many indirect effects on agriculture, food and energy production and overall water infrastructure. To this end, several individual researches have been done to study the impacts of climate change on the water resources of Ethiopian river basins from one or more GCMs, emission scenario(s), and downscaled GCM output for driving a hydrological model.

Abebe and Kebede (2017) assessed climate change impacts in the Megech River catchment, Ethiopia, using the Regional Climate Model (REMO) for future periods (2015-2050) under the A1B and B1 emission scenarios. They downscaled the REMO data to the station level with SDSM v5.1.1 for the HBV-Light hydrological model. Projected mean monthly maximum temperatures are expected to increase (A1B: +0.1 °C to +0.51 °C, B1: +0.12 °C to +0.57 °C). The mean monthly precipitation was projected to decrease (A1B: -1.14% to -31.88%, B1: -1.6% to -36.42%). The results also indicate a reduced peak discharge in August and September, a shift in the wet season to May-July, and a decreasing trend in dry season low flow, except for April,

which increased.

Ayele et al. (2016) evaluated the influence of climate change on the Gilgel Abbay watershed through the application of statistical downscaling and the GWLF hydrological model. Seven distinct climate models (GCMs) were utilized to examine the watershed's response. The study considered both RCP 8.5 and RCP 4.5 scenarios, focusing on two time frames: 2021-2040 and 2081-2100. The results indicated an estimated reduction of approximately 11.6% and 10.1% in runoff volume during the wet season for the 2080s, depending on the emission scenario. It was further observed that alterations in precipitation patterns significantly impacted the seasonal flow variability, subsequently affecting the storage and discharge capacity of Lake Tana.

WaleWorqlul et al. (2018) assess climate change's impact on water availability and variability in two upper Blue Nile basin subbasins in Ethiopia, using the HBV model. It compared future climate data downscaled from HadCM3, considering A2 and B2 scenarios, with a 1961–1990 baseline. The findings indicated potential alterations in rainfall patterns, with no consistent trends in primary rainy months (June and July), a decline in May and June, and an increase in September, October, and November. Additionally, a steady increase in both minimum and maximum temperatures was observed across all timeframes (2030s, 2060s, and 2080s), intensifying toward the century's end. This temperature rise is expected to disrupt the hydrological cycle, leading to a 2% increase in evapotranspiration by the 2030s, 4.7% by the 2060s, and 7.8% by the end of the century. Furthermore, the monthly streamflow hydrograph suggested potential dry season increases in both subbasins, with the most substantial monthly flow surge projected for November in the 2060s and 2080s. However, it's essential to acknowledge study limitations, including uncertainties tied to climate change projections, GCM models, emission scenarios, and hydrological modeling.

Taye et al. (2018) quantified the potential impact of climate change on water availability within the Awash basin across various seasons. They employed three climate models sourced from the Coupled Models Inter-comparison Project phase 5 (CMIP5) and examined three future periods (2006–2030, 2031–2055, and 2056–2080). The findings across these future periods consistently pointed to an increase in water deficiency across all seasons and within specific parts of the basin. This unfavorable trend was primarily attributed to the projected increase in temperature coupled with a decrease in precipitation. The research highlights the significant implications of climate

change on water resources within the Awash basin, particularly heightening water stress in the irrigation sector and posing challenges for water allocation practices.

Tesfaye et al. (2014) examined surface runoff sensitivity to climate change in Ethiopia's Geba catchment for the 2020s, 2050s, and 2080s within the Geba catchment, situated in the Tekez Basin of Ethiopia. They used SDSM 4.1 to downscale HadCM3 GCM data for A2a and B2a scenarios and the WetSpass model for runoff estimation. Interestingly, downscaled precipitation data showed no consistent trend, but all scenarios indicated significant warming. This warming trend is expected to substantially reduce annual runoff, leading to pronounced seasonal and monthly variations. During the main rainy season (June-September), runoff is projected to decrease by 12.9% (A2) and 11.1% (B2) in the 2080s, highlighting the impact of climate change on the Geba catchment's hydrology.

In the Upper Wabe Shebele River Basin, Gurara et al. (2021) assessed climate change's impact on streamflow using the SWAT model and CORDEX-Africa climate model data for RCP4.5 and RCP8.5 scenarios. Their analysis covered two future periods: 2041–2070 and 2071–2099. The results indicated substantial climate shifts, with mean temperatures projected to rise by 3.46 °C and 5.15 °C (RCP4.5) and 4.78 °C and 5.88 °C (RCP8.5) in the mid and long-term periods. Annual precipitation showed a pronounced upward trend, with anticipated increases of +26.3% (RCP4.5) and +31.85% (RCP8.5) by the century's end. During the Kiremt (rainy) season, precipitation substantially increased by +44.28% (RCP4.5) and +59.34% (RCP8.5). Conversely, the Bega (dry) season exhibited a declining trend. Crucially, annual streamflow projections consistently showed increases under both scenarios across both projection periods. These findings underscore the significant climate-induced transformations anticipated in the Upper Wabe Shebele River Basin, carrying implications for water resource management and ecosystem dynamics in the region.

Probst and Mauser (2023) assessed climate change's impact on key hydrological factors in the Danube River Basin (DRB). It considered parameters like temperature, precipitation, soil water content, plant water stress, snow water equivalent (SWE), and runoff dynamics. Using the PROMET model driven by EURO-CORDEX climate projections, it examined RCP2.6 and RCP8.5 scenarios for the near (2031–2060) and far (2071–2100) future against a reference period (1971–2000). Results showed moderate impact under RCP2.6 and severe under RCP8.5, with

year-round warming trends, wetter winters in the Upper Danube, drier summers in the Lower Danube, reduced summer soil water, increased plant stress, and less SWE. River discharge seasonality shifted, raising high flow risks throughout the Danube mainstream and low flow risks in the Lower Danube River. These findings feature climate change's profound impact on the DRB's hydrology.

## 2.2 Land Use Land Covers Change

Since the beginning of civilization, humans have deliberately managed and converted the landscape to derive valuable natural resources such as food, fiber, fresh water, and pharmaceutical products (Goldewijk and Ramankutty, 2004). Since humans have controlled fire and domesticated plants and animals, they have cleared forests to wring higher value from the land. About half of the ice-free land surface has been converted or substantially modified by human activities over the last 10,000 years (Lambin et al., 2003). Thus, the footprint of human disturbance on the land ecological through land use land cover change is becoming larger and larger. Concerns about land use land cover change emerged in the research agenda on global environmental change several decades ago with the realization that land surface processes influence climate (Lambin et al., 2003; Swarna Latha and Rao, 2020).

Although the terms land cover and land use are often used interchangeably, their actual meanings are quite distinct. Land cover refers to the surface cover on the ground, whether vegetation, urban infrastructure, water, bare soil or other. Land use refers to the purpose the land serves, for example, recreation, wildlife habitat, or agriculture. Identification of land cover establishes the baseline from which monitoring activities (change detection) can be performed, and provides the ground cover information for baseline thematic maps. Land use applications involve both baseline mapping and subsequent monitoring, since timely information is required to know what current quantity of land is in what type of use and to identify the land use changes from year to year. This knowledge will help develop strategies to balance conservation, conflicting uses, and developmental pressures. Issues driving land use studies include the removal or disturbance of productive land, urban encroachment, and depletion of forests.

### 2.2.1 Data Sources and Classification Techniques

The studies of LULC change has used different source of data based on the advancement of remote sensing and GIS technologies. In first of 19 centuries, Arial photo captured from lower

altitude using short range camera mounted on birds and small aircraft were the data source before 1980 (source). Later, due to the development of aviation industries, high altitude aircraft were used to collect aerial photo covering vast area. In 1972, land observational satellite named Landsat1 were launched by NASA even though the data has been made public in 1984 (Loveland and Dwyer, 2012). In late 2008, following changes to the USGS-NASA Landsat data policy, the U.S. Department of the Interior announced that all Landsat data would be "web-enabled", meaning that a standard Landsat product would be made available from the USGS archives via electronic distribution at no cost to the end user (Loveland and Dwyer, 2012). In the short time since the USGS made their entire Landsat archive available to anyone at no cost via the Internet, significant benefits are already being realized within the Landsat data user community (Loveland and Dwyer, 2012). Currently, Landsat images are by far the most utilized sources of satellite images. Thus, land use land cover studies covering period starting from 1984 relies on satellite images.

Satellite image is a relatively inexpensive and rapid method of acquiring up-to-date information over a large geographical area owing to its synoptic coverage and repetitive measurements. Remote-sensing data usually acquired in digital form are easier to manipulate and analyze; they can be acquired not only from visible but also from spectral ranges that are invisible to human eyes; they can be acquired from remote areas where accessibility is a concern; and they provide an unbiased view of land use/land cover. Remote sensing data and geographic information system are increasingly becoming important tools in hydrology and land use land cover analysis. This is due to the fact that most of the data required for hydrological and land use land cover analysis can easily be obtained from remotely sensed images. Remote sensing has the capability to acquire signatures instantaneously over large areas. The selection of the satellite data mainly relays on the objective of the study and the quality of the data required.

After acquiring and preprocessing the satellite image for land use land cover change analysis, Classifying remote sensing imageries to obtain reliable and accurate land use land cover (LULC) information still remains a challenge that depends on many factors such as complexity of landscape, the remote sensing data selected, image processing and classification methods, etc (Manandhar et al., 2009). There are several methods and techniques for satellite image classification (Abburu and Golla, 2015). Broadly, classified into land use land cover mapping through image classification per-pixel image classification and Object-based image analysis.

Likewise, pixel based classification further categorized into supervised and unsupervised techniques. Unsupervised classification is a means by which pixels in an image are assigned to spectral classes without the user having foreknowledge of the existence or names of those classes. It is performed most often using clustering methods. The analyst then identifies those classes afterwards by associating a sample of pixels in each class with available reference data, which could include maps and information from ground visits. Whereas, supervised classification relays on prior knowledge of the study area to assign training sites for each LULC classes on the ground. Supervised classification can be much more accurate than unsupervised classification, but depends heavily on the training sites, the skill of the individual processing the image, and the spectral distinctness of the classes (Tempfli et al., 2013). A variety of algorithms is available for this, ranging from those based upon probability distribution models for the classes of interest to those in which the multispectral space is partitioned into class-specific regions using optimally located surfaces (Richards and Jia, 2006). The choice of the algorithm depends on the purpose of the classification, the characteristics of the image, and training data (Tempfli et al., 2013).

There is no standard method for choosing and applying classification techniques and algorithms in satellite image classification. Supervised classification is the procedure most often used for quantitative analysis of remote sensing image data (Richards and Jia, 2006). It rests upon using suitable algorithms to label the pixels in an image as representing particular ground cover types, or classes. Similarly, numerous researchers have used supervised classification technique for satellite image classification in Ethiopia (Kenea et al., 2021; Markos et al., 2018). Whereas, the hybrid classification technique, which combines both unsupervised and supervised classification techniques, was used to improve the accuracy of the classification (Betru et al., 2019; Gashaw et al., 2017; Shawul and Chakma, 2019; Wang et al., 2020).

Finally, a fundamental feature of significance to the user of the land use land cover data is its quality. Therefore, classification of satellite image should be reported with a standard method of evaluation of classified thematic map. Kappa statistics the common index to evaluate the classified image with existing high resolution map or training ground control points (GCPs) (Olofsson et al., 2014; Richards and Jia, 2006; Rwanga and Ndambuki, 2017). In data scarcity area, high-resolution images from Google Earth Engine were also used as a supplementary tool (Betru et al., 2019).

### 2.2.2 Future LULC Prediction Methods

Modeling of future changes in land use cover over time is important for multiple reasons. Firstly, these models serve as invaluable tools for predicting future land use land cover patterns. Such predictions find application across various domains, including hydrological modeling, where impermeable surfaces play a pivotal role, landscape assessments concerning their impact on conservation and biodiversity, and the evaluation of forthcoming carbon budgets. Secondly, retrospective modeling of historical land use and cover changes offers valuable insights into underlying processes and the effectiveness of land use planning policies.

In the literature, there are two commonly used methods for projection of future LULC projection; the first one is based on theoretical/planned/expert assumption or storyline, and the second one is based on modeling using different algorithms capable of temporal and spatial transformation. Future land use is greatly influenced by current land use, autonomous socio-economic developments, and spatial policies, and long-term climate changes, and other changes in the physical environment (Dekkers and Koomen, 2005). By using scenarios, hypotheses about developments in government policy, socio-economic factors, the climate, and the physical environment can be combined. Various studies have already begun developing these scenarios (Hu et al., 2019; Pikounis et al., 2003). Under this approach, a panel of experts is convened to consider possible 'alternative futures' affecting the underlying drivers of land use / cover change. This expert panel will develop a set of possible concrete future scenarios for the underlying drivers that could affect land use land cover in a given area.

The other method of future land use land cover projection includes Markov chain and cellular automata modeling. A Markov chain is a relatively simple means of modelling how land use cover changes over time. In a classic Markov chain, the probability that a given area will change its land use land cover between one time period and the next depends on only one thing: its land use land cover in the initial time period. In order to model the relationship between land use/cover in an initial time period, and land use land cover in a subsequent time, a transition probability matrix is often used. Such a matrix shows the probability of a land use land cover change from one state to another taking place within a specified time period.

Whilst Markov chains are attractive because of their simplicity, they do make a number of assumptions that are unlikely to be met in 'real world' situations. For this reason, other approaches

have been adopted that relax some of these assumptions. One such approach is the cellular automata methodology, in which the future state of a given grid square or parcel depends not only on its current state, but also on the current state of surrounding grid squares. The approach can be further modified so that – for example, transition probabilities depend on the suitability of a given grid square for a particular land use. Numerous researcher have used cellular automata to project future LULC in Ethiopia and abroad (Baig et al., 2022; Girma et al., 2022; Islam et al., 2023; Lukas et al., 2023; Kafy et al., 2021; Kamaraj and Rangarajan, 2022). Some used hybrid classification techniques to analyse the satellite images and CA-Markov models for predicting land use changes (Gashaw et al., 2017).

The land use land cover maps that are generated can serve as input data for specialized hydrological tools, enabling the assessment of how changes in land use affect water scarcity (Dekkers and Koomen, 2005). The anticipated consequences of these impacts could potentially necessitate revisions to existing policies.

### 2.2.3 LULC Change and Impact Studies

Understanding and monitoring land use land cover change is vital for addressing issues such as land degradation, deforestation, and climate change at both local and global levels. This knowledge helps predict future changes, informs effective land management policies, and underscores the critical role that land use and cover changes play in shaping the environment (Muluneh, 2010). These changes impact ecosystems by directly altering both aquatic and terrestrial systems and contribute significantly to climate change by emitting carbon (Muluneh, 2010). Over the past three decades, research on land use land cover change has become widespread across various regions, reflecting their increasing importance in addressing pressing environmental challenges.

#### LULC Changes

To use land and land resources optimally, it is not only necessary to have the information on existing land use land cover but also the capability to monitor the dynamics of land use resulting out of both changing demands of increasing population and forces of nature acting to shape the landscape. Numerous researcher have tried to quantify the magnitude and rate change in LULC change in Ethiopia, and abroad. Conversion of vegetated land into cultivated, built-up/settlement, and degraded land was the most reported in different parts of the world which become a general truth.

According to Lambin et al. (2003), FAO estimated that tropical regions lost 15.2 million hectares of forests per year during the 1990s. In the past few decades, significant losses in forests and shrub land and significant increase in agricultural land reported (Amsalu et al., 2006; Betru et al., 2019; Garedew et al., 2009; Gashaw et al., 2017; Hailemariam et al., 2016; Kenea et al., 2021). Unlike, significant loss of agricultural land was found in the Kathmandu district of Nepal (Wang et al., 2020). Water body converges also showed decreased pattern (Shawul and Chakma, 2019; Wang et al., 2020). Similarly, grass land coverage depicted a decreasing pattern (Gashaw et al., 2017; Meshesha et al., 2016; Shawul and Chakma, 2019).

#### LULC change impacts on hydrological processes

Land use land cover changes have a wide range of impacts on environmental and landscape attributes including the quantity and quality of water, land and air resources, ecosystem processes and functions. The impacts of land use land cover change on water resources are influenced by interactions with other factors, including climate variability and anthropogenic activities. Researchers have been studying the impact of land use land cover change on hydrological processes.

Alibuyog et al. (2009) used the SWAT model to assess land-use changes in Philippine watersheds. Results showed a 3% to 14%increase in runoff volume and a 200% to 273% increase in sediment yield when converting 50% of pasture and grasslands to agriculture. This led to a 2.8% to 3.3% decrease in baseflow, with the higher value indicating no soil conservation intervention. Converting the entire sub-watershed to agriculture increased runoff volume by 15% to 32%. Mango et al. (2011) found land use changes, particularly deforestation, have resulted in reduced baseflow and average flow in river basins in the upper Mara River Basin, Kenya. Their study also suggested, the conversion of forest to agricultural and pasture lands has led to a decrease in precipitation and an increase in evapotranspiration, which reduces runoff. This dynamic is further exacerbated by projected increases in temperature.

Similarly, Wang et al. (2014) found inverse relationships between forest cover and water yield whereas this indicates that land use changes, such as urbanization and deforestation, can lead to an increase in runoff. Getahun and Haj (2015) assessed land use-cover change impacts on the Melka Kuntrie sub-basins hydrology in the Upper Awash River Basin. They used the semi-distributed HBV hydrological model and Landsat imagery for 1986 and 2003. The results indicated reduced evapotranspiration in the 2003 land use. Streamflow increased by 25% in June, 4% in July, 6% in August, and 9% in September, corresponding to 0.065 mm/day, 0.077 mm/day,

0.07 mm/day, and 0.039 mm/day, respectively, during the main rainy season compared to 1986 land use.

In their study, Gessesse et al. (2019) explored the hydrological impact of land use land cover changes in the Choke mountain range, utilizing remote sensing and the SWAT model in Muga and Suha watersheds. Their findings indicated that between 1985 and 2004, total annual surface and lateral streamflows increased by 1.2 mm/year and 0.57 mm/year, respectively. Meanwhile, annual groundwater flow and percolation decreased by 1.6 mm/year and 1.77 mm/year. The reduction in streamflow was more notable during the dry season (October to May), with significant baseflow declines of 0.37 m3/year in Muga and 0.73 m3/year in Suha watersheds. Conversely, in the wet season (June to September), peak flow exhibited a 50% increase in Muga and a 94% increase in Suha watersheds. Näschen et al. (2019) examined historical LULC patterns and projected future LULCC impacts on water quantities in a complex Tanzanian tropical catchment. They employed the Land Change Modeler (LCM) for LULC analysis until 2030 and the SWAT model to simulate water balance under diverse LULC conditions. Findings indicate a 6-8% decrease in low flows under LULC scenarios, while high flows increase by up to 84% in combined LULC and climate change scenarios.

Engida et al. (2021) highlighted the profound impacts of land use land cover changes in Ethiopia's Upper Baro Basin. These changes, including reduced forest cover due to logging and agricultural expansion, conversions of grasslands and bushes to farmland, and increased settlements, occurred over three decades. These alterations significantly affected the basin's hydrological regime, impacting streamflow characteristics like flood frequency, peak flows, base flow, soil erosion, and annual mean discharge. Notably, they led to increased surface runoff, reduced groundwater and lateral flow, and soil erosion, resulting in the loss of essential nutrients. Aredo et al. (2021) observed that the mean monthly streamflow exhibited an increase during the wet season, contrasting with a decrease during the dry season as a consequence of a significant expansion of settlement and agricultural area, while there was a decrease of bare land, forest, and bushland in the Shaya catchment by employing the MIKE SHE hydrological model the catchment.

Contrary to others, Owuor et al. (2016) investigated the effect of land use land cover changes on groundwater recharge and surface runoff in semi-arid environments. Studies have shown that

the conversion of forest land or native vegetation to managed land use types, such as agricultural fields, can lead to increased groundwater recharge. Forests have been found to have lower groundwater recharge rates and runoff compared to other land uses in semi-arid regions. On the other hand, the conversion of grassland to forest vegetation can result in reduced surface runoff. In addition, the effects of land use change on groundwater recharge and surface runoff are influenced by factors such as soil texture and the specific types of land use involved. Additionally, Birhanu et al. (2019) quantified the rate of LULC in the Gumara catchment, an important tributary of Lake Tana in northwest Ethiopia. Landsat images from three years (1986, 2001, and 2015) were processed using the supervised classification method. Contrary to the expected impact of LULC changes on hydrology, only a slight change in water balance components (±5%) was observed using the HBV model. Runoff and all other water balance components remained stable despite considerable LULC changes.

Overall, it's important to note that the impacts of LULCC can vary widely depending on the specific changes and the context in which they occur. Sustainable land management practices and informed land-use planning are essential for minimizing negative impacts and promoting environmental and societal well-being.

#### Drivers of land use land cover change

Land use land cover change (LULCC) is driven by a complex interplay between natural and human forces (Amsalu et al., 2006). Natural drivers, such as climate change, exert their influence gradually over extended periods, whereas human drivers often manifest more immediately and can be quite extreme. One of the foremost human-driven factors behind LULCC, globally, including Ethiopia, is population growth. The increasing population necessitates increased land for agriculture, fuelwood production, charcoal production, and infrastructure development (Amsalu et al., 2006; Betru et al., 2019; Kenea et al., 2021; Reis, 2008). In various parts of Ethiopia, such as the central Rift Valley, Garedew et al. (2009) identified population growth, recurrent droughts, rainfall variability, and declining crop productivity as the key drivers of LULCC. Moreover, in the Derekolli catchment, factors such as population growth, drought, limited cultivated land availability, and land tenure systems have collectively contributed to observable land cover changes (Belay Tegene, 2002).

In the Bale mountain eco-region of Ethiopia, Hailemariam et al. (2016) pinpointed farmland expansion and population growth as major drivers of LULCC and deforestation. These alter-

ations in land cover are closely tied to human activities such as forest clearance for agriculture and housing (Kenea et al., 2021). Betru et al. (2019) categorized LULCC drivers in western Ethiopia into proximate and underlying causes. Proximate drivers, including agricultural expansion, over-extraction of forest resources (e.g., fuelwood and charcoal), and forest fires, are instrumental in deforestation. Meanwhile, the increasing human population has served as a significant underlying cause, driving both agricultural expansion and overexploitation of forest resources.

Furthermore, a decline in per capita cropland and limited increases in crop yields prompted farmers to explore alternative land uses, such as grazing land and plantations, influenced by socio-economic factors, policy changes, and the introduction of crossbred cattle (Amsalu et al., 2006; Gashaw et al., 2017). These complex interactions underline the multifaceted nature of LULCC drivers and their implications in land and resource management.

## 2.3 Hydrological Models Classification and Selection

Hydrological models play a crucial role in understanding and managing water resources, making them indispensable tools in environmental studies and water management. These models serve as simplified representations of the hydrological cycle or/and its components (Refsgaard, 1996; Singh, 2018). Moreover, hydrologic models are rooted in our interpretation and comprehension of hydrologic processes. They make use of numerous mathematical equations that incorporate parameters and variables to effectively represent hydrological phenomena (Devia et al., 2015). In this context, a variable can be defined as any characteristic of a system that exhibits variations in numeric value over time or space (Singh, 1988), with examples including daily precipitation, evaporation, and temperature. On the other hand, a parameter represents a quantity that characterizes a hydrologic system and tends to remain constant over time include hydraulic conductivity, time of concentration, and Manning's roughness factor (Clarke, 1973; Singh, 1988).

The complexity of hydrologic models varies from simpler data-driven models to more intricate process-oriented ones. The optimal model is the one that closely approximates reality while employing minimal parameters and model complexity (Devia et al., 2015). Models are commonly employed to predict system behavior and enhance our understanding of diverse hydrological processes. Nowadays, hydrological models are regarded as indispensable tools for effective water

and environmental resource management. The classification of hydrologic models holds significance due to their distinctive as well as shared properties (Pechlivanidis et al., 2011). Previous studies have explained various methods for categorizing hydrological models, considering their inherent characteristics.

### 2.3.1 Classifications of Hydrological Models

Hydrologic models can be classified as deterministic or stochastic models based on the presence of randomness (Pechlivanidis et al., 2011; Singh, 2018). Deterministic hydrological models produce similar outputs for the same input data and fixed parameter values, functioning without accounting for randomness. These models are primarily oriented towards making forecasts and can be further categorized into steady flow and unsteady flow hydrological models. Conversely, stochastic hydrological models introduce an element of variability by generating different output values for a single set of input parameters. These models inherently incorporate randomness into their outputs, reflecting varying degrees of uncertainty. The output of a stochastic model follows a statistical distribution, effectively capturing uncertainties originating from input variables, boundary conditions, or model parameters (Refsgaard, 1996; Singh, 2018). These models are utilized for making predictions and can be classified into various subtypes, including time-independent, time-correlated, and space-correlated variations. A mixed deterministic-stochastic model, achieved by integrating stochastic error models into deterministic models (Pechlivanidis et al., 2011). This integration enables the combination of deterministic predictive capabilities with the stochastic representation of uncertainties, enhancing the model's overall utility and accuracy.

Deterministic hydrological models can be classified based on spatial representation: Lumped, Distributed, and Semi-Distributed models (Pechlivanidis et al., 2011; Singh, 2018; Sitterson et al., 2017). Lumped models work based on treating an entire basin as a single entity, disregarding spatial variability in their approach (Singh, 2018; Sitterson et al., 2017). In such hydrological models, the input parameters do not represent the physical features of hydrological processes. Instead, they utilize spatially averaged or mean values to depict watershed characteristics, including factors such as soil type, land use, and slope. A defining characteristic of lumped models is their focus on simulating total runoff and streamflow solely at the outlet point, without examining into specific flows within a catchment (Sitterson et al., 2017). Due to their simplicity, these models necessitate minimal input data to operate effectively. Their design revolves around a straightforward representation of hydrological behavior in a catchment, making

them suitable for scenarios where a broad overview suffices.

In contrast, distributed models are the most complex because they account for spatial heterogeneity in inputs and parameters (Sitterson et al., 2017). These models achieve this by dividing catchments into multiple grid cells or elements and then solving the equations that define the state variables for each element or grid cell (Pechlivanidis et al., 2011). Distributed models offer the advantage of addressing the spatial variability of catchment characteristics, input variables, and parameters to a certain extent. The governing physical processes occurring in nature are modeled in detail in these models (Singh, 2018). Typically, distributed models are governed by partial differential equations. However, distributed models do come with certain drawbacks. One of these is the substantial amount of data and computing power required to accurately account for the spatial variability of model parameters.

Semi-distributed models combine the advantages of distributed and lumped models. The input parameters in a semi-distributed model are allowed to vary in space partially by dividing the basin into several smaller sub-basins (Pechlivanidis et al., 2011; Singh, 2018). The unique advantage of a semi-distributed model lies in its ability to strike a balance between computational efficiency and spatial detail. With this model, computational time remains relatively short, and the reliance on data inputs and parameters is reduced compared to a fully distributed model (Pechlivanidis et al., 2011). Often, these models are preferred due to constraints related to data availability. They cover a wide spectrum ranging from lumped to distributed models, accommodating various degrees of spatial resolution and complexity.

Deterministic hydrological models can also be categorized based on their structural nature, encompassing empirical, conceptual, and physically-based models. Empirical or metric models primarily focus on observation data without considering the complicated features and processes of the hydrological system (Singh, 2018). Consequently, these models are often referred to as data-driven models (Sitterson et al., 2017). In these models, equations are constructed based on the observed input-output relationships, rather than being derived from the physical properties of catchments or hydrologic processes. Statistical techniques like regression and correlation are employed to establish these input-output correlations.

Conceptual models serve as simplified representations of the complex runoff generation pro-

cesses within a catchment (Dwarakish and Ganasri, 2015; Singh, 2018; Sitterson et al., 2017). These models describe the various hydrological processes, presenting an overview of the component interactions (Pechlivanidis et al., 2011). Comprising interconnected reservoirs, conceptual models match the physical elements of a catchment. These reservoirs are replenished by factors like rainfall, infiltration, and percolation, while they are depleted by processes such as evaporation, runoff, and drainage (Singh, 2018). The functionality of a conceptual model rests on two fundamental criteria. First, the model's structure is defined prior to the commencement of the modeling process. Second, it is often not feasible to determine all model parameters based solely on the physical properties of the watershed. Consequently, certain parameters within the model are established through a calibration process. These models demonstrate how conceptual approaches can effectively capture key hydrological behaviors while accommodating the limitations inherent to empirical derivations.

On the other hand, Physical models, also called process-based or mechanistic models, are based on the understanding of the physics related to the hydrological processes (Refsgaard, 1996; Singh, 2018; Sitterson et al., 2017). These models rely on established physics laws and principles, incorporating water balance equations, principles of mass and energy conservation, momentum considerations, and kinematics (Sitterson et al., 2017). Notable equations such as St. Venant, Boussinesq's, Darcy, and Richard's equations are harnessed by physical models (Pechlivanidis et al., 2011; Refsgaard, 1996). The distinctive feature of physically-based models lies in their capability to offer continuous runoff simulations using quantifiable parameters, often without requiring extensive calibration. These parameters are typically derived from laboratory experiments or small-scale in-situ studies. It's worth noting that the spatial heterogeneity present in larger catchments poses limitations on the applicability of physically-based models, making them more suitable for small-scale investigations. Nevertheless, their greatest strength lies in the direct link between model parameters and the physical characteristics of the catchment, which enhances their realism.These models showcase how a physics-based approach can offer a robust representation of complex hydrological dynamics while being grounded in well-established scientific principles.

### 2.3.2 Choosing Appropriate Hydrological Model

Numerous studies revealed the uses, abilities, and performances of different models in simulating the hydrological processes of watersheds under changing climate and land use land cover.

Each type of hydrological model serves a specific purpose, and it's important to note that no particular model type can be universally considered more suitable than others in every scenario. The appropriateness of a model structure is greatly influenced by the intended function it is supposed to fulfill (Merritt et al., 2003). However, it is a quite challenging task to select the right hydrological model which can simulate specific watershed hydro-climatological and geophysical processes. This selection process often takes into account factors such as data availability, spatial representation, computational complexity, and the model's overall robustness (Pechlivanidis et al., 2011). In general, physically-based semi distributed models are very flexible to represent the real ground features and simulating the hydro-geophysical processes of watersheds (Arnold et al., 1998; Chen and Mackay, 2004; Gebreyohannes et al., 2013; Yen et al., 2016). In this study, the Soil and Water Assessment Tool (SWAT) was chosen as the most suitable model (Arnold et al., 2012; Neitsch et al., 2011; Gassman et al., 2007). Moreover, hydrological models are valuable to simulate watershed hydrology and sediment yield in data-scarce regions.

In general, when deciding on a hydrological model, one should consider the research or project's objectives and scale. Given the extensive studies conducted using the SWAT model, its consistently satisfactory performance, adaptability in data-scarce regions, and access to global datasets, and the choice to employ the SWAT model for this study in the WSRB was well-founded. The following sections detail the attributes of the SWAT model that substantiate its selection for this research effort.

## 2.4 SWAT Model Description

The Soil and Water Assessment Tool (SWAT) model, developed to predict the impact of land management practices on water, sediment, and agricultural chemical yields in large watersheds with varying soils, land use, and management conditions over long periods, is a crucial tool for hydrological research (Arnold et al., 2012, 1998). This hydrological model, created by the United States Department of Agriculture's Agricultural Research Service (USDA-ARS), operates as a continuous-time, semi-distributed, process-based river basin model (Arnold et al., 2012; Gassman et al., 2007) . Since its inception in the early 1990s as version 94.2, SWAT has undergone significant development and refinement, with continued reviews and expansion of its capabilities (Neitsch et al., 2011; Gassman et al., 2007).

The model encompasses a comprehensive range of components, totaling eight major categories:

weather, hydrology, soil temperature and properties, plant growth, nutrients, pesticides, bacteria and pathogens, and land management (Neitsch et al., 2011; Gassman et al., 2007). Within the realm of hydrological processes, SWAT provides a multifaceted simulation that covers a spectrum of phenomena. These processes include canopy storage, surface runoff, infiltration, evapotranspiration, lateral flow, tile drainage, redistribution of water within the soil profile, and potential consumption through pumping, return flow, and recharge by seepage from surface water bodies, ponds, and tributary channels (Arnold et al., 2012).

In SWAT, the approach to address the large-scale spatial heterogeneity of the study area involves dividing the watershed into sub-basins (Arnold et al., 2012; Neitsch et al., 2011; Gassman et al., 2007). Each of these sub-basins is further refined by discretizing them into a series of hydrologic response units (HRUs), each characterized by unique combinations of soil type, land use, and slope (Arnold et al., 1998; Neitsch et al., 2011). Within these HRUs, the model simulates various parameters, including soil water content, surface runoff, nutrient cycles, sediment yield, crop growth, and management practices. These individual HRU simulations were then aggregated for the sub-basins using a weighted average approach (Arnold et al., 2012). Moreover, physical characteristics such as slope, reach dimensions, and climatic data were carefully considered for each sub-basin to ensure a comprehensive representation of the spatial variability of the study area.

The hydrological cycle, which plays a pivotal role in SWAT's modeling framework, is primarily influenced by climatic factors. These climate-driven processes deliver crucial moisture and energy inputs, including daily precipitation, maximum/minimum air temperature, solar radiation, wind speed, and relative humidity, all of which control the water balance within the system (Arnold et al., 2012, 1998; Srinivasan et al., 1998). SWAT retrieves climate data from the nearest weather station located to the center of each sub-basin. These data can be directly obtained from files containing observed records, or SWAT has the capability to generate simulated data in runtime based on observed monthly statistics. This flexibility allows SWAT to effectively incorporate climate influences into hydrological modeling processes.

SWAT employs a variety of modeling techniques to comprehensively address the different aspects of watershed dynamics. SWAT relies on the Modified Universal Soil Loss Equation (MUSLE) established by Williams (1975) to predict sediment yield from the landscape. This approach

provides a valuable tool for estimating the sediment loss within watersheds. Moreover, SWAT simplifies its vegetation model by employing a single plant growth model capable of simulating all types of land cover while distinguishing between annual and perennial plants. This versatile plant growth model plays a pivotal role in assessing various processes, including the removal of water and nutrients from the root zone, transpiration, and biomass/yield production. Beyond plant growth, SWAT extends its modeling process to encompass the movement and transformation of several critical elements within the watershed, including different forms of nitrogen and phosphorus, pesticides, and sediment. This holistic approach allows the SWAT to provide a comprehensive understanding of the complex dynamics within the watershed.

SWAT allows the user to define management practices taking place in every HRUs (Folle et al., 2007; Waidler et al., 2009). After establishing the quantities of water, sediment, nutrients, and pesticides transferred from the land phase to the primary channel, these loadings are then directed through the streams and reservoirs situated throughout the watershed (Arnold et al., 2012). In the context of reservoirs, the water balance for reservoirs includes inflow, outflow, rainfall on the surface, evaporation, seepage from the reservoir bottom, and diversions. Calculated flow, sediment yield, and nutrient loading obtained for each sub-basin are then routed through the river system. Channel routing is simulated using the variable storage or Muskingum method (Neitsch et al., 2011). This method aids in accurately depicting the movement of water and its associated constituents through the river network, facilitating a holistic understanding of watershed behavior.

### 2.4.1 Theoretical Description of SWAT Model

For a comprehensive understanding of the SWAT model's key components, processes, and equations, interested parties can refer to the SWAT theoretical documentation available at `https://swat.tamu.edu/docs/` (Neitsch et al., 2011; Srinivasan et al., 2010). This documentation serves as a valuable resource for gaining insight into the intricacies and functionalities of the model. In the context of this study, the focus is on describing specific processes and equations that are particularly pertinent to this research objectives.

#### Hydrological simulation in SWAT model

In the SWAT model, simulation of the hydrology of a watershed is done in two separate components. One is the land phase of the hydrologic cycle that controls the water movement in the land and determines the water, sediment, nutrient, and pesticide amount that will be loaded into

the mainstream. The second component is the routing phase of the hydrological cycle in which the water is routed in the channels network of the watershed, carrying the sediment, nutrients, and pesticides to the outlet. Major hydrological processes that can be simulated include evapotranspiration (ET), surface runoff, infiltration, percolation, shallow aquifer, and deep aquifer flow, and channel routing (Neitsch et al., 2011). The land phase of the hydrologic cycle is based on the water balance equation 2.1.

$$SW_t = SW_0 + \sum_{i}^{t}(R_{day} - Q_{surf} - ET_a - w_{seep} - Q_{gw}) \tag{2.1}$$

where $SW_t$ is the final soil water content (mm H2O), $SW_0$ is the initial soil water content (mm H2O), t is the time (days), $R_{day}$ is the amount of precipitation on day i (mm H2O), $Q_{surf}$ is the amount of surface runoff on day i (mm H2O), $ET_a$ is the amount of evapotranspiration on day i (mm H2O), $w_{seep}$ is the amount of percolation and bypass flow exiting the soil profile bottom on day i (mm H2O), and $Q_{gw}$ is the amount of return flow on day i (mm H2O).

Surface runoff occurs whenever the rate of precipitation exceeds the rate of infiltration. SWAT offers two methods for estimating surface runoff: the SCS curve number and the Green and Ampt infiltration method. Using daily or sub-daily rainfall, SWAT simulates surface runoff volumes and peak runoff rates for each HRU and antecedent moisture condition. Peak runoff predictions are based on a modification of the Rational Formula. The watershed concentration time is estimated using Manning's formula, considering both overland and channel flow. In this document, only the SCS curve number method is explained (Neitsch et al., 2011). The SCS curve number equation is:

$$Q_{surf} = \frac{(R_{day} - 0.2S)^2}{(R_{day} + 0.8S)} \tag{2.2}$$

In which, $Q_{surf}$ is the accumulated runoff or rainfall excess (mm), $R_{day}$ is the rainfall depth for the day (mm), S is the retention parameter (mm).

The retention parameter, S, varies spatially due to changes in soils, land use, management and slope and temporally due to changes in soil water content (Arnold et al., 1998). The parameter S is related to curve number (CN) by the SCS equation (USDA-SCS, 1972). The retention parameter is defined by equation 2.3:

$$S = 25.4 * (\frac{1000}{CN} - 10) \tag{2.3}$$

SWAT2009 version includes two methods for calculating the retention parameter; the first one is retention parameter varies with soil profile water content and the second method is the retention parameter varies with accumulated plant evapotranspiration. Calculation of the daily

CN value as a function of plant evapotranspiration was added because the soil moisture method was predicting too much runoff in shallow soils using equation 2.4. But calculating daily CN as a function of plant evapotranspiration, the value is less dependent on soil storage and more dependent on antecedent climate.

$$S = S_{max} * \left(1 - \frac{SW}{(SW + \exp(w_1 - w_2 * SW}\right) \tag{2.4}$$

where S is the retention parameter for a given day (mm), $S_{max}$ is the maximum value the retention parameter can achieve on any given day (mm), SW is the soil water content of the entire profile excluding the amount of water held in the profile at wilting point (mm), and $w_1$ and $w_2$ are shape coefficients. The maximum retention parameter value, $S_{max}$, is calculated by solving equation 2.5 using $CN_1$.

$$S_{max} = 25.4 * (\frac{1000}{CN_1} - 10) \tag{2.5}$$

when the retention parameter varies with plant evapotranspiration, equation 2.6 is used to update the retention parameter at the end of every day

$$S = S_{prev} + E_0 * \exp\left(\frac{-cncoef * S_{prev}}{S_{max}}\right) - R_{day} + Q_{surf} \tag{2.6}$$

where S is the retention parameter for a given day (mm), $S_{prev}$ is the retention parameter for the previous day (mm),$cncoef$ is the weighting coefficient used to calculate the retention coefficient for daily curve number calculations dependent on plant evapotranspiration, $S_{max}$ is the maximum value the retention parameter can achieve on any given day (mm). The initial value of the retention parameter is defined using equation 2.7.

$$S = 0.9 * S_{max} \tag{2.7}$$

The SCS curve number is a function of the soil permeability, land use, and antecedent soil water condition. SCS defines three antecedent moisture conditions: I —dry (wilting point), II—average moisture, and III—wet (field capacity). The moisture condition I curve number is the lowest value the daily curve number can assume in dry conditions. The curve numbers for moisture conditions I and III are calculated with equations 2.8 and 2.9, respectively.

$$CN_1 = CN_2 - \frac{20 * (100 - CN_2)}{(100 - CN_2 + \exp[2.533 - 0.0636 * (100 - CN_2)])} \tag{2.8}$$

$$CN_3 = CN_2 * (\exp(0.00673 * (100 - CN_2))) \tag{2.9}$$

where $CN_1$ is the moisture condition I curve number, $CN_2$ is the moisture condition II curve number, and $CN_3$ is the moisture condition III curve number. Typical curve numbers for moisture condition II are listed in various tables Neitsch et al. (2011), for various land covers and soil types. These values are appropriate for a slope of 5%. Williams (1995) developed an equation 2.10 to adjust the curve number to a different slope:

$$CN_{2s} = \left(\frac{CN_3 - CN_2}{3}\right) * (1 - 2 * \exp(-13.86 * slp)) + CN_2) \tag{2.10}$$

where $CN_{2s}$ is the moisture condition II curve number adjusted for slope, $CN_3$ is the moisture condition III curve number for the default 5% slope, $CN_2$ is the moisture condition II curve number for the default 5% slope, and slp is the average percent slope of the sub-basin.

The model computes evaporation from soils and plants separately. Potential evapotranspiration can be modeled with the Penman-Monteith, Priestley–Taylor, or Hargreaves methods, depending on data availability. Potential soil water evaporation is estimated as a function of potential ET and leaf area index (area of plant leaves relative to the soil surface area). Actual soil evaporation is estimated by using exponential functions of soil depth and water content. Plant water evaporation is simulated as a linear function of potential ET, leaf area index, and root depth, and can be limited by soil water content. More detailed descriptions of the model can be found (Neitsch et al., 2011).

#### Sediment simulation in SWAT model

SWAT uses Modified Universal Soil Loss Equation (MUSLE) Williams (1975) to estimate soil erosion and sediment yield caused by rainfall and runoff. Sediment yield prediction is improved because runoff is a function of antecedent moisture conditions as well as rainfall energy. The modified universal soil loss equation (Williams, 1975) is given by equation 2.11

$$sed = 11.8 * (Q_{surf} * q_{peak} * area_{hru})^0.56 * K_{USLE} * C_{USLE} * P_{USLE} * LS_{USLE} * CFGR \tag{2.11}$$

where $sed$ is the sediment yield on a given day (metric tons), $Q_{surf}$ is the surface runoff volume (mm/ha), $q_{peak}$ is the peak runoff rate (m3/s), $area_{hru}$ is the area of the HRU (ha), $K_{USLE}$ is the USLE soil erodibility factor, $C_{USLE}$ is the USLE cover and management factor, $P_{USLE}$ is the USLE support practice factor, $LS_{USLE}$ is the USLE topographic factor and $CFRG$ is the coarse fragment factor.

### 2.4.2 SWAT Calibration and Validation/ Performance Evaluation

The ability of a watershed model to mimic specified watershed processes is assessed through the calibration and validation process after model parameter sensitivity analysis (White and Chaubey, 2005). The first step in the calibration and validation process in SWAT is the determination of the most sensitive parameters for a given watershed or sub-watershed. Sensitivity is measured as the response of an output variable to a change in an input parameter, with the greater the change in output response corresponding to a greater sensitivity. Sensitivity analysis evaluates how different parameters influence a predicted output. SWAT input parameters are process based and must be held within a realistic uncertainty range (Arnold et al., 2012). Parameters identified in sensitivity analysis that influence predicted outputs are often used to calibrate a model. Model calibration entails the modification of parameter values and comparison of predicted output of interest to measured data until a defined objective function is achieved (James and Burges, 1982). After achieving the objective function for calibration, validation of the model ensues. Validation procedures are similar to calibration procedures in that predicted and measured values are compared to determine if the objective function is met. However, a dataset of measured watershed response selected for validation preferably should be different than the one used for model calibration, and the model parameters are not adjusted during validation. Validation provides a test of whether the model was calibrated to a particular dataset or the system it is to represent. If the objective function is not achieved for the validation dataset, calibration and/or model assumptions may be revisited. The sensitivity, calibration and validation can be performed manually and automatically using appropriate software. Although manual approaches are still frequently used for calibration, they are tedious, time consuming, and require experienced personnel (Muleta and Nicklow, 2005).

### 2.4.3 Application and Limitation of SWAT Model

The Soil and Water Assessment Tool (SWAT) has been tested in different environment around the world, especially in research related to include hydrology, erosion, climate, soil, temperature, plant growth, nutrients, pesticides and land management. The model has been applied in various regions worldwide and has contributed significantly to the understanding of watershed processes and the development of sustainable water resources management practices. Up to date, more than 6000 peer-reviewed papers was published on SWAT model worldwide nearly 200 in Ethiopia. The SWAT model has been widely used for various applications, including water resources management, environmental assessment, and climate change impact studies. The wide

application of SWAT model at both domestic and abroad has confirmed that it is a powerful and comprehensive hydrological model. The model was selected because of its robust approach of soil water balance at the watershed/basin scale.

#### Hydrological process

The first and most application of the SWAT model is to predict streamflow from small to large gauge and ungauged basin (Arnold et al., 2012; Gassman et al., 2007; Neitsch et al., 2011; Schuol et al., 2008; Srinivasan et al., 1998; Wang et al., 2019). Liew and Garbrecht (2003) evaluated SWAT's ability to predict streamflow under varying climatic conditions for three nested sub-watersheds in the 610 $km^2$ Little Washita River experimental watershed in southwestern Oklahoma. In Ethiopia, Setegn et al. (2008) applied SWAT2005 to the Lake Tana Basin for modeling the hydrological water balance. The main objective of this study was to test the performance and feasibility of the SWAT model for the prediction of streamflow in the Lake Tana Basin. In addition, Lee et al. (2011) applied the model to estimate the freshwater inflow to coastal bays, including Galveston Bay and Matagorda Bay in Texas, in order to obtain information on water quantity, quality, and temporal variation to help understand estuary hydrology.

#### Watershed scale soil erosion assessment and prioritization

The SWAT model has been used to assess the risks of soil erosion (Betrie et al., 2009; Chekol et al., 2007), sediment yield (Ayana et al., 2012; Setegn et al., 2009; Yesuf et al., 2015) and prioritization of intervention area (Betrie et al., 2009; Setegn et al., 2009). Chekol et al. (2007) used the model to identify hotspot sediment sources within the Hombole sub watersheds and to simulate the effect of management/conservation measures on water and sediment yield in the Upper Awash River watershed. The Lake Tana Basin is one of the most affected area by soil erosion, sediment transport and land degradation. Setegn et al. (2009) used SWAT model to estimate the sediment yield within each sub-basin and identify the most sediment contributing areas in the Lake Tana Basin, Ethiopia. Betrie et al. (2011) used SWAT to model soil erosion, identify soil erosion prone areas and assess the impact of BMPs on sediment reduction. Ayana et al. (2012) applied SWAT model to simulate the sediment yield from the Fincha watershed, located in Western Oromiya Regional State, Ethiopia. Yesuf et al. (2015) successfully applied SWAT model to quantify sediment yield at a monthly time-step in Maybar hydrometric station.

#### Land use land cover change impact

Study of the land use changes and their effects on runoff and sediment patterns for the watershed level are essential in water resource planning and management. The land use land cover and climate change impact on hydrology and water quality is the major issue that has been addressed using SWAT as well as other hydrological models (Gessesse et al., 2019; Näschen et al., 2019). Chaemiso et al. (2016) simulated the hydrological responses due to land use and climatic changes in the Omo-Gibe river basin, Ethiopia utilizing an ArcSWAT model. The studies showed that there is an overall increasing trend in future annual temperature and significant variation of monthly and seasonal precipitation from the base period 1985–2005. Also, the annual potential evapotranspiration showed an increasing trend for future climate change scenarios. Similarly, the surface water decreases in terms of mean monthly discharge in the dry season and increases in the wet season.

In addition, Gessesse et al. (2019) assessed the hydrological response of the Choke mountain range to land-use dynamics using integrated applications of remote sensing and the Soil Water Assessment Tool (SWAT) in Muga and Suha watersheds. Näschen et al. (2019) investigated historic land use land cover (LULC) patterns as well as potential future LULCC and its effect on water quantities in a complex tropical catchment in Tanzania. Pikounis et al. (2003) used the SWAT model to simulate the main components of the hydrologic cycle, to study the effects of land-use changes. Three land-use change scenarios were examined, namely the expansion of agricultural land, complete deforestation of the Trikala sub-basin, and expansion of urban areas in the Trikala sub-basin. The model was applied to quantify the impacts of implementing Water Quality Management Plans (WQMPs) in the West Fork Watershed of Trinity River Basin in Texas, USA on sediment and nutrients (Santhi et al., 2006).

#### Climate change impact assessment

Assessing impact of future climate change on hydrology and water quality is the major issue that has been addressed using SWAT as well as other hydrological models. Improved understanding of future impact helps towards establishments of watershed management plans and provides a guideline for effective dealing with climate changes. Tuppad et al. (2011) used the Global Climate Model (GCM) MIROC3.2 for simulating future weather conditions and downscaled with bias correction and local adaption studies. Climate change scenarios such as A1B, B1, or both, set by the Intergovernmental Panel on Climate Change (IPCC), were selected to simulate

various levels of future greenhouse gas emissions. The estimate future climates were applied into a calibrated SWAT model to assess impacts of climate change in the watersheds hydrology. Setegn et al. (2011b) investigated the sensitivity of water resources to climate change in the Lake Tana Basin, Ethiopia, using outputs from global climate models (GCMs). Climate change has the potential to reduce water resource availability in the Nile Basin countries in the forthcoming decades.

#### Simulation of BMPs

SWAT also allows for the simulation of different land use and management scenarios to assess their impact on water resources and the environment.SWAT is widely used in assessing soil erosion prevention and control, non-point source pollution control, and regional management in watersheds. A key strength of SWAT is a flexible framework that allows the simulation of a wide variety of conservation practices and other BMPs, such as fertilizer and manure application rate and timing, cover crops (perennial grasses), filter strips, irrigation management, grassed waterways, and wetlands (Folle et al., 2007; Waidler et al., 2009). The majority of conservation practices can be simulated in SWAT with straightforward parameter changes (Gassman et al., 2007). In different parts of the world, different land management practices were evaluated for the redaction effect on non-point sources pollution in the critical sub-basins. Kirsch (2002) described SWAT results showing that improved tillage practices could result in reduced sediment yields of almost 20 % within the Rock River in Wisconsin, USA. Chaplot (2014) found that adoption of no-tillage, changes in nitrogen application rates, and land-use changes could greatly impact nitrogen losses in the Walnut Creek watershed in central Iowa, USA.

Similarly, Bracmort et al. (2006) showed results of three 25-year SWAT scenario simulations for two small watersheds in Indiana, USA where the impacts of no BMPs, BMPs in good conditions, and BMPs in varying conditions are reported for streamflow, sediment, and total phosphate. Betrie et al. (2011) applied the SWAT model to assess spatially distributed of soil erosion/sedimentation processes at daily time step and to assess the impact of three Best Management Practices (BMPs) scenarios on sediment reductions in the Upper Blue Nile River basin. Folle et al. (2007) evaluated various BMPs to reduce upland sediment loads to the Le Sueur River Watershed, South-Central Minnesota, and its tributaries using the SWAT model. The BMPs tested for specific land use and potential sediment source areas are conservation tillage, vegetative filter strip, and cover crops. The scenarios that were most effective at reducing sediment loss (53 % reduction from the baseline scenario) included a combination of cover crops and

filter strips on steep croplands as well as conservation tillage on all cropland in the watershed.

#### SWAT model limitations

SWAT is widely used in many aspects of water cycle simulation, but it still has certain limitations. Despite the strengths mentioned SWAT model has some known weaknesses (Folle et al., 2007). It is incapable of simulating single flood events, while its database must be modified when used in different study areas (Adu and Kumarasamy, 2018; Folle et al., 2007). Targeted placement of BMPs like filter strips, grassed waterways, riparian buffer zones, wetlands, grassland, or other land use within a given sub-watershed is not possible and cannot specify actual areas to apply fertilizers (Adu and Kumarasamy, 2018). It is unable to simulate daily changes of dissolved oxygen in water bodies. The tile drainage routine of SWAT does not account for the drain spacing and depth of the shallow water table (Folle et al., 2007). Besides, during model development the number of free model parameters (used for calibration) shall be kept to a minimum. But, in SWAT model higher number of model parameters open for calibration.

This page is intentionally left blank.

# Chapter 3

# Wabi Shebele River Basin

## 3.1 Research Area

### 3.1.1 Location of Study Site

Ethiopia, situated in East Africa, holds the distinction of being the most populous landlocked country in the world. Within its borders, the Wabi Shebele River Basin (WSRB) stands out as one of the nation's largest river basins in terms of its expansive coverage. WSRB is located southeast of Ethiopia. Covering a vast area of 189,655 $km^2$, it encompasses nearly 17% of Ethiopia's total land area. Geographically, the basin stretches between 4.91° and 9.59° N latitude and 38.69° and 45.33° E longitude, as illustrated in Figure 3.1. It is bordered to the north by the Awash River and Rift Valley lake basins, to the west by the Genale Dawa River basin, to the east by the Ogaden dry basin, and to the south by a section of the Ethio-Somali boundary. Administratively, the Wabi Shebele River Basin encompasses multiple regional states within Ethiopia, including Oromiya in the North West covering 72,465.9 $km^2$, Somali in the South East spanning 116,786.1 $km^2$, Harari in the northeastern part with 373.4 $km^2$, Sidama in the northwestern area covering 21.4 $km^2$, and Dire Dawa Administration, encompassing 8.2 $km^2$ in the north.

### 3.1.2 Water Resource Potential and Wabi Shebele River Basin

Ethiopia, referred to as the water tower of East Africa, with an annual surface water potential of 124.4 billion cubic meters (BCM) (Berhanu et al., 2013). The country is endowed with 12 major basins, 12 large lakes, and variously sized water bodies (Berhanu et al., 2013; Awulachew et al., 2007) . It is significant that out of the total runoff, only 3% of it remains within Ethiopia, while a significant 97% is lost as runoff to the lowlands of neighboring countries. These basins are categorized into three principal drainage systems, all originating from the central highlands.

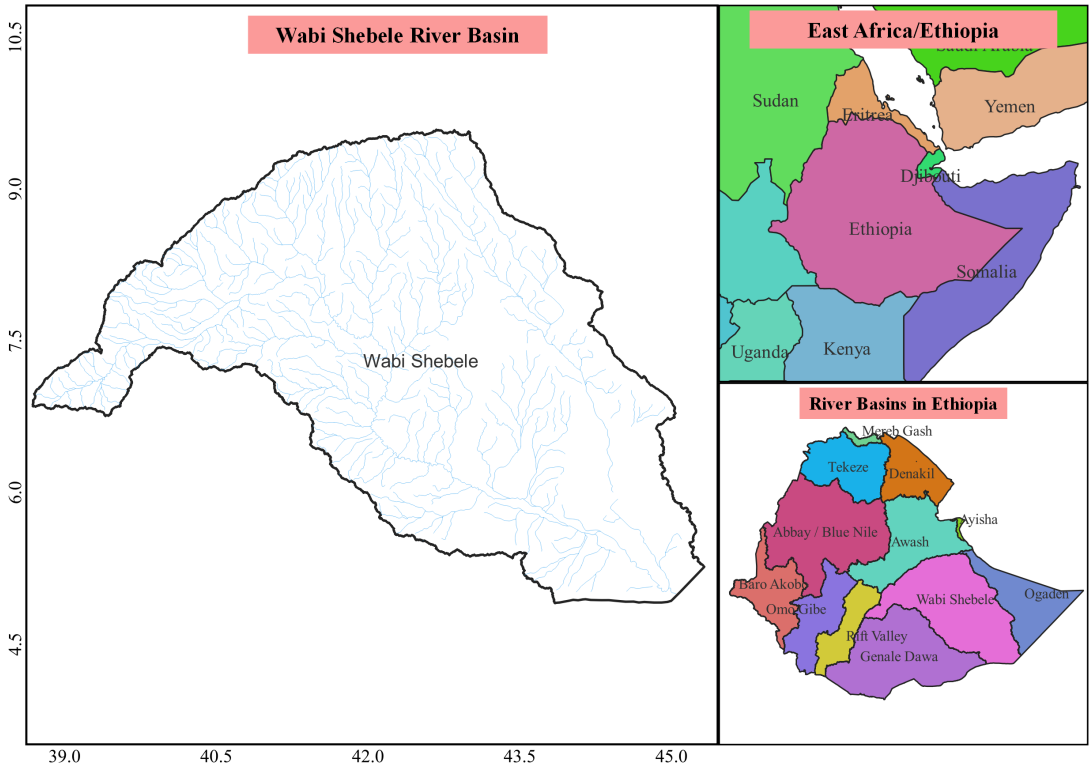


Figure 3.1: Location map of Wabi Shebele River basin

The first and most substantial is the western system, rich in water resources (68%), encompassing the basins of Abay (Blue Nile), Tekeze, and Baro-Akobo, all flowing westward into the Nile Basin. The second system is the rift valley internal drainage system, which includes the Awash, rift Lakes, and the Omo-Ghibe basins. Lastly, the third system consists of the Wabi-Shebele and Genale-Dawa rivers, ultimately draining into the Indian Ocean through Somalia. Notably, the surface water potential of the Wabi Shebele and Genale Dawa basins stands at 3.14 $BM^3$ and 6 $BM^3$, respectively.

Despite its extensive geographical coverage, the Wabi Shebele river basin grapples with water scarcity issues. Within this basin, there are ten major sub-basins, including Melka Wakena, Alkeso, Robe, Golocha, JawesLabu, Ramis, Errer-Mojo, Daceta, FafenJerer, and Lower Wabi, as depicted in Figure 3.2. The basin remains underdeveloped due to a combination of natural and socioeconomic challenges. Specifically, the basin holds the potential for 237,905 ha of irrigable land, representing 5.4% of the country's total irrigable area potential. However, irrigation is currently limited to the downstream portion of the basin, primarily along the flooding plain (Awulachew et al., 2007). Similarly, despite a hydropower potential of 5,400 GWh/year (Berhanu et al., 2013), only 153 GWh/year has been developed to date.

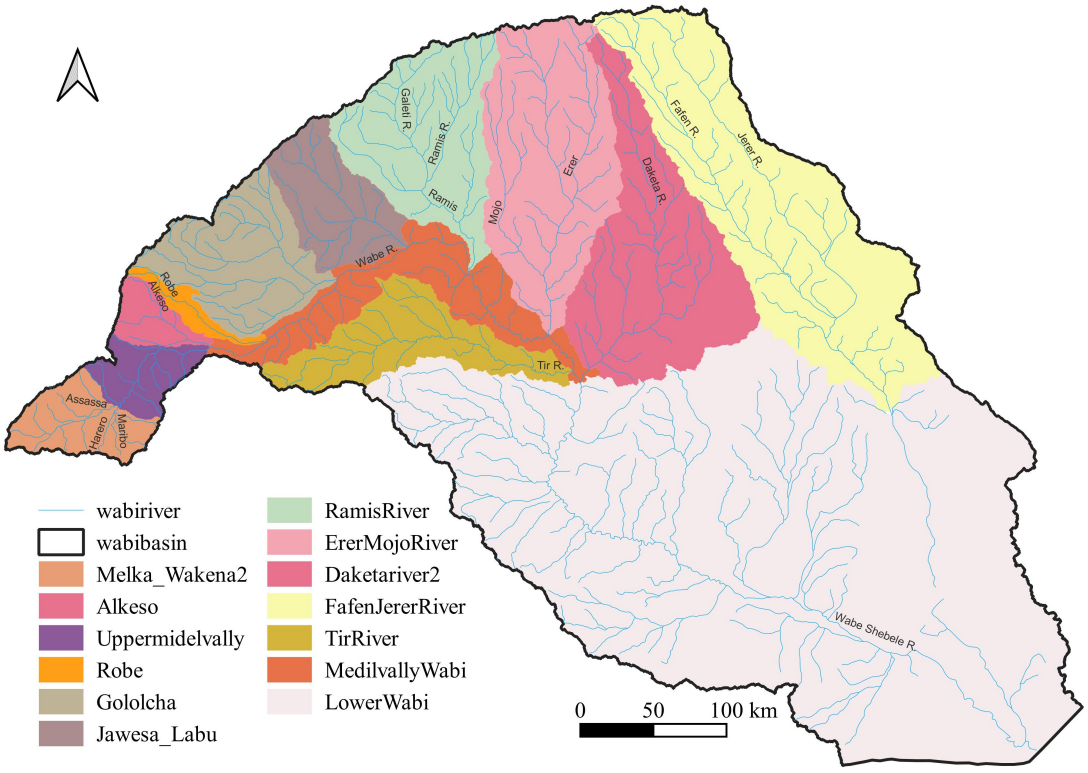


Figure 3.2: Major sub basins/tributary in Wabi Shebele River Basin

### 3.1.3 Topography of WSRB

The Wabi Shebele River Basin (WSRB) displays a diverse topography, encompassing flat plains, undulating terrain, rolling landscapes, and steep-sloped valley regions. This basin extends across a wide range of elevations, starting at 179 meters above sea level (m.a.s.l) along the Ethio-Somalia border in the south and rising to more than 4,188 m.a.s.l in the northwestern Bale Mountains area (as shown in Figure 3.3). Within the WSRB, over 80% of the area is situated at elevations below 1,500 meters, classifying it as lowland, typically characterized by arid and semi-arid conditions with limited surface water contributions to the river (as depicted in Figure 3.4a). The basin's features transition as one moves from the upstream to the middle section, with the former dominated by steep slopes gradually giving way to gentler slopes in the lowland (as illustrated in Figure 3.4b). As a result, the middle stretch of the basin is primarily defined by its steep valley slopes, marked by abrupt faults. These varied physical conditions and elevation disparities contribute significantly to the basin's wide-ranging climates, soil types, and vegetation.

The Wabi Shebelle River stretches for a length of 1,200 kms within Ethiopia, extending from its source to the end of the Ethio-Somali border. Most of its tributaries within this region originate along the northern and northwestern boundaries of the basin, specifically in the Arsi Bale and

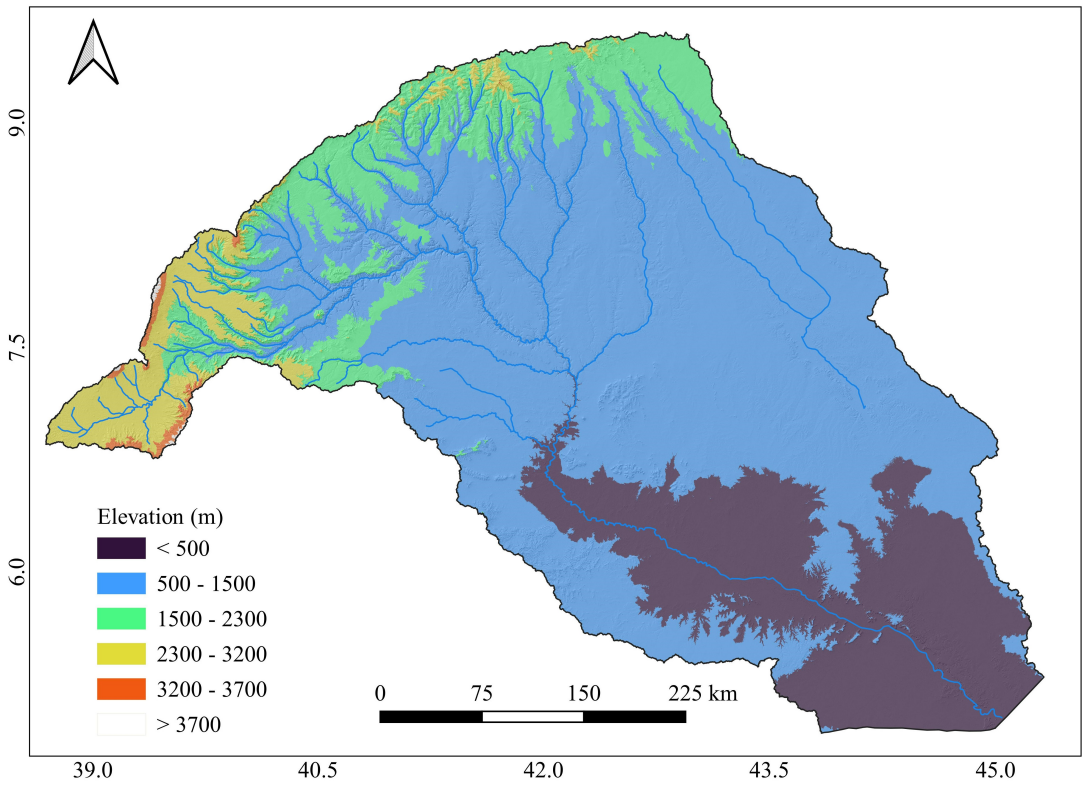


Figure 3.3: Topographic map of the Wabi Shebele River basin

Hararghe Plateau areas. These tributaries then flow with a pronounced steep gradient towards the east and southeast, eventually merging with the Wabi Shebele River. The main river initially flows in an eastern direction before turning to the southeast and ultimately reaching the border with Somalia.

### 3.1.4 Climate Characteristics of WSRB

Ethiopia's climate is a product of its complicated topography and the seasonal movement of the Inter-Tropical Convergence Zone (ITCZ) and associated atmospheric circulations. Similarly, the Wabi Shebele River Basin (WSRB) experiences substantial variations in rainfall due to both altitude and the influence of air masses linked to the ITCZ. The climate in this region is notably diverse, encompassing semi-arid desert conditions in the lowlands and a more humid, temperate climate in the northwestern highlands. Owing to the variations in altitude across the basin, annual rainfall varies substantially, from approximately 227 mm in the southeast to 1240 mm in the northwest.

The eastern basin in Ethiopia stands out for its distinctive bimodal rainfall pattern. In WSRB, This unique pattern results in two distinct rainy seasons. The primary rainy season, known

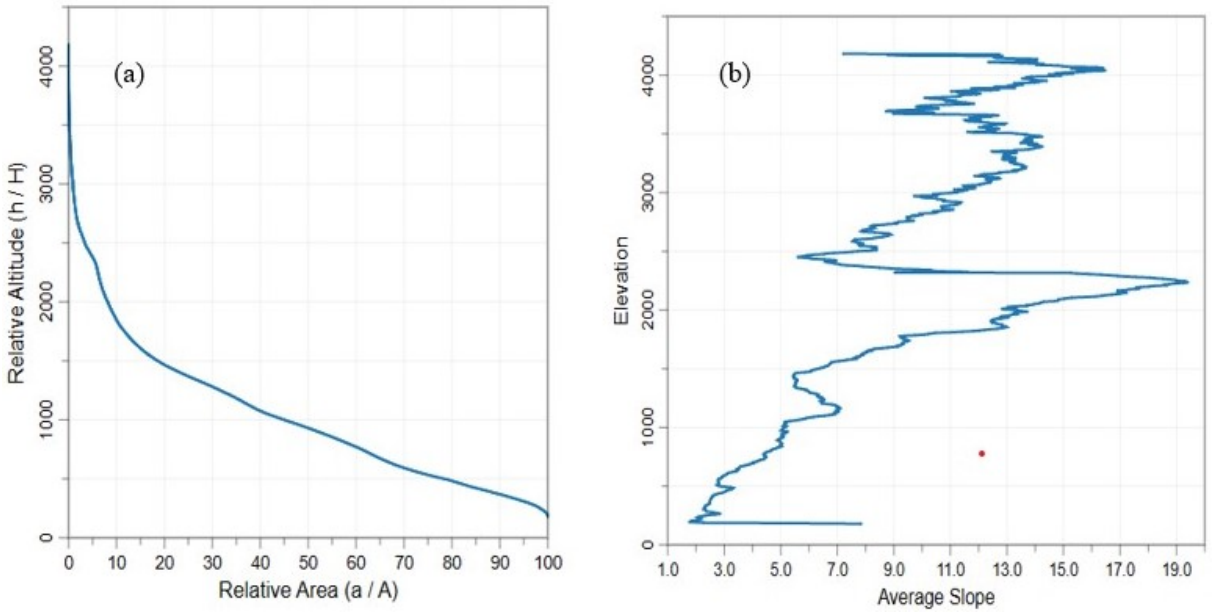


Figure 3.4: Elevation vs Area (a) and elevation vs slope (b) relationship in WSRB

as "Kiremt" or "Summer," spans from June to September, while the secondary rainy season, referred to as "Belg" or "Spring," extends from March to May. Besides, the basin displays a wide range of mean annual temperatures, with values ranging from 6.29°C in the northwest to 35.98°C in the southeast. Furthermore, potential evapotranspiration, like rainfall, exhibits considerable variations, primarily associated with altitude. On average, the annual potential evaporation in the basin stands at approximately 1500 mm (Awass, 2009).

### 3.1.5 Major Land Use Land Cover and Soil Types in WSRB

In the WSRB, forested areas are limited in extent, primarily concentrated in the North-Western highlands. Unfortunately, much of the forested land has been cleared for cultivation or used as a source of household energy, particularly for firewood. The dominant land cover in the basin is open shrubland, prevalent in the semi-arid regions, characterized by patches of shrubs interspersed with grasslands and occasional low trees. The dominant land cover in the basin is open shrubland, mainly found in the semi-arid regions, characterized by patches of shrubs interspersed with grasslands and occasional low trees. Cultivation is the primary land use land cover in the highland areas of the WSRB, with seasonal crops such as maize, barley, wheat, and sorghum being the primary focus. Additionally, perennial crops such as coffee, chat, and a variety of fruit trees are cultivated. Lastly, certain parts of the southeast, particularly in Bale and Hararghe lowlands, exhibit exposed rock or sand surfaces.

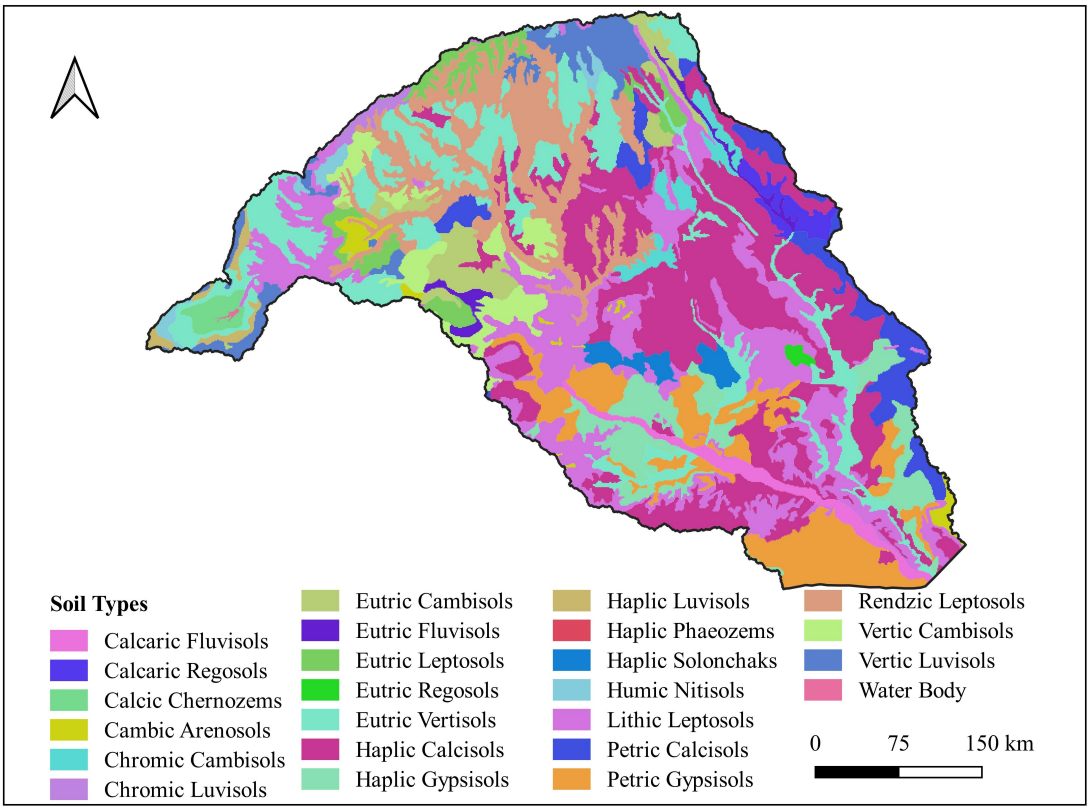


Figure 3.5: Spatial distribution of major soils in WSRB

According to FAO Harmonized World soil database, the dominant soil types in WSRB are Leptosols, Calcisols, Gypsisols, and Vertisols covering 80.3% of the basin. The major soil types in the WSRB are highlighted in Figure 3.5, and their respective area coverages are provided in Table 3.1. Leptosols dominate the region, encompassing the largest area at 29.1%. Calcisols, which cover 25.7% of the land, making it the second most prevalent soil type. Gypsisols hold the third position with an area coverage of 13.0%, while Vertisols come in fourth, occupying 12.5% of the landscape. In addition, Cambisols, Luvisols, Fluvisols, and Solonchaks cover 7.6%, 3.3%, 1.6%, and 1.2% of WSRB respectively. A considerable area (5.9%) is occupied by an addition 10 types of soil that cover an area less than 1% of the basin. The wide ranges of topographic and climatic factors, parent material and land use have resulted in extreme variability of soils. This distribution of soil types provides insight into the varying ecological characteristics within the area, with Leptosols and Calcisols being the dominant soil types in this landscape.

### 3.1.6 Population and Livelihood in WSRB

The elevation of this region plays a crucial role in determining the availability of adequate rainfall for agricultural activities, making it a favorable environment in Ethiopia. Significantly, agricultural production and higher population density are predominantly concentrated in the highland

Table 3.1: Areal distribution of major soil types in WSRB

| No | Soil Name | Area (Km2) | Area (%) |
|---|---|---|---|
| 1 | Calcaric Fluvisols | 3128.2 | 1.6 |
| 2 | Chromic Cambisols | 2587.4 | 1.4 |
| 3 | Eutric Cambisols | 5646.1 | 3.0 |
| 4 | Eutric Leptosols | 4637.1 | 2.4 |
| 5 | Eutric Vertisols | 23679.4 | 12.5 |
| 6 | Haplic Calcisols | 40626.2 | 21.4 |
| 7 | Haplic Gypsisols | 9552.6 | 5.0 |
| 8 | Haplic Solonchaks | 2238.2 | 1.2 |
| 9 | Lithic Leptosols | 31023.2 | 16.4 |
| 10 | Petric Calcisols | 8237.2 | 4.3 |
| 11 | Petric Gypsisols | 15168.2 | 8.0 |
| 12 | Rendzic Leptosols | 19558.1 | 10.3 |
| 13 | Vertic Cambisols | 6044.2 | 3.2 |
| 14 | Vertic Luvisols | 6250.9 | 3.3 |
| 15 | Others (less than 1%) | 11278.0 | 5.9 |
| | **Total** | **189655.0** | **100** |

areas of the WSRB. In the upstream part of the basin, cultivation is the predominant agricultural practice, while animal husbandry is more prevalent in the middle and lower regions (Figure 3.6a). In between, there's a mixed form of production known as agro-pastoral production. The lower valley of the Wabi Shebele River basin is known for its common practice of irrigated crop production. Population distribution is also significantly influenced by elevation (Figure 3.6b). The highlands, particularly in the northeastern part, show the highest population density, with 550 persons per square kilometer, whereas the middle and lower parts of the basin have a much lower population density, as low as one person per square kilometer. Additionally, pastoralist communities often need to relocate in search of water and grazing resources, particularly during periods of drought, which are frequent in the area. In summary, the population distribution can be categorized into highland and lowland residents. A considerable percentage of the highland population relies on agriculture, whereas the lowlanders are primarily pastoralists.

## 3.2 Hydro-Meteorological Data Sources

In this study, hydro-meteorological data served three primary purposes. Firstly, it was essential for the analysis of historical hydro-climatic variability and trends. Secondly, the data played a crucial role in downscaling the CMIP6 GCMs for climate change projections. Thirdly, it served as the input for the SWAT model in hydrological model simulation, as well as calibration

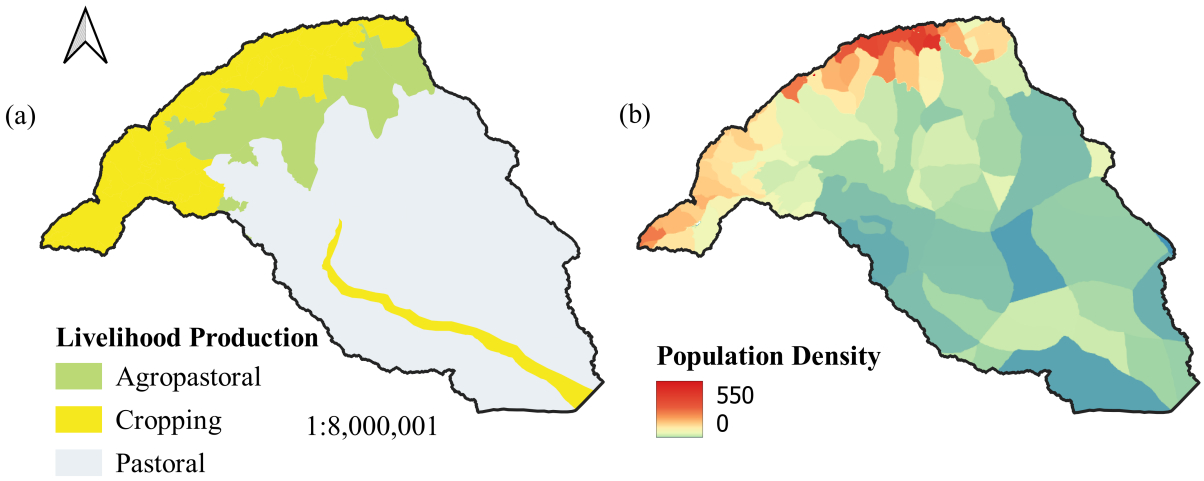


Figure 3.6: Map of livelihood (a) and population density (b) in WSRB

and validation. To achieve these objectives, hydro-meteorological data were obtained from the Ethiopian National Meteorological Agency (NMA) and the Ministry of Water, Irrigation and Electricity (MoWIE).

### 3.2.1 Meteorological data

Rainfall and temperature represent the two most essential variables in climate and hydrological studies. In this research, daily rainfall data were collected from 45 stations, and minimum and maximum temperature data were collected from 27 stations situated within the basin. Additionally, data from 22 rainfall stations and 13 minimum and maximum temperature stations, all located within a 20 km proximity of the basin, were obtained from the National Meteorological Agency (NMA) Figure 3.7. The station selection criteria were based on minimizing data gaps within the period from 1987 to 2016. Climate data are recorded on a daily time scale at different meteorological station. Thus, it is important to obtain them in sufficient temporal and spatial resolution. Within the WSRB, meteorological stations are primarily concentrated in the northwestern and northeastern parts of the basin, primarily following the major roads and towns. In contrast, the central and southern regions of the basin are lacking in climatic stations. Due to limited data availability within the basin, TAMSAT reanalysis climate data with a spatial resolution of 4 × 4 km covering the time span from 1987 to 2016, sourced from the NMA, was employed to address data gaps at the station level. Furthermore, the inherent climate unpredictability in tropical regions emphasizes the enhanced reliability of TAMSAT dataset compared to statistical methods. The locations of all weather stations within the WSRB and its vicinity are showed in Figure 3.7. Specific details about the meteorological stations utilized in this study can be found

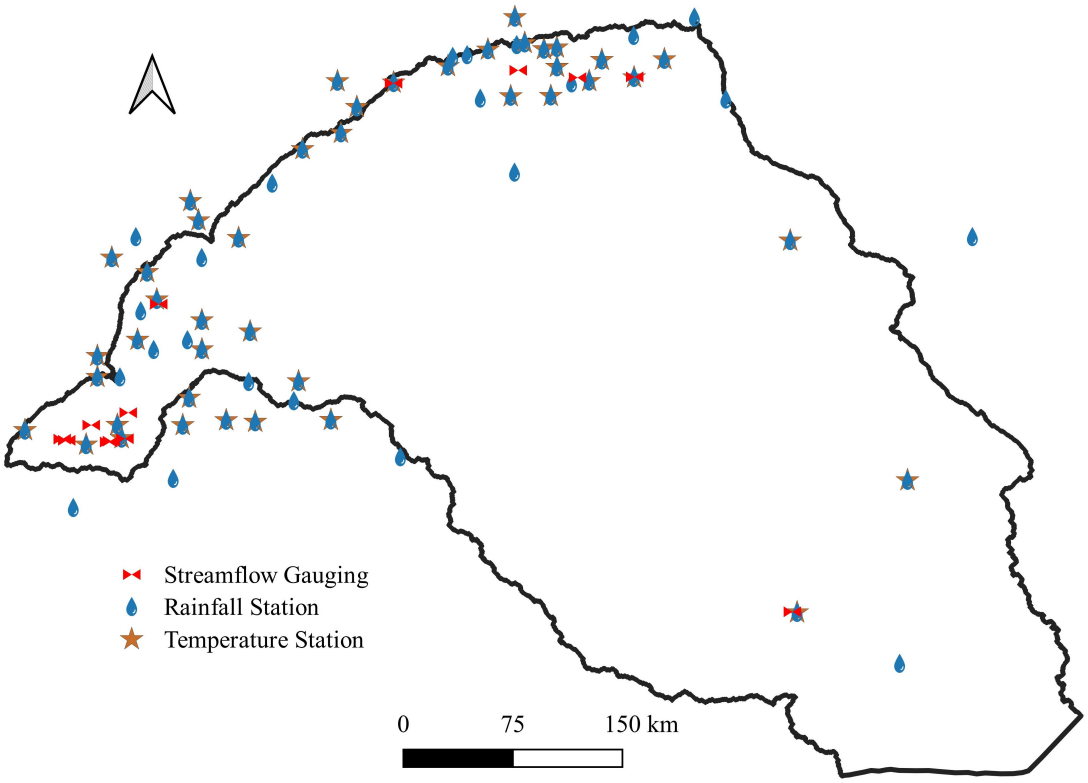


Figure 3.7: Hydro-Meteorological stations in and nearby the WSRB

in Appendix Table A.1.

### 3.2.2 Streamflow data

Streamflow data records play a crucial role in the calibration and validation of models, as well as in examining the statistical features of time series. To realize these objectives, available records were obtained from the Ministry of Water, Irrigation and Electricity (MOWIE). However, it's worth noting that out of the 13 stream gauging stations with daily records in the basin, most are currently non-operational, and a few have limited recorded data. These records are based on staff gauge water level measurements, which are then converted into discharge using established rating curves at specific stations. However, it's essential to acknowledge the potential limitations of manual measurements, particularly in accurately capturing both low and high discharges, especially during extreme weather conditions. Furthermore, the records have limitations in terms of their temporal coverage, and the spatial distribution of gauging stations across the basin is uneven, with many clustered in the northwestern and northeastern part. The gaps in the data were imputed by using the long-term monthly averages specific to each gauging station. The spatial distribution of stream flow gauging stations within the WSRB is depicted in Figure 3.7.

This page is intentionally left blank.

# Chapter 4

# Agroclimatic Zone-Based Analysis of Hydroclimatic Trends and Climate Change in the Wabi Shebele River Basin, Ethiopia

## 4.1 Overview

Climate change became a mega trend in 21st century due to its global coverage (No nation spared from climate change). Climate change is already affecting every inhabited region across the globe with human influence contributing to many observed changes in weather and climate extremes (IPCC, 2021a). In many regions, agricultural production is being adversely affected by rising and variability of temperatures, changes in amounts and frequency of precipitation, the increasing intensity of extreme weather events, rising sea levels, and the salinization of arable land and freshwater (FAO, 2016). Africa is one of the most vulnerable regions highly affected and to be affected by the impacts of climate change (IPCC, 2014b). Due to its low adaptive capacity and high sensitivity to socio-economic systems. Similarly, Ethiopia relies on subsistence rainfed agriculture as the main source of national income (Asfaw et al., 2018; World Bank, 2010); consequently, the importance of the timing and amount of rainfall that occurs cannot be overstated (Cheung et al., 2008).

Besides, Ethiopia generates most of the energy needed from hydropower plants which depend on the amount of water stored in the reservoirs. The government of Ethiopia is currently implementing large-scale investments in hydropower and irrigation projects along the major river basins (Degefu and Bewket, 2017). Thus, the country is vulnerable to climate variability, and climate change is likely to increase the frequency and magnitude of climate disasters (Addisu et al.,

2015; Admassu and Seid, 2006; NMSA, 2007). These have made the country most susceptible to famine usually caused by drought (Degefu and Bewket, 2017). As a result, climate variability and trend analysis at appropriate spatial and temporal scales are crucial for understanding and mitigating problems in hydrology and water resources, such as water resource development, environmental protection, and ecological balance (Alemayehu et al., 2020; Hänsel et al., 2016; Yang et al., 2011).

In the past three decades, climate variability and trend analysis in hydro-meteorological data has been conducted by numerous researchers using different methods, data sources, and spatial and temporal scales. Among the methods, the Mann–Kendall test is the most widely used test for detecting monotonic upward or downward trends in hydrometeorological and environmental data on the assumption that the observations in the time series are independent (Mann, 1945). Accordingly, checking autocorrelation in the time series became a common practice before any analysis of trend detection is performed using the MK test. This test is mostly supported by Sen's slope estimator for estimating the magnitude of a trend in the time series (Sen, 1968). Both tests are non-parametric tests that do not require the data set to be normally distributed. A score of studies used this method to estimate temporal trends for different climatic variables (Aamir and Hassan, 2018; Addisu et al., 2015; Ademe et al., 2020; Admassu and Seid, 2006; Ahmad et al., 2015; Alemu and Dioha, 2020; Bayable et al., 2021; Berhane et al., 2020; Chattopadhyay and Edwards, 2016; Hänsel et al., 2016). Simulation experiments demonstrated that the existence of autocorrelation in the time series alters the Mann–Kendall (MK) statistics (Collaud Coen et al., 2020; Hamed and Rao, 1998; Hamed, 2009; Yue et al., 2002). Accordingly, checking autocorrelation in the time series became a common practice before any analysis of trend detection is performed using the MK test.

Even though, most of the researchers adapted commonly used MK tests the spatial discretization resolution (size, spatial scale) and data source used for trend analysis varies. Different studies used a different spatial frames for analysis including station (Aamir and Hassan, 2018; Addisu et al., 2015; Ahmad et al., 2015; Bayable et al., 2021; Berhane et al., 2020; Asfaw et al., 2018; Beyene, 2015; Gedefaw et al., 2018), agroecosystem zonation (Ademe et al., 2020; Esayas et al., 2018; Taye et al., 2019), temperature-based zonation (Aamir and Hassan, 2018), and subbasin (Addisu et al., 2015; Ahmad et al., 2015; Alemayehu et al., 2020; Cheung et al., 2008). Similarly, the sources of the data used for the trend analysis also vary based on availability and

accessibility. Observed station data is the most common source of data in climatic variabilities and trend analysis studies (Aamir and Hassan, 2018; Admassu and Seid, 2006; Ahmad et al., 2015; Alifujiang et al., 2020; Beyene, 2015; Taye et al., 2019) in recent years, reanalyzed gridded satellite climatic data have been used in different studies (Addisu et al., 2015; Ademe et al., 2020; Alemayehu et al., 2020; Asfaw et al., 2018; Bayable et al., 2021; Esayas et al., 2018).

Numerous studies were conducted on climate variability and trend analysis in Ethiopia River basins. Some of the studies include, in Abay basin (Addisu et al., 2015; Ademe et al., 2020; Gedefaw et al., 2018; Tekleab et al., 2013), in Awash basin (Admassu and Seid, 2006; Eshetu, 2020; Shawul and Chakma, 2020; Tadese et al., 2019; Taye et al., 2019), in Omo Gibe basin (Degefu and Bewket, 2015, 2017; Esayas et al., 2018), and Tekeze basin (Berhane et al., 2020; Beyene, 2015; Gebrehiwot, 2013). Those studies revealed that the variabilities and trends of rainfall vary at different localities. The rainfall amount showed a general statistically decreasing trend (Aamir and Hassan, 2018; Addisu et al., 2015; Ademe et al., 2020; Admassu and Seid, 2006; Berhane et al., 2020), insignificant trends (Ahmad et al., 2015; Eshetu, 2020), and increasing trend (Alemayehu et al., 2020). In general, these studies revealed that there is no uniform temporal and spatial rainfall pattern in Ethiopia's river basins.

Although climate variability and change have location-specific impacts especially in Ethiopia due to spatial and temporal variation of rainfall and topography variation, few studies have been carried out regarding precipitation variabilities and change in the Wabi Shebele River basin (WSRB). In the upper and middle part of the basin, Harka et al. (2021) assessed the spatiotemporal distribution and variability of rainfall in seasonal and annual time series using station data in MK and ITA tests. In the northern district of middle WSRB, Bayable et al. (2021) investigated the spatiotemporal variability and trends of rainfall and its association with Pacific Ocean SST in the West Harerge Zone of eastern Ethiopia using satellite-based rainfall data and the Mann-Kendall Trend Test. Regarding to climate change, Gurara et al. (2021) evaluated the change in streamflow in two future projection scenarios (2041–2070 and 2071–2099) using regional climate models and SWAT model. Because of unevenly distributed rainfall recording stations in the basin, a study based on station data may not be sufficient for water resources planning and decision-making. Therefore, this study investigated variations, trend, and change of hydroclimatic variables over time in WSRB, at each agro-climatic zone. In general, a study based on local agroclimatic zonation overcomes the data scarcity challenge and simplifies sharing the

findings with the local community.

## 4.2 Material and Methods

### 4.2.1 Study Site

Wabi Shebele River Basin (WSRB) is one of the largest river basins in Ethiopia in terms of area coverage. The basin, which occupies a total area of 189,655 $km^2$ comprising nearly 17% of the country's total land area, lies between 4.91° and 9.59° N latitude and 38.69° and 45.33° E longitude (Figure 4.1). The basin is characterized by a broad range of elevations varying from 179 m.a.s.l along the Ethio-Somalia border in the south to more than 4188 m.a.s.l in the northwest part of the Bale mountains. More than 80% of the area has an elevation of less than 1500 m considered low land (arid and semi-arid) in the country. The basin, the upstream is characterized by steep valley slopes while the lowland has gentle slopes. Annual average precipitation over the state varies from 227 mm in the southeast to 1240 mm in the northwest with average annual temperature ranging from 6.29 °C in the northwest to 35.98 °C in the southeast. Due to bimodal rainfall distribution in the basin, there are two rainy seasons, the main rainy season (Kiremt/summer) spans from June to September and the short rainy season (Belg/spring) extends from March to May. The dominant soil types are Gypsisols, Calcisols, and Leptosols covering 68% of the basin. A large percentage of the population in the highlands depends on crop cultivation while the lowlanders, in general, are pastoralists.

### 4.2.2 Data Source and Agroclimatic Zonation

In this research, historical hydro-climatic variability and trends were analyzed using observed daily rainfall, minimum and maximum temperature data obtained from the meteorological stations (as described in section 3.2.1), along with streamflow gauging data (as discussed in section 3.2.2). To project future climate changes in the Wabi Shebele River Basin (WSRB), the ensemble mean derived from eight CMIP6 Global Climate Models (GCMs) was employed, as explained in section 4.2.4.

#### Agroclimatic zonation

There are 17 local agroclimatic zones (ACZs) in Ethiopia based on the annual average rainfall (AARF) amount and elevation of the area (Bekele-Tesemma, 2007). Similarly, DEM of 30 m grid size and annual average rainfall were used for agroclimatic zonation of WSRB. No data and sink values of the DEM were filled using the QGIS tool. The annual average station rain-

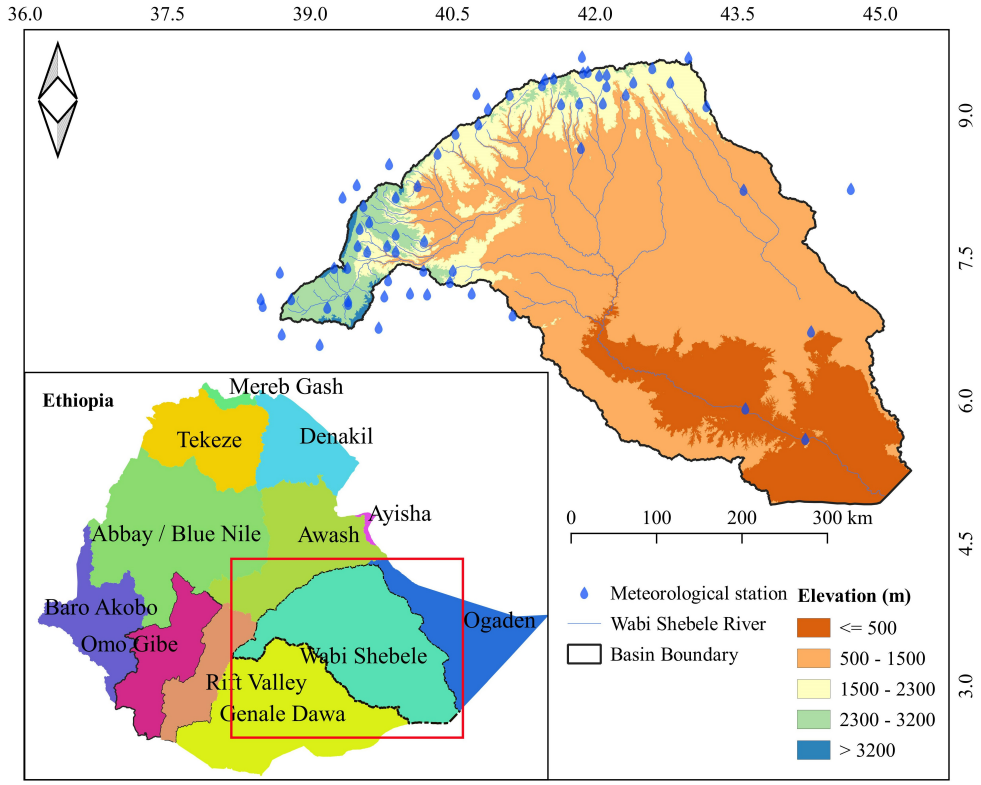


Figure 4.1: Location map of study area

fall data was converted to a spatial rainfall map using an interpolation algorithm in the QGIS environments. The elevation (filled DEM) and rainfall spatial data were reclassified based on the value range given in Table 4.1. Then, the reclassified maps merged to create new classes representing the unique agroclimatic zone. The basin consists of 9 out of 17 ACZs in Ethiopia. The spatial coverage and characteristic of each ACZ are presented in Figure 4.2 and Table 4.1 respectively. Based on annual rainfall amount, ACZ1, ACZ2, ACZ3, and ACZ4 are categorized as dry regions covering 81.2% of the basin whereas ACZ5, ACZ6, and ACZ7 are categorized as humid regions covering only 18.8% of the basin. This makes the basin significantly vulnerable to climatic-related issues, especially drought. On other hand, ACZs are grouped as Low land (ACZ1, ACZ2, and ACZ5), Mid-Highland (ACZ3 and ACZ6), and Highland (ACZ4, ACZ8, ACZ7, ACZ9) based on the elevation.

Table 4.1: Summary of Agro-climatic zones and selected stations

| ACZ: Agroclimatic Zones | MAR (mm) | Elevation (m) | Area | | Selected station | | | |
|---|---|---|---|---|---|---|---|---|
| | | | Km² | % | Site | Latitude | Longitude | Elevation (m) |
| ACZ1: Dry Bereha (Hot-lowlands) | Less than 900 (Dry= Arid and Semi-Arid) | < 500 | 42113.71 | 22.20 | Gode | 5.92 | 43.58 | 290 |
| ACZ2: Dry Kolla (Lowlands) | | 500-1500 | 104350.7 | 55.00 | Degahabour | 8.22 | 43.56 | 1070 |
| ACZ3: Dry Weyna Dega (Midlands) | | 1500-2300 | 11973.94 | 6.31 | Gursum | 9.35 | 42.4 | 1900 |
| ACZ4: Dry Dega (Highlands) | | 2300-3200 | 795.35 | 0.42 | Indeto | 7.57 | 39.9 | 2416 |
| ACZ8: Dry Wurch (Frost zones) | | 3200-3700 | 37.46 | 0.02 | Not Available | | | |
| ACZ5: Moist Kolla (Lowlands) | Greater than 900 (Moist= humid) | 500-1500 | 7599.37 | 4.01 | Gololcha | 8.26 | 40.13 | 1372 |
| ACZ6: Moist Weyna Dega (Midlands) | | 1500-2300 | 12489 | 6.59 | Bedessa | 8.91 | 40.77 | 1703 |
| ACZ7: Moist Dega (Highlands) | | 2300-3200 | 9335.57 | 4.92 | Arsi Robe | 7.88 | 39.62 | 2441 |
| ACZ9: Moist Wurch (Frost zones) | | 3200-3700 | 960.6 | 0.51 | Not Available | | | |
| **Total Area** | | | **189655.7** | **100** | | | | |

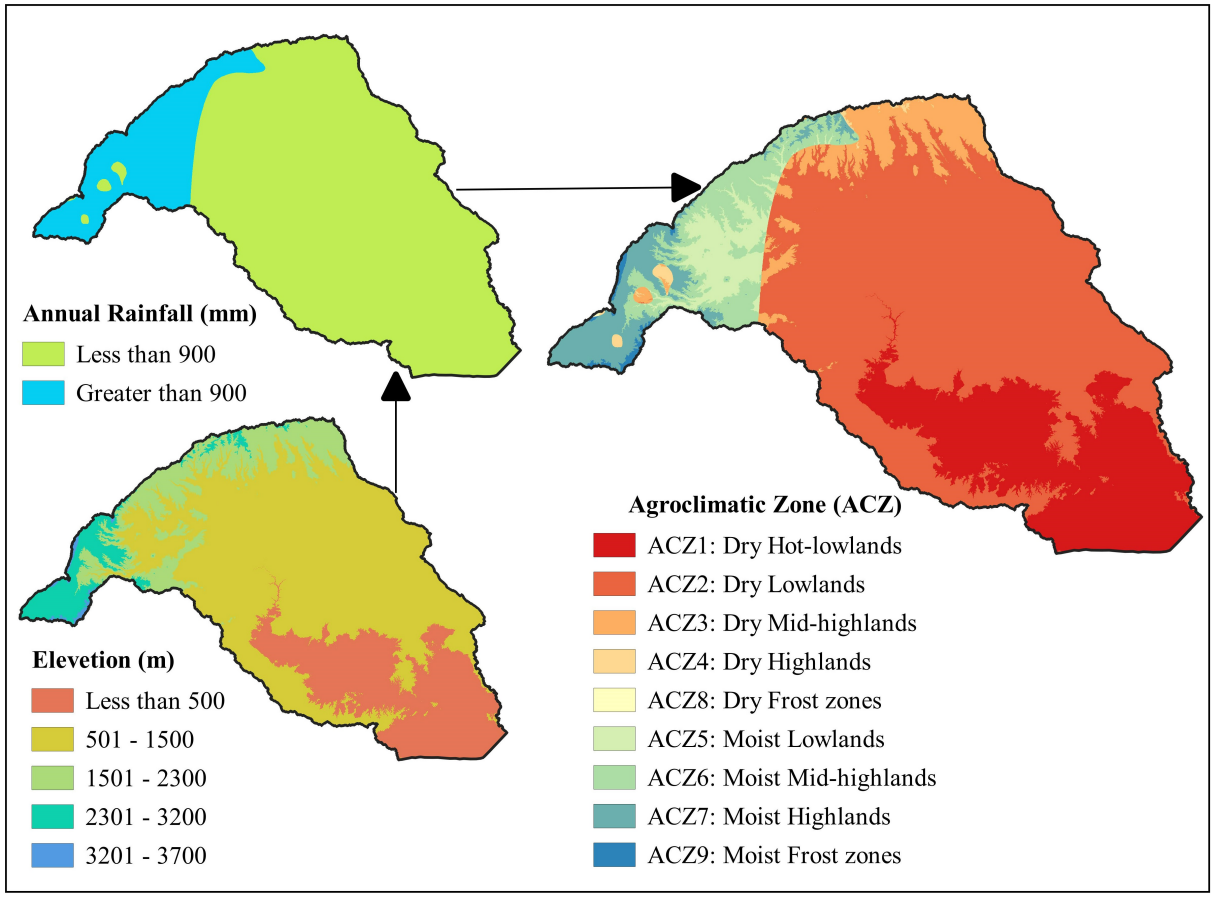


Figure 4.2: Agroclimatic Zone map of Wabi Shebele River basin

**Rainfall distribution in each ACZ**

After local agroclimatic zonation, one station from each ACZ was selected based on the long-term availability of records and less than 10% of missing records. Dry Wurch and humid Wurch agroclimatic zone were excluded from the analysis due to the unavailability of a rainfall recording station. Besides, these zones cover less than 0.6% of the basin. Thus, rainfall data representing only 7 ACZs were considered for further analysis. The details of the meteorological stations used in this study are presented in Table 4.1.

Rainfall distribution in the area is bimodal where two rainfall seasons are recorded March, April, and May (MAM) and June, July, August, and September (JJAS) as spring (light rainy) and summer (heavy rainy) seasons respectively Figure 4.3. But, in the low land area, spring is a heavy rain season than summer which is occurred in September, October, and November (SON). The major concern of this research was water resources-related climatic parameters such as Belg/Spring, Kiremt/Summer, and annual precipitation were considered in the analysis. The monthly values were summed up to arrange the seasonal precipitation as required for the analysis.

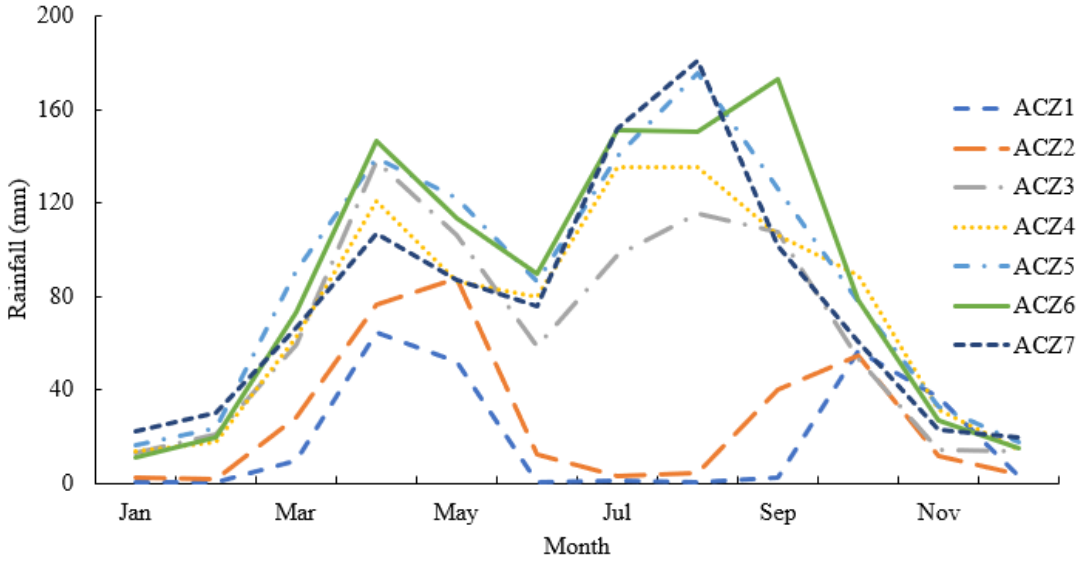


Figure 4.3: Rainfall monthly distribution in WSRB at each agroclimatic zone

The reliability and quality of the data to be used in the analysis should be checked statistically. In this study, Standard Normal Homogeneity Test (SNHT) (Alexandersson, 1986) and Pettitt tests (Pettitt, 1979) were used for detecting the inhomogeneity of seasonal and annual rainfall data. Due to uneven distribution and scarcity of stations in the study area, only the station found inhomogeneous in each test was eliminated from further analysis. The result of the SNHT and Pettitt test is summarized in Table 4.2

Table 4.2: Summary of rainfall data homogeneity test result

| Zone | Spring | | Summer | | Annual | |
|---|---|---|---|---|---|---|
| | Pettitt | SNHT | Pettitt | SNHT | Pettitt | SNHT |
| ACZ1 | 0.19 | 0.36 | 0.30 | 0.21 | 0.74 | 0.63 |
| ACZ2 | 0.51 | 0.08 | 0.56 | 0.69 | 0.21 | 0.78 |
| ACZ3 | 0.31 | 0.14 | 0.25 | **0.04*** | **0.02*** | 0.11 |
| ACZ4 | **0.04*** | 0.13 | 0.27 | 0.46 | 0.54 | 0.35 |
| ACZ5 | 0.53 | 0.13 | 0.69 | 0.49 | 0.82 | 0.42 |
| ACZ6 | **0.02*** | 0.93 | 0.68 | 0.11 | 0.29 | 0.36 |
| ACZ7 | 0.73 | 0.33 | 0.23 | **0.04*** | 0.41 | 0.59 |

Note: * Non-homogeneous at a 5% significant level.

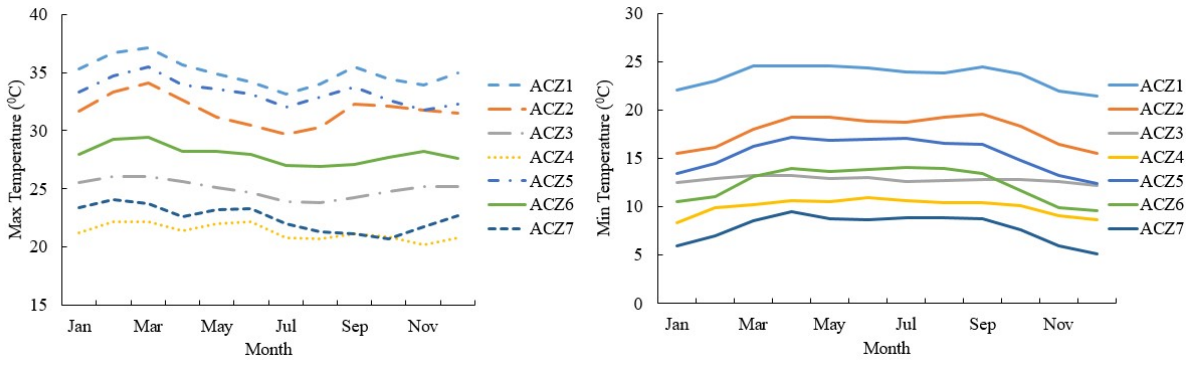


Figure 4.4: monthly distribution of Minimum and Maximum Temperature in each ACZ

#### Minimum and Maximum Temperature

Figure 4.4 presents a comprehensive overview of the monthly maximum and minimum temperature distributions across various Agro-climatic Zones (ACZs). ACZ1 consistently registers the highest maximum temperatures, particularly peaking from March to May, while ACZ3 and ACZ4 maintain lower maximum temperatures year-round. In contrast, ACZ2, ACZ5, ACZ6, and ACZ7 fall within an intermediate temperature range. In terms of minimum temperatures, ACZ1 retains relatively warmer values year-round, with ACZ2 and ACZ5 showing similar patterns but slightly cooler temperatures during the months of December January, and February. ACZ3 and ACZ4 consistently experience cooler minimum temperatures throughout the year. ACZ7 distinguishes itself with consistently cooler temperatures, notably during December and January. This dataset proves invaluable for climate analysis and regional planning, offering insights into temperature variations across these locations.

### 4.2.3 Hydro-Climatic Time-series Trend and Climate Change Analysis

#### Seasonal and annual variability

For each ACZ and period, descriptive statistics for the long-term temporal data were computed using standard statistical procedures using Microsoft excel including mean, minimum, maximum, variance, standard deviation (SD), and Coefficient of Variation (CV). The sample CV is defined as the standard deviation of the sample divided by the mean of the sample. It is dimensionless and it can be very useful in characterizing the degree of variability in datasets. The CV is a statistical measure of the inter-annual variation of climate variables in the data series. In this study, the coefficient of variation (CV) was calculated on rainy seasons, and annual precipitation, to investigate the inter-annual variability of rainfall distribution. Greater values of CV indicate larger variability and vice versa. The CV (%) value for each series can be computed as

follows:

$$CV = \frac{\sigma}{\mu} \times 100 \tag{4.1}$$

where $\sigma$ is the annual precipitation standard deviation and $\mu$ is the mean annual precipitation. The degree of variability of rainfall events classified as low (CV < 20), moderate (20 < CV < 30), and high (CV > 30) (Addisu et al., 2015; Ademe et al., 2020; Elzopy et al., 2021).

#### Trend analysis

The assessment of temporal and spatial trends in hydroclimatic variables across seasonal and annual timeframes in the Wabi Shebele River basin was conducted using modified Mann-Kendall and Sen's slope estimator methods. This analysis encompassed time series data for rainfall, minimum and maximum temperatures spanning from 1987 to 2016. For the trend analysis of streamflow, four gauging stations in the headwater catchment, each with more than 20 years of records, were selected. The specific methodology for these analyses is detailed in the subsequent subsections.

**Modified Mann-Kendall (MK) test** : is perhaps the most widely used non-parametric test for detecting trends in hydro-meteorological and environmental data. It is a nonparametric test for monotonic trends where data is either consistently increasing or decreasing over time. It does not assume the data to be normally distributed and is flexible to outliers in the data. The test assumes a null hypothesis, $H_O$, of no trend and an alternate hypothesis, $H_A$, of increasing or decreasing monotonic trend. The mathematical equations for Mann-Kendall Statistics S, V(S), and standardized test statistics Z are as follows (Aamir and Hassan, 2018; Hamed, 2009; Mann, 1945).

$$S = \sum_{i=1}^{n-1} \sum_{j=k+1}^{n} sgn\left(x_j - x_i\right) \tag{4.2}$$

$$sgn\left(x_j - x_i\right) = \begin{cases} +1, & \text{if } \left(x_j - x_i\right) > 0 \\ 0, & \text{if } \left(x_j - x_i\right) = 0 \\ -1, & \text{if } \left(x_j - x_i\right) < 0 \end{cases} \tag{4.3}$$

$$V\left(S\right) = \frac{1}{18}\left[n\left(n-1\right)\left(2n+5\right) - \sum_{p=1}^{q} t_p\left(t_p - 1\right)\left(2t_p + 5\right)\right] \tag{4.4}$$

$$Z = \begin{cases} \frac{S-1}{\sqrt{V(S)}}, & \text{if } S > 0 \\ 0, & \text{if } S = 0 \\ \frac{S+1}{\sqrt{V(S)}}, & \text{if } S < 0 \end{cases} \tag{4.5}$$

In these equations, $x_i$ and $x_j$ are the time series observations in chronological order, n is the length of the time series, $t_p$ is the number of ties for $p^{th}$ value, and q is the number of tied values. A positive (negative) value of Z indicates that the data tend to increase (decrease) with time. The strength of the trend is proportional to the magnitude of the Mann–Kendall Statistic. The null hypothesis of no trend is rejected if the absolute value of Z is higher than 1.65, 1.96, and 2.58 at 10%, 5%, and 1% significance levels respectively.

**Sen's slope estimates** : Sen (Sen, 1968) developed more robust and non-parametric procedure for estimating the magnitude of a trend in the time series. The slopes of data value pairs were calculated to get the Sen's slope estimate $Q_i$ by the relationship:

$$Q_i = \frac{x_j - x_k}{j - k}, \text{for } i = 1,2,3...\text{N} \tag{4.6}$$

where $x_j$ and $x_k$ are the data values at times j and k (j > k). If there is only one datum in each time period, then $N = \frac{n(n-1)}{2}$, where n is the number of periods. If there are multiple observations in one or more time periods, then $N < \frac{n(n-1)}{2}$ , where n is the total number of observations.
The N values of $Q_i$ are ranked from smallest to largest and the median of slope or Sen's slope ($Q_{med}$) estimator is computed as:

$$Q_{med} = \begin{cases} Q_{\left[\frac{(N+1)}{2}\right]}, & \text{if N is odd.} \\ \frac{Q_{\left[\frac{(N)}{2}\right]} + Q_{\left[\frac{(N+2)}{2}\right]}}{2}, & \text{if N is even.} \end{cases} \tag{4.7}$$

Positive/negative values of $Q_{med}$ indicate an increasing/decreasing trend, respectively, while its value indicates the steepness of the trend.

Simulation experiments demonstrated that the existence of serial correlation alters the variance of the estimate of the Mann–Kendall (MK) statistic; and the presence of a trend alters the estimate of the magnitude of serial correlation (Yue et al., 2002). Several modifications in the MK test have been proposed by different authors to remove the influence of the autocorrelation procedure including variance correction Hamed and Rao (1998), effective sample size (Yue and Wang, 2004), and trend-free pre-whitening (TFPW) (Hamed, 2009; Yue et al., 2002). In this study for

the time series where serial correlations were detected in the data, Hamed and Rao (1998) procedure was applied to eliminate the autocorrelation before performing Mann- Kendall trend tests and Sen slope estimation. Serial autocorrelation was calculated with an autocorrelation function (modifiedmk package) (Patakamuri and O'Brien, 2021) using R software. Detrending was performed for some analysis and was applied as a simple removal of the linear trend calculated over the full period of record. Numerous researchers have also used this approach to eliminate serial correlation in time series data (Aamir and Hassan, 2018; Admassu and Seid, 2006; Alemu and Dioha, 2020).

Finally, interpolation of station trend z score was performed to prepare the spatial trend map of the study area. The interpolation was conducted using inverse distance weighted interpolation tool in QGIS.

### 4.2.4 Climate Change Analysis

Climate models are the primary tools available for investigating the response of the climate system to various forcings, for making climate predictions on seasonal to decadal time scales and for making projections of future climate over the coming century and beyond (Flato et al., 2013). These models simulate the physics, chemistry and biology of the atmosphere, land and oceans in great detail, and require some of the largest supercomputers in the world to generate their climate projections.

Global climate model (GCM) projections are the primary sources of information on future climate change. Currently, CMIP6 climate model was developed with better knowledge on realization, initialization method, physics and forcing than its predecessor (CMIP5). More than 100 climate projection model results are published in CMIP6 from different climate institutions (centers). Unfortunately, climate model expririance uncertenty on the prediction due to less simulation real system. Thus, climate change studies involves selection of climate models and bias correction before applied on any climate change analysis and impact modelling. In this study, the timeframe was segmented into quarters covering the 21st century. The initial quarter has already passed, prompting the investigation to encompass the remaining three quarters of the century, specifically the second quarter Q2 (2026-2050), third quarter Q3 (2051-2075), and fourth quarter Q4 (2076-2100).

#### Climate model selection

The absence of standard procedure and recommendation for the selection of climate models for climate impact studies made the selection of future projection climate model cumbersome for climate researchers.The number of climate model made consideration of all model very difficult because of resource and time available to extract and analysis climate data. Thus, climate researcher devised two methods for selection of GCMs, the first one is to consider more number of climate models and select one best model among considered model whereas others have used less number of models than the former group, in this method the ensemble mean value of climate models were used it can be single model or multiple models ensemble. It is known that single-GCM projections of the long-term trend give greater uncertainty than the MME mean (Xu et al., 2021).

Thus, in this study, the multi-model ensemble mean approach was implemented after selecting 8 CMIP6 GCMs for climate change and impact study. Multi-model ensemble approach has an advantage for minimizing uncertainties that most GCMs experienced when they are downscaled at station/local level studies. The choice of eight GCMs was based on data availability for Historical and 4 scenarios (SSP1-2.6, SSP2-4.5, SSP3-7.0, and SSP5-8.5) at the time of the analysis for precipitation and temperature both minimum and maximum. The evaluation of climate change projection under all SSP scenarios in CMIP6 GCM, available during the study period, was conducted. Further, selection were also made based on the temporal frequency (days) and nominal spatial resolution (100 km). In general, 120 climate data (3 parameters, 8 climate models, 1 historical and 4 scenarios) data were accessed from the ESGF archive of the Program for Climate Model Diagnosis and Intercomparison (`https://esgf-data.dkrz.de/search/cmip6-dkrz/` and `https://esgf-node.llnl.gov/search/cmip6/`) as a contribution to CMIP6 through the World Climate Research Programme's (WCRP) working group on coupled modelling. Additional information on selected CMIP6 GCMs are shown on Table 4.3.

#### Spatial downscaling and bias correction

Even though, climate models are the primary sources of information, direct application of model results for impact studies are limited due to course resolution and systematic bias resulted from partial model of Earth system. Commonly, the impacts of climate change are evaluated using hydrological models which need high resolution (station based) unbiased input data. Measured (observed) climate data are only available at station level (point data). Thus, gridded climate

Table 4.3: List of CMIP6 GCMs used in the study

| No | Climate model | Institution | Country | Resolution | Sources/Reference |
|---|---|---|---|---|---|
| **1** | CMCC-ESM2 | Fondazione Centro Euro-Mediterraneo sui Cambiamenti Climatici (CMCC) | Italia | 1.25°×0.9° | Lovato et al. (2021) |
| **2** | EC-EARTH3 | EC-EARTH consortium | Europe | 0.70×0.70 | EC-Earth (2019a) |
| **3** | EC-EARTH3-Veg | EC-EARTH consortium | Europe | 0.70×0.70 | EC-Earth (2019b) |
| **4** | GFDL-ESM4 | Geophysical Fluid Dynamics Laboratory (GFDL) | USA | 1.25×1.00 | John et al. (2018) |
| **5** | INM-CM4-8 | Russian Institute for Numerical Mathematics | Russia | 2.0×1.5 | Volodin et al. (2019) |
| **6** | MPI-ESM1-2-HR | Max Planck Institute for Meteorology (MPI-M) | Germany | 0.94×0.94 | Schupfner et al. (2019) |
| **7** | MRI-ESM2-0 | Meteorological Research Institute (MRI) | Japan | 1.125×1.125 | Yukimoto et al. (2019) |
| **8** | NorESM2-MM | Norwegian Climate Centre | Norway | 1.25×0.9 | Bentsen et al. (2019) |

model data should be spatially and temporally downscaled using spatial interpolation and temporal downscaling (bias correction) techniques. Thus, many users of climate model data apply some form of spatial downscaling and bias correction (Maraun, 2016).

Spatial downscaling is remapping course resolution grid climate model data into existing stations. Numerous interpolation method was employed by climate change and impact studies. Similarly, in this study, distance-weighted average remapping interpolation method was used to extract historical and future projected daily precipitation and temperature for corresponding observed stations using climate data operator (CDO). The Climate Data Operator (CDO) software is a collection of many operators for standard processing of climate and forecast model data. The operators include simple statistical and arithmetic functions, data selection and subsampling tools, and spatial interpolation.

Whereas, bias adjustment is the practice of statistically transforming climate model data in order to reduce systematic deviations from observed values (Berg et al., 2022). Teutschbein and Seibert (2012) reviewed several available bias correction procedures that can easily be implemented by any impact modeler to correct for GCM and RCM biases. Bias correction procedures include simple scaling approaches and advanced multi-variate distribution-based mapping. Existing bias correction methods are assumed to be stationary, i.e. the correction algorithm and its parametrization for current climate conditions are assumed to be valid for future conditions as well (Teutschbein and Seibert, 2012).

Even though the latest CMIP6 models were developed based on new and better representation of physical, chemical and biological processes, as well as higher resolution, bias correction is a critical step for improving the accuracy of regional climate projection and for the application of these models in research using downscaling to study issues related to water resources, flooding, and drought projection (Akinsanola et al., 2021). Then, bias correction was performed using quantile mapping based on statistical distribution correction method. Quantile mapping algorithms are commonly used to bias correct daily precipitation series from climate models so that distributional properties more closely match those of historical observations (Cannon et al., 2015). Quantile mapping bias correction algorithms are commonly used to correct systematic distributional biases in precipitation outputs from climate models (Cannon et al., 2015). Quantile mapping using distribution derived transformations to adjust the distribution of a modelled variable (Pm) such that it matches the distribution of an observed variable ( $P_o$). The distribution derived transfer function is defined as 4.8 (Gudmundsson et al., 2012).

$$P_o = F_o^{-1}(F_m(P_m)) \tag{4.8}$$

where F is a CDF and F−1 is the corresponding quantile function (inverse CDF). The subscripts o and m indicate parameters of the distribution that correspond to observed and modelled data respectively. For bias correction at the station level, the qmap r package was utilized (Gudmundsson, 2016).

#### Climate change detection

After downscaling and bias correction, the average annual projected GCM climate data for the future period of the 21st century were compared with the observed annual mean in the baseline period (1987 - 2014).Thus, the change in mean precipitation and minimum and maximum temperatures for three periods Q2 (2026-2050), Q3 (2051-2075), and Q4 (2076-2100) for the four selected scenarios SSP1-2.6, SSP2-4.5, SSP3-7.0, and SSP5-8.5 were evaluated with the baseline period for each ACZ. The changes were expressed as a percentage change in precipitation and relative change in temperature. Changes were calculated using equation 4.9 and 4.10:

$$\Delta P_i(\%) = \frac{((P_i) - (P_{\text{ref}}))}{(P_{\text{ref}})} \times 100 \tag{4.9}$$

$$\Delta T_i(^{\circ}C) = (T_i) - (T_{\text{ref}}) \tag{4.10}$$

where, $\Delta P_i$ (%) and $\Delta T_i$ ($^{\circ}C$) are change in precipitation and temperature respectively, ($P_i$ ) future period annual mean precipitation, ($T_i$ ) is future period annual average temperature, ($P_{\text{ref}}$)

and ($T_{ref}$) are reference period precipitation and temperature respectively, i is future periods (Q2, Q3, and Q4).

## 4.3 Results and Discussion

### 4.3.1 Hydro-Climatic Variability Analysis

Table 4.4 presents the statistical analysis results for rainfall in each Agroclimatic Zone (ACZ). The results from the rainfall time series analysis reveal a minimum mean annual rainfall of 227.2 mm in ACZ1 and a maximum of 1047.6 mm in ACZ6. Interestingly, ACZ5, despite its lower elevation, recorded relatively higher rainfall, likely attributable to its position on the windward side of the topography. Seasonally, a significant amount of rainfall was observed during the Kiremt/Summer period, except for ACZ1 and ACZ2. The coefficient of variation (CV) results indicate that the annual rainfall exhibits substantial inter-annual variability, ranging from 16.7% to 46.7% across the basin. Notably, Belg/Spring rainfall exhibited the highest inter-annual variability in all ACZs. However, the most pronounced inter-annual variability was observed in the Kiremt rainfall of ACZ1 (87.4%) and ACZ2 (68.9%). In comparison, annual rainfall exhibited lower CV values across all ACZs. ACZ1, in particular, displayed higher seasonal and annual variability in rainfall. Interestingly, the ACZs at higher elevations generally exhibited lower inter-annual variation (CV < 20%), while ACZs at lower elevations displayed moderate to high variation (CV > 20%) in annual rainfall.

In terms of spatial distribution, the northwestern and northern regions of the basin exhibit relatively high amount of rainfall, whereas the southern and southeastern parts experience considerably lower precipitation. The results of this study are generally consistent with others research findings that were conducted in different parts of the country. These research documents reported that rainfall in Belg/Spring exhibits higher inter-annual variability than Kiremt/Summer rainfall (Asfaw et al., 2018; Elzopy et al., 2021; Eshetu, 2020; Gedefaw et al., 2018). Similarly, previous studies found that the areas with high rainfall amounts exhibit a low coefficient of variations at different time series (Ademe et al., 2020; Cheung et al., 2008; Elzopy et al., 2021; Esayas et al., 2018; Eshetu, 2020; Harka et al., 2021). Generally, Rainfall is highly variable in both time and space over the east Africa (Akinsanola et al., 2021).

The statistical analysis of maximum temperatures across various Agroclimatic Zones (ACZs) indicates that ACZ1 consistently recorded the highest temperatures during the spring, summer,

Table 4.4: Statistical summary on annual rainy seasons, and annual rainfall

| Temporal Scale | ACZ | Minimum | Maximum | Mean | Variance | SD | CV (%) |
|---|---|---|---|---|---|---|---|
| **Spring** | ACZ1 | 26.9 | 300.4 | 126.4 | 3378.2 | 58.1 | 46.0 |
| | ACZ2 | 59.9 | 374.8 | 192.1 | 5597.7 | 74.8 | 39.0 |
| | ACZ3 | 172.7 | 620.8 | 302.9 | 11528.2 | 107.4 | 35.4 |
| | ACZ4 | 94.3 | 620.1 | 269.6 | 12519.6 | 111.9 | 41.5 |
| | ACZ5 | 176.7 | 568.1 | 352.4 | 13764.8 | 117.3 | 33.3 |
| | ACZ6 | 160.0 | 818.4 | 333.3 | 17183.4 | 131.1 | 39.3 |
| | ACZ7 | 115.0 | 429.0 | 260.3 | 7020.0 | 83.8 | 32.2 |
| **Summer** | ACZ1 | 0.0 | 338.8 | 95.5 | 6966.1 | 83.5 | 87.4 |
| | ACZ2 | 16.7 | 299.3 | 106.7 | 5397.0 | 73.5 | 68.9 |
| | ACZ3 | 154.8 | 631.7 | 379.4 | 11143.4 | 105.6 | 27.8 |
| | ACZ4 | 275.9 | 851.3 | 456.0 | 15727.2 | 125.4 | 27.5 |
| | ACZ5 | 334.0 | 1009.7 | 527.8 | 17850.9 | 133.6 | 25.3 |
| | ACZ6 | 181.5 | 882.2 | 563.7 | 23640.9 | 153.8 | 27.3 |
| | ACZ7 | 205.3 | 801.4 | 510.2 | 12350.2 | 111.1 | 21.8 |
| **Annual** | ACZ1 | 100.1 | 535.3 | 227.2 | 11275.1 | 106.2 | 46.7 |
| | ACZ2 | 161.4 | 564.3 | 326.3 | 12731.6 | 112.8 | 34.6 |
| | ACZ3 | 459.1 | 1538.4 | 797.2 | 45085.9 | 212.3 | 26.6 |
| | ACZ4 | 646.1 | 1505.2 | 892.0 | 29667.9 | 172.2 | 19.3 |
| | ACZ5 | 778.4 | 1440.3 | 1047.2 | 33181.4 | 182.2 | 17.4 |
| | ACZ6 | 732.4 | 1667.5 | 1047.4 | 42891.4 | 207.1 | 19.8 |
| | ACZ7 | 576.9 | 1326.3 | 926.0 | 23943.1 | 154.7 | 16.7 |

Note: ACZ = Agroclimatic Zone, SD = Standard Deviation, CV = Coefficient of Variation.

and annual periods, as detailed in Table 4.5. Conversely, ACZ4 registered the lowest maximum temperature values, attributable to its lower annual rainfall and elevated location. Additionally, a coefficient of variation (CV) analysis was conducted for all ACZs across different temporal periods, revealing that the CV values were consistently less than 20. This finding suggests that the annual variation in maximum temperature across the WSRB exhibited minimal inter-annual variation.

Similarly, an analysis of minimum temperatures reveals that ACZ1 consistently registered the highest temperatures during the spring, summer, and annual periods, as illustrated in Table 4.6. In contrast, ACZ7 displayed the lowest minimum temperature values, which can be attributed to its elevated location. Moreover, the coefficient of variation (CV) was calculated for all ACZs across different temporal periods, and the results consistently showed values below 20. This indicates that the inter-annual variation in minimum temperatures across the WSRB remained notably low, with values falling below 10 in ACZ1, 2, 3, 5, and 6, and ranging between 10 and 20 in ACZ4 and 7. Notably, minimum temperatures exhibited relatively higher variation compared with the maximum temperature. The values in parentheses represent the average station values

Table 4.5: Statistical summary on rainy seasons, and annual maximum temperature

| Season | Zone | Minimum | Maximum | Mean | Variance | Kurtosis | Skewness | CV |
|---|---|---|---|---|---|---|---|---|
| **Belg/ Spring** | ACZ1 | 33.1 | 37.3 | 35.9 | 0.7 | 2.4 | -1.1 | 2.4 |
| | ACZ2 | 30.2 | 34.1 | 32.6 | 0.8 | 0.5 | -0.4 | 2.8 |
| | ACZ3 | 24.1 | 28.1 | 25.6 | 1.0 | 0.3 | 0.7 | 3.9 |
| | ACZ4 | 20.4 | 23.3 | 21.9 | 0.5 | -0.4 | -0.1 | 3.3 |
| | ACZ5 | 27.8 | 36.9 | 34.3 | 5.5 | 0.6 | -1.1 | 6.8 |
| | ACZ6 | 26.9 | 30.2 | 28.6 | 1.0 | -1.1 | 0.0 | 3.5 |
| | ACZ7 | 21.7 | 24.9 | 23.2 | 0.8 | -0.9 | -0.1 | 3.9 |
| **Kiremt/ Summer** | ACZ1 | 33.2 | 35.4 | 34.2 | 0.2 | 0.7 | 0.2 | 1.3 |
| | ACZ2 | 29.1 | 32.7 | 30.7 | 0.9 | -0.3 | 0.5 | 3.1 |
| | ACZ3 | 22.9 | 25.9 | 24.1 | 0.5 | -0.2 | 0.2 | 3.0 |
| | ACZ4 | 20.3 | 22.1 | 21.2 | 0.2 | -0.1 | -0.1 | 2.1 |
| | ACZ5 | 29.0 | 34.8 | 33.0 | 3.3 | -0.6 | -1.0 | 5.5 |
| | ACZ6 | 25.8 | 29.0 | 27.3 | 0.5 | 0.6 | 0.7 | 2.6 |
| | ACZ7 | 20.6 | 23.2 | 21.9 | 0.4 | -0.1 | 0.3 | 2.8 |
| **Annual** | ACZ1 | 34.1 | 35.6 | 35.0 | 0.1 | -0.3 | -0.6 | 1.1 |
| | ACZ2 | 30.3 | 33.2 | 31.8 | 0.4 | 0.4 | 0.2 | 2.0 |
| | ACZ3 | 24.1 | 26.1 | 25.0 | 0.3 | -0.3 | 0.4 | 2.1 |
| | ACZ4 | 20.4 | 22.4 | 21.3 | 0.2 | 0.6 | 0.3 | 1.9 |
| | ACZ5 | 29.4 | 35.2 | 33.3 | 3.7 | -1.2 | -0.6 | 5.8 |
| | ACZ6 | 27.0 | 29.6 | 28.0 | 0.4 | 0.0 | 0.7 | 2.3 |
| | ACZ7 | 21.4 | 24.0 | 22.5 | 0.3 | 1.9 | 0.6 | 2.4 |

within a given agroclimatic zone.

The Table 4.7 provides these statistical measures for each station during the spring, summer, and annual periods, allowing for a comprehensive analysis of streamflow characteristics and variations across different seasons and locations. These statistics are vital for understanding the behavior of streamflow in each region and can be invaluable for various hydrological and environmental assessments. All stations show an increase in streamflow from spring to summer, with the highest streamflow values consistently observed during the summer season. Wabi@ Bridge exhibits a substantial increase in streamflow from spring to summer, with the highest values during the summer season. The annual streamflow typically falls between the spring and summer values, indicating a seasonal pattern in streamflow that is common to these stations. The magnitude of this seasonal variation varies from station to station.

On evaluation of CV, Hararo has the highest CV values in all seasons, indicating relatively high variability in streamflow. Spring and summer exhibit particularly high CVs. Ukuma follows with moderately high CV values, with spring showing the highest variability. Fruna and Wabi@ Bridge have lower CV values in comparison. Fruna's CV values are similar in spring and sum-

Table 4.6: Statistical summary on rainy seasons, and annual minimum temperature

| Season | Zone | Minimum | Maximum | Mean | Variance | Kurtosis | Skewness | CV |
|---|---|---|---|---|---|---|---|---|
| **Belg/ Spring** | ACZ1 | 23.4 | 25.6 | 24.5 | 0.4 | -0.9 | -0.1 | 2.5 |
| | ACZ2 | 13.1 | 20.4 | 18.8 | 2.3 | 8.7 | -2.8 | 8.1 |
| | ACZ3 | 11.3 | 15.1 | 13.1 | 0.6 | 1.4 | 0.3 | 5.8 |
| | ACZ4 | 6.1 | 13.2 | 10.4 | 2.9 | 0.3 | -0.8 | 16.2 |
| | ACZ5 | 13.5 | 18.8 | 16.8 | 0.9 | 3.2 | -1.0 | 5.8 |
| | ACZ6 | 9.9 | 15.9 | 13.6 | 1.8 | 1.2 | -1.1 | 10.0 |
| | ACZ7 | 7.2 | 13.3 | 9.0 | 1.6 | 3.8 | 1.4 | 14.0 |
| **Kiremt/ Summer** | ACZ1 | 23.6 | 25.2 | 24.1 | 0.2 | 1.0 | 1.0 | 1.7 |
| | ACZ2 | 15.3 | 21.0 | 19.1 | 1.1 | 4.6 | -1.6 | 5.5 |
| | ACZ3 | 11.4 | 14.0 | 12.8 | 0.4 | 0.2 | -0.6 | 4.9 |
| | ACZ4 | 5.3 | 14.3 | 10.6 | 3.8 | 1.7 | -1.1 | 18.3 |
| | ACZ5 | 12.6 | 18.1 | 16.7 | 1.2 | 6.8 | -2.1 | 6.5 |
| | ACZ6 | 11.4 | 15.2 | 13.8 | 1.1 | 0.2 | -1.1 | 7.6 |
| | ACZ7 | 7.3 | 11.3 | 8.8 | 0.9 | 0.6 | 0.7 | 10.7 |
| **Annual** | ACZ1 | 22.8 | 24.0 | 23.5 | 0.1 | 0.3 | -0.7 | 1.3 |
| | ACZ2 | 14.5 | 19.1 | 17.9 | 0.9 | 6.1 | -2.2 | 5.2 |
| | ACZ3 | 11.3 | 13.9 | 12.8 | 0.4 | -0.3 | -0.7 | 5.0 |
| | ACZ4 | 5.4 | 13.5 | 10.0 | 3.1 | 1.0 | -0.8 | 17.8 |
| | ACZ5 | 11.8 | 16.9 | 15.5 | 0.9 | 7.4 | -1.9 | 6.0 |
| | ACZ6 | 9.5 | 14.6 | 12.4 | 1.2 | 0.7 | -0.6 | 8.7 |
| | ACZ7 | 6.2 | 9.9 | 7.8 | 1.0 | -0.4 | 0.4 | 12.7 |

mer, while Wabi@ Bridge has the highest CV in spring.

In terms of Kurtosis and Skewness analysis, Hararo tends to have relatively light-tailed distributions and is closer to symmetry. Ukuma and Wabi@Bridge exhibit right-skewed distributions, but Ukuma's annual data shows a heavier tail. Fruna, especially during spring, exhibits heavy-tailed and right-skewed distributions, indicating a greater presence of extreme values in this period.

### 4.3.2 Trend Analysis

To identify trends within a time series, statistical tests require that subsequent data points in the series are treated as independent. Therefore, serial autocorrelation was assessed for Belg (short rainy season), Kiremt (heavy rainy season), annual rainfall, minimum and maximum temperatures, and streamflow data. In the case of a time series comprising 30 observations, the critical value is set at ± 0.358 within a 95% confidence interval. Consequently, if a time series exhibited statistically significant serial autocorrelation, a pre-whitening process was performed before applying trend analysis methods. This procedure ensured that any correlated data patterns were appropriately addressed before trend detection.

Table 4.7: Summary of streamflow data in selected stations in WSRB ($m^3$/s)

| Station | Period | Minimum | Maximum | Mean | Variance | Kurtosis | Skewness | CV |
|---|---|---|---|---|---|---|---|---|
| **Fruna** | *Spring* | 1.96 | 4.79 | 2.67 | 0.50 | 4.72 | 2.13 | 26.6 |
| | *Summer* | 2.53 | 6.53 | 4.43 | 1.42 | -1.09 | 0.29 | 26.9 |
| | *Annual* | 2.31 | 4.54 | 3.21 | 0.26 | 0.56 | 0.49 | 15.9 |
| **Hararo** | *Spring* | 0.14 | 3.71 | 1.50 | 0.91 | -0.30 | 0.62 | 63.3 |
| | *Summer* | 1.39 | 4.79 | 3.26 | 0.81 | -0.44 | -0.11 | 27.6 |
| | *Annual* | 0.85 | 3.05 | 2.03 | 0.37 | -0.83 | -0.17 | 30.0 |
| **Ukuma** | *Spring* | 0.27 | 1.00 | 0.48 | 0.03 | 0.91 | 1.20 | 39.6 |
| | *Summer* | 0.66 | 1.43 | 0.96 | 0.04 | 0.07 | 0.82 | 21.9 |
| | *Annual* | 0.45 | 1.02 | 0.63 | 0.02 | 1.30 | 1.24 | 22.2 |
| **Wabi@ bridge** | *Spring* | 1.70 | 14.21 | 4.95 | 9.47 | 1.48 | 1.35 | 62.2 |
| | *Summer* | 6.67 | 22.33 | 13.40 | 15.91 | -0.34 | 0.42 | 29.8 |
| | *Annual* | 4.05 | 12.26 | 7.46 | 4.52 | -0.35 | 0.58 | 28.6 |

**Rainfall**

The MK and Sen Slope analyses conducted for spatial and temporal assessments of seasonal and annual trends revealed a mixed results, indicating both increasing and decreasing trends across various Agroclimatic Zones (ACZs), as shown in Table 4.8. Particularly, the declining trend in Belg/Spring rainfall was found to be statistically insignificant in all ACZs, except for ACZ4. In ACZ7, ACZ3, and ACZ4, the most maximum rate of change in Belg/Spring rainfall was observed, with values of -2.22, -2.38, and -4.11 mm/year, respectively. Regarding Kiremt/Summer precipitation, only ACZ3 exhibited a statistically significant decreasing trend at a 5% significance level, while the remaining ACZs indicated statistically insignificant increases. The analysis further revealed that three ACZs (ACZ2-4) displayed decreasing trends in annual rainfall, with ACZ3 being the only one found to be statistically significant. The highest annual decreasing rates were observed in ACZ2, ACZ4, and ACZ3, with values of -0.59, -1.96, and -12.3 mm/year, respectively, between the years 1987 and 2016. In contrast, the highland area represented by ACZ6 exhibited the most substantial increase in annual rainfall, with a positive trend of 3.73 mm/year. These findings provide insights into the dynamic and diverse nature of rainfall trends across different regions and seasons within the study area.

In the WSRB, non-uniform trend was detected among ACZs that were considered at different temporal scales using the MK method. The finding agrees with previous studies conducted in the different river basins of the country (Elzopy et al., 2021; Eshetu, 2020; Gedefaw et al.,

2018; Harka et al., 2021; Shawul and Chakma, 2020; Tadese et al., 2019; Taye et al., 2019). In Lake Tana Sub-basin, Addisu et al. (2015) revealed a general decreasing trend in annual rainfall. Ademe et al. (2020) reported dominantly decreasing trends in small and main rain seasons and annual rainfall in the Choke Mountain Watersheds (1981–2016). Eshetu (2020) found an increasing trend in the Kiremt season and annual rainfall in most of the stations investigated, however, the Belg season rainfall showed a non-significant declining trend in four of the five representative stations in Modjo River Watershed, Awash River Basin of Ethiopia. Similarly, Berhane et al. (2020) reported a decreasing trend in all stations located in the semi-arid areas of Western Tigray, Ethiopia. Harka et al. (2021) found mixed results of increasing and decreasing seasonal and annual rainfall in the Upper Wabi Shebelle River Basin, Ethiopia. On the contrary, Alemayehu et al. (2020) found annual and seasonal rainfall totals showed increasing trends in the Alwero watershed, in western Ethiopia.

Table 4.8: Mann- Kendall and Sen Slope trend analysis results for different time series

| ACZ | Spring | | Summer | | Annual | |
|---|---|---|---|---|---|---|
| | Z-Value | Sen's Slope | Z-Value | Sen's Slope | Z-Value | Sen's Slope |
| **ACZ1** | -0.82 | -1.00 | 1.53 | 3.27 | 0.46 | 0.85 |
| **ACZ2** | -0.62 | -0.85 | 0.14 | 0.16 | -0.29 | -0.59 |
| **ACZ3** | -1.03 | -2.38 | **-2.00*** | -3.97 | **-8.59**** | -12.30 |
| **ACZ4** | **-2.32*** | -4.11 | 1.46 | 3.36 | -0.86 | -1.96 |
| **ACZ5** | -0.25 | -0.47 | 1.46 | 3.33 | 0.21 | 0.97 |
| **ACZ6** | -0.36 | -1.10 | 1.36 | 5.84 | 0.77 | 3.73 |
| **ACZ7** | -0.86 | -2.22 | 1.61 | 3.65 | 0.32 | 1.54 |

Note: *, ** statistically significant at 0.05 and 0.01 alpha levels.

In a spatial context Figure 4.5, the monthly analysis revealed distinct trends within the study area. July and August exhibited increasing trends, which, in turn, contributed to an overall rise in Kiremt/Summer rainfall. On the other hand February, March, and April displayed decreasing trends, leading to a reduction in Belg/Spring rainfall across the basin. The decreasing pattern in February rainfall was notably widespread, encompassing a significant portion of the basin. Additionally, May and November demonstrated an increasing trend in rainfall, indicating a notable shift in rainy seasons. This shift has implications for various hydrological and agricultural practices throughout the entire basin, highlighting the significance of these findings in the context of regional climate and water resource management.

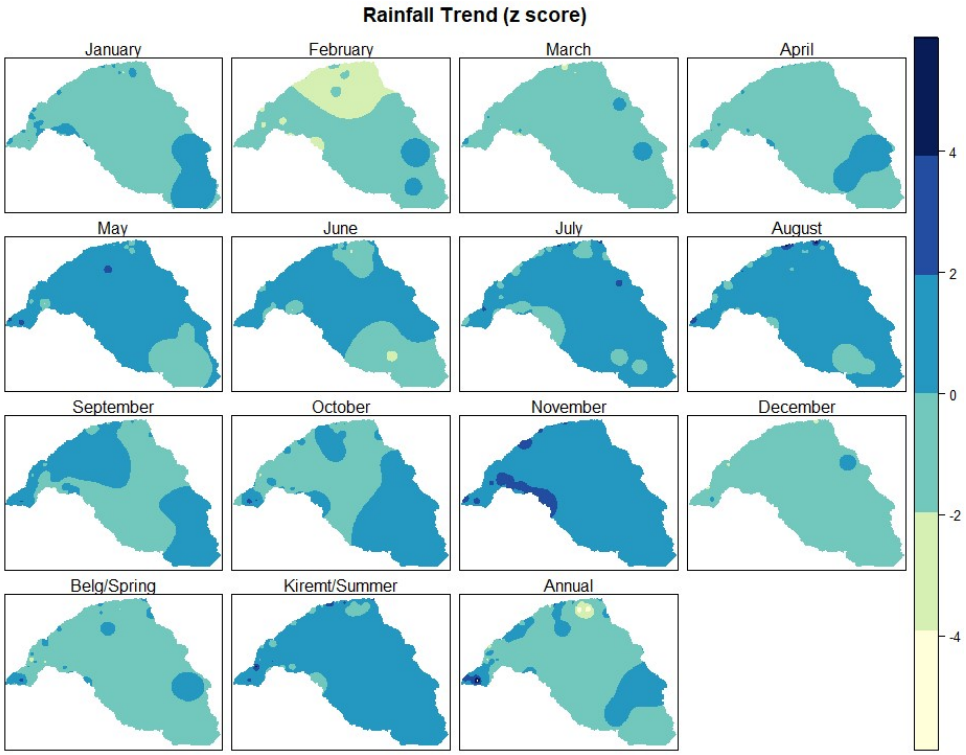


Figure 4.5: Spatial distribution of z score for monthly, rainy seasons, and annual rainfall

**Temperature**

The trend analysis of maximum temperatures within the WSRB did not reveal clear and consistent patterns during the spring, summer, and on an annual basis, as presented in Table 4.9. However, statistically significant differences were observed. Specifically, during spring, ACZ 3 and 5 displayed a significant decreasing trend in maximum temperature, while ACZ 4 and 6 exhibited a statistically significant increasing trend. ACZ2 and ACZ1-2-6 showed statistically insignificant decreasing and increasing trends, respectively. In the summer, statistically insignificant increasing patterns were detected in ACZ1, ACZ2, ACZ6, and ACZ7, with ACZ3 demonstrating a decreasing trend in maximum temperature. Furthermore, ACZ5 displayed a statistically significant decreasing trend, while ACZ4 showed a statistically significant increasing trend in maximum temperature during the summer season. On an annual basis, ACZ3 and ACZ5 exhibited a statistically significant decreasing trend, while ACZ4 and ACZ7 showed a statistically significant increasing trend in maximum temperature. ACZ2 and ACZ 6 displayed a statistically insignificant increase. The rate of change in maximum temperatures across the various ACZs ranged from -0.5 to 0.7 °C, except for ACZ5, which recorded the most substantial rate change during both seasonal and annual periods.

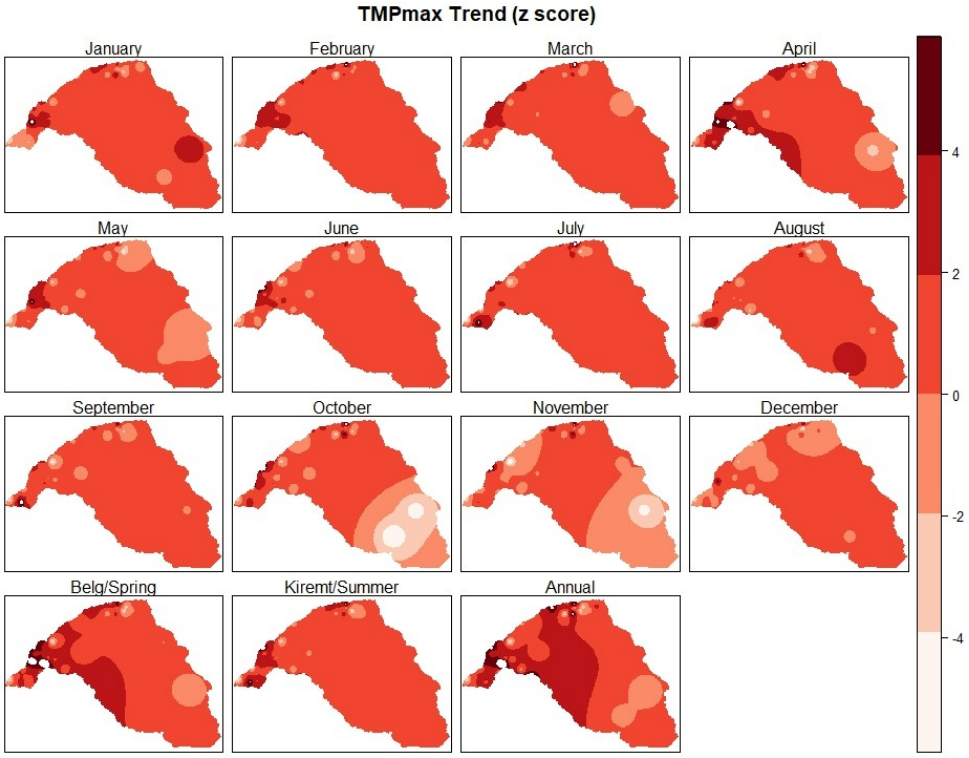


Figure 4.6: Spatial distribution of z score for monthly, rainy seasons, and annual maximum Temperature

From a spatial perspective Figure 4.6, the trend values of maximum temperatures exhibited irregularity when compared to the patterns observed in rainfall and minimum temperatures within the basin. In particular, October and November revealed a decreasing trend in maximum temperatures, highlighting the variability in temperature patterns across different months and regions.

Table 4.9: Annual and seasonal trends in mean maximum temperature in each agroclimatic zone of WSRB

| Zone | Spring | | Summer | | Annual | |
|---|---|---|---|---|---|---|
| | Z-Value | Sen's Slope | Z-Value | Sen's Slope | Z-Value | Sen's Slope |
| **ACZ1** | 0.68 | 0.01 | 1.53 | 0.02 | -0.75 | -0.01 |
| **ACZ2** | -0.02 | 0.00 | 1.28 | 0.03 | 1.20 | 0.01 |
| **ACZ3** | **-2.60**** | -0.05 | -0.68 | -0.01 | **-3.07**** | -0.02 |
| **ACZ4** | **16.49**** | 0.06 | **3.89**** | 0.04 | **17.57**** | 0.04 |
| **ACZ5** | **-3.89**** | -0.15 | **-2.98**** | -0.13 | **-3.93**** | -0.14 |
| **ACZ6** | 1.50 | 0.03 | 0.04 | 0.00 | 0.71 | 0.01 |
| **ACZ7** | **2.82**** | 0.07 | 1.39 | 0.02 | **2.59**** | 0.03 |

The trend analysis for the rainy seasons and annual minimum temperature in the WSRB followed a similar procedure as the maximum temperature Table 4.10. During spring, there were no significant increasing trends in minimum temperature observed in ACZ1 and ACZ2, with the computed Z-values falling below the significance level of $\alpha = 0.05$. However, ACZ 3-6 dis-

played statistically significant increasing trends. This pattern extended to the summer season and the annual average basis, where ACZ1, 3, 4, and 8 exhibited statistically significant increasing trends, while ACZ2 and 5 showed statistically insignificant increasing patterns. On the other hand, ACZ7 displayed a statistically insignificant decreasing trend during spring, summer, and annually. Based on Sen slope result, the rate of change in minimum temperature fell within the range of -0.03 to 0.11 °C per year or 0.1 to 0.5 °C per decade, which translates to 1 to 5 °C per century. This observed trend emphasizes the widespread nature of rising minimum temperatures across the study area, underscoring the significance of these temperature changes over time.

In the spatial monthly trend analysis Figure 4.7, a mixed result emerged, with the central and downstream regions of the basin showing decreasing trends in August and September. However, the Z-score interpolation map revealed that a vast area of the basin exhibited an increasing trend in minimum temperature. These findings highlight the complexity and spatial variability of temperature trends across different seasons and regions within the basin.

Table 4.10: Annual and seasonal trends in mean minimum temperature in each agroclimatic zone of WSRB

| Zone | Spring | | Summer | | Annual | |
|---|---|---|---|---|---|---|
| | Z-Value | Sen's Slope | Z-Value | Sen's Slope | Z-Value | Sen's Slope |
| **ACZ1** | 1.57 | 0.02 | **13.06**** | 0.03 | **3.70**** | 0.01 |
| **ACZ2** | 1.50 | 0.01 | 0.76 | 0.00 | 0.00 | 0.00 |
| **ACZ3** | **3.95**** | 0.03 | **4.72**** | 0.03 | **7.89**** | 0.05 |
| **ACZ4** | **4.30**** | 0.11 | **2.82**** | 0.07 | **4.62**** | 0.10 |
| **ACZ5** | **2.14*** | 0.04 | 0.64 | 0.01 | 1.78 | 0.03 |
| **ACZ6** | **2.50*** | 0.06 | **8.53**** | 0.07 | **10.00**** | 0.07 |
| **ACZ7** | -0.46 | -0.02 | -1.21 | -0.03 | -0.71 | -0.01 |

Various researchers have reported a range of findings regarding the trends in minimum and maximum temperatures based on different time series. A generally increasing trend in mean, maximum, and minimum temperatures within the Lake Tana Sub-basin (Addisu et al., 2015). Additionally, in the mountainous Choke area, most agroecosystems showed a statistically significant increasing trend in both minimum and maximum temperatures (Ademe et al., 2020). In the Upper Blue Nile basin, Tekleab et al. (2013) found that among climate variables, the minimum temperature exhibited a more significant increase compared to maximum and mean temperatures. Conversely, Alemayehu et al. (2020), using gridded monthly data, identified statistically non-significant decreasing trends in mean annual minimum and maximum temperatures. In

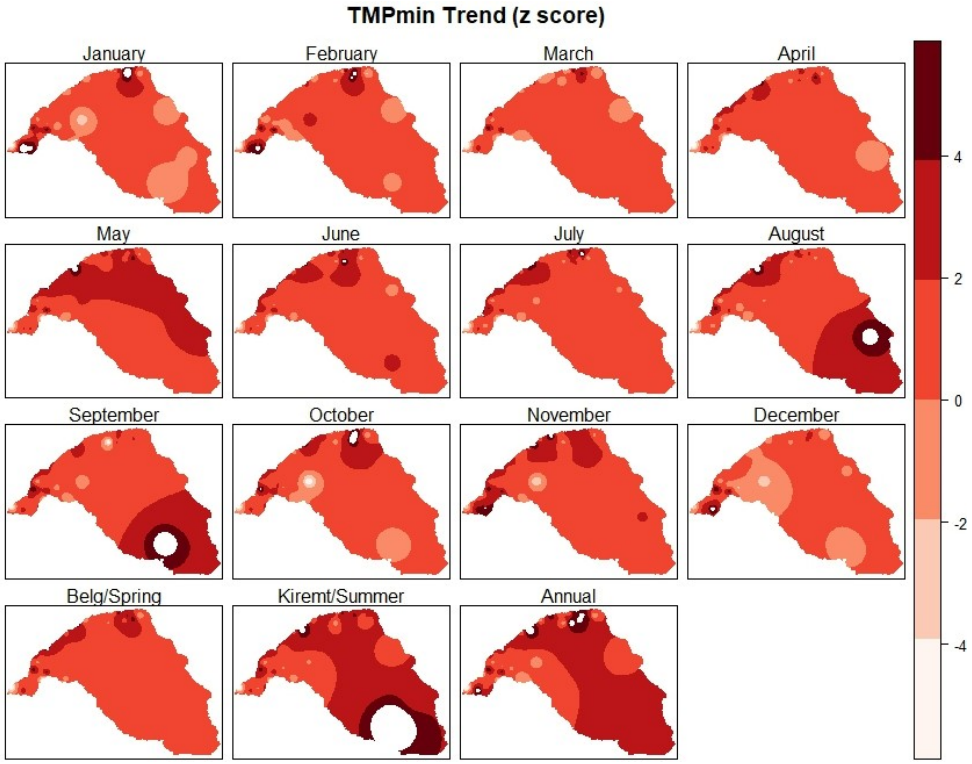


Figure 4.7: Spatial distribution of z score for monthly, rainy seasons, and annual minimum Temperature

contrast, the MK trend test conducted by Shawul and Chakma (2020) revealed that maximum temperatures at most stations showed statistically increasing trends, while most stations upstream of the Awash River basin exhibited decreasing trends in minimum temperature. These varying outcomes highlight the importance of considering local contexts and research methodologies when interpreting temperature trends.

#### Streamflow trend in headwater catchments

The summarized results of the seasonal and annual trend analysis for headwater catchment streamflow, conducted using the MK test and Sen's slope estimator, are presented in Table 4.11. The analysis of trends during the spring season yielded a mix of results for the examined catchments. Harero and Ukuma catchments displayed statistically significant decreasing trends, whereas Furuna and Wabi@Bridge catchments exhibited statistically significant increasing trends in spring streamflow. In the context of summer streamflow, Furuna stations showed a decreasing trend, whereas Harero, Ukuma, and Wabi@bridge stations demonstrated an increasing trend. Ukuma station displayed a statistically significant increasing trend during the summer season. Similarly, the mean annual streamflows for the examined catchments displayed a combination of increasing and decreasing trends. Furuna stations exhibited a decreasing trend, while Harero and Wabi@bridge stations indicated statistically insignificant increasing trends. How-

ever, Ukuma station revealed a statistically significant increasing trend in annual streamflow.

Based on the value of Sen slope result Table 4.11, the maximum annual change in streamflow was found to be 0.02 $m^3$/s/year for Furuna, 0.11 $m^3$/s/year for Wabi@bridge, and 0.05 $m^3$/s/year for Wabi@bridge station, considering both spring, summer, and annual streamflow. These mixed results suggest that the changes in streamflows may be influenced by a range of factors, including human interventions and natural causes, which may vary across the examined catchments. Additionally, the limited and relatively short streamflow data available for analysis may contribute to these variations. It's important to note that a comparative assessment among Agroclimatic Zones (ACZs) was not feasible due to the concentration of all streamflow gauging stations with record periods exceeding 20 years within a single ACZ.

Table 4.11: Streamflow trend statistic summary for selected gauging stations

| **Gauge Station** | **Belg/Spring** | | **Kiremt/Summer** | | **Annual** | |
|---|---|---|---|---|---|---|
| | Z score | Sen's slope | Z score | Sen's slope | Z score | Sen's slope |
| Fruna | 1.38 | 0.02 | -1.42 | -0.06 | -1.05 | -0.02 |
| Hararo | -0.07 | -0.01 | 1.52 | 0.05 | 1.19 | 0.02 |
| Ukuma | 1.26 | 0.00 | **3.02**** | 0.01 | **3.26**** | 0.01 |
| Wabi@bridge | -0.09 | -0.01 | 1.68 | 0.11 | 1.22 | 0.05 |

The discovery of mixed trend results in the analyzed headwater catchments is consistent with findings from several other studies conducted in Ethiopian basins. For example, Tekleab et al. (2013) reported both statistically significant increasing and decreasing streamflow trends in seasonal and extreme flow within upper Blue Nile tributaries. Degefu and Bewket (2017) identified mixed annual and wet season streamflow trends in 8 out of 15 stations in the Omo-Ghibe River Basin. Conversely, they observed an increasing trend in dry season flow in 9 out of the 15 stations. Similarly, a mixed trend was observed in the upper and middle Awash, with most stations showing an increasing trend, while a decreasing trend was revealed in the lower Awash (Tadese et al., 2019). These findings highlight the variability in streamflow trends across different regions and seasons, emphasizing the complex nature of hydroclimatic changes in Ethiopian basins.

### 4.3.3 Climate Change

Future climate change signals for rainfall, maximum, and minimum temperature were assessed by utilizing a multi-model ensemble mean derived from eight CMIP6 GCMs. This assessment

was carried out across each agroclimatic zone in the WSRB, within four shared socioeconomic pathways (SSP1-2.6, SSP2-4.5, SSP3-7.0, and SSP5-8.5) scenario. In this analysis the period from 1987 to 2014 considered as the baseline, using observed data as the reference for future climate change signals.

**Rainfall**

In the SSP1-2.6 scenario projection, there was an observed pattern of precipitation change depicted in Figure 4.8. In ACZs 1, 4, 6, and 7, there was an increase in precipitation during the Q2 and Q3, followed by a decrease during the transition from the Q3 to the Q4. In contrast, ACZ2 experienced a decrease in precipitation during the Q2 and Q3, followed by an increase during the transition from the Q3 to the Q4. On the other hand, both ACZ 3 and ACZ 5 consistently experienced a decrease in precipitation throughout the study period. In a broader context, the multimodal ensemble projection of precipitation in the SSP1-2.6 scenario depicted a mixed pattern when compared to the baseline periods across all ACZs within the WSRB.

In the context of the SSP2-4.5 scenario projection, there was a noticeable alteration in precipitation patterns shown in Figure 4.8. Specifically, in ACZs 1, 2, and 3, there was an increase in precipitation during the Q2 and Q3, followed by a decrease during the transition from the Q3 to the Q4. Conversely, ACZs 4, 5, 6, and 7 consistently experienced an increase in precipitation throughout the study period.

In contrast to the precipitation trends seen in SSP1-2.6 and SSP2-4.5, the SSP3-7.0 and SSP5-8.5 scenarios exhibited a clear upward trend in precipitation during the Q2, Q3, and Q4 of the 21$^{st}$ century, as compared to the baseline period. This pattern was consistently observed across all ACZs within the WSRB. Across all the scenarios for future precipitation projections, the most significant percentage increase from the baseline scenario was projected during the Q3 and Q4 in ACZ1.

Due to recent release of CMIP6 GCM projection less number of studies conducted in Ethiopian and abroad compare to previous version of IPCC acknowledged climate projection. In this study, precipitation projection of three quarter of 21$^{st}$ century, showed mixed in pattern in SSP1-2.6 and SSP2-4.5, but an apparent increasing projection were observed in SSP3-7.0 and SSP5-8.5 or with higher emission scenarios. In the Upper Blue Nile Basin of Ethiopia, Alaminie et al. (2021) investigated historical and projected climate trends for the 21$^{st}$ century using various CMIP6-

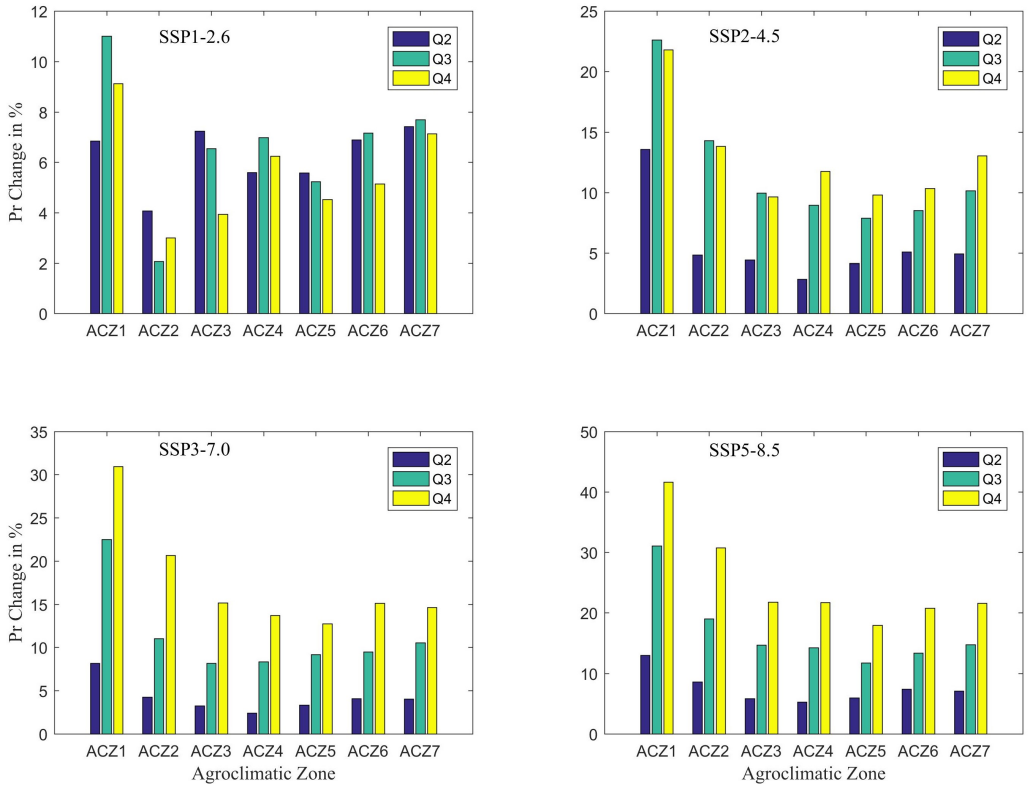


Figure 4.8: Future projected precipitation change in percent for four scenario in agro-climatic zone of WSRB

SSPs scenarios and selected CMIP6 models. They employed quantile mapping for systematic bias correction and the Mann–Kendall trend test. Among the 12 models assessed, MRI-ESM2-0 was chosen to represent temperature, and BCC-CSM-2MR was chosen for precipitation due to their strong performance. The study projected an increase in precipitation by 5.9 (6.1)%, 12.8 (13.7)%, 9.5 (9.1)%, and 17.1(17.7)% for the near(long)-term period under SSP1-2.6, SSP2-4.5, SSP3-7.0 and SSP5-8.5 scenarios, respectively.

#### Minimum and maximum Temperature

The significance of temperature as a crucial and sensitive parameter in climate science cannot be overlooked. In this study, all scenarios generated by CMIP6 Global Climate Models (GCMs) consistently depict an increase in both maximum and minimum temperatures across three future periods, covering all Agro-Climatic Zones (ACZs) as shown in Figure 4.9 and Figure 4.10. When the temperature changes within Q2, Q3, and Q4 are examined across the four Shared Socioeconomic Pathway (SSPs) scenarios, distinctive trends emerge. In Q2, SSP1-2.6 and SSP2-4.5 initiate with comparatively lower temperatures, while SSP3-7.0 and SSP5-8.5 exhibit more substantial temperature changes, with SSP5-8.5 consistently demonstrating the most pronounced changes. As the transition to Q3 occurs, temperature increases are experienced in most scenar-

ios, with SSP2-4.5 often displaying significant changes. In Q4, the temperature continues to rise across the ACZs, but SSP5-8.5 frequently demonstrates the most substantial increase, leading to the highest temperature by the end of the century.

The results revealed that ACZ3 and ACZ4 will experience comparatively less fluctuation in minimum and maximum temperatures across all scenarios and time periods. When the changes in minimum and maximum temperatures among the SSPs scenario and future time intervals are compared, a higher increase in minimum temperature than in maximum temperature is observed in all ACZs, with the exception of ACZ3. In general, the temperature increments follow a progressive trend for all scenarios over time within each ACZ. These comparisons highlight how different SSP scenarios can lead to diverse trajectories for temperature values across the three quarters, reflecting the distinct socioeconomic pathways considered within these scenarios.

The temperature increase towards the end of the 21$^{st}$ century has been reported by numerous researchers, which aligns with this findings. In the Upper Blue Nile Basin of Ethiopia, Alaminie et al. (2021) investigated historical and projected climate trends for the century using various CMIP6-SSPs scenarios and selected CMIP6 models. They employed quantile mapping for systematic bias correction and the Mann–Kendall trend test. Among the 12 models assessed, MRI-ESM2-0 was chosen to represent temperature due to its strong performance. The study indicated that temperature could increase by 1.1 (1.5) °C, 1.3 (2.2) °C, 1.2 (2.8) °C, and 1.5 (3.8) °C for the near (long)-term period under SSP1-2.6, SSP2-4.5, SSP3-7.0 and SSP5-8.5 scenarios, respectively. In similarly, WaleWorqlul et al. (2018) found a consistent increasing trend for both minimum and maximum temperature in all studied headwater catchments. In contrary to this study findings, the rate of change of maximum temperature is higher than the rate of change of minimum temperature.

## 4.4 Conclusions

For the countries, rainfed agriculture is a major source of income generation and employment opportunities, any change in the amount and distribution of rainfall causes a major economic, environmental, social, and political failure. Understanding spatial and temporal variability and trends of rainfall in the WSRB remain a challenge to assess. This is due to a combination of complex topography, higher climatic variation, and low spatial coverage of observation stations. Therefore, this study investigated agroclimatic zone-based variability and trend in rainy seasons,

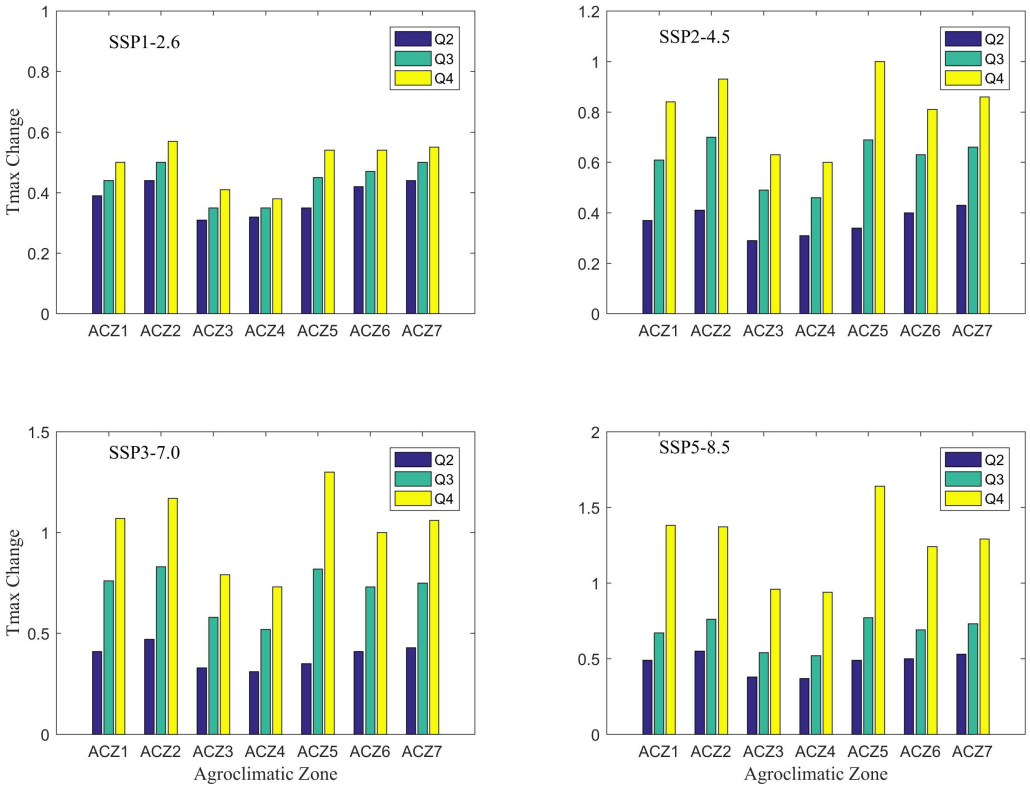


Figure 4.9: Future projected maximum temperature (Tmax) changes across four scenarios within the ACZ of WSRB.

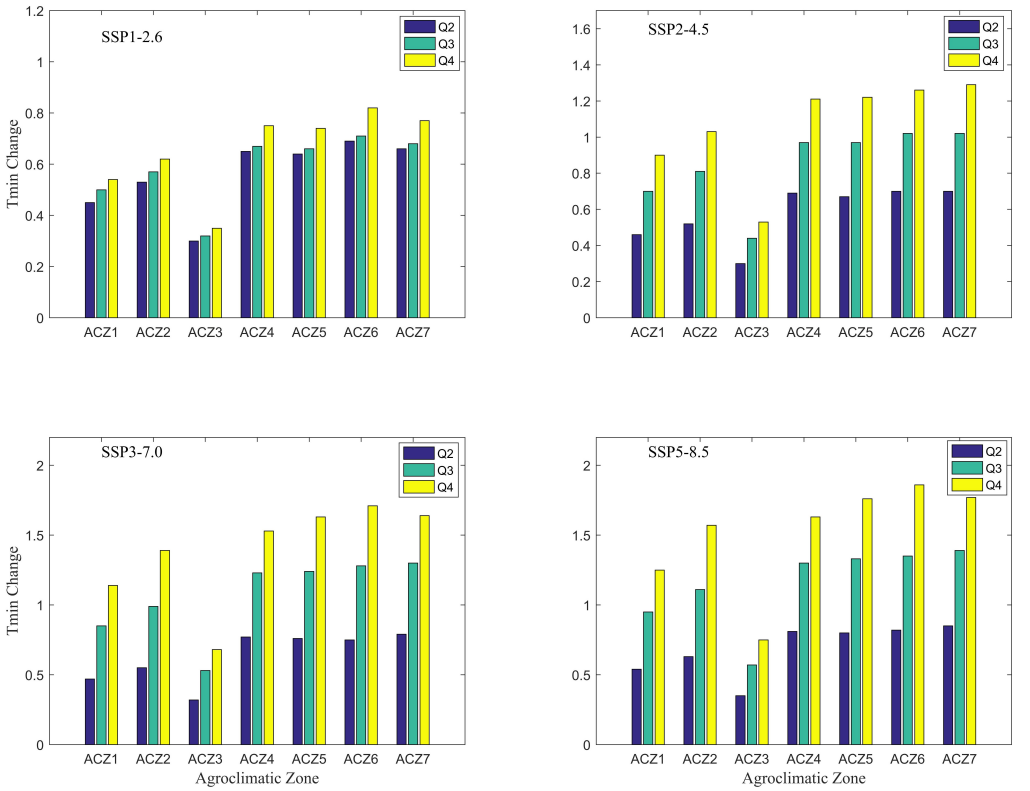


Figure 4.10: Future projected minimum temperature (Tmin) changes across four scenarios within the ACZ of WSRB.

and annual time series of rainfall in the Wabi Shebele River basin over a 30-year study period (1987–2016) using modified MK methods. From the agroclimatic zonation of the WSRB, arid and semi-arid cover 81% of the area whereas only 19% is considered as humid. This study shows the annual rainfall distribution in the basin is entirely bimodal. In this study, low land and low rainfall areas tend to experience high rainfall variability than highland and higher annual rainfall areas. The trend tests found decreasing in Belg/Spring precipitation, an insignificant increase in Kiremt/Summer precipitation, and a decreasing trend in annual precipitation in ACZs covering more than 70% of the basin.

Future climate projections from eight CMIP6 Global Climate Models (GCMs) corresponding to SSP scenarios (SSP1-2.6, SSP2-4.5, SSP3-7.0, and SSP5-8.5) were utilized, selected for their superior spatial and temporal resolutions from diverse global climate modeling institutions during accessing period. Downscaling and bias correction procedures were applied at meteorological stations using distance-weighted average remapping interpolation and non-parametric quantile mapping respectively. To address uncertainties associated with climate models, a multi-model ensemble mean approach was employed, incorporating results from all eight CMIP6 GCMs for climate change and impact assessments. The findings reveal projected increases in mean annual precipitation during Q2, Q3, and Q4 for all emission scenarios across each ACZ. Similarly, mean annual maximum and minimum temperatures are expected to rise during these periods across all ACZs. Notably, the rate of increase in minimum temperatures exceeds that of maximum temperatures in nearly all ACZs.

In line with this, agricultural practices in Belg/Spring season will be affected if a similar trend continues especially in low land areas where Belg is the main rainy season. In general, the amount of water resources shows a decreasing trend with higher interannual variability. Coupling with climate change, a decreasing trend of rainfall severely impacts the livelihoods of the rural communities relying on subsistence rainfed agriculture. Compared to rainfall and temperature variability and trend, most of stations showed increasing trend in temperature than precipitation. The analysis revealed that temperature increase both minimum and maximum will leads to spike in evaporation and increase water stresses for crops production. In general, the findings of this study provide valuable information on the characteristics and variability of rainfall in the WSRB essential for planning and designing sustainable water management strategies and minimizing the impact of extreme climate events.

This page is intentionally left blank.

# Chapter 5

# Assessment of Land Use Land Cover Changes and Future Predictions Using MLP-ANN Simulation for Upper and Central WSRB

## 5.1 Overview

Land and water resources stand as critical foundations for supporting life, serving as indispensable sources of food, fiber, and minerals essential for the survival of all living organisms. The ever-expanding global population and increasing socio-economic demands place substantial pressure on the management of land use land cover (Reis, 2008). Human activities, encompassing agriculture, energy production, construction, and various other endeavors, constantly transform the Earth's surface. Particularly in Ethiopia, there is a notable and rapid increase in cultivated land at the expense of natural vegetation (Ayele et al., 2016; Betru et al., 2019; Garedew et al., 2009; Gashaw et al., 2017; Kenea et al., 2021; Shawul and Chakma, 2019). The degradation of Ethiopia's forests is closely linked to the ongoing population growth (Reusing, 2000). As the population continues to rise, the demand for land for both residential and agricultural purposes intensifies. Human-induced changes in land use land cover have the potential to disrupt the integrity of the natural resource system and affect the delivery of ecosystem goods and services (Memarian et al., 2014).

Human activities that alter land use land cover can significantly impact the water cycle and

its dynamics within a given watershed (Descroix and Amogu, 2012). Vegetation cover plays a pivotal role in shaping the behavior of precipitation, determining whether it becomes surface runoff, infiltrates into the soil, or is lost through evapotranspiration. Extensive research has been conducted to understand the ramifications of land use land cover changes on hydrological processes. The conversion of vegetated land, including grasslands, forests, and shrubs, into agricultural land has been associated with several hydrological transformations. Such conversions have been observed to result in increased runoff volumes (Alibuyog et al., 2009; Aredo et al., 2021; Engida et al., 2021; Gessesse et al., 2019; Getahun and Haj, 2015; Mango et al., 2011), a decrease in baseflow (Alibuyog et al., 2009; Gessesse et al., 2019; Mango et al., 2011), reduced annual groundwater flow and percolation (Engida et al., 2021; Gessesse et al., 2019), lower low and higher high flows (Näschen et al., 2019), and an increase in sediment yield (Alibuyog et al., 2009; Engida et al., 2021) across various regions worldwide. However, in contrast to these findings, Owuor et al. (2016) have reported that the conversion of forested land or native vegetation into managed land use types, such as agricultural fields, can lead to increased groundwater recharge, particularly in semi-arid regions.

The utilization of satellite data gained popularity in the 1980s, as a result of the increasing and consistent availability of satellite imagery to the general public. Significant progress in remote scanning and camera technology has been made since the launch of the first Earth observatory satellite in 1972 (Loveland and Dwyer, 2012). The introduction of Geographic Information Systems (GIS) and remote sensing has greatly advanced the processing and application of satellite images for monitoring and assessing land resources. The classification of land use land cover from satellite imagery primarily falls into two broad categories: supervised and unsupervised techniques, with hybrid methods also in use (Abburu and Golla, 2015; Richards and Jia, 2006). Notably, the accurate classification of satellite images, which relies on the recorded spectral reflectance of objects on Earth, has been made possible through significant advancements in classification algorithms, particularly those related to machine learning. Furthermore, various machine learning algorithms have been developed to predict future changes in land use land cover based on existing explanatory factors in specific geographic locations.

Land use land cover maps are used in numerous natural resource applications to describe the spatial distribution and pattern of land use land cover, to estimate the areal extent of various cover classes, or as input into habitat suitability models, land use land cover change analyses,

hydrological models, and risk analyses (Stehman and Czaplewski, 1998). Furthermore, understanding the future land use land cover within watersheds and its implications for water resources is of paramount importance in watershed management and policy development (Marshall and Randhir, 2008). In recent years, hydrologists have been increasingly focused on quantifying the impact of land use land cover changes on runoff dynamics in river basins (Wang et al., 2014). In line with this, a considerable amount of research has been dedicated to studying land use land cover dynamics in Ethiopian basins. However, within the WSRB, no prior studies have been published concerning changes in land use land cover and their associated impacts using the conventional methods. Consequently, this study aims to fill this knowledge gap by investigating the dynamics of land use land cover and future projection using MLP- ANN in the upper and central parts of WSRB, making use of freely available Landsat imagery. The findings of this research are anticipated to provide essential knowledge that can support local-level planning, environmental monitoring, and the effective management of natural resources within the watershed. In this study, the classified image, following established protocols, is utilized as input for hydrological modeling, a crucial tool for evaluating the impact of land use land cover changes, in conjunction with climate change, on the hydrological responses of headwater catchments in WSRB.

## 5.2 Material and Methods

### 5.2.1 Location of study area

Geographically, the upper and central parts of WSRB encompass the area between 6.11° and 9.52° North latitude and 38.67° to 43.34° East longitude, as illustrated in Figure 5.1. Specifically, the upstream and central part of the Wabi Shebele covers 92,349.85 $km^2$, constituting 48.7% of the total area of WSRB, which spans 189,655 $km^2$. The elevation in this area varies between 366 and 4,188 m above sea level.

### 5.2.2 Data and its Sources

The Landsat series of satellite sensors are one of the longest-running Earth observation programs and it is still monitoring the Earth. Thus, the satellite images were obtained from the US Geological Survey (USGS) Center for Earth Resources Observation and Science (EROS) found at `http://glovis.usgs.gov/`. To investigate changes in the spatiotemporal patterns of land use land cover in the central and upper parts of the Wabi Shebele river basin, 11 scenes of Landsat-5 Thematic Mapper (TM) and Landsat-8 Operational Land Imager (OLI) images with

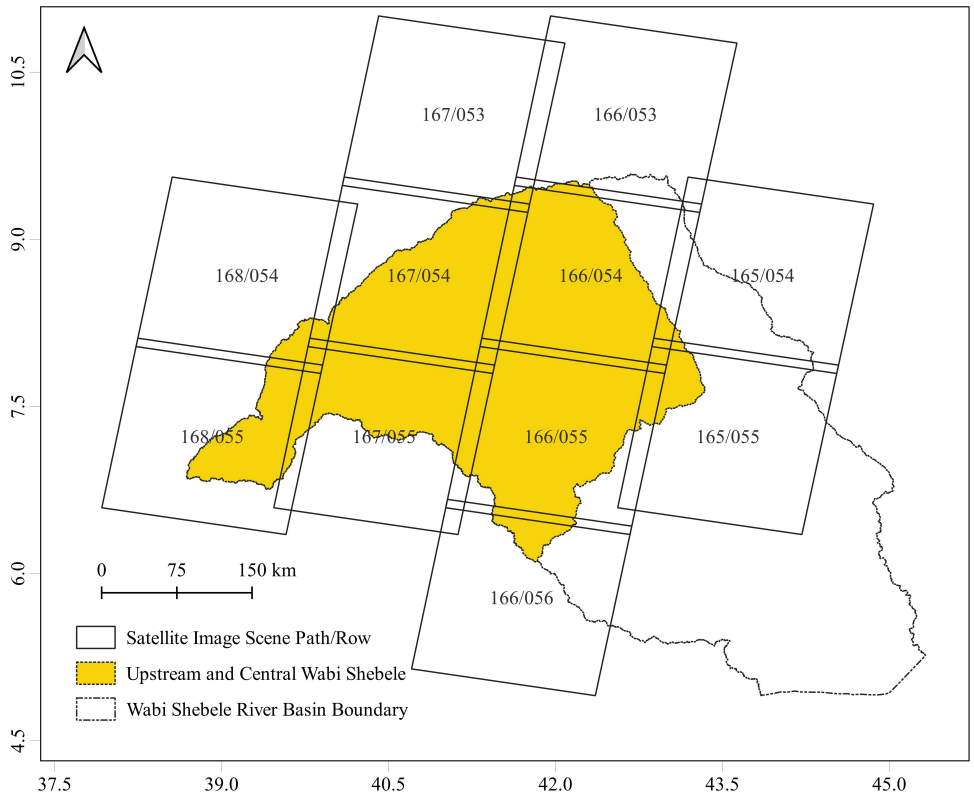


Figure 5.1: Location map and selected scene of Landsat image with Path/Row

a 30 m resolution were obtained for the years 1990, 2000, 2010, and 2020. The selected satellite image path/row covering the study area are depicted in Figure 5.1.

The dry period, typically spanning December, January, and February, is frequently utilized for land use and land cover analysis in Ethiopia due to the distinct variations in reflectance and vegetation cover across seasons (Birhanu et al., 2019; Garedew et al., 2009; Hailemariam et al., 2016). Utilizing images from a similar season helps reduce misclassification (Markos et al., 2018). Moreover, the quality of images for analysis is significantly compromised during the rainy season because of high cloud cover. Therefore, satellite images with minimal cloud cover ($\leq 5\%$) were accessed between December and February for the study years to ensure quality and uniform weather conditions throughout the study period. Detailed information on the downloaded and used satellite images is presented in Appendix Table A.2.

### 5.2.3 Image Preprocessing

Satellite image preprocessing is normally executed before further manipulation, and analysis of the image data to extract specific information. Preprocessing functions involve the process required before the classification of land use land cover or final data analysis to improve the ability

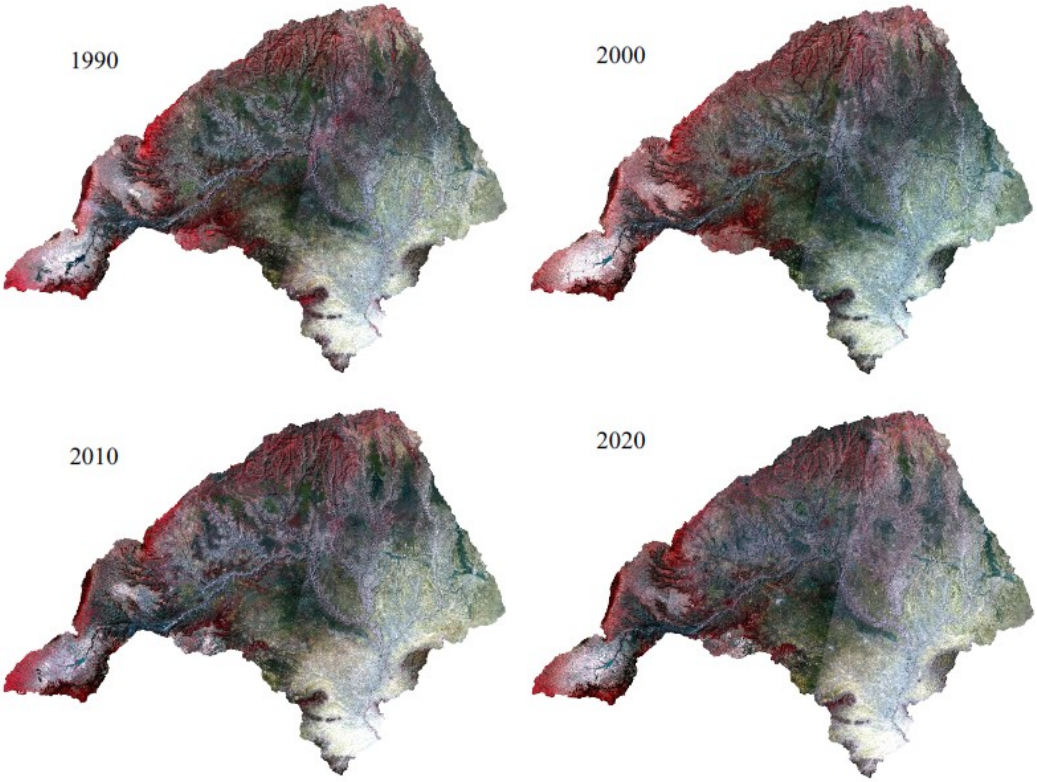


Figure 5.2: False color image of 1990, 2000, 2010, and 2020

to interpret the image components qualitatively and quantitatively. Images acquired by Landsat sensors are subject to distortion owing to sensor, solar, atmospheric, and topographic effects (Young et al., 2017). In general, preprocessing attempts to minimize these effects to the desired extent for a particular application. However, preprocessing steps are time-consuming, and have the potential to introduce additional sources of error (Young et al., 2017).

Thus, the highest-quality Landsat image collection 2 (Tier 1) data was used in this study. Tier 1 products are consistently georeferenced within a radial root mean square error of ≤ 12 m, making them suitable for time-series pixel-level analyses (Young et al., 2017; Loveland and Dwyer, 2012). They have precise terrain processing and have been calibrated across Landsat sensors. Cloud cover in the satellite images was removed by masking the images with the nearest images of the required area. Finally, selected raw images for the study years were projected to be similar to the UTM zone 37 N for the time-series analysis. The preprocessed false-color composite Landsat images for the years 1990, 2000, 2010, and 2020 in upper and central WSRB are depicted in Figure 5.2.

### 5.2.4 Image Classification

Satellite image classification involves labeling the pixels as belonging to particular spectral (and thus information) classes using the spectral data available (Abburu and Golla, 2015; Richards and Jia, 2006). Several satellite image classification methods and techniques are available. There are two broad classes of classification procedure and each finds application in the analysis of remote sensing image data (Richards and Jia, 2006). The first one, supervised classifications require a priori knowledge of the scene area in order to provide the computer with unique material groups or what are called "training classes". The second one, unsupervised classification compare pixel spectral signatures to the signatures of computer-determined clusters and assign each pixel to one of these clusters. These can be used as alternative approaches but are often combined into hybrid methodologies. Thus, hydrid method, both supervised and unsupervised were employed in this study.

In this study, the Maximum Likelihood Classification has been applied as the most commonly utilized per-pixel method. The maximum likelihood algorithm was used to classify land use land cover because the algorithm takes the distributions of the classes into account via a variance-covariance matrix (Richards and Jia, 2006). Based on the multivariate Gaussian distribution the algorithm estimates the probability that a given pixel belongs to a specific land use land cover class (Richards and Jia, 2006). It is a common and powerful classifier in remote sensing and machine learning. Larger deviations from the centre point is allowed where a pixel is not in the area of a contesting category.

The ML-supervised classification techniques work with Bayes theorem and uses a discriminant function to assign the pixel to the class with the highest probability. Each image pixel belongs to the land cover class for which they have the highest membership likelihood following the Gaussian normal distribution function. Although the ML classifier is slow in computation and sometimes unsafe in assuming Gaussian-distributed input data classes, yet, it is a more accurate statistical decision criterion in classifying overlapping signatures.

Maximum Likelihood algorithm calculates the probability distributions for the classes, related to Bayes' theorem, estimating if a pixel belongs to a land cover class (Richards and Jia, 2006). The Bayes theorem is given as follows: Let the spectral classes for an image be represented by $\omega_i$

$$p(\omega_i \mid x) = \frac{p(x \mid \omega_i) \cdot p(\omega_i)}{p(x)} \tag{5.1}$$

where $p(\omega_i \mid x)$ is the likelihood function, a posteriori distribution, ie, the probability that a pixel with feature vector x belongs to class $\omega_i$; p($\omega_i$)) is the priori information, ie, the probability that class $\omega_i$ occurs in the study area (either made equal, or they are given values from prior mapping information) and p(x)is the probability that x is observed. p(x) can be written as follows:

$$p(x) = \sum_{i=1}^{m} p(x \mid \omega_i) \cdot p(\omega_i) \tag{5.2}$$

where m is the number of classes. p(x) is a normalization constant to ensure that $p(\omega_i \mid x)$ sums to l. Any pixel x is assigned to class $\omega_i$ by the following rule:

$$x \in \omega_i \quad \text{if} \quad p(x \mid \omega_i) \cdot p(\omega_i) > p(x \mid \omega_j) \cdot p(\omega_j) \quad \text{for all } j \neq i \tag{5.3}$$

Maximum likelihood classification assumes that the statistics for each class in each band are normally distributed and calculates the probability that a given pixel belongs to a specific class (i). The following discriminant functions as described by Richards and Jia (2006), is calculated for each pixel in the image:

$$g_i(x) = \ln(p(\omega_i)) - \frac{1}{2}\ln(|\Sigma_i|) - \frac{1}{2}(x - \mu_i)^T \Sigma_i^{-1} (x - \mu_i) \tag{5.4}$$

where, x is n-dimensional data (where n is the number of bands), p($\omega_i$)) is probability that class $\omega_i$ occurs in the image and is assumed the same for all classes $\omega_i$ ; $|\Sigma_i|$ is determinant of the covariance matrix of the data in class $\omega_i$, $\Sigma_i^{-1}$ is inverse of the covariance matrix; $\mu_i$ is spectral signature vector of class i.

Unless a probability threshold is selected, all pixels are classified. Each pixel is assigned to the class that has the highest probability (that is, the maximum likelihood). If the highest probability is smaller than a threshold value specified, the pixel remains unclassified.

In this study, owing to the lack of existing high-resolution land use land cover maps, before conducting supervised classification, unsupervised classification was performed to identify possible spectrally different classes. Several clustering methods can be used for unsupervised classifications. The Iterative Self-Organizing Data Analysis Technique (ISODATA) is the most commonly used method. The ISODATA clustering method uses the spectral distance of pixels and

iteratively clusters pixels, redefines the criteria for each class, and classifies them again so that spectral distance patterns in the data gradually emerge (Leica, 2002a).

To process the resulting data, the Semi-Automatic Classification Plugin (SCP) and the Quantum Geographic Information System (QGIS3) were used to classify the satellite images. SCP is a free open-source plugin for QGIS that allows for the semi-automatic classification (also known as supervised classification) of remote sensing images (Congedo, 2021). It provides several tools for downloading free images, preprocessing, post-processing, and raster calculation.

For supervised classification eight land use land cover classes were identified from local knowledge, literature, and existing studies in the area typical for Ethiopian case. This is the first study on land use land cover change analysis in the basin. Eight different types of land use land covers have been identified for upper and central part of WSRB. These are water bodies, builtup, forest, open shrub, dense shrub, grass land, cultivated land, and bare land. The shrub class was divided into dense and open shrub to consider shrub and shrub with grassland. In this document, the terms ”agricultural land” and ”cultivated land,” as well as ”bare land” and ”degraded land,” are used interchangeably. The brief description of each land use land cover class are given in Table 5.1.

### 5.2.5 Image Postprocessing

Post-classification refinement was conducted in order to improve classification accuracy and to reduce the number of inconsistent misclassifications. The classified images were then sieved, clumped, and filtered before yielding a final output. Finally, after accuracy assessment, class statistics of each classified image were computed in using SCP QGIS plugin.

#### Classification accuracy assessment

Accuracy assessment or validation has become an important step in evaluating the performance of a land use land cover classification using remotely sensed data (Congalton, 2005). It involves comparing the results of a classification to a reference dataset to determine the degree of agreement between the two (Foody, 2002; Stehman and Czaplewski, 1998). The error matrix, also known as the confusion matrix, is a commonly used method for assessing the accuracy of satellite image classification (Richards and Jia, 2006; Congalton, 2005). It is performed by comparing the result created by remote sensing analysis to a reference data for selected sample points (Congalton, 2005; Foody, 2002; Kim, 2016; Olofsson et al., 2014; Stehman and Czaplewski, 1998).

Table 5.1: Descriptions of LULC classes identified in the study area

| No | Land Use classes | Brief description | Code |
|---|---|---|---|
| 1 | Waterbody | Area covered by a small dammed lake fed by rainfall and small streams (lakes, dammed reservoir ) | WtB |
| 2 | Built-ups | The settlement comprises all developed land, including areas of human habitation and transportation infrastructure. | BtU |
| 3 | Forest Land | Areas covered by trees forming closed or nearly closed canopies; natural forest; plantation forest; forest along the banks of streams, rivers, and open bodies of water. | Forest |
| 4 | Open Shrubs | Areas covered with sparse small trees, bushes, and shrubs, with grass open canopy areas | OpSH |
| 5 | Dense Shrubs | Areas covered with small trees, bushes, and shrubs, mainly ranged from closed canopy to open canopy areas are considered shrub land | DeSH |
| 6 | Grasslands | Grasslands are those areas that are predominantly covered with grass. Areas covered with grass with some scattered trees and pastures are assumed as grassland. | GrSS |
| 7 | Cultivated Land | The land area that is either arable under permanent crops or land used primarily for the production of food and fiber | AgRL |
| 8 | Barren Land | Areas with little or no vegetation cover consisting of exposed soil and/or bedrock | BaRL |

The error matrix was employed by numerous researchers for evaluating the accuracy of land use land cover maps derived from satellite images (Garedew et al., 2009; Kenea et al., 2021; Meshesha et al., 2016; Wang et al., 2020). The error matrix can be used to calculate various accuracy metrics such as overall accuracy, kappa coefficient, producer accuracy, and user accuracy, etc.

Using an error matrix to represent accuracy has been recommended by many researchers and should be adopted as the standard reporting convention. An error matrix is a square array of numbers set out in rows and columns which express the number of sample units (i.e., pixels, clusters of pixels, or polygons) assigned to a particular category relative to the actual category as verified on the ground (Congalton, 1991). The columns usually represent the reference data while the rows indicate the classification generated from the remotely sensed data.

Overall accuracy and the kappa coefficient were used to evaluate the accuracy of the classified images based on the elements of the error matrix. Overall accuracy has a direct interpretation

in terms of the area of the region of interest (ROI), representing the proportion of the area that is correctly classified (Foody, 2002; Olofsson et al., 2014). Even though, overall accuracy provides a very coarse assessment because it aggregates information over all map classes thereby obscuring important class-specific information. Consequently, it is strongly recommended to provide estimates of user's and producer's accuracies or to provide the error matrix when reporting an accuracy assessment so that these class-specific measures can be estimated by others if desired (Foody, 2002; Olofsson et al., 2014). Whereas, the Kappa coefficient is used to measure the agreement between two sets of categorizations of a dataset while correcting for chance agreements between the categories (Jenness and Wynne, 2007). All performance metrics can be calculated based on the provided error matrix in Table 5.2.

In this matrix, each cell represents the number of sample points that were classified as i and observed to be j. The diagonal (where i = j) represents cases where the predicted value agreed with the observed value. The off-diagonal cells contain misclassified values, and the row and column describe exactly how those values were misclassified (Jenness and Wynne, 2007).

Table 5.2: Error matrix for LULC classification accuracy assessment

| | | **j = Columns(Reference** | | | **Row Totals** | **User Accuracy (UAi)** |
|---|---|---|---|---|---|---|
| **i=Rows(Classified)** | | j1 | j2 | jk | ni. | |
| | i1 | n11 | n12 | n1k | n1. | UAi1=n11/n1. |
| | i2 | n21 | n22 | n2k | n2. | UAi2=n22/n2. |
| | ik | nk1 | nk2 | nkk | nk. | UAik=nkk/nk. |
| **ColumnTotals** | n.j | n.1 | n.2 | n.k | n..=n | |
| **Producer accuracy (PAj)** | | PAj1=n11/n.1 | PAj2=n22/n.2 | PAjk=nkk/n.k | | |

The overall accuracy of the model is simply defined as the total number of correct classifications divided by the total number of sample points, and is calculated using equation 5.5:

$$\text{Overall Accuracy} = \frac{\sum_{i=1}^{k} n_{ii}}{n} \tag{5.5}$$

Kappa coefficient was calculated using equation 5.6;

$$\text{Estimated Kappa } \widehat{K} = \frac{n \sum_{i=1}^{k} n_{ii} - \sum_{i=1}^{k} n_{i.} n_{.i}}{n^2 - \sum_{i=1}^{k} n_{i.} n_{.i}} \tag{5.6}$$

where, i is the class number; n is the total number of classified pixels that are being compared to actual data; $n_{ii}$ is the number of pixels belonging to the actual data class i; that were classified with a class i; Ci is the total number of classified pixels belonging to class i ;and Gi is the total number of actual data pixels belonging to class i.

The major problem during reference data sampling is the proportion of classes in thematic map produced. That is, large classes tend to be represented by a larger number of sample points than the smaller classes; indeed some very small classes may not be represented at all (Richards and Jia, 2006). Relative area proportion of waterbody, built-up, and bare land class is very small in the basin. To ensure small classes are represented adequately, minimum of 30 samples per class was considered during stratified random sampling. Stratified random sampling were conducted using thematic classes for stratification. Stratified random sampling has historically prevailed for assessing the accuracy of remotely sensed maps (Congalton, 2005). The Google Earth image was the only available reference for the study areas and served as the primary reference image.

AcATaMa was used to perform accuracy assessment more interactively on several sources (existing images considered for land use land cover classification accuracy assessment). AcATaMa (sort for Accuracy Assessment of Thematic Maps) is a QGIS plugin that provides comprehensive support for sampling, response design, and estimation in a design-based inference framework (Llano, 2022).

#### LULC dynamics analysis

The estimated conversion of one land use land cover class to other land use land cover class was compared with the total estimation of LULC conversion of respective pair of years for each land use land cover. Cross tabulation analysis was conducted in order to determine the quantitative conversions from a particular category to another LULC category and their corresponding area over the evaluated period (1990 and 2000, 2000 and 2010, 2010 and 2020, and 1990 to 2020) on pixel to pixel basis. The magnitude of change and percent changes in land use land cover (LULC) were calculated using equations 5.7 and 5.8 respectively:

$$\Delta\text{magnitude}(ha) = A_f - A_i \tag{5.7}$$

$$\Delta_{\text{LULC}}(\%) = \frac{A_f - A_i}{A_i} \times 100 \tag{5.8}$$

where $A_f$ is area of LULC (ha) in final year, $A_i$ is area of LULC (ha) in initial year. $\Delta_{\text{LULC}}$ is the change in LULC between the final and initial years. Finally, the LULC conversion matrix between 1990 and 2020 was generated using SCP in QGIS.

### 5.2.6 Future LULC Projection

Future land use land cover predictions are essential for various stakeholders involved in the sustainable development of a basin. To this end, a future land use land cover projection for the study basin was conducted to assess potential changes in these aspects and their combined impact on streamflow in the context of climate change. To accurately project future LULC, it is crucial to model both temporal and spatial pattern changes while considering influencing factors within the study area. This comprehensive approach provided valuable insights into potential alterations in land use land cover over time and their environmental implications. Consequently, it serves as a crucial tool for informed decision-making and planning in the context of basin sustainability.

The MOLUSCE plugin, integrated into the QGIS software, was designed to analyze the changes in land use land cover and to predict potential future changes. This model is based on a multilayer perceptron-artificial neural network (MLP-ANN), Weights of Evidence (WoE), Logistic Regression (LR), and Multi-Criteria Evaluation (MCE) (Akdeniz et al., 2023; Amgoth et al., 2023; Girma et al., 2022; Kafy et al., 2021; NextGIS, 2017). Using MLP-ANN algorithms, potential LULC changes for the year 2040 were predicted and determined in the study area. These projections were then applied to future impact modeling. The MOLUSCE user interface offers an easy-to-use interface with specific modules and functions (NextGIS, 2017). These modules, which include Area Analysis, Modeling, Simulation, and Validation, enable the comprehensive analysis and simulation of future land use land cover changes.

The first step in the model involves utilizing the LULC maps for both the initial year (2000) and the final year (2010), and spatial variables, including DEM, slope map, distance from streams, distance from roads, distance from built-up areas, and population density maps, are incorporated into the model. These inputs were used to generate a land use land cover change map, which served as the foundation for establishing the changing patterns within the study area between 2000 and 2010. Importantly, all explanatory maps share the same raster format across datasets,

maintaining consistent geographical projected coordinates in UTM 37 N and a pixel resolution of 30 m to align with classified Landsat images.

An evaluation of the correlation among the driving factors, which are the spatial variables, was proceeded with after ensuring that the projections of all classified Landsat images matched those of the explanatory maps. In MOLUSCE, three techniques are available for conducting this correlation analysis: Pearson's correlation, Cramer's coefficient, and joint information uncertainty. It is worth noting that Cramer's coefficient and joint information uncertainty are specifically designed to work with categorical data (NextGIS, 2017). Therefore, in the analysis, Pearson's correlation coefficient was used to assess the relationships among the explanatory datasets. Any spatial variable with a correlation greater than 0.8 was exempted from further analysis. Subsequently, the Area Analysis module within MOLUSCE was utilized to generate a class statistics table and a transition matrix. These outputs provide valuable insights into the initial and final LULC change areas as well as the proportion of pixels transitioning from one LULC category to another.

The modeling module offers four distinct algorithms designed to establish a relationship between input and output data for predicting future LULC transitions. In this study, MLP-ANN algorithms were employed to project and determine potential land use land cover changes for the year 2040. During the modeling process, users have the flexibility to define several key parameters, including the number of samples and the sampling mode, as well as specifications such as the number of neighboring pixels, learning rate, momentum, maximum iteration, and number of hidden layers for ANN modeling. As the module progresses, it generates a learning curve, which serves as a valuable tool for assessing the dataset properties and representativeness. The ANN algorithm analyzes the accuracy achieved on both the training and validation sets of samples, storing the best-performing neural network in memory. The training process continues until it reaches either the maximum specified number of iterations or attains the best accuracy, ensuring that the model optimally captures the relationships between the input and output data for future LULC transitions.

After the model is trained using ANN algorithms, the Cellular Automata simulation module comes into play, enabling the simulation of future LULC scenarios based on the best-performing neural network stored during training. However, it is important to note that this simulation relies

on a major assumption – the stationarity of existing patterns and dynamics, as indicated by the transition matrix–in the future period. Additionally, the prediction of LULC transitions for 2040 was based on the analysis of classified Landsat images from 2000 and 2010. These historical data serve as the foundation for projecting how land use land cover will evolve in the future, considering past patterns.

Finally, the validation module provides a means to assess the accuracy of the simulation. This validation process took place after loading both the reference and simulated land use land cover maps (NextGIS, 2017). Within this module, three types of kappa statistics are calculated: Kappa overall (K), Kappa location ($K_{\text{loc}}$), and Kappa histogram ($K_h$). These statistics help evaluate the degree of agreement between the simulated and reference land use land cover maps, providing valuable insights into the reliability of the simulation results. Equations (5.9)-(5.14) were used to calculate kappa statistics are:

$$K = \frac{P(A) - P(E)}{1 - P(E)} \tag{5.9}$$

$$K_{\text{loc}} = \frac{P(A) - P(E)}{P_{\max} - P(E)} \tag{5.10}$$

$$K_h = \frac{P_{\max} - P(E)}{1 - P(E)} \tag{5.11}$$

where

$$P(A) = \sum_{i=1}^{c} p_{ii} \tag{5.12}$$

$$P(E) = \sum_{i=1}^{c} p_i \cdot p_j \tag{5.13}$$

$$P_{\max} = \sum_{i=1}^{c} \min(p_{iT}, p_{Tj}) \tag{5.14}$$

and $p_{ij}$ is the i.j-th cell of contingency table, $p_{iT}$ is the sum of all cells in i-th row, $p_{Tj}$ is the sum of all cells in j-th column, c is the count of raster categories. The accuracy of the agreement in all kappa indices ranges from 0 to 1 and a value closer to 1 is a better agreement between the modeled and predicted maps whereas when closer to 0, then the simulation is considered imperfect.

In general, MOLUSCE, a user-friendly plugin for QGIS, provides a convenient and efficient solution for simulating potential future land use land cover changes. A detailed description of MOLUSCE's methods and algorithms can be found at this link: `https://wiki.gis-lab.info/w/Landscape_change_analysis_with_MOLUSCE_-_methods_and_algorithms`.

## 5.3 Result and Discussion

The LULC classification was performed using satellite images obtained from the USGS Landsat open-source portal. Thus, both Landsat 5 and 8 were used to study the time series trends of LULC changes in the upper and central parts of the Wabi Shebele River Basin (WSRB). This study employs a hybrid approach, combining unsupervised and supervised classification techniques, for satellite image classification. A widely used supervised classification technique, the maximum-likelihood classification algorithm, was applied after collecting the training data. After the classification, the accuracy of the thematic maps was evaluated. Finally, the magnitude and rate of change, along with the transition matrix, were generated and the results are presented in the following sections.

### 5.3.1 LULC Classification Accuracy

After classification of Landsat images for four epochs, the classification images were validated against a reference map using standard image accuracy metrics, including the user and produced accuracy, overall accuracy, and kappa coefficient. The AcATaMa QGIS3 plugin was used for stratified random sampling and accuracy assessments. Stratified random sampling was employed to sample points proportional to the area of each land use class, implying that a large number of random points are generated for the land use class with a larger area and vice versa. The total number of samples collected in 1990, 2000, 2010, and 2020 were 893, 890, 888, and 889, respectively. Finally, an error matrix was generated for the validation of classified thematic images for 1990, 2000, 2010, and 2020, and the accuracy metrics were estimated. The error matrices for each year are presented in the Appendix Table A.3.

The summary of the classification accuracy analysis results is provided in Table 5.3. The estimated accuracy metric values showed higher agreement between the classified and reference maps for all years of study. All user and producer accuracy values were above the recommended limit (greater than 0.8). Overall, the LULC classification performed well throughout the study period, with high overall accuracy and significant agreement with the reference data, as in-

dicated by the kappa coefficient. The results showed that accuracy and kappa coefficients of 0.94/0.92, 0.95/0.93, 0.93/0.90, and 0.94/0.91 were achieved for 1990, 2000, 2010, and 2020 LULC, respectively (Table 5.3). The slight fluctuations observed in the overall accuracy and kappa coefficient values between different years could be attributed to changes in land use land cover patterns, data quality, or classification methodology. Based on these ranges, the classification results in this study exhibited strong concurrence with the validation dataset and satisfied the minimum accuracy criteria necessary for conducting subsequent change detection and impact analysis.

Table 5.3: Summary of LULC classification accuracies for the 1990, 2000, 2010 and 2020

| **LULC Classes** | **1990** | | **2000** | | **2010** | | **2020** | |
|---|---|---|---|---|---|---|---|---|
| | UA | PA | UA | PA | UA | PA | UA | PA |
| WtB | 1.00 | 1.00 | 1.00 | 1.00 | 1.00 | 1.00 | 1.00 | 1.00 |
| BtU | 0.93 | 1.00 | 0.93 | 1.00 | 0.87 | 1.00 | 0.94 | 1.00 |
| Forest | 0.95 | 0.91 | 1.00 | 0.95 | 0.94 | 1.00 | 0.91 | 0.97 |
| OpSH | 0.94 | 0.97 | 0.96 | 0.95 | 0.97 | 0.92 | 0.95 | 0.95 |
| DeSH | 0.96 | 0.88 | 0.87 | 0.90 | 0.84 | 0.90 | 0.96 | 0.84 |
| GrSS | 0.95 | 0.92 | 0.94 | 0.94 | 0.81 | 0.81 | 0.84 | 0.91 |
| AgRL | 0.90 | 0.99 | 0.94 | 0.98 | 0.88 | 0.97 | 0.90 | 0.94 |
| BaRL | 0.97 | 0.77 | 0.95 | 0.88 | 1.00 | 0.91 | 0.95 | 0.84 |
| Overall Accuracy | 0.94 | | 0.95 | | 0.93 | | 0.94 | |
| Kappa Coefficient | 0.92 | | 0.93 | | 0.90 | | 0.91 | |

UA= User's Accuracy and PA = Producer's accuracy

### 5.3.2 LULC Classification

The final classified maps are shown in Figure 5.3, and the areal distribution of each land use land cover class is summarized in hectares and percentages for 1990, 2000, 2010, and 2020 in Table 5.4. Based on the classification results, open shrublands were the major LULC type in all study years, covering more than 65% of the land. Cultivated land was the second most dominant land use land cover type, accounting for 13.6%, 16.8%, 24.8%, and 27.1% in 1990, 2000, 2010, and 2020, respectively. Following open shrubs and agricultural land, dense shrubs covered 11.4% in 1990, 7.9% in 2000, 5.4% in 2010, and 4.0% in 2020. Forest, grass, and bare land cover 1 – 5% of the area in all study periods. In addition, the proportion of water bodies, and built-up areas in the basin is relatively small (less than 0.1%).

Spatially, the distribution of land use land cover classes in the basin is apparent based on the topography of the area shown in Figure 5.3. Cultivated land was the dominant land cover in the highlands, whereas open shrubs were dominant in lower elevation areas. Forest lands exist only in the highlands part of the basin. Dense shrubs were found on the steep middle slope of the basin, and degraded land in the lower part of the basin. In general, open shrubs and cultivated land cover the dominant parts of the basin, greater than 75% in all study years.

Table 5.4: Areal coverage of Land Use Land cover classes in Upper and Central WSRB

| LULC Class | 1990 | | 2000 | | 2010 | | 2020 | |
|---|---|---|---|---|---|---|---|---|
| | ha | % | ha | % | ha | % | ha | % |
| WtB | 9863.3 | 0.1 | 8576.1 | 0.1 | 6592.6 | 0.1 | 7646.7 | 0.1 |
| BtU | 607.5 | 0.0 | 1240.9 | 0.0 | 3983.9 | 0.0 | 11486.7 | 0.1 |
| Forest | 214766.9 | 2.3 | 119416.9 | 1.3 | 87202.8 | 0.9 | 79416.5 | 0.9 |
| OpSH | 6111938 | 66.2 | 6350824 | 68.8 | 6091083 | 66.0 | 5935513 | 64.3 |
| DeSH | 1055812 | 11.4 | 725605.2 | 7.9 | 495467.5 | 5.4 | 372646.9 | 4.0 |
| GrSS | 485169.3 | 5.3 | 344925 | 3.7 | 111850.6 | 1.2 | 117783.5 | 1.3 |
| AgRL | 1258042 | 13.6 | 1547361 | 16.8 | 2292871 | 24.8 | 2498732 | 27.1 |
| BaRL | 98785.3 | 1.1 | 137036.9 | 1.5 | 145933.9 | 1.6 | 211760.5 | 2.3 |
| **Total** | **9234985** | **100** | **9234985** | **100** | **9234985** | **100** | **9234985** | **100** |

### 5.3.3 Magnitude and Rate of LULC change

The magnitude and rate of decadal LULC changes were evaluated for the periods 1990-2000, 2000-2010, 2010-2020, and 1990-2020 to assess the trends of each LULC class in the upstream and central parts of the Wabi Shebele River Basin. These changes were calculated in terms of area (hectares) and percentage, as presented in Table 5.5 and Figure 5.4. The implications of each LULC change for environmental sustainability are explained in detail in this section.

The coverage of water bodies decreased by 1,282.2 hectares (-13.1%) from 1990 to 2000, and by an additional 1,983.5 hectares (-23.1%) from 2000 to 2010. However, from 2010 to 2020, there was an increase of 1,054.1 hectares (16.0%). Overall, from 1990 to 2020, there was a net decrease of 2,216.7 hectares (-22.5%).

From 1990 to 2000, there was an increase of 633.4 hectares of built-up area, which accounted for a growth of 104.3% in relation to the initial area in 1990. There was a substantial increase

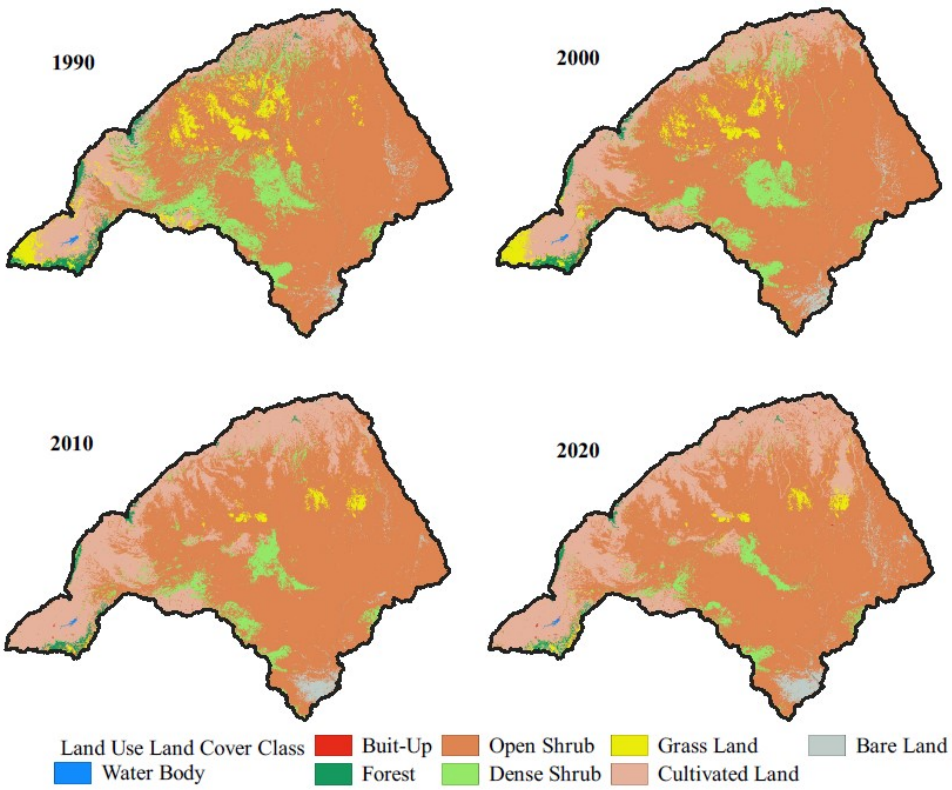


Figure 5.3: Classified LULC map of 1990, 2000, 2010, and 2020

in built-up areas with 2,743.0 hectares and 7,502.8 hectares and 221.0% and 188.3% from 2000 to 2010 and 2010 to 2020 respectively. Overall, from 1990 to 2020, there was a cumulative increase of 10,879.2 hectares, which corresponded to a remarkable growth of 1,790.8% compared to the initial area in 1990.

From Table 5.5, land use land cover change analysis showed that from 1990 to 2020, there was a cumulative decrease of 135,350.4 hectares in forested areas, corresponding to a significant decline of 63.0% compared to the initial forested area in 1990. In terms of area in hectares, forest areas decreased substantially by 95,349.9 hectares, 32,214.2 hectares, and 7,786.3 hectares from 1990 to 2000, 2000 to 2010, and 2010 to 2020, respectively. In terms of percentage, there was a decline in the forest area by 44.4%, 27.0%, and 8.9% compared to the preceding years. These results suggest a considerable loss of forested land over the entire period under consideration.
According to Table 5.5 and Figure 5.4, the open shrub land experienced various changes over the examined periods. From 1990 to 2000, there was an increase of 238,885.7 hectares, accounting for a growth of 3.9% relative to the initial area in 1990. However, from 2000 to 2010, there was a significant decrease of 259,740.5 hectares, representing a decline of 4.1% compared to the area in 2000. From 2010 to 2020, the category showed a further decrease of 155,570.4 hectares,

Table 5.5: Magnitude and rate of decadal LULC change in the Upper and Central WSRB

| LULC Class | 1990 -2000 | | 2000-2010 | | 2010-2020 | | 1990-2020 | |
|---|---|---|---|---|---|---|---|---|
| | ha | % | ha | % | ha | % | ha | % |
| WtB | -1287.2 | -13.1 | -1983.5 | -23.1 | 1054.1 | 16.0 | -2216.7 | -22.5 |
| BtU | 633.4 | 104.3 | 2743.0 | 221.0 | 7502.8 | 188.3 | 10879.2 | 1790.8 |
| Forest | -95349.9 | -44.4 | -32214.2 | -27.0 | -7786.3 | -8.9 | -135350.4 | -63.0 |
| OpSH | 238885.7 | 3.9 | -259740.5 | -4.1 | -155570.4 | -2.6 | -176425.3 | -2.9 |
| DeSH | -330207.2 | -31.3 | -230137.7 | -31.7 | -122820.6 | -24.8 | -683165.6 | -64.7 |
| GrSS | -140244.3 | -28.9 | -233074.4 | -67.6 | 5932.9 | 5.3 | -367385.8 | -75.7 |
| AgRL | 289318.1 | 23.0 | 745510.2 | 48.2 | 205861.0 | 9.0 | 1240689.3 | 98.6 |
| BaRL | 38251.6 | 38.7 | 8897.0 | 6.5 | 65826.5 | 45.1 | 112975.2 | 114.4 |

indicating a decline of 2.6% compared to the area in 2010. Overall, from 1990 to 2020, there was a cumulative decrease of 176,425.3 hectares, corresponding to a decline of 2.9% relative to the initial area in 1990. These results indicate a complex pattern of changes in the open shrub land, with an initial increase followed by significant decreases in subsequent periods.

The results showed that dense shrub land decreased substantially during the study period. There was a decrease of 330,207.2 hectares, 230,137.7 hectares, and 122,820.6 hectares in dense shrub land areas during the period of 1990 to 2000, 2000 to 2010, and 2010 to 2020 respectively. These represented a decline of 31.3% in 2000, 31.7% in 2010, and 24.8% in 2020 compared to 1990, 2000, and 2010, respectively. Overall, from 1990 to 2020, there was a cumulative decrease of 683,165.6 hectares in the dense shrub land, corresponding to a substantial decline of 64.7% compared to the initial area in 1990.

Grassland experienced a significant decrease of 140,244.3 hectares from 1990 to 2000 and 233,074.4 hectares from 2000 to 2010, accounting for declines of 28.9% and 67.6% compared to the initial areas in 1990 and 2000, respectively. However, from 2010 to 2020, there was a modest increase of 5,932.9 hectares, indicating a growth of 5.3% relative to the area in 2010. Overall, from 1990 to 2020, there was a cumulative decrease of 367,385.8 hectares, corresponding to a substantial decline of 75.7% compared to the initial area in 1990. These results suggest a significant loss in grassland during the first two decades, followed by a slight recovery in the last decade.

According to Table 5.5 and Figure 5.4, cultivated land showed significant and consistent expansion throughout the study period. There was an increase of 289,318.1 hectares from 1990

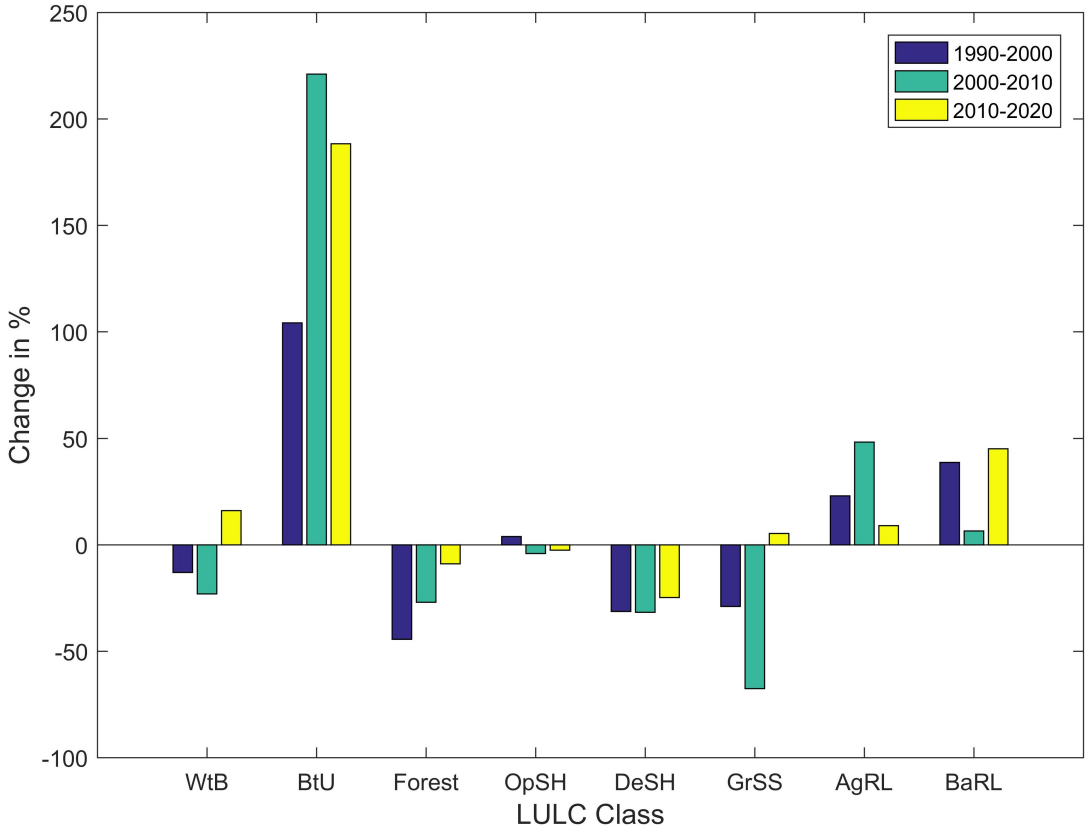


Figure 5.4: Rate of LULC change in the upper and central WSRB

to 2000, 745,510.2 hectares from 2000 to 2010, and 205,861.0 hectares from 2010 to 2020. In percentage terms, cultivated land expanded by 23.0% in 2000, 48.2% in 2010, and 9.0% in 2020 compared to the preceding periods. Overall, from 1990 to 2020, there was a cumulative increase of 1,240,689.3 hectares in cultivated land coverage, corresponding to a substantial growth of 98.6% compared to the coverage in 1990.

From the analysis results, the coverage of bare land in the upper and central Wabi Shebele River basin increased by 38,251.6 hectares, 8,897.0 hectares, and 65,826.5 hectares between 1990 and 2000, 2000–2010, and 2010–2020, respectively. Similarly, the rate of change was 38.7% in 2000, 6.5% in 2010, and 45.1% in 2020, compared to 1990, 2000, and 2010, respectively. Overall, during the study years, there was a cumulative increase of 112,975.2 hectares in the coverage of degraded land in the basin, corresponding to a growth of 114.4% compared to the initial area in 1990.

Overall, the results indicate a significant expansion in built-up areas, cultivated land, and bare land, while forest land and dense shrubs experienced a substantial and consistent decline through-

out the study period. Water bodies, open shrubs, and grasslands exhibited fluctuating patterns during this time.

### 5.3.4 LULC Dynamics Analysis

Table 5.6 presents the transition matrix in LULC classes between consecutive periods (1990-2000, 2000-2010, and 2010-2020) and the whole period (1990 - 2020). The coverage of the water body and built-up area was insignificant compared to the total area of the study. Thus, the conversion result table might not show the figure correctly. However, the Water body and built-up area mainly shifted to open shrub and agricultural land. Similarly, a substantial coverage of forest land transformed into open and dense shrub, grassland, and cultivated land with 17%, 12%, 2%, and 34%, respectively, during the study period. The open shrub also expanded to cultivated land with a maximum of 10% during the 2000 to 2010 period.

A considerable percentage of bare land was also converted to open shrub land in the study area. Overall, 13% of open shrubs shifted to cultivated land during the 1990 to 2020 period. Dense shrub diminished mainly to open shrub land. Grassland expanded to open shrub and cultivated land. Cultivated land, the second major category of the land use land cover classes in the basin, expanded at the expanse of all LULC classes except degraded land. During the study period (1990 – 2020), cultivated land expanded at the expense of 16% of the water body, 24% of built-up, 34% of forest, 13% of open shrub, 18% of dense shrub, and 60% of grassland. Finally, bare land expanded at the expanse of mainly from open shrub land with 3% based on this study.

### 5.3.5 Future LULC Projection

Future land use land cover changes in the basin were predicted using the MLP-ANN model, employing the MOLUSCE software. Six explanatory factors, comprising both physical and socioeconomic elements, were incorporated to enhance the accuracy of the predictions. The evaluation of Pearson's correlations among these spatial variable factors revealed significant relationships, particularly between distance from town and distance from road, as well as between distance to stream and distance to town. Pearson's correlation results are summarized in Table 5.7. Consequently, due to the collinearity between distance from road and distance from town, as well as distance from stream and distance from town, the decision was made to exclude distance from road and distance from stream from further analysis. The transition model simulation relied on the initial classified image from 2000, the final classified image from 2010, and the remaining four explanatory maps.

Table 5.6: LULC transition matrix for 1990-2000, 2000-2010, 2010-2020 and 1990-2020

| Period | LULC | WtB | BtU | Forest | OpSH | DeSH | GrSS | AgRL | BaRL |
|---|---|---|---|---|---|---|---|---|---|
| | | | | | **2000** | | | | |
| **1990** | WtB | 0.62 | 0.00 | 0.00 | 0.18 | 0.04 | 0.03 | 0.12 | 0.01 |
| | BtU | 0.00 | 0.45 | 0.00 | 0.02 | 0.00 | 0.02 | 0.51 | 0.00 |
| | Forest | 0.00 | 0.00 | 0.51 | 0.12 | 0.13 | 0.07 | 0.17 | 0.00 |
| | OpSH | 0.00 | 0.00 | 0.00 | 0.91 | 0.02 | 0.01 | 0.04 | 0.01 |
| | DeSH | 0.00 | 0.00 | 0.00 | 0.40 | 0.51 | 0.01 | 0.07 | 0.00 |
| | GrSS | 0.00 | 0.00 | 0.00 | 0.32 | 0.01 | 0.51 | 0.15 | 0.00 |
| | AgRL | 0.00 | 0.00 | 0.00 | 0.09 | 0.02 | 0.02 | 0.87 | 0.00 |
| | BaRL | 0.00 | 0.00 | 0.00 | 0.35 | 0.00 | 0.00 | 0.00 | 0.64 |
| | | | | | **2010** | | | | |
| **2000** | WtB | 0.53 | 0.00 | 0.00 | 0.30 | 0.01 | 0.05 | 0.11 | 0.00 |
| | BtU | 0.00 | 0.56 | 0.00 | 0.21 | 0.00 | 0.00 | 0.23 | 0.00 |
| | Forest | 0.00 | 0.00 | 0.60 | 0.16 | 0.07 | 0.03 | 0.14 | 0.00 |
| | OpSH | 0.00 | 0.00 | 0.00 | 0.86 | 0.02 | 0.01 | 0.10 | 0.01 |
| | DeSH | 0.00 | 0.00 | 0.01 | 0.41 | 0.46 | 0.00 | 0.12 | 0.00 |
| | GrSS | 0.00 | 0.00 | 0.01 | 0.43 | 0.01 | 0.09 | 0.47 | 0.00 |
| | AgRL | 0.00 | 0.00 | 0.00 | 0.07 | 0.00 | 0.00 | 0.92 | 0.00 |
| | BaRL | 0.00 | 0.00 | 0.00 | 0.44 | 0.00 | 0.00 | 0.01 | 0.55 |
| | | | | | **2020** | | | | |
| **2010** | WtB | 0.71 | 0.00 | 0.00 | 0.25 | 0.02 | 0.00 | 0.00 | 0.02 |
| | BtU | 0.00 | 0.71 | 0.00 | 0.28 | 0.00 | 0.00 | 0.00 | 0.00 |
| | Forest | 0.00 | 0.00 | 0.77 | 0.00 | 0.22 | 0.00 | 0.00 | 0.00 |
| | OpSH | 0.00 | 0.00 | 0.00 | 0.89 | 0.02 | 0.00 | 0.08 | 0.01 |
| | DeSH | 0.00 | 0.00 | 0.02 | 0.46 | 0.51 | 0.00 | 0.00 | 0.00 |
| | GrSS | 0.00 | 0.00 | 0.00 | 0.02 | 0.00 | 0.94 | 0.03 | 0.00 |
| | AgRL | 0.00 | 0.00 | 0.00 | 0.13 | 0.00 | 0.01 | 0.86 | 0.00 |
| | BaRL | 0.00 | 0.00 | 0.00 | 0.00 | 0.00 | 0.00 | 0.00 | 1.00 |
| | | | | | **2020** | | | | |
| **1990** | WtB | 0.54 | 0.00 | 0.00 | 0.23 | 0.02 | 0.04 | 0.16 | 0.01 |
| | BtU | 0.00 | 0.69 | 0.00 | 0.07 | 0.00 | 0.00 | 0.24 | 0.00 |
| | Forest | 0.00 | 0.00 | 0.34 | 0.17 | 0.12 | 0.02 | 0.34 | 0.00 |
| | OpSH | 0.00 | 0.00 | 0.00 | 0.82 | 0.01 | 0.01 | 0.13 | 0.03 |
| | DeSH | 0.00 | 0.00 | 0.00 | 0.55 | 0.27 | 0.00 | 0.18 | 0.00 |
| | GrSS | 0.00 | 0.00 | 0.00 | 0.32 | 0.01 | 0.07 | 0.60 | 0.00 |
| | AgRL | 0.00 | 0.01 | 0.00 | 0.07 | 0.00 | 0.00 | 0.92 | 0.00 |
| | BaRL | 0.00 | 0.00 | 0.00 | 0.39 | 0.00 | 0.00 | 0.03 | 0.58 |

To ensure representative sampling using the sampling tab, 50,000 sample pixels were extracted using stratified sampling procedures, encompassing all categories of the LULC classes. In the ANN modeling approach, the default settings were adhered to, including a 3 × 3 pixel neighborhood, a learning rate of 0.001, a momentum of 0.001, and 1000 iterations, with 10 hidden layers. The performance of the model was reassuring, as indicated by the excellent fit observed between the training and validation sets, as depicted in the ANN learning curve presented in Figure 5.5. These comprehensive steps and results strengthen the reliability of the predictions for future land use land cover changes in the basin.

Table 5.7: Pearson's correlation between the explanatory factors

| | DEM | PopD | DfRoad | DfTown | Slope | DfStream |
|---|---|---|---|---|---|---|
| DEM | – | 0.59 | -0.53 | -0.53 | 0.21 | -0.53 |
| PopD | | – | -0.47 | -0.47 | 0.22 | -0.47 |
| DfRoad | | | – | **1.00** | -0.13 | **1.00** |
| DfTown | | | | – | -0.13 | **1.00** |
| Slope | | | | | – | -0.13 |
| DfStream | | | | | | – |

Note: DEM = Digital Elevation Model, PopD = Population Density, DfRoad = Distance from a Road, DfTown = Distance from a Town, DfStream = Distance from a stream

Table 5.8: Projected magnitude and rate of land use land cover change 2020 to 2040

| **LULC Class** | **2020** | | **2040** | | **2020-2040** | |
|---|---|---|---|---|---|---|
| | $km^2$ | % | $km^2$ | % | $km^2$ | % |
| WtB | 76.5 | 0.1 | 60.4 | 0.1 | -16.1 | -21.0 |
| BtU | 114.9 | 0.1 | 151.9 | 0.2 | 37.0 | 32.2 |
| Forest | 794.2 | 0.9 | 716.7 | 0.8 | -77.5 | -9.8 |
| OpSH | 59355.1 | 64.3 | 54435.8 | 58.9 | -4919.3 | -8.3 |
| DeSH | 3726.5 | 4.0 | 4290.1 | 4.6 | 563.6 | 15.1 |
| GrSS | 1177.8 | 1.3 | 1233.2 | 1.3 | 55.4 | 4.7 |
| AgRL | 24987.3 | 27.1 | 28769.8 | 31.2 | 3782.5 | 15.1 |
| BaRL | 2117.6 | 2.3 | 2692.0 | 2.9 | 574.4 | 27.1 |
| Total | 92349.9 | 100 | 92349.9 | 100 | | |

Following the training of the model using the ANN algorithms, a Cellular Automata simulation

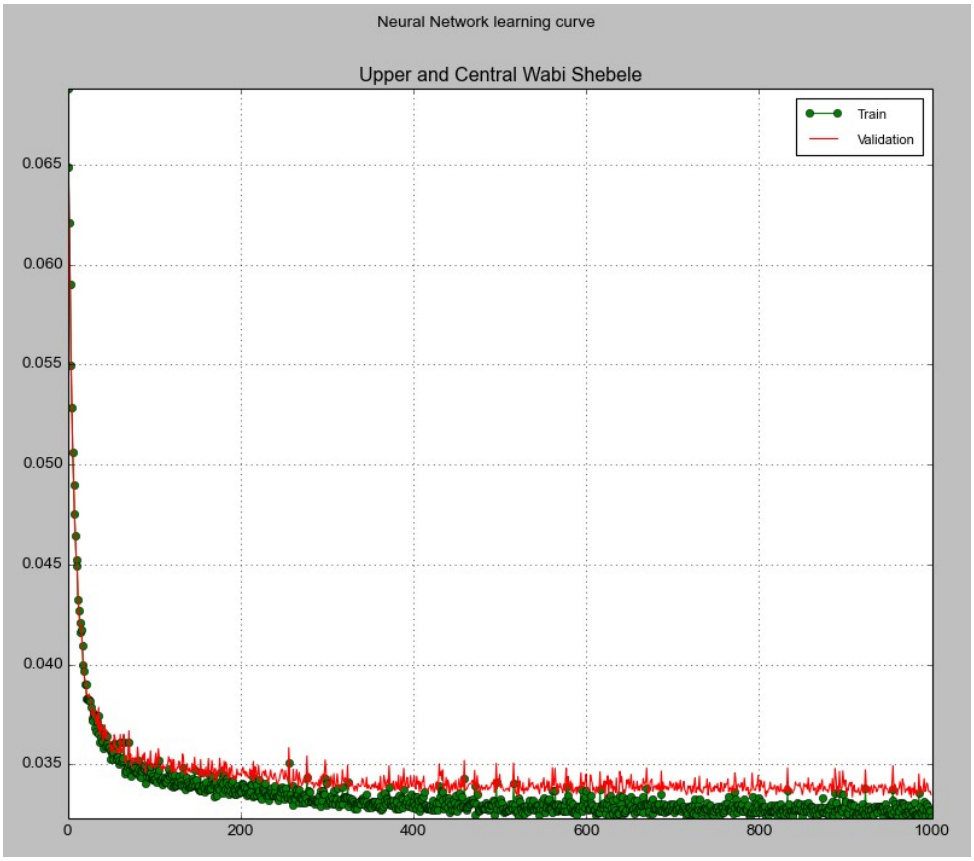


Figure 5.5: ANN learning curve for LULC projection in Upper and central WSRB

module was employed. This module enabled the simulation of LULC for 2020, utilizing the best-performing neural network that had been stored during the training process. The assessment of the resulting LULC maps for the year 2020 yielded promising outcomes. Specifically, an overall kappa coefficient value of 81%, kappa histogram of 89% and kappa location of 82% were achieved. These metrics indicate the quality of the reference and projected LULC maps for 2020, suggesting a high degree of agreement between the predicted and actual LULC images for that year. Such favorable results sustained confidence in the model's ability to accurately forecast future land use land cover patterns up to 2040.

Once an acceptable performance is achieved, a LULC map for 2040 is predicted. Subsequently, the analysis of land use land cover change, along with the magnitude and rate of change, was conducted between 2020 and 2040 using the classified and projected images presented in Table 5.8. The prediction of LULC changes for the year 2040, carried out using MLP – ANN revealed several apparent trends. Notably, there might be an increase in a built-up areas, dense shrubs, grasslands, agricultural land, and barren land. In contrast, the categories of the water body, forest land, and open shrub land exhibited a substantial reduction in the upper and central parts of

the Wabi Shebele River basin.

According to the LULC transition matrix in Table 5.9, significant land use land cover changes are projected between 2020 and 2040. Notably, 35% of water bodies are expected to convert to open shrublands. Forest land will also transform substantially, with 18% transitioning to denseshrub lands and another 18% converting to agricultural land. Additionally, 12% of open shrublands are projected to become agricultural land. Dense shrub areas will experience significant changes, with 36% transitioning to open shrublands and 21% shifting to agricultural areas. Grasslands are expected to convert 46% to open shrublands and 16% to agricultural land. Furthermore, 16% of agricultural land is projected to change to open shrublands. Lastly, barren land is primarily expected to shift to open shrublands, with a notable transition of 4%.

Table 5.9: Projected land use land cover change matrix 2020 to 2040

| **Period** | **LULC** | **WtB** | **BtU** | **Forest** | **OpSH** | **DeSH** | **GrSS** | **AgRL** | **BaRL** |
|---|---|---|---|---|---|---|---|---|---|
| | | | | | 2040 | | | | |
| 2020 | WtB | 0.50 | 0.00 | 0.00 | 0.35 | 0.01 | 0.06 | 0.08 | 0.00 |
| | BtU | 0.00 | 1.00 | 0.00 | 0.00 | 0.00 | 0.00 | 0.00 | 0.00 |
| | Forest | 0.00 | 0.00 | 0.59 | 0.03 | 0.18 | 0.02 | 0.18 | 0.00 |
| | OpSH | 0.00 | 0.00 | 0.00 | 0.82 | 0.04 | 0.01 | 0.12 | 0.01 |
| | DeSH | 0.00 | 0.00 | 0.04 | 0.36 | 0.38 | 0.01 | 0.21 | 0.00 |
| | GrSS | 0.00 | 0.00 | 0.02 | 0.46 | 0.01 | 0.34 | 0.16 | 0.00 |
| | AgRL | 0.00 | 0.00 | 0.00 | 0.16 | 0.00 | 0.00 | 0.83 | 0.00 |
| | BaRL | 0.00 | 0.00 | 0.00 | 0.04 | 0.00 | 0.00 | 0.00 | 0.96 |

Similarly, notable trends have been reported for future land use land cover changes. Lukas et al. (2023), found a discernible increase in built-up areas, which contrasts with a decrease in forest cover and shrubland in the upper Omo-Gibe river basin over the period from 2022 to 2067. This transformation aligns with the findings of another study conducted in the Gidabo River Basin (GRB) within the Main Ethiopian Rift Valley, as noted by Girma et al. (2022). In their study, significant gains in agricultural land and settlements were observed, accompanied by a decrease in forests, shrubs, and grasslands. However, unlike this study and the results presented by Lukas et al. (2023), the coverage of water bodies is predicted to increase in their study area. These distinct findings highlight regional variations in land use land cover dynamics. These collective insights contribute to a broader understanding of LULC changes in diverse ecosystems.The outcomes of the model should not be interpreted as fixed predictions for particular locations but rather as probable spatial patterns. Moreover, the results of these studies hold promise for

the development of more effective watershed and basin management techniques, particularly in the context of natural resource preservation, including sustainable management of freshwater resources.

## 5.4 Conclusion

Land use land cover changes in the upper and central parts of the WSRB, Ethiopia, were evaluated over the past three decades, from 1990 to 2020. A hybrid image classification methodology was employed using the Semi-Automatic Classification Plugin (SCP) in the QGIS environment. This approach involves the use of the ISODATA algorithm for unsupervised classification and the ML classification algorithm for supervised classification. Raw satellite imagery from Landsat 5 TM and Landsat 8 OLI was processed to generate land use land cover maps for 1990, 2000, 2010, and 2020. Comprehensive preprocessing and processing activities were conducted before the Landsat images were classified to enhance the accuracy of the classification results. Accuracy validation was performed on the classified thematic maps using an error matrix and kappa index to test the accuracy of the classified imagery. Additionally, future land use land cover changes in the basin were predicted using the MLP-ANN model within MOLUSCE software for 2040. Four out of six explanatory factors were incorporated to enhance the accuracy of the model predictions due to the higher degree of correlation among three factors. The accuracy of the predicted images was evaluated using similar indices.

The results of the validation indices applied to compare the reference Land Use Land Cover (LULC) with the predicted LULC consistently exceeded the acceptable threshold for prediction accuracy in both classified Landsat images and future LULC projections. The analysis of the classified Landsat images for the years 1990, 2000, 2010, and 2020 revealed significant LULC changes in the upper and central parts of WSRB. Notably, a substantial expansion of agricultural lands over the years was observed in the upper basin, attributed to the increasing encroachment on forests and shrublands driven by rapid population growth in the country. Meanwhile, extensive open shrubland was found to be covering the central part of the basin.

However, the predominant change in land use land cover observed throughout the entire period was the increase in cultivated and built-up areas, particularly in the upper part of the basin, accompanied by an overall decline in forested areas, grasslands, and woodlands. Between 1990 and 2020, the results of the classified images revealed a 22.5% reduction in water bodies, a sig-

nificant 1,790.8% increase in built-up areas, a 63.0% reduction in forest cover, a 67.6% decrease in open and dense shrubland, a 75.7% reduction in grasslands, a substantial 98.6% increase in agricultural land, and a remarkable 114.4% surge in bare land in the upper and central regions of the basin. Similarly, between 2020 and 2040, the future projected image indicated an anticipated 21% reduction in waterbodies, a 32.2% increase in built-up areas, a 9.8% reduction in forest cover, an 8.3% decrease in open shrubland, a 15.1% increase in dense shrubland, a 4.7% increase in grasslands, a 15.1% increase in agricultural land, and a substantial 27.1% expansion in bare land coverage.

In general, the expansion of cultivated and built-up areas at the expense of forest and shrubland is a foreseeable scenario in the future, highlighting the need for the anticipated adverse impacts of LULC changes to be addressed by planners and policymakers. Due to the reduction in vegetation cover, which leads to decreased infiltration and increased surface runoff, the entire hydrological regime of the basin is significantly altered. Therefore, the implementation of extensive afforestation programs and projects should be considered to restore the natural ecosystem of the basin. Therefore, chapter 7 conducts the assessment of the impact of LULC changes, both individually and combined with climate change, on the hydrological regime of headwater catchments in WSRB. This follows chapter 6, which focuses on the calibration and evaluation of the SWAT model for each respective headwater catchment.

This page is intentionally left blank.

# Chapter 6

# Calibration and Validation of SWAT Model for Headwater Catchments

## 6.1 Overview

Modeling of the streamflow under changing climate and human impact is a significant part of watershed planning and sustainable water resource management (Dwarakish and Ganasri, 2015; Kale and Sönmez, 2019). Hydrological models are important for a wide range of applications, including water resources planning, development and management, flood prediction and design, and coupled systems modelling including, for example, water quality, hydro-ecology and climate (Pechlivanidis et al., 2011). Many hydrological models have been developed to understand hydrological processes on local and global spatial scales. Thus, selection and application of appropriate hydrological model to examine the impact of climate and land use land cover change is crucial.

Hydrological models have different degrees of complexity and conceptualization of physical processes. They can be classified, considering their spatial distribution, as lumped or distributed models. In a lumped model, the catchment is regarded as a unit. The variables and parameters thus represent average values for the entire catchment. On the other hand, a distributed model takes spatial variations into account (e.g., topography, vegetation, and soils) in all variables and parameters. As previously mentioned, hydrological models also differ in their representation of physical processes: a physically-based model describes the natural system using mathematical formulations of physical processes while a conceptual model is constructed based on physical processes, in which physically-based equations are used along with semi-empirical equations (Refsgaard, 1996).

On a temporal scale, models are also classified as event-based and continuous models. The former produces output only for specific periods while the latter produces a continuous output. One of the most important classifications is empirical model, conceptual models, and physically based models (Devia et al., 2015). Also, hydrological models can be grouped into deterministic and stochastic types (Refsgaard, 1996). Recent research in hydrological modeling tried to take a more physically-based approach to understand hydrologic systems' behavior to make better future streamflow predictions and to face major challenges in water resource management (Velázquez et al., 2015).

Numerous studies revealed the uses, abilities, and performances of different models in simulating the hydrological processes of watersheds under changing climate and land use land cover. However, it is a quite challenging task to select the right hydrological model which can simulate specific watershed hydro-climatological and geophysical processes. In general, physically-based distributed models are very flexible to represent the real ground features and simulating the hydro-geophysical processes of watersheds (Arnold et al., 1998; Chen and Mackay, 2004; Gebreyohannes et al., 2013; Yen et al., 2016). Moreover, hydrological models are valuable to simulate watershed hydrology and sediment yield in data-scarce regions. Headwater catchments serve as the primary freshwater sources in a basin, characterized by mountainous terrain and seasonal rainfall, particularly in Ethiopia. This study was focused on evaluating the Soil and Water Assessment Tool (SWAT) model within selected headwater catchments of the Wabi Shebele River Basin. The goal is to analyze the impact of climate and land use land cover (LULC) changes on streamflow in these specific catchments.

#### Model Description

In this study, the SWAT model was applied to simulate the hydrological processes on the headwater catchments. The SWAT model is a physically based, computationally efficient, semi-distributed watershed model that is designed to simulate and predict the impact of land management practices on water, sediment, and agricultural chemical yields in large complex watersheds with varying soils, land use, and management conditions over long periods (Arnold et al., 2012; Gassman et al., 2007). SWAT is a continuation of nearly 40 years of modeling efforts conducted by the United States Department of Agriculture (USDA) Agricultural Research Service (ARS) (Abbaspour et al., 2018). A large number of SWAT-related papers have appeared in Institute for Scientific Information (ISI) journals, building a worldwide consensus around the model's

stability and usefulness. In SWAT, the target watershed is divided into sub-basins linked by the channel network, which are further subdivided into several hydrological response units (HRUs) of homogeneous land use, slope, management, and soil characteristics (Arnold et al., 2012; Gassman et al., 2007; Neitsch et al., 2011). Using the HRU as the basic unit, the hydrological components, nutrients, and sediment yield were simulated and aggregated for each sub-basin. This model can be used for various applications, such as streamflow simulation and forecasting, and can predict the environmental impacts of land use land cover, land management practices, and climate change. SWAT models have been widely applied to simulate similar problems worldwide and have shown excellent performance.

The model was selected in this research because of its minimum input data and capacity to provide continuous, long-term simulations. Moreover, the model has been widely used in different watersheds worldwide and has proven to be an effective tool for examining hydrological responses to land use and climate change (Betrie et al., 2011; Kim and Kaluarachchi, 2009; Kim, 2016; Stehman and Czaplewski, 1998; Zhang et al., 2016). Akoko et al. (2021) reviewed the SWAT model application in Africa using published papers and found that the SWAT model is widely used in Africa, particularly in Ethiopia. In addition, it is a user-friendly model that technical documentation, executable programs, open source codes, pre- and post-processing tools, and software manuals can be downloaded from `https://swat.tamu.edu/`.

## 6.2 Material and Methods

### 6.2.1 Study Site

The selected catchments are predominantly situated in the northwest, with one exception in the northeast, within the Wabi Shebele River basin. Specifically, the headwater catchments are defined by their geographic coordinates as follows: Errer catchment spans between 9.24° and 9.49° North latitude and 42.11° to 42.31° East longitude. Furuna catchment is located between 6.92° and 7.02° North latitude and 39.42° to 39.54° East longitude, while Harero catchment lies within the region of 6.87° to 7.00° North latitude and 39.26° to 39.35° East longitude. The Maribo catchment covers the area between 6.79° and 7.00° North latitude and 39.33° to 39.42° East longitude, the Robe catchment extends from 7.85° to 7.97° degrees North latitude and 39.50° to 39.63° East longitude, and Wabi@Bridge catchment encompasses the region between 6.85° and 7.02° North latitude and 38.73° to 39.03° East longitude. This study was limited in its scope to cover the entire basin due to the absence of streamflow records with acceptable temporal coverage. The

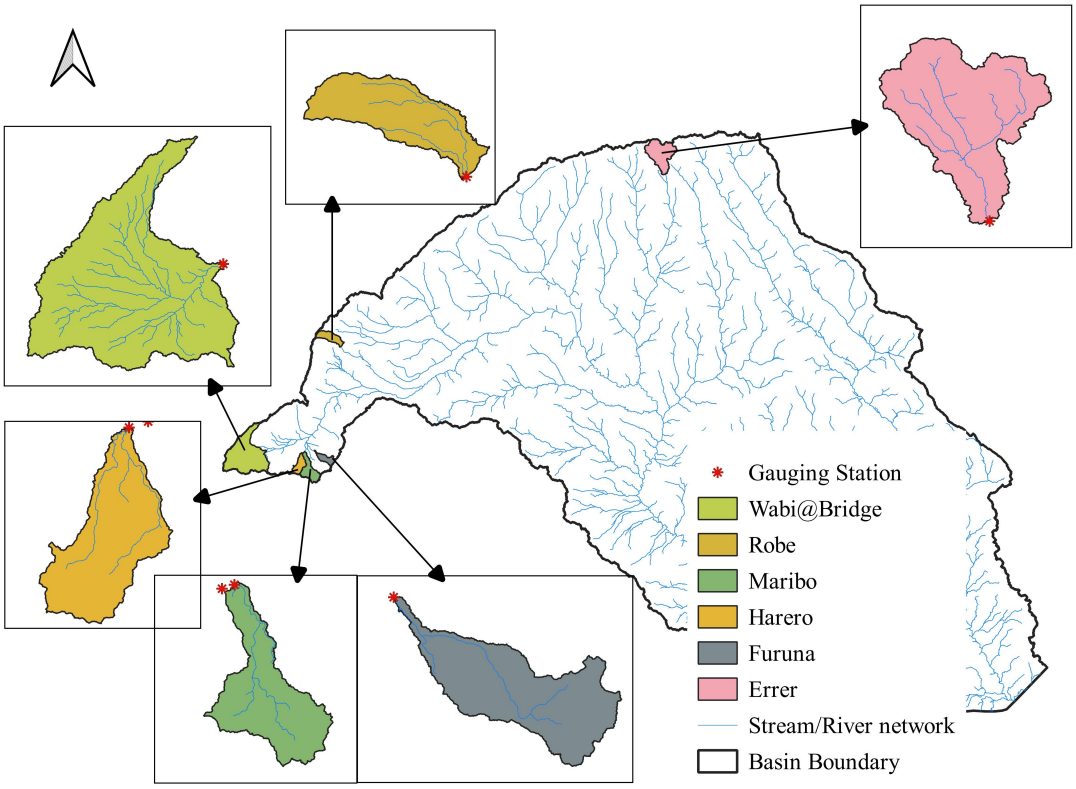


Figure 6.1: Location map of the selected headwater catchments in the WSRB

geographical location of each headwater catchment is depicted in Figure 6.1.

### 6.2.2 Model Input Preparation

The SWAT model is a semi-distributed continuous model that requires spatial and temporal data (Arnold et al., 2012; Gassman et al., 2007). Spatial data include the Digital Elevation Model (DEM), soil data, land use, and stream network layers with similar projection, whereas temporal data include climate (rainfall, minimum and maximum temperatures, solar radiation, wind speed, and relative humidity) and stream flow (Neitsch et al., 2011; Srinivasan et al., 2010; Wang et al., 2019). The first set of data was required for watershed delineation and discretization, whereas the second set of data was required for continuous hydrological simulation, model calibration, and validation. The performance of the model highly relies on the quality and quantity of input data. Inputs are used to model processes at the basin, sub-basin or HRU level. The preparation and sources of each input of the SWAT model are described in the following section.

#### Digital elevation model (DEM)

The DEM is one of the main inputs of the SWAT model. The Shuttle Radar Topography Mission (SRTM) 30 m grid size DEM, latest openly available, dataset was accessed from USGS website

https://earthexplorer.usgs.gov. The DEM data is required to delineate the watersheds and define the location of the streams in the watershed. In addition, terrain parameters such as slope gradient and slope length, and stream network characteristics such as channel slope, length, and width were derived from the DEM for each subbasin.

#### Land use land cover data (LULC)

The land use land cover (LULC) of a watershed significantly impacts runoff, evapotranspiration, and surface erosion (Neitsch et al., 2011). LULC data can be obtained from two primary sources, existing records and satellite imagery. In Chapter 5, LULC maps for 1990, 2000, 2010, and 2020 were prepared using Landsat images, employing a hybrid classification algorithm. For the SWAT model simulation, the LULC map from 2000 was used as the baseline. To accurately represent land use land cover, the LULC map was reclassified based on SWAT predefined land use land cover types, and the corresponding crop/plant growth and urban parameters were selected from the SWAT databases. A lookup table was prepared that associates the land use land cover map grid values with the 4-letter SWAT code for different land use land cover categories. This code is printed to the output files. SWAT also calculate the area covered by each land use category during HRU definition. Table 6.1 provides a comprehensive summary of the land use land cover categories within each headwater catchments.

Table 6.1: LULC classes distribution in selected headwater catchments in WSRB

| LULC Class | SWAT code | Errer | | Furuna | | Harero | | Maribo | | Robe | | Wabi_bridge | |
|---|---|---|---|---|---|---|---|---|---|---|---|---|---|
| | | ha | % | ha | % | ha | % | ha | % | ha | % | ha | % |
| BtU | URBN | 35.8 | 0.1 | | | 2.9 | 0.0 | | | 43.9 | 0.3 | 91.0 | 0.1 |
| Forest | FOEB | | | 4400.2 | 48.0 | 7843.2 | 65.0 | 13349.5 | 63.5 | 1981.3 | 12.3 | 4311.5 | 4.4 |
| OpSH | BSVG | 7536.4 | 15.8 | 2561.0 | 27.9 | 268.9 | 2.2 | 216.0 | 1.0 | 811 | 5.0 | 101.7 | 0.1 |
| DeSH | SHRB | 2062.5 | 4.3 | | | 0.4 | 0.0 | 0.6 | 0.0 | 6.8 | 0.0 | 1567.0 | 1.6 |
| GrSS | GRAS | | | 1233.4 | 13.5 | 2027.1 | 16.8 | 4700.1 | 22.3 | 298.6 | 1.9 | 76177.2 | 78.5 |
| AgRL | AGRL | 38064.5 | 79.7 | 973.8 | 10.6 | 1928.9 | 16.0 | 2769.3 | 13.2 | 12971.8 | 80.5 | 14799.0 | 15.2 |
| BaRL | BARR | 66.9 | 0.1 | | | | | | | | | | |
| **Total** | | 47766.0 | 100 | 9168.3 | 100 | 12071.3 | 100 | 21035.5 | 100 | 16113.5 | 100 | 97047.4 | 100 |

#### Soil data

Soil is a three phase material cover the surface of the earth with different physicochemical properties. The physical properties of the soil govern the movement of water and air through the profile and have a major impact on the hydrological process/water cycling. Whereas the chemical properties plays a major role in nutrients cycling in the soil profile. In Ethiopia, the accesses

of soil information is very limited or small scale coverage which impractical to use in any hydrological model for land surface simulation. The soil physicochemical properties required by the SWAT model include soil texture, available water content, hydraulic conductivity, bulk density, and organic carbon content for each soil type and its layers. Inputs for chemical characteristics are used to set initial levels of the different nutrients in the soil. While the physical properties are required for hydrological simulations in SWAT, information on chemical properties is optional. Table 6.2 provides a comprehensive summary of major soil coverage within each headwater catchments.

Table 6.2: Major soil coverage in selected headwater catchments in WSRB

| Soil Name | SWAT code | Errer | | Furuna | | Harero | | Maribo | | Robe | | Wabibrige | |
|---|---|---|---|---|---|---|---|---|---|---|---|---|---|
| | | ha | % | ha | % | ha | % | ha | % | ha | % | ha | % |
| Chromic Luvisols | LVx | 39792.4 | 83.3 | 5903.4 | 64.4 | 6625.7 | 54.9 | 14875.4 | 70.7 | 2776.8 | 17.2 | 2876.2 | 3.0 |
| Haplic Luvisols | LVh | | | 3146.2 | 34.3 | 3687.7 | 30.5 | 2935.1 | 14.0 | 1329 | 8.2 | 26821.6 | 27.6 |
| Eutric Cambisols | CMe | | | | | 762.5 | 6.3 | 1828.2 | 8.7 | | | | |
| Eutric Vertisols | VRe | | | 118.7 | 1.3 | 995.4 | 8.2 | 1396.9 | 6.6 | 12007.7 | 74.5 | 30722.2 | 31.7 |
| Humic Nitisols | NTu | 830.2 | 1.7 | | | | | | | | | 36627.4 | 37.7 |
| Lithic Leptosols | LPq | 7143.4 | 15 | | | | | | | | | | |
| Total | | 47766.0 | 100 | 9168.3 | 100 | 12071.3 | 100 | 21035.5 | 100 | 16113.5 | 100 | 97047.5 | 100 |

The soil and land cover data are important to define the subbasin into the HRUs. Soil information at a higher resolution is not available in developing countries including Ethiopia. Since, preparation of soil at higher resolution is expensive and cumbersome. Thus, the soil data was prepared from primary and secondary data sources available in national and international data sources. After reviewing the SWAT model application in Africa, Akoko et al. (2021) found that the Food and Agricultural Organization (FAO) soil database was the most common source of soil data in the SWAT model simulation. In this study, the Harmonized World Soil Database (HWSD v1.2) was used to prepare the spatial map and extract soil parameters for the SWAT model. The HWSD was developed by FAO and IIASA and is organized for applications in biophysical models and agro-ecological assessments. The additional parameters were extracted using the pedo-transfer formula using Soil-Plant-Air-Water (SPAW) software. For the SWAT model simulation, it is a common practice that the user should prepare the soil parameter table (usersoil), soil lookup table, and soil spatial map in a tiff or grid format.

#### Climate data

The climatic variables required by the SWAT model for driving hydrological and nutrient balance are daily precipitation, maximum/minimum air temperature, solar radiation, wind speed, and relative humidity. The model allows climatic values to be input from records of observed data or generated during the simulation (Neitsch et al., 2011). Records of daily rainfall and minimum and maximum temperature for the study catchment were obtained from the National Meteorological Agency (NMA). The period of observation 1987 - 2016 was retained as the simulation period because it is common to all stations and available stream flow data. Hence, the long-term daily mean filling method was used to impute the missed data for analyzing rainfall data of selected stations. A user weather generator database was created to store local weather stations including their statistics. These statistics parameters are needed by the SWAT weather generator to fill in missing values during the running time. The location and some statistical parameters of the stations are presented in Chapter 4. The model utilizes text files for input, which include gauge location tables specifying station positions. Precipitation and temperature data files with daily measurements were also prepared with text format. These files were edited to provide essential climate data for the model. The SWAT model assigns gauging stations to subbasins based on proximity to the subbasin's centroid for efficient spatial allocation.

#### Hydrological data

The SWAT model parameters must be calibrated and validated for specific areas to minimize the uncertainty of the simulation results. But, relative to the size of the basin, the distribution of operational streamflow gauging station is very poor/sparse in WSRB. The common practice for calibrating hydrological model parameters is to use the observed streamflow and sediment yield. Sequentially, the SWAT model should first be calibrated for the flow pattern and then for the sediment yield parameters (Abbaspour, 2015). The observed daily runoff data at the outlets of the study catchments were obtained from the Hydrology Department of the Ministry of Water, Irrigation and Electricity of Ethiopia. Daily data were summarized into a monthly time series for calibration and validation. The missing records were filled through multiple method considering monthly long term average the missing month and relating with presence and absence of rainfall in respective month. The location of the gauging stations is depicted in Figure 3.7.

### 6.2.3 Model Setup and Simulation

The QGIS interface was employed to configure the SWAT model and conduct hydrological simulations on a monthly time series basis. The initial step in the model setup process involved establishing a project for each selected headwater catchment under study. Subsequently, the catchment was demarcated and subdivided into sub-catchments, relying on a corrected Digital Elevation Model (DEM) with a resolution of 30 meters. A designated threshold drainage area of 1000 hectares was maintained, and additional outlets were introduced at the sites of stream gauging stations. This enabled a comparison between observed and simulated streamflow results when evaluating the model's performance. Except for the sub-catchment at the outlet of the catchment, any sub-catchment area that was less than 10% of the mean area of all sub-catchments was merged with an upstream sub-catchment. The model also generated a comprehensive stream network, including its pertinent characteristics such as length, width, depth, slope, and elevation difference.

Following the delineation of catchment and sub-catchments, land use land cover, soil types, and slope characteristics were imported, superimposed, and linked with the corresponding SWAT databases using the lookup table. This overlaying led to the subdivision of each sub-catchment into Hydrological Response Units (HRUs). These HRUs were distinct areas characterized by unique combinations of soil, land use land cover, and slope attributes. The classification of slope classes was categorized into four ranges (0-8%, 8-16%, 16-30%, and greater than 30%) as per the guidelines of the Food and Agriculture Organization (FAO). This classification facilitated the study of the effects of Land Use Land Cover (LULC) changes, as well as diverse management practices, on the hydrological processes of the catchment. HRUs with coverage percentages of soil, LULC, and slope class below 10% were subject to filtering and subsequently merged with the dominant HRU present within each sub-catchment. This stage of the process allowed for the division and exemption of specific LULC classes during the simulation.

After this, climate data were imported into the model, and the nearest weather station to the centroid of each sub-catchment was chosen for further simulation purposes. To accommodate the nature of the SWAT model, text tables were generated for simulation, given its text-based framework. Before the initiation of the simulation, it was essential to ensure that every datasets was incorporated into the model's text file whenever adjustments were made to model parameters or input data.

To establish appropriate initial conditions and stabilize the model, the first three years of the simulation were designated as a warm-up period. An exception was made for the Errer catchment, where only one year was utilized for model warm-up due to the limited streamflow record available for model calibration and validation. For calculating surface runoff volume, a modified Soil Conservation Service (SCS) curve number method was adopted. Flow routing through channels was determined using the variable storage coefficient method, and the estimation of potential evapotranspiration was calculated through the Penman-Monteith method. Finally, simulations were conducted over the stipulated study period for each headwater catchment, and a comprehensive assessment of the model's hydrological balance was undertaken using the SWATcheck tool.

### 6.2.4 SWAT Model Parameter Sensitivity Analysis

Complex environmental/hydrological models are controlled by a large number of parameters such as SWAT. An accurate estimation of the values of all these parameters is almost impossible. Sensitivity analysis (SA) results enable the selection of parameters to be included in a calibration procedure, but can also assist in the identification of the model processes (Arnold et al., 2012). It is the process of determining the rate of change in the model output with respect to changes in the model inputs (parameters). The uniqueness of each watershed must be captured by model parameters to properly represent the physical processes at work.

Additionally, sensitivity analysis can yield crucial information on the use and meaning of the model parameters. Two general types of sensitivity analysis are typically performed. These include one-at-a-time (OAT), local sensitivity analysis, and all-at-a-time (AAT) or global sensitivity analyses (Abbaspour et al., 2018). In OAT, all parameters are held constant while changing one to identify its effect on some model output or objective functions. In this case, only a few (3–5) model runs are sufficient. In the AAT, however, all parameters change; hence, a larger number of runs (500–1000 or more, depending on the number of parameters and procedure) are needed to determine the impact of each parameter on the objective function.

Numerous SWAT model modelers utilized various flow parameters, including CN2, SOL_AWC, SOL_K, ESCO, GWQMN, GW_REVAP, REVAMPM, HRU_SLP, CH_N2, OV_N, SLSUBBSN, CH_K2, CANMX, SURLAG, and EPCO, to assess their sensitivity during the simulation of the SWAT model (Abbaspour, 2015; Addis et al., 2016; Chekol et al., 2007; Leta et al., 2016;

Liew and Garbrecht, 2003; Negewo and Sarma, 2021; Setegn et al., 2009; Betrie et al., 2011; van Griensven et al., 2006). During parameter sensitivity analysis, only streamflow data were available and major consideration was given to parameters related to surface runoff and baseflow processes in the SWAT models. In this study, 16 commonly used flow parameters were selected for sensitivity analysis in six headwater catchments of the WSRB. The list of parameters is presented with a description, and the value range is listed in Table 6.3.

Table 6.3: Description of selected SWAT flow parameters for sensitivity analysis.

| Parameter Name | Description Curve | Value Range | Parameter | | |
|---|---|---|---|---|---|
| | | | Minimum | Maximum | Default |
| R_CN2.mgt | Moisture condition II curve number | -0.2 – 0.2 | 35 | 98 | * |
| V_ESCO.hru | Soil evaporation compensation factor | 0.4 – 0.95 | 0 | 1 | 0.95 |
| R_OV_N.hru | Manning's "n" value for overland flow | -0.1 – 0.1 | 0.01 | 30 | 0.15 |
| R_SOL_K.sol | Saturated hydraulic conductivity (mm/hr) | -0.3 – 0.3 | 0 | 2000 | * |
| R_SOL_BD.sol | Soil bulk density | -0.2 – 0.2 | 0.9 | 2.5 | * |
| R_SOL_AWC.sol | Available water capacity | -0.3 – 0.3 | 0.01 | 1 | * |
| V_GW_REVAP.gw | Ground water "revap" coefficient | 0.02 – 0.2 | 0.02 | 0.2 | 0.02 |
| V_ALPHA_BF.gw | Baseflow recession constant | 0 – 1 | 0 | 1 | 0.048 |
| V_GWQMN.gw | Threshold water level in shallow aquifer for base flow (mm H2O) | 0 – 2000 | 0 | 5000 | 1000 |
| V_REVAPMN.gw | Threshold water level in shallow aquifer for revap (mm H2O) | 0 – 1000 | 0 | 1000 | 750 |
| V_GW_DELAY.gw | Delay time for aquifer recharge | 30-450 | 0 | 500 | 31 |
| R_CH_K2.rte | Effective hydraulic conductivity in main channel | -0.1 – 0.1 | -0.01 | 500 | 0 |
| R_CH_N2.rte | Manning's "n" value for the main channel | -0.1 – 0.1 | -0.01 | 0.3 | 0.014 |
| V_ALPHA_BNK.rte | Bank flow recession constant | 0-1 | 0 | 1 | 0 |
| V_SURLAG.bsn | Surface runoff lag coefficient | 1 – 10 | 1 | 24 | 4 |
| V_EPCO.bsn | Plant uptake compensation factor | 0.4 – 0.95 | 0 | 1 | 1 |

The qualifier (v) refers to the substitution of a parameter by a value from the given range. The qualifier (r) refers to a relative change in the parameter where the value from the SWAT database is multiplied by 1 plus a factor in the given range.

The global sensitivity analysis was performed on selected model flow parameters using the SWAT Calibration and Uncertainty Programs SWAT-CUP version 2012 applying Sequential Uncertainty Fitting version 2 (SUFI-2) (Abbaspour, 2015; Abbaspour et al., 2007). In SWAT-CUP, AAT uses a multiple regression approach to quantify the sensitivity of each parameter, which regresses the Latin hypercube-generated parameters against the objective function values (in file goal.txt) (Abbaspour et al., 2007):

$$g = \alpha + \sum_{i=1}^{m} \beta_i b_i \tag{6.1}$$

where g is the objective function value, $\alpha$ is the regression constant, and $\beta$ is the coefficient of parameters.

A t-test is then used to identify the relative significance of each parameter $b_i$. The sensitivities given above are estimates of the average changes in the objective function resulting from changes

in each parameter, while all other parameters are changing. This gives relative sensitivities based on linear approximations and, hence, only provides partial information about the sensitivity of the objective function to model parameters. In this analysis, the largest absolute value of the t-stat, and the smaller the p-value, the more sensitive the parameter. The p-value is an indicator to judge the level of statistical significance of the sensitivities.

### 6.2.5 Model Calibration and Validation

After sensitivity analysis, the SWAT model was calibrated using the parameters to which the model showed high sensitivity. Calibration is an effort to better parameterize a model to a given set of local conditions, thereby reducing the prediction uncertainty (Abbaspour, 2015; Arnold et al., 2012; Refsgaard, 1997; Van Liew and Veith, 2010; Wang et al., 2019). Calibration of watershed models is a long and often tedious process of refining the model for processes and calibrating parameters (Abbaspour et al., 2018). Commonly, hydrological model calibration can be done manually, automatically, and a combination of the two methods. The manual calibration uses trial and error techniques in parameter adjustment through several simulation runs. Manual procedure is when the modeler modifies model parameters manually whereas automatic procedure is when the modeler limit the realistic range of parameter and parameter values are generated based on different sampling techniques. Automatic calibration is computer-based and involves the use of a numerical algorithm that maximizes and minimizes a given numerical objective function. Since, manual calibration of distributed watershed models like SWAT is difficult and almost infeasible in many large-scale applications (Arnold et al., 2012; Gupta et al., 1999).

Whereas, model validation is the process of demonstrating that a given site-specific model is capable of making sufficiently accurate simulations, although "sufficiently accurate" can vary based on project goals (Refsgaard, 1997). Validation involves running a model using parameters that were determined during the calibration process, and comparing the predictions to observed data not used in the calibration.

In this study similar to sensitivity analysis, automatic calibration and validation were performed within the SWAT Calibration and Uncertainty Programs SWAT-CUP version 2012 using Sequential Uncertainty Fitting version 2 (SUFI-2) (Abbaspour, 2015). The daily streamflow of six gauging stations in the headwater part of the WSRB was obtained from the MWIE of Ethiopia. Daily streamflow data were summarized into monthly time series and split into two datasets for

calibration and validation based on the length of the records. A more extended recording period was considered during the calibration than during the validation. It is commonly accepted that the measured data should be split for calibration and validation in the SWAT model (Arnold et al., 2012; Refsgaard, 1997). During the calibration process, the model parameters were adjusted until a reasonably good fit between the observed and simulated variables was achieved, which was measured using the selected statistical methods/objective functions. To standardize the number of simulations, 1000 simulations were performed each during the calibration and validation of the selected headwater catchments.

### 6.2.6 Model Performance Evaluation Criteria

Model performance evaluation is necessary for the verification of the robustness of the model. The goodness of fit evaluation is a common practice during hydrological model simulation and application. Hydrological models performance evaluation is performed using graphical and statistical method. The advantage and disadvantage of different performance evaluation criteria were reviewed (Moriasi et al., 2015). Statistical method is adopted by numerous researchers. Due to varied strengths of the different performance measures, Moriasi et al. (2015) recommend the use of multiple graphical and statistical measures.

Accordingly, during the calibration and validation periods of this study, both graphical and statistical methods were employed to assess the quality of model predictions. Scatter and probability plots were used for the graphical evaluation of model performance. The statistical performance measures were used included $R^2$ (Krause et al., 2005), Nash-Sutcliffe Efficiency (NSE) (Nash and Sutcliffe, 1970), Percentage Bias (PBIAS) (Gupta et al., 1999), and Kling-Gupta Efficiency (KGE) (Gupta et al., 2009). In addition to the recommended performance measures, the mean and standard deviation of the observed and simulated outputs are presented for a relative comparison. A detailed description of each statistical performance measure selected in this research is presented considering o as the observed data and s as the simulated data.

Coefficient of determination ($R^2$) is the squared ratio between the covariance and the multiplied standard deviations of the observed and predicted values (Krause et al., 2005). $R^2$ ranges from 0 to 1, with higher values indicating less error variance, and typically values greater than 0.5 are considered acceptable. Moriasi et al. (2015) recommended that the regression line gradient and intercept to be reported when $R^2$ is used as a performance measure. For a good agreement, the intercept should be close to zero and the gradient should be close to one (Krause et al., 2005).

$$R^2 = \left[ \frac{\sum_{i=1}^{n}(O_i - \bar{O})(S_i - \bar{S})}{\sqrt{\sum_{i=1}^{n}(O_i - \bar{O})^2}\sqrt{\sum_{i=1}^{n}(S_i - \bar{S})^2} } \right]^2 \tag{6.2}$$

The Nash-Sutcliffe efficiency (NSE) is a normalized statistic that was calculated to determine the relative magnitude of the residual variance compared to the measured data variance (Nash and Sutcliffe, 1970). NSE indicates how well the plot of observed versus simulated data fits the 1:1 line. NSE ranges between -∞ and 1.0 (1 inclusive), with NSE = 1 being the optimal value. NSE is computed by equation 6.3:

$$NSE = 1 - \frac{\sum_{i=1}^{n}(O_i - S_i)^2}{\sum_{i=1}^{n}(O_i - \bar{O})^2} \tag{6.3}$$

Percent bias (PBIAS %) measures the model's average tendency to predict higher or lower values than the observed data (Gupta et al., 1999). The optimal value of PBIAS is 0.0, with low-magnitude values indicating accurate model simulation. Positive values indicate model underestimation bias, and negative values indicate model overestimation bias (Gupta et al., 1999). PBIAS is calculated with equation 6.4:

$$PBIAS(\%) = \frac{\sum_{i=1}^{n}(O_i - S_i) \times 100}{\sum_{i=1}^{n} O_i} \tag{6.4}$$

Additionally, the Kling–Gupta efficiency (KGE) is based on a decomposition of NSE into its constitutive components (correlation, variability bias and mean bias), addresses several perceived shortcomings in NSE and is increasingly used for hydrological model calibration and evaluation (Gupta et al., 2009). A value of KGE = 1, indicates a perfect agreement between simulations and observations. If the mean flow is used as a KGE benchmark, all model simulations with -0.41 < KGE < 1 could be considered as reasonable performance (Knoben et al., 2019). A slightly revised version of the KGE statistic suggested by (Kling et al., 2012) was used to ensure that the bias and variability ratios were not cross-correlated when measuring the agreement between the simulated values and observations. KGE is calculated using equation 6.5:

$$KGE' = 1 - \sqrt{(r-1)^2 + (\beta - 1)^2 + (\gamma - 1)^2} \tag{6.5}$$

$$\beta = \frac{\mu_p}{\mu_o} \tag{6.6}$$

$$\gamma = \frac{CV_s}{CV_o} = \frac{\frac{\sigma_S}{\mu_S}}{\frac{\sigma_o}{\mu_o}} \tag{6.7}$$

where KGE, is the modified KGE-statistic (dimensionless), r is the correlation coefficient between simulated and observed runoff (dimensionless), $\beta$ is the bias ratio (dimensionless), $\gamma$ is the variability ratio (dimensionless), $\mu$ is the mean runoff in $m^3$/s, CV is the coefficient of variation (dimensionless), $\sigma$ is the standard deviation of runoff in m3/s, and the indices s and o represent simulated and observed runoff values, respectively. KGE,, r, $\beta$ and $\gamma$ have their optimum at unity.

Moriasi et al. (2015) established certain statistical tests and performance ratings to determine the fit of a model to the observed hydrological variables in the watershed. A summary of the evaluation metrics are provided in Table 6.4.

Table 6.4: Performance evaluation criteria for selected statistical performance measures

| Measure | Performance Evaluation Criteria for Discharge | | | | Sources |
|---|---|---|---|---|---|
| | Very good | Good | Satisfactory | NotSatisfactory | |
| R2 | $R2 > 0.85$ | $0.75 < R2 \leq 0.85$ | $0.60 < R2 \leq 0.75$ | $R2 \leq 0.60$ | Moriasi et al. (2015) |
| NSE | $NSE > 0.80$ | $0.70 < NSE \leq 0.80$ | $0.50 < NSE \leq 0.70$ | $NSE \leq 0.50$ | |
| PBIAS | $PBIAS < \pm 5$ | $\pm 5 < PBIAS < \pm 10$ | $\pm 10 \leq PBIAS < \pm 15$ | $PBIAS \geq \pm 15$ | |

The above statistical metrics only apply to the comparison of two signals and are not adequate when outputs are expressed as uncertainty bands (Arnold et al., 2012). Identifying all acceptable model solutions considering all input uncertainties allows to express model uncertainty in SWAT-CUP as the 95% prediction uncertainty (95PPU) Abbaspour et al. (2018). The 95PPU is calculated at the 2.5% and 97.5% levels of the cumulative distribution of an output variable obtained through Latin hypercube sampling. In this case, as the simulation results are usually expressed by the 95% prediction uncertainties (95PPU), they cannot be compared with the observation signals using traditional performance statistics.

For this reason, Abbaspour et al. (2018, 2007) devised two measures, referred to as the p-factor and the r- factor based on 95% prediction uncertainty (95PPU) to account for all sources of uncertainties such as uncertainty in driving variables (e.g., rainfall), conceptual model, parameters, and measured data. The p-factor is the percentage of measured data bracketed by the 95PPU band. The r-factor is a measure of the thickness of the 95PPU band and is calculated as the average 95PPU thickness divided by the standard deviation of the corresponding observed variable. The goodness of calibration and prediction uncertainty is judged based on the closeness of the p-factor to 100% (i.e., all observations bracketed by the prediction uncertainty band) and the

r-factor close to 0 (less than 2 for monthly streamflow) Abbaspour et al. (2018).

$$p_{\text{factor}} = \frac{NQ_{\text{in}}}{n} \times 100 \tag{6.8}$$

$$r_{\text{factor}_j} = \left( \frac{1}{n_j} \sum_{i=1}^{n_j} x_s^{t_i,97.5\%} - x_s^{t_i,2.5\%} \right) / \sigma_{oj} \tag{6.9}$$

where $NQ_{\text{in}}$ is the number of observed discharge falling in the 95PPU, $x_s^{t_i,97.5\%}$ and $x_s^{t_i,2.5\%}$ are the upper and lower boundary of the 95PPU at time-step t and simulation i, $n_j$ is the number of data points, and $\sigma_{oj}$ is the standard deviation of the $j^{th}$ observed variable.

## 6.3 Result and Discussion

### 6.3.1 SWAT Model Simulation

The headwater catchments were discretized into subbasins using a Digital Elevation Model (DEM), and Hydrological Response Units (HRU) were generated using the DEM, Soil map, and Land Use Land Cover (LULC) map prior to simulating streamflow at the catchment outlet. Consistent threshold criteria were applied for generating streams, determining the number of sub-basins and HRUs based on the total area of the basin, as summarized in Table 6.5.

Table 6.5: SWAT model discretisation result for selected headwater catchments

| Catchment | Area (ha) | Number of Subbasin | Number of HRUs |
|---|---|---|---|
| Errer | 47,766.01 | 20 | 133 |
| Furuna | 9,168.28 | 5 | 57 |
| Harero | 12,071.26 | 7 | 67 |
| Maribo | 21,035.53 | 11 | 98 |
| Robe | 16,113.48 | 7 | 44 |
| Wabi@bridge | 97,047.45 | 62 | 468 |

### 6.3.2 Parameter Sensitivity

Global sensitivity analysis supports determining the dominant processes within a watershed, thereby identifying the most influential parameters by evaluating how alterations in input parameters value correspond to changes in model outcomes. This research undertook a sensitivity analysis for 16 hydrological parameters using the parameter solution optimization technique via

auto-calibration in the SWAT-CUP software. The outcomes of this analysis are depicted in Figure 6.2 and detailed in Appendix Table A.4.

The findings from this study revealed that during hydrological modeling of headwater catchments within the WSRB, the most crucial parameters were CN2.mgt, GW_DELAY.gw, ESCO.hru, GW_REVAP.gw, and GWQMN.gw, as illustrated in Figure 6.2. Notably, CN2 stands out as the parameter with the highest sensitivity in streamflow simulation across all catchments except Furuna, where GW_delay.gw took precedence, as depicted in Figure 6.2. CN2 substantially influences the generation of high and low runoff from HRUs, thus predicting a relatively elevated sensitivity index across most basins (Abbaspour, 2015).

Among groundwater parameters, GW_DELAY.gw exhibited notable sensitivity, followed by GW_REVAP.gw, predominantly impacting baseflow volumes in the catchment. Concerning HRU parameters, ESCO emerged as the most sensitive (within the top five) across all study catchments. Among soil parameters, Sol_BD.sol displayed relatively high sensitivity, except in Maribo and Robe catchments, where Sol_AWC.sol and Sol_K respectively took precedence. In a broader context, groundwater parameters were found to be considerably more sensitive compared to soil parameters. Furthermore, channel parameters demonstrated relatively lower sensitivity in headwater catchment SWAT simulations.

Overall, CN2 emerged as the most sensitive parameter within the selected headwater catchment in the WSRB. This outcome was consistent with numerous similar studies, confirming that these five parameters are crucial for water balance and streamflow Abbaspour (2015); Addis et al. (2016); Chekol et al. (2007); Leta et al. (2016); Liew and Garbrecht (2003); Setegn et al. (2009). However, Setegn et al. (2009) identified ESCO as highly sensitive in the Gilgel Abay River, Megech River, Ribb River, and Gumera River. Unlike other studies, Alpha-bf.gw exhibited relatively lower sensitivity in the studied headwater catchments. Finally, the top 10 sensitive parameters were considered for model calibration and validation in the selected headwater catchment.

### 6.3.3 Calibration and Validation

After conducting the sensitivity analysis, the SWAT model was automatically calibrated (auto-calibration) using the Sequential Uncertainty Fitting (SUFI-2) procedure, based on the 10 most sensitive SWAT parameters of the headwater catchment. The comparison of simulated and ob-

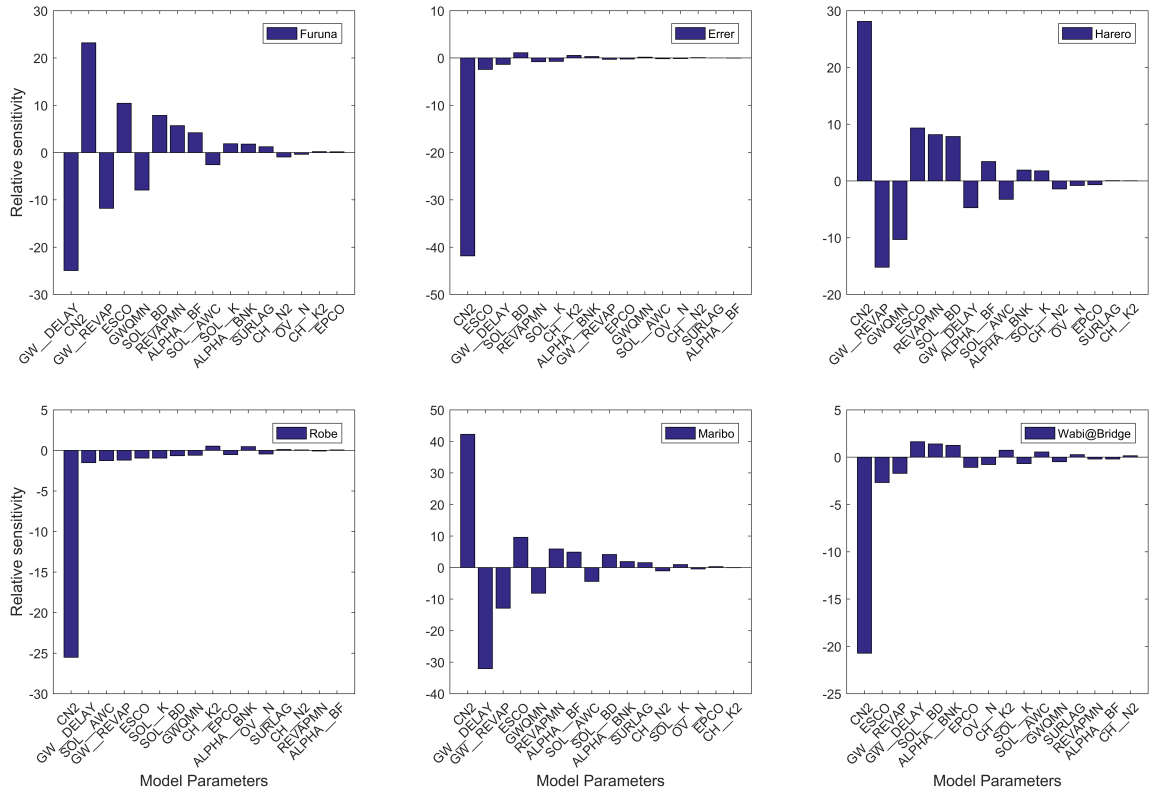


Figure 6.2: Relative sensitivity of SWAT model parameters in selected Headwater catchments

served streamflow was analyzed on a monthly time series. For each catchment, the simulation was performed for 1,000 runs in SWAT-CUP 2012. Different calibration periods were considered for each selected headwater catchment, depending on the availability and quality of streamflow data during the simulation period (1987 to 2016).

In this study, four statistical performance metrics were calculated during calibration to assess the accuracy and performance of the SWAT model simulation for six headwater catchments in the WSRB. These statistical measures were designed to provide comprehensive information about the model's performance. The results of the statistical performance measures and the scatter plot for the calibration period are presented in Table 6.6 and Figure 6.3, respectively.

In the Errer catchment, the results indicated a good fit between the model simulations and observed streamflow ($R^2$ = 0.81, NS = 0.8), with a slight tendency to over-predict (PBIAS = 3.3). Overall, the model's performance was considered good (KGE = 0.89). In the Furuna catchment, the model performed moderately well, with $R^2$ = 0.65, NS = 0.64, PBIAS = 5.3%, and KGE = 0.78. The model also showed a slight tendency to over-predict, as indicated by the positive PBIAS value of 5.3%.

For the Harero catchment, the $R^2$, NS, and KGE values were greater than 0.5, indicating a reasonable fit with the observed records. The catchment had a PBIAS value of 6.6, showing the model slightly overpredicted the observed data by approximately 6.6%. In the Maribo catchment, the $R^2$ and NS values were above 0.7, indicating a relatively good fit with the observed records. However, the model showed a significant overprediction tendency, as indicated by the relatively high positive PBIAS value of 18.3%.

In the Robe catchment, the $R^2$ and NS values were greater than 0.6, indicating a reasonable fit with the observed data. Despite the model showing a notable overprediction tendency (PBIAS = 11.7%), the overall model performance was still considered relatively good (KGE = 0.78). In the Wabi@Bridge catchment, the $R^2$ and NS values were greater than 0.6, indicating a reasonable fit with the observed data. The model showed a slight tendency to underpredict, as indicated by the negative PBIAS value of -7.2%. Overall, the model's performance was considered relatively good, with a KGE value of 0.77.

Table 6.6: Performance measures for the SWAT model during calibration in headwater catchments

| **Catchment** | **p-factor** | **r-factor** | **Mean_sim (Mean_obs)** | **StdDev_sim (StdDev_obs)** | $R^2$ | **NS** | **PBIAS** | **KGE** |
|---|---|---|---|---|---|---|---|---|
| Errer | 0.87 | 1.69 | 3.02(3.13) | 3.36(3.44) | 0.81 | 0.8 | 3.3 | 0.89 |
| Furuna | 0.83 | 0.87 | 1.00(1.06) | 1.15(1.26) | 0.65 | 0.64 | 5.3 | 0.78 |
| Harero | 0.77 | 1.21 | 1.95(2.09) | 1.46(1.60) | 0.60 | 0.57 | 6.6 | 0.75 |
| Maribo | 0.71 | 0.91 | 2.44(2.99) | 2.70(3.29) | 0.74 | 0.71 | 18.3 | 0.71 |
| Robe | 0.94 | 1.59 | 1.20(1.36) | 1.50(1.64) | 0.69 | 0.68 | 11.7 | 0.78 |
| Wabi@bridge | 0.94 | 2.11 | 7.28(6.79) | 4.88(5.37) | 0.65 | 0.63 | -7.2 | 0.77 |

Overall, the model demonstrated varying levels of performance across the different headwater catchments in the WSRB during the SWAT model calibration. The Errer and Robe catchments exhibited the best overall performance, with higher $R^2$, NS, and KGE values, indicating a better fit and greater accuracy in predicting the observed data. The Furuna, Harero, and Wabi@bridge catchments showed moderate performance, while the Maribo catchment had the lowest overall performance, primarily due to a relatively high PBIAS value, indicating significant overprediction.

After calibrating the model for each headwater catchment, it was validated against an independent data set that was not used during the calibration. The validation used the best parameter

range identified during the calibration period. Similar performance statistics and scatter plots were employed during the validation period, considering different periods for each headwater catchment and a similar number of simulations. The results of the statistical performance measures and scatter plots during validation period are presented in Table 6.7 and Figure 6.4, respectively.

In the Errer catchment, the results demonstrated a good fit between the model predictions and observed data, with $R^2$ = 0.72 and NS = 0.71, and a slight tendency to overestimate (PBIAS = 5.4). Overall, the model's performance was considered good, with a KGE of 0.80. In the Furuna catchment, the model performed relatively poorly, with $R^2$ = 0.49 and NS = 0.49. A minimal underestimation tendency was indicated by a negative PBIAS value of -1.5%. Despite this, the KGE value showed good model performance (KGE = 0.62). For the Harero catchment, the $R^2$, NS, and KGE values were greater than 0.5, suggesting a satisfactory fit with the observed data. However, the model showed a notable underestimation, evident from the substantial negative PBIAS value of approximately -17.2%.

In the Maribo catchment, the $R^2$ and NS values were 0.55 and 0.47, respectively, indicating a relatively poor fit with the observed data. The model also showed a significant overprediction tendency, with a relatively high positive PBIAS value of 13.0%. However, the KGE value was within the acceptable range (KGE = 0.71). In the Robe catchment, $R^2$ and NS values were greater than 0.6, indicating a reasonable fit with the observed data. The model had an overestimation tendency, highlighted by a positive PBIAS of 3.1%. Despite this, the overall model performance was relatively good (KGE = 0.78). Similarly, in the Wabi@bridge catchment, $R^2$ and NS values surpassed 0.6. There was a slight underestimation tendency, shown by the negative PBIAS of -7.4%. Overall, the model performed well, as reflected by the KGE value of 0.71.

Table 6.7: Performance measures for the SWAT model during validation in headwater catchments

| **Catchment** | **p-factor** | **r-factor** | **Mean_sim (Mean_obs)** | **StdDev_sim (StdDev_obs)** | $R^2$ | **NS** | **PBIAS** | **KGE** |
|---|---|---|---|---|---|---|---|---|
| Errer | 0.67 | 1.33 | 2.56(2.70) | 2.74(3.11) | 0.72 | 0.71 | 5.4 | 0.80 |
| Furuna | 0.71 | 1.19 | 1.48(1.46) | 1.01(1.30) | 0.49 | 0.49 | -1.5 | 0.62 |
| Harero | 0.75 | 1.21 | 2.34(2.00) | 1.68(1.60) | 0.61 | 0.49 | -17.2 | 0.72 |
| Maribo | 0.77 | 1.18 | 2.63(3.02) | 3.03(3.04) | 0.55 | 0.47 | 13.0 | 0.71 |
| Robe | 0.90 | 1.15 | 1.07(1.10) | 1.12(1.28) | 0.68 | 0.67 | 3.1 | 0.78 |
| Wabi@bridge | 0.74 | 1.57 | 10.07(9.38) | 6.15(7.95) | 0.69 | 0.68 | -7.4 | 0.71 |

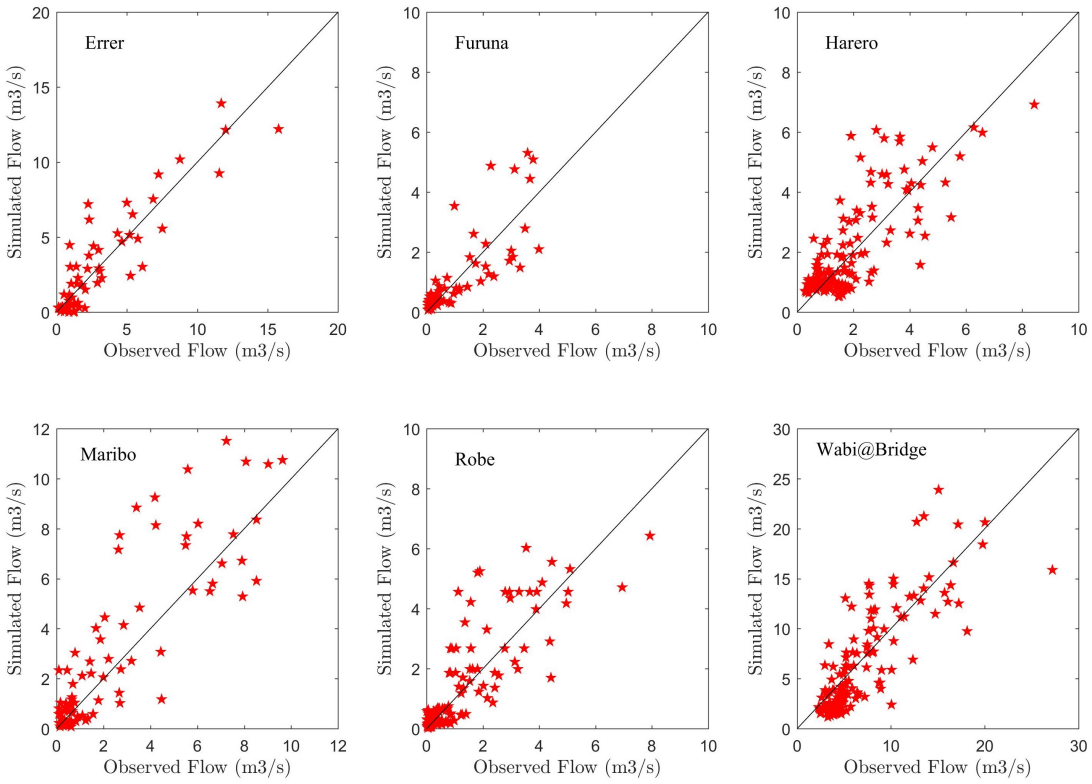


Figure 6.3: Scatter plot between observed and simulated streamflow during the calibration phase

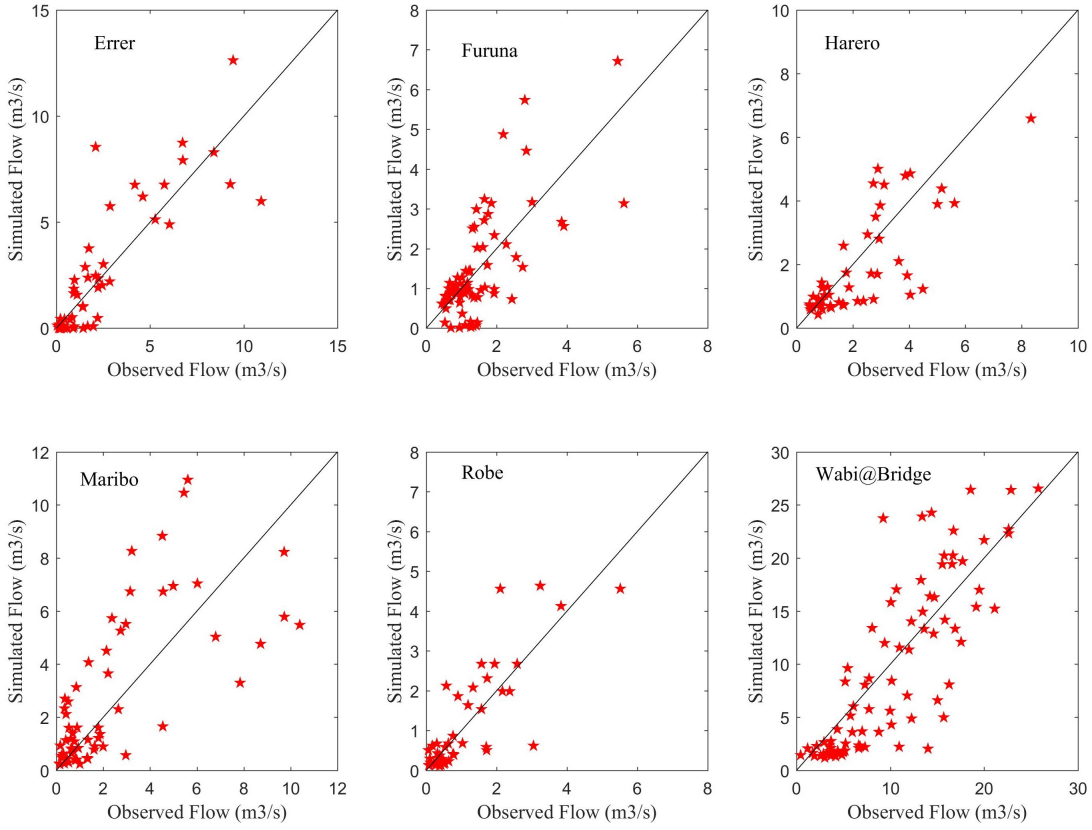


Figure 6.4: Scatter plot between observed and simulated streamflow during the validation phase

### 6.3.4 Model Uncertainty

Hydrological model inherently introduces uncertainties, primarily due to simplification of the model structure, input data variability, and parameter uncertainty (Abbaspour, 2015). These uncertainties must be acknowledged, and it is important to recognize that not all can be precisely quantified. Therefore, the findings of this research should be approached with due caution. A valuable benchmark for assessing the model's performance is comparing it against the uncertainties present in the available field observations (Refsgaard and Henriksen, 2004). Figures 6.5 and 6.6 illustrate the 95% Prediction Uncertainty (95PPU) bands of the model during both the calibration and validation periods for each headwater catchment.

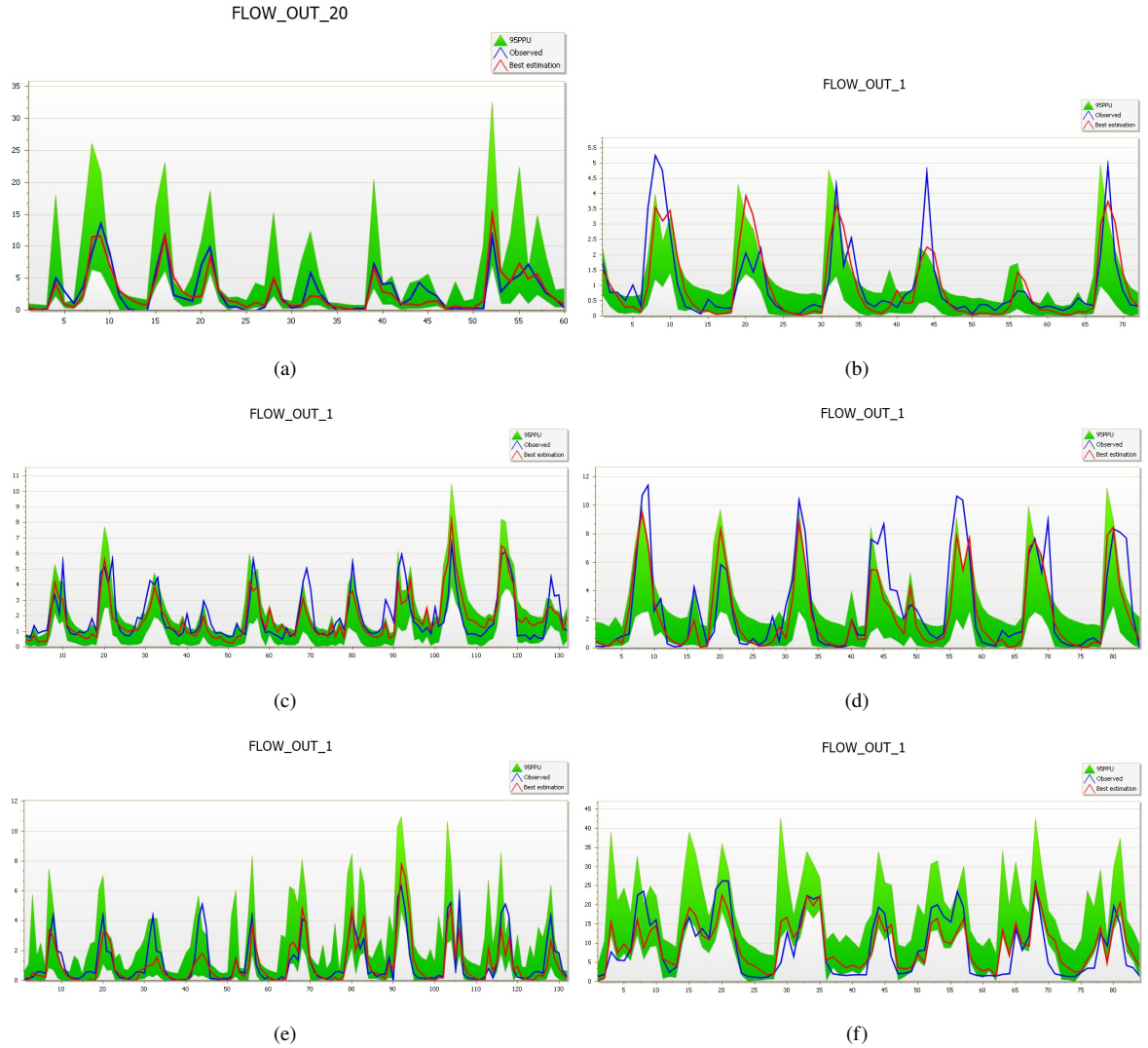


Figure 6.5: 95PPU band plot during the calibration period for (a) Errer (b) Furuna (c) Harero (d) Maribo (e) Robe (f) Wabi@bridge

To evaluate the performance of the SWAT model, the p-factor and r-factor were used, based on the 95% prediction uncertainty (95PPU) band. The results are presented in Tables 6.6 and 6.7

for the calibration and validation phases, respectively. During calibration, the p-factor, which represents the percentage of measured data falling within the 95PPU band, ranged from 0.71 at Maribo to 0.94 at Robe and Wabi@bridge. The r-factor, indicating the width of the 95PPU band, ranged from 0.87 at Furuna to 2.11 at Wabi@bridge.

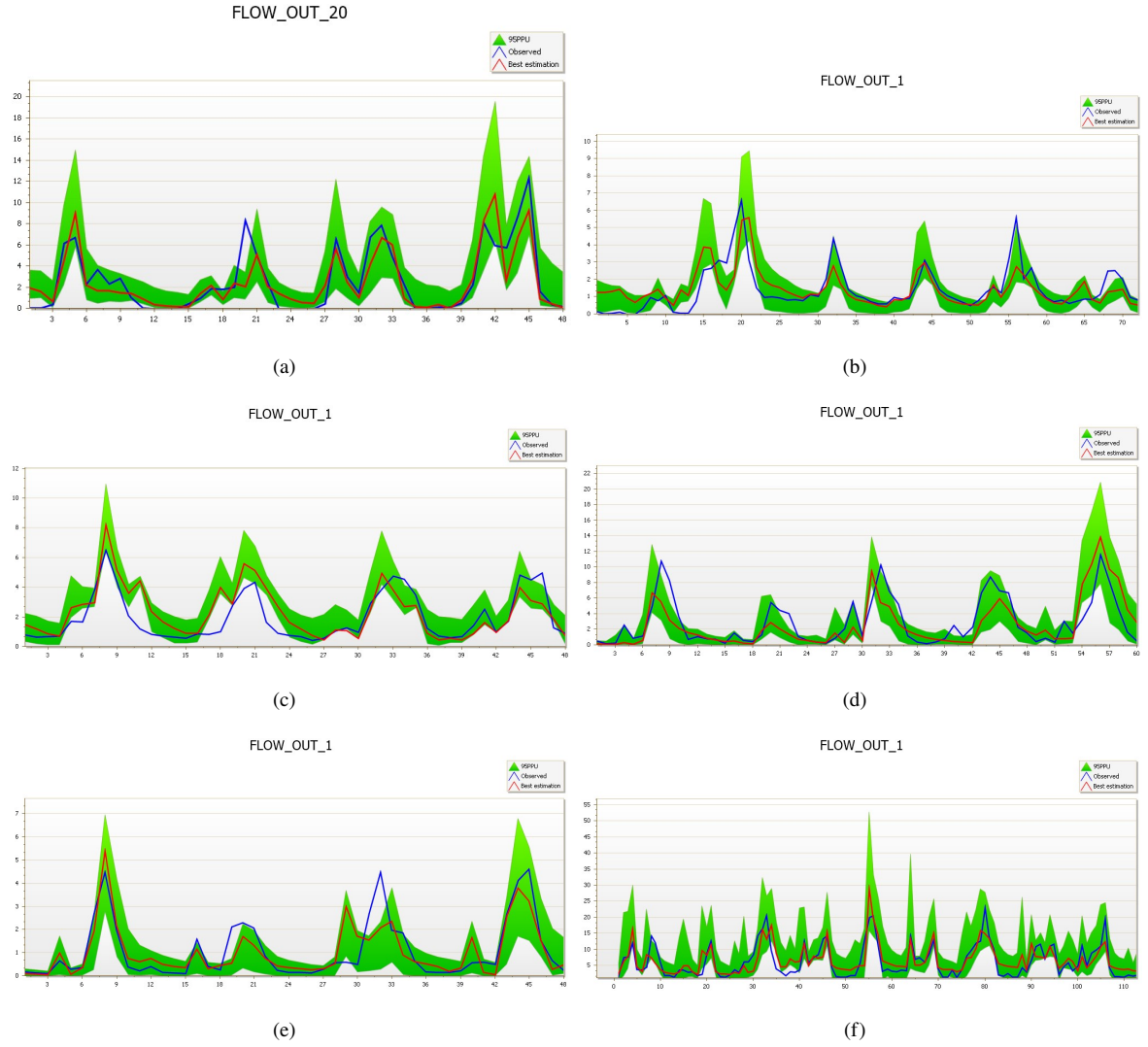


Figure 6.6: 95PPU band plot during the validation period for (a) Errer (b) Furuna (c) Harero (d) Maribo (e) Robe (f) Wabi@bridge

During the validation phase, the p-factor ranged from 0.67 at Errer to 0.90 at Robe, while the r-factor varied from 1.15 at Robe to 2.11 at Wabi@bridge headwater catchment. According to Abbaspour et al. (2018), it is recommended that the p-factor should exceed 0.70 and the r-factor should remain below 2 for monthly flow simulations. Overall, the p-factor values were within the recommended range during both calibration and validation periods for monthly flow, except for the Errer catchment. Similarly, the r-factor values were within the recommended limits during calibration and validation for monthly flow, except for the Wabi@bridge catchment.

This discrepancy highlights the high uncertainty in simulated streamflow, likely stemming from various sources of error. In summary, the SWAT model simulations generally showed favorable agreement between observed and simulated flows across all simulated headwater catchments.

## 6.4 Conclusion

The SWAT model simulation was conducted and evaluated for six headwater catchments in the Wabi Shebelle River Basin (WSRB). The study included sensitivity analysis of model parameters, calibration, validation, and uncertainty analysis using the SUFI-2 algorithm within SWAT-CUP. During calibration and validation, the NS efficiency served as the objective function, computed by comparing simulated and observed monthly streamflow data. Sensitivity analysis considered sixteen SWAT model parameters, with ten selected for subsequent calibration and validation. Graphical and statistical techniques were employed to assess the model's performance during both calibration and validation phases.

Statistical evaluation of the SWAT model performance was carried out across all selected headwater catchments, using metrics including $R^2$, NSE, PBIAS, and KGE. Results from this evaluation during both the calibration and validation periods demonstrated satisfactory performance meeting acceptable criteria. In addition to statistical assessments, the model's performance was visually inspected, revealing a generally uniform distribution on scatter plots, albeit with some exceptions observed at higher and lower values. To assess simulation uncertainty, an evaluation was conducted to determine how well the simulation results fit within the 95% Prediction Uncertainty (95PPU) band (p-factor), and the average width of this band (r-factor). These evaluations indicated that the results fell within acceptable ranges for the majority of the headwater catchments evaluated in this study.

The models' underperformance may be attributed to inadequate spatial and temporal distribution of input data during the modeling process. Uneven distribution of meteorological stations across the basin poses challenges, potentially leading to diminished model performance during calibration and validation. Additionally, maintaining consistent land cover and soil properties throughout simulation periods significantly impacts the precision of streamflow projections in the basin. Moreover, shortcomings in gauge station maintenance and observational oversight by personnel could further contribute to model underperformance (Haile et al., 2022). These factors collectively underscore the challenges in achieving optimal model outcomes.

In conclusion, the SWAT model demonstrated strong performance across all evaluation metrics within the six selected headwater catchments of the Wabi Shebelle River Basin (WSRB). This highlights the model's robustness, especially for smaller catchments. Additionally, numerous studies, both in Ethiopia and internationally, have evaluated the SWAT model across varied hydroclimatic, topographic, and landscape settings, consistently reporting performance that meets or exceeds acceptable standards. In the subsequent chapter, all calibrated SWAT model parameters will remain constant to assess the impacts of land use land cover (LULC) and climate change on future streamflow in the selected headwater catchments.

# Chapter 7

# Hydrological Impact of Climate and Land Use Land Cover Change in Headwater Catchments

## 7.1 Overview

Rivers and streams play a crucial role in flood prevention and mitigating various damages caused by climate change and human activities (Kale and Sönmez, 2019). In Ethiopia, headwater streams, although the smallest components of river and stream networks, comprise the majority of river due to the country's mountainous terrain. These headwater catchments, situated at high altitudes with substantial rainfall, serve as the primary freshwater sources for the basin.

The combined impact of climate and land use land cover (LULC) change on headwater catchments in Ethiopia has been insufficiently studied. Most hydrological research in the country has focused on potential streamflow alterations due to climate change, with an emphasis on the Abaya/Nile and Awash River basins. Consequently, there is a significant gap in understanding the comprehensive effects of both climate and LULC change on hydrological components in Ethiopian headwater catchments. Research in this area has been limited, with only a few studies addressing this critical issue. One notable study by WaleWorqlul et al. (2018) examined the impact of climate change on water availability and variability in two headwater catchments of the upper Blue Nile basin. However, further research is needed to gain a more holistic understanding of the interactions between climate and LULC change in Ethiopian headwater catchments.

The insights gained from assessing the potential impacts of climate change, land use land cover

(LULC) change, and their combined effects are crucial for advancing nature-based mitigation and adaptation measures and sustainable environmental planning. These measures are consistent with the Paris Climate Agreement, highlighting the importance of nature-based strategies for climate change mitigation and adaptation. This study provides valuable knowledge for comprehensively understanding headwater catchments within the dynamic interplay of changing climate and LULC due to both natural and human factors. By exploring these complex interactions, the research offers essential information to inform strategic decision-making and the implementation of effective measures to address environmental challenges and promote sustainability.

## 7.2 Scenario Development

### 7.2.1 Impact of Climate Change Scenario

To investigate the impacts of climate change on six headwater catchments, a structured approach with a series of interconnected steps was adopted. First, the ensemble means of the eight CMIP6 GCMs were subjected to downscaling and bias-correction procedures. These processed climate datasets were then used in hydrological impact analyses. The study examined four distinct CMIP6 shared socioeconomic pathways (SSP1-2.6, SSP2-4.5, SSP3-7.0, and SSP5-8.5) across three future periods within the 21st century: Q2 (2026–2050), Q3 (2051–2075), and Q4 (2076–2100). This temporal division allowed for a comprehensive assessment of the effects of climate change on six headwater catchments in the WSRB.

For a detailed explanation of the methodology, including climate model selection, downscaling, and bias correction, refer to Chapter 4. Throughout the simulation, land use land cover and calibrated SWAT model parameters were kept constant, using the year 2000 LULC data as the baseline. Additionally, a calibrated model covering the period from 1990 to 2014 served as the baseline simulation. The changes resulting from climate change were quantified by calculating the percentage change in the annual mean streamflow relative to the baseline period, and these findings were subsequently presented for each headwater catchment.

### 7.2.2 Land Use Land Cover Change Scenario

To study the impact of Land Use Land Cover (LULC) changes on mean streamflow, two distinct LULC datasets representing the years 2020 and 2040 were used for six selected headwater catchments. Detailed procedures for image classification and prediction for these years are explained in Chapter 5. As a reference point, LULC data from 2000, derived through hybrid classification

techniques (also detailed in Chapter 5), was used in alignment with historical climate data from 1990 to 2014. A baseline simulation was established using a calibrated SWAT model covering this period. To quantitatively assess the impacts of LULC changes, the percentage variation in annual mean streamflow relative to the baseline period was calculated for each headwater catchment, and the findings were summarized in tables.

### 7.2.3 Integrated Impact of Climate and LULC Change Scenario

To comprehensively investigate the integrated impact of climate change and land use land cover (LULC) changes in six headwater catchments within the WSRB, using projected climate change and LULC datasets. The approach utilized the ensemble mean of eight CMIP6 GCMs across four future projection scenarios (SSP1-2.6, SSP2-4.5, SSP3-7.0, and SSP5-8.5) during three future periods: Q2 (2026–2050), Q3 (2051–2075), and Q4 (2076–2100). Two LULC datasets were used, representing 2020 and 2040 years. The LULC data for 2020 were combined with the Q2 (2026-2050), while the LULC data for 2040 were integrated with Q3 (2051–2075) and Q4 (2076–2100) projected climate data. This approach allowed for the assessment of the sensitivity of mean streamflow in headwater catchments to the combined impact of future climate conditions and LULC changes.

Throughout this simulation, consistency was maintained by keeping the calibrated parameters of the SWAT model constant. The year 2000 LULC dataset was used as the baseline, aligning with historical climate data available from 1990 to 2014. The calibrated SWAT model for 1990–2014 served as the baseline streamflow simulation. To quantify changes due to these integrated factors, the percentage variation in mean streamflow relative to the baseline period in each headwater catchment was estimated, and the results were then presented.

### 7.2.4 Assumptions and Limitations

Even though periodic changes in soil properties are natural processes or can be aggravated by land degradation, this study assumed that soil properties and landscape topography remain constant.

## 7.3 Result and Discussion

### 7.3.1 Impact of Climate Change on Streamflow

To assess the impact of climate change on annual streamflow within the highlands of the Wabi Shebelle River Basin (WSRB), this study employed a comprehensive approach. Climate change was evaluated by calculating the area-averaged values of observed climate data and the ensemble mean of eight CMIP6 global climate model (GCM) datasets. This analysis included future scenarios SSP1-2.6, SSP2-4.5, SSP3-7.0, and SSP5-8.5, examining changes in rainfall, minimum temperature, and maximum temperature across six headwater catchments in the upper WSRB. Three future periods of the current century—Q2 (2026-2050), Q3 (2051-2075), and Q4 (2076-2100)—were applied to evaluate the changes. The study compared climate change indicators in terms of the percentage change in precipitation and relative change in temperature against a baseline period from 1990 to 2014. The results of this analysis are summarized in Table 7.1 for precipitation and Table 7.2 for minimum and maximum temperatures.

Table 7.1: Projected future changes in rainfall based on multimodel ensemble mean

| Catchment | SSP1-2.6 | | | SSP2-4.5 | | | SSP3-7.0 | | | SSP5-8.5 | | |
|---|---|---|---|---|---|---|---|---|---|---|---|---|
| | Q2 | Q3 | Q4 | Q2 | Q3 | Q4 | Q2 | Q3 | Q4 | Q2 | Q3 | Q4 |
| Errer | 12.8 | 12.1 | 9.5 | 10.3 | 15.7 | 15.9 | 9.0 | 14.2 | 21.4 | 11.9 | 20.7 | 28.0 |
| Furuna | 4.8 | 6.5 | 5.5 | 2.9 | 8.5 | 12.0 | 2.1 | 7.0 | 12.4 | 4.1 | 13.3 | 19.9 |
| Harero | 5.1 | 5.7 | 5.4 | 2.7 | 7.9 | 10.7 | 2.0 | 6.0 | 11.4 | 4.2 | 12.0 | 18.0 |
| Maribo | 4.8 | 6.5 | 5.5 | 2.9 | 8.5 | 12.0 | 2.1 | 7.0 | 12.4 | 4.1 | 13.3 | 19.9 |
| Robe | 16.7 | 16.6 | 16.1 | 13.9 | 19.1 | 22.0 | 12.6 | 19.5 | 23.9 | 16.1 | 24.0 | 31.0 |
| Wabi@bridge | -6.6 | -7.1 | -6.2 | -9.3 | -3.4 | 0.1 | -9.9 | -5.3 | 1.8 | -7.7 | 1.9 | 8.4 |

Under the SSP1-2.6 scenario, Table 7.1 reveals a mixed pattern of precipitation changes across all headwater catchments, with the exception of Wabi@bridge. These catchments generally displayed a decreasing trend in precipitation when compared to the baseline period. However, in the remaining catchments, an increase in precipitation was observed during the Q2 and Q3 periods, followed by a decrease in the Q4 period. In contrast, under the SSP2-4.5, SSP3-7.0, and SSP5-8.5 scenarios, precipitation exhibited a consistent upward trend throughout all studied periods, except in the case of the Wabi@bridge catchment. The findings also show a consistent increasing trend for both minimum and maximum temperature in all studied headwater catchments Table 7.2. The minimum temperature exhibited a larger increase compared to the maximum

Table 7.2: Projected future Tmin and Tmax change using multimodel ensemble in selected headwater catchments

| Catchment | SSP1-2.6 | | | SSP2-4.5 | | | SSP3-7.0 | | | SSP5-8.5 | | |
|---|---|---|---|---|---|---|---|---|---|---|---|---|
| | Q2 | Q3 | Q4 | Q2 | Q3 | Q4 | Q2 | Q3 | Q4 | Q2 | Q3 | Q4 |
| **Tmax** | | | | | | | | | | | | |
| Errer | 0.29 | 0.37 | 0.48 | 0.27 | 0.61 | 0.88 | 0.33 | 0.77 | 1.17 | 0.42 | 0.69 | 0.94 |
| Furuna | 0.42 | 0.46 | 0.53 | 0.38 | 0.68 | 0.89 | 0.40 | 0.77 | 1.10 | 0.52 | 0.72 | 0.88 |
| Harero | 0.37 | 0.42 | 0.49 | 0.34 | 0.63 | 0.85 | 0.36 | 0.73 | 1.06 | 0.48 | 0.68 | 0.85 |
| Maribo | 0.42 | 0.46 | 0.53 | 0.38 | 0.68 | 0.89 | 0.40 | 0.77 | 1.10 | 0.52 | 0.72 | 0.88 |
| Robe | 0.43 | 0.50 | 0.55 | 0.42 | 0.67 | 0.88 | 0.43 | 0.76 | 1.09 | 0.53 | 0.75 | 0.91 |
| Wabi@bridge | 0.67 | 0.73 | 0.79 | 0.63 | 0.95 | 1.19 | 0.66 | 1.07 | 1.45 | 0.79 | 1.02 | 1.21 |
| **Tmin** | | | | | | | | | | | | |
| Errer | 0.39 | 0.42 | 0.50 | 0.39 | 0.68 | 0.86 | 0.43 | 0.85 | 1.17 | 0.50 | 0.93 | 1.31 |
| Furuna | 0.53 | 0.55 | 0.65 | 0.57 | 0.95 | 1.24 | 0.67 | 1.27 | 1.64 | 0.73 | 1.36 | 1.75 |
| Harero | 0.60 | 0.63 | 0.72 | 0.64 | 0.99 | 1.25 | 0.73 | 1.27 | 1.61 | 0.81 | 1.37 | 1.73 |
| Maribo | 0.53 | 0.55 | 0.65 | 0.57 | 0.95 | 1.24 | 0.67 | 1.27 | 1.64 | 0.73 | 1.36 | 1.75 |
| Robe | 0.59 | 0.60 | 0.69 | 0.61 | 0.93 | 1.18 | 0.70 | 1.19 | 1.53 | 0.76 | 1.28 | 1.65 |
| Wabi@bridge | 0.85 | 0.87 | 0.95 | 1.26 | 1.69 | 1.98 | 1.35 | 2.00 | 2.43 | 1.47 | 2.14 | 2.59 |

temperature. These climate shifts are anticipated to significantly impact the hydrological cycle, leading to alterations in streamflow and potentially affecting the availability of freshwater resources within a catchment.

The results of this study align with previous research, indicating varying patterns of precipitation—decreasing (Abebe and Kebede, 2017), mixed (Tesfaye et al., 2014; WaleWorqlul et al., 2018), and increasing (Gurara et al., 2021) across all projection scenarios. Additionally, a consistent trend of rising minimum and maximum temperatures has been observed throughout the country (Abebe and Kebede, 2017; Ayele et al., 2016; Taye et al., 2018; Tesfaye et al., 2014; WaleWorqlul et al., 2018). Variations in these findings may be attributed to differences in climate model selection and the methods used for downscaling and bias correction.

To study the impact of climate change on streamflow, the calibrated SWAT model was executed using the ensemble mean of eight CMIP6 GCMs under four future scenarios across three 25-year periods for six headwater catchments in the WSRB. The future scenarios included SSP1-2.6, SSP2-4.5, SSP3-7.0, and SSP5-8.5. This study compared the baseline period (1990-2014) with three future periods: Q2 (2026-2050), Q3 (2051-2075), and Q4 (2076-2100). The changes in streamflow were assessed on an annual average timescale, and the results are presented in Table

7.3.

Across all headwater catchments and under the four future prediction scenarios, a consistent increase in streamflow was observed for all study periods, except for the Wabi@bridge catchment (see Table 7.3). The Wabi@bridge catchment presented mixed outcomes. Specifically, under the SSP1-2.6 scenario, streamflow decreased during all three future periods compared to the baseline. In the remaining scenarios, streamflow decreased during the Q2 period but increased during the Q3 and Q4 periods.

A similar pattern emerged in the Errer catchment under the SSP2-4.5 scenario, while the Furuna, Harero, Maribo, and Robe catchments demonstrated a consistent increase in streamflow across all periods and scenarios. Under the SSP3-7.0 and SSP5-8.5 scenarios, a continuous rise in streamflow was observed in all headwater catchments except for Wabi@bridge. For Wabi@bridge, streamflow decreased during Q2 but increased during Q3 and Q4 relative to the baseline period.

The observed patterns in streamflow align with the identified precipitation trends, reflecting overall consistency. In catchments where precipitation is projected to increase under all future scenarios, streamflow also tends to increase. Conversely, in catchments where precipitation is expected to decline, streamflow tends to decrease. These findings are consistent with results reported by various researchers in different parts of the country. Previous studies have documented decreasing streamflow (Taye et al., 2018; Tesfaye et al., 2014), mixed trends (Ayele et al., 2016), and increasing streamflow (Gurara et al., 2021), highlighting the sensitivity of streamflow patterns to changes in precipitation across diverse geographical regions.

### 7.3.2 Land Use Land Cover Change Impact on Streamflow

With historical climate data (1990 to 2014) and SWAT-calibrated parameters held constant, this study aimed to evaluate the impact of Land Use Land Cover (LULC) changes on the average streamflow in six headwater catchments. The approach involved altering LULC maps for the years 2000, 2020, and 2040 while keeping all other variables constant. The annual mean streamflow for each scenario was then computed and compared with the baseline simulation of the SWAT model using the 2000 LULC data. The summarized results of this simulation are presented in Table 7.4.

Table 7.3: Impact of Climate Change on mean Streamflow in Headwater Catchments

| Catchment | Period | Baseline | Average streamflow for the period | | | | Change in streamflow (%) | | | |
|---|---|---|---|---|---|---|---|---|---|---|
| | | | SSP1-2.6 | SSP2-4.5 | SSP3-7.0 | SSP5-8.5 | SSP1-2.6 | SSP2-4.5 | SSP3-7.0 | SSP5-8.5 |
| **Errer** | Q2 | 1.77 | 2.76 | 3.20 | 3.08 | 3.33 | 55.98 | 81.10 | 74.61 | 88.43 |
| | Q3 | | 2.61 | 3.60 | 3.43 | 4.13 | 47.73 | 103.58 | 94.12 | 134.07 |
| | Q4 | | 2.18 | 3.49 | 4.17 | 4.73 | 23.35 | 97.83 | 136.09 | 168.05 |
| **Furuna** | Q2 | 1.33 | 1.38 | 1.37 | 1.34 | 1.38 | 3.72 | 2.96 | 1.00 | 4.18 |
| | Q3 | | 1.40 | 1.48 | 1.43 | 1.60 | 5.35 | 11.36 | 7.94 | 20.33 |
| | Q4 | | 1.36 | 1.56 | 1.55 | 1.72 | 2.34 | 17.29 | 17.10 | 29.37 |
| **Harero** | Q2 | 2.00 | 2.19 | 2.18 | 2.15 | 2.21 | 9.67 | 8.79 | 7.38 | 10.33 |
| | Q3 | | 2.18 | 2.31 | 2.23 | 2.44 | 9.01 | 15.43 | 11.32 | 22.12 |
| | Q4 | | 2.16 | 2.39 | 2.40 | 2.58 | 7.78 | 19.17 | 19.86 | 29.01 |
| **Maribo** | Q2 | 2.66 | 2.88 | 2.91 | 2.85 | 2.94 | 8.35 | 9.46 | 7.22 | 10.76 |
| | Q3 | | 2.94 | 3.17 | 3.06 | 3.44 | 10.82 | 19.37 | 15.10 | 29.57 |
| | Q4 | | 2.82 | 3.31 | 3.31 | 3.69 | 6.21 | 24.73 | 24.72 | 38.84 |
| **Robe** | Q2 | 1.44 | 2.43 | 2.42 | 2.37 | 2.52 | 69.09 | 68.18 | 64.37 | 74.67 |
| | Q3 | | 2.37 | 2.59 | 2.61 | 2.81 | 64.75 | 79.53 | 81.20 | 95.19 |
| | Q4 | | 2.30 | 2.69 | 2.78 | 3.06 | 59.75 | 87.12 | 92.81 | 112.26 |
| **Wabi@bridge** | Q2 | 9.17 | 7.82 | 8.16 | 7.76 | 8.23 | -14.78 | -11.00 | -15.39 | -10.24 |
| | Q3 | | 7.56 | 9.32 | 8.80 | 10.92 | -17.61 | 1.64 | -4.03 | 19.01 |
| | Q4 | | 7.53 | 10.13 | 10.70 | 12.17 | -17.88 | 10.38 | 16.68 | 32.66 |

Table 7.4: Impact of LULC Change on mean Streamflow in Headwater Catchments

| Catchments | Average streamflow for the period | | | Change in streamflow (%) | |
|---|---|---|---|---|---|
| | 2000 (Baseline) | 2020 | 2040 | 2000 to 2020 | 2000 to 2040 |
| Errer | 1.77 | 1.80 | 1.20 | 1.98 | -32.17 |
| Furuna | 1.33 | 1.31 | 1.31 | -0.93 | -1.51 |
| Harero | 2.00 | 2.03 | 2.02 | 1.33 | 0.87 |
| Maribo | 2.66 | 2.72 | 2.70 | 2.31 | 1.43 |
| Robe | 1.44 | 1.44 | 1.43 | 0.27 | -0.60 |
| Wabi@bridge | 9.17 | 9.48 | 9.49 | 3.32 | 3.45 |

The results highlight variations in streamflow responses to Land Use Land Cover (LULC) changes, with the Errer catchment demonstrating a larger percentage change during 2020 and 2040 compared to the baseline period. Specifically, between 2000 and 2020, an increasing trend in streamflow was observed in all headwater catchments except for the Furuna catchment, with streamflow changes ranging from -0.93% to 3.32%. The most significant change occurred in the Wabi@bridge catchment, with a 3.32% increase.

However, a mixed pattern emerged between 2000 and 2040. The Errer, Furuna, and Robe catchments exhibited a projected decrease in streamflow, while the Harero, Maribo, and Wabi@bridge catchments showed an increase. Notably, the Errer catchment experienced a substantial shift in streamflow between 2020 and 2040, ranging from a 1.98% increase to a significant 32.17% decrease compared with the baseline period of 2000.

The LULC changes simulation resulted in a mixed trend in mean streamflow across all headwater catchments in the WSRB. The Harero, Maribo, and Wabi@bridge catchments showed increasing streamflow, while the Furuna catchment exhibited a decrease. The Errer and Robe catchments displayed an increasing trend followed by a decrease when using the 2020 and 2040 LULC data, respectively. It's essential to note that a catchment's response to LULC alterations is closely tied to its specific characteristics and size. These factors can modify the degree to which LULC changes affect streamflow, making it crucial to consider catchment-specific attributes when assessing hydrological responses.

### 7.3.3 Integrated Impact of Climate and LULC Change on Streamflow

In addition to individually examining the impacts of climate change and land use land cover (LULC) change on mean streamflow, this study adopted a holistic approach by combining these two factors to assess their combined hydrological response in six headwater catchments within the WSRB. Recognizing the simultaneous occurrence of these conditions in the real world, the objective was to understand their combined effects on the streamflow. To estimate the combined impacts of LULC and climate change on streamflow, seven simulations were conducted, incorporating four climate change and three LULC scenarios.

This study focuses on three future periods in the 21st century: Q2 (2026–2050), Q3 (2051–2075), and Q4 (2076–2100). The results were compared with a baseline scenario involving climate data from 1990 to 2014 and LULC data from 2000. Table 7.5 provides a concise overview of these combinations, revealing the complex relationship between climate change and LULC change, and their cumulative influence on streamflow in the investigated headwater catchments.

The findings from Table 7.5 highlight that the Errer and Robe catchments exhibit a comparatively higher sensitivity to the combined effects of climate change and land use land cover (LULC) change. These catchments consistently demonstrated an increasing streamflow trend under all Shared Socioeconomic Pathways (SSPs) across all future periods. For the Furuna, Harero, and Maribo catchments, a modest overall increase in annual mean streamflow was observed under all SSP scenarios and future periods, except for Furuna under SSP3-7.0 during Q2, where a decrease was found.

In contrast, Wabi@bridge displayed mixed results regarding the impact of climate and LULC changes on annual mean streamflow. Specifically, during Q2, all SSP scenarios indicated a decreasing pattern in the Wabi@bridge catchment. A similar decreasing trend was observed under the SSP1-2.6 scenario for all periods. These results underscore the variability of impacts across different landscapes and periods.

## 7.4 Conclusion

In this chapter, a calibrated and validated SWAT model was employed to simulate future changes in streamflow over three distinct periods: Q2 (2026–2050), Q3 (2051–2075), and Q4 (2076–2100). The simulation incorporated three input conditions: climate change, land use land cover

Table 7.5: Integrated impact of climate and LULC change on mean streamflow in Headwater catchments

| Catchment | Period | Baseline | LULC | Average streamflow for the period | | | | Change in streamflow (%) | | | |
|---|---|---|---|---|---|---|---|---|---|---|---|
| | | | | SSP1-2.6 | SSP2-4.5 | SSP3-7.0 | SSP5-8.5 | SSP1-2.6 | SSP2-4.5 | SSP3-7.0 | SSP5-8.5 |
| **Errer** | Q2 | 1.77 | 2020 | 2.8 | 3.2 | 3.1 | 3.3 | 55.5 | 80.8 | 74.5 | 88.2 |
| | Q3 | | 2040 | 1.8 | 2.4 | 2.3 | 2.7 | 1.8 | 33.6 | 27.9 | 51.8 |
| | Q4 | | 2040 | 1.5 | 2.3 | 2.7 | 3.0 | -13.6 | 30.0 | 52.9 | 71.8 |
| **Furuna** | Q2 | 1.33 | 2020 | 1.4 | 1.4 | 1.3 | 1.4 | 2.4 | 1.6 | -0.3 | 3.0 |
| | Q3 | | 2040 | 1.4 | 1.5 | 1.4 | 1.6 | 3.4 | 9.7 | 6.7 | 18.9 |
| | Q4 | | 2040 | 1.3 | 1.5 | 1.5 | 1.7 | 0.0 | 15.6 | 15.6 | 28.0 |
| **Harero** | Q2 | 2.00 | 2020 | 2.2 | 2.2 | 2.2 | 2.3 | 12.1 | 10.6 | 9.2 | 12.5 |
| | Q3 | | 2040 | 2.2 | 2.3 | 2.3 | 2.5 | 9.8 | 16.5 | 12.8 | 23.7 |
| | Q4 | | 2040 | 2.2 | 2.4 | 2.4 | 2.6 | 8.1 | 20.6 | 21.6 | 31.0 |
| **Maribo** | Q2 | 2.66 | 2020 | 2.9 | 2.9 | 2.9 | 3.0 | 8.0 | 9.2 | 7.2 | 11.1 |
| | Q3 | | 2040 | 2.9 | 3.2 | 3.1 | 3.4 | 10.3 | 19.1 | 15.4 | 29.6 |
| | Q4 | | 2040 | 2.8 | 3.3 | 3.3 | 3.7 | 5.2 | 24.6 | 24.8 | 38.9 |
| **Robe** | Q2 | 1.44 | 2020 | 2.4 | 2.4 | 2.4 | 2.5 | 69.1 | 68.2 | 64.4 | 74.6 |
| | Q3 | | 2040 | 2.4 | 2.6 | 2.6 | 2.8 | 64.3 | 79.0 | 80.8 | 94.7 |
| | Q4 | | 2040 | 2.3 | 2.7 | 2.8 | 3.1 | 59.2 | 86.6 | 92.3 | 111.8 |
| **Wabi@bridge** | Q2 | 9.17 | 2020 | 7.8 | 8.2 | 7.8 | 8.3 | -15.1 | -11.2 | -14.6 | -9.4 |
| | Q3 | | 2040 | 7.5 | 9.3 | 8.9 | 11.0 | -18.2 | 1.5 | -3.0 | 19.5 |
| | Q4 | | 2040 | 7.4 | 10.1 | 10.9 | 12.4 | -19.1 | 10.6 | 18.3 | 34.9 |

(LULC) change, and their combined influence. To project future climate change, the ensemble mean of eight CMIP6 GCMs across four scenarios (SSP1-2.6, SSP2-4.5, SSP3-7.0, and SSP5-8.5) was utilized for headwater catchments. These models were subsequently downscaled and bias-corrected to ensure their applicability in hydrological impact analysis.

For predicting future LULC, the MLP-ANN transition algorithm, using six explanatory factors, was employed. This algorithm was crucial in projecting LULC changes for the year 2040 across the six headwater catchments. By integrating these components into the SWAT model, the study aimed to comprehensively assess and understand potential alterations in streamflow dynamics over the specified future periods, considering the impacts of climate change, LULC change, and their combined effects.

The study reveals that, in the Errer and Furuna catchments, the combined impact of climate and land use land cover (LULC) change led to a reduction in streamflow compared to the impact of climate change alone across all SSPs scenarios and future periods. Conversely, in the Harero catchment, the combined impact resulted in greater streamflow than the impact of climate change alone across all SSP scenarios and future periods. In the Robe catchment, the separate impact of climate change induced more significant changes than the combined impact under SSP1-2.6, SSP2-4.5, and SSP3-7.0 during the Q2 period (2026-2050). Notably, Maribo and Wabi@bridge exhibited similar trends compared to the baseline period owing to the impacts of climate change and the combined impact of climate and LULC change.

In SSP1-2.6 and SSP2-4.5 scenarios, the impact of climate change on streamflow exceeded the combined impact of climate and LULC change for all future periods in the Maribo and Wabi@bridge catchments. Conversely, in the SSP3-7.0 and SSP5-8.5 scenarios, the impact of climate change was less than the combined impact on streamflow throughout all future periods. Overall, the study found mixed results between the impacts of climate change and the combined impacts of climate and LULC change in headwater catchments. The examination of the separate impact of land use land cover change resulted in an insignificant change in future mean streamflow. However, a significant change was observed due to climate change, with precipitation change identified as the most crucial driving factor for the alteration of mean streamflow in all headwater catchments.

This page is intentionally left blank.

# Chapter 8

# Conclusions and Recommendations

## 8.1 Conclusions

This study focused on evaluating hydro-climatic trends, climate change, and the potential impacts of future climate change and land use land cover (LULC) dynamics on the hydrological response of headwater catchments in the WSRB in Ethiopia. To achieve this, a comprehensive analysis of historical hydro-climatic seasonal and annual variability and trends within the WSRB was conducted, utilizing two non-parametric statistical methods: the modified Mk test and the Sen Slope estimator. The modified MK test was employed to assess monotonic trends in the seasonal and annual rainfall, minimum and maximum temperatures, and streamflow. The Sen Slope estimator was used to quantify the magnitude of the changes in the time series. The basin was spatially discretized into local agro-climatic zones, with each zone representing the available climatic data.

The assessment revealed a mixed trend in rainfall and maximum temperature during the rainy season and annual time series. In contrast, the minimum temperature exhibited a clear increasing trend, except for ACZ7, which is located in the highland part of the basin. Similarly, streamflow exhibited mixed trends in the seasonal and annual analyses. Out of the four streamflow gauging stations, two showed increasing trends and two showed decreasing trends during spring seasons. In contrast, during the summer season and the annual flow, the three stations displayed an increasing trend. These findings provided valuable insights into the trends and changes associated with rainfall and temperature in the WSRB.

The assessment aimed to evaluate the scope of climate change by examining rainfall and minimum and maximum temperatures under four shared socioeconomic pathway (SSPs) scenarios

across all Agro-Climatic Zones (ACZs) during three future time periods. Future climate data projected from eight CMIP6 Global Climate Models (GCMs) corresponding to SSP scenarios (SSP1-2.6, SSP2-4.5, SSP3-7.0, and SSP5-8.5) were utilized. The selection of GCMs is considered to have superior spatial and temporal resolutions from diverse global climate modeling institutions. Downscaling and bias correction procedures were applied at each meteorological station to refine the data. This involved a distance-weighted average remapping interpolation and non-parametric quantile mapping. Recognizing the uncertainties associated with climate models, a multi-model ensemble mean approach was employed on selected eight CMIP6 GCMs for climate change and impact studies. The findings indicate a projected increase in the mean annual precipitation during Q2, Q3, and Q4 for all emission scenarios across each ACZ. Similarly, the mean annual maximum and minimum temperatures are expected to increase during the same future periods in each ACZ. Notably, the rate of change in the minimum temperature is higher than that of the maximum temperature in nearly all the ACZs.

In addition, this research focused on investigating the long-term dynamics of land use land cover changes in the upstream and central parts of the WSRB while also projecting future LULC changes. The study employed the Semi-Automatic Classification Plugin (SCP) within the QGIS environment, utilizing hybrid classification techniques, specifically, maximum likelihood algorithms. Landsat 5 TM and Landsat 8 OLI satellite images from 1990, 2000, 2010, and 2020 were processed to produce land use land cover maps. The analysis uncovered significant changes in land use land cover over the past 30 years (1990 – 2020) within the basin. Notable transformations included the depletion of natural vegetation, expansion of cultivated and built-up areas, and a slight increase in bare land, largely at the expense of forests and shrublands. The MLP-ANN model was employed to project future changes, predicting an anticipated increase in built-up areas, dense shrubs, grasslands, agricultural land, and barren land by 2040. Conversely, water bodies, forestland, and open shrublands are expected to undergo substantial reduction.

Hydrological models play a crucial role in understanding and simulating the processes within a catchment, particularly for sustainable management of natural resources, with a primary focus on water resources. Among these models, the SWAT model serves as a continuous-time, semi-distributed, process-based river basin model. Key spatial inputs encompass a 30-meter Digital Elevation Model (DEM), soil data, land use, and stream network layers with similar projections. Temporal inputs include rainfall, minimum and maximum temperatures for model simulation,

and streamflow for calibration and validation. During the calibration process, 10 model parameters were identified as essential for representing the hydrological dynamics of the headwater catchments, with a particular emphasis on parameters related to surface runoff processes. CN2 emerged as the most sensitive parameter influencing streamflow simulation across all headwater catchments. Graphical and statistical metrics of model performance and uncertainty indicated that the model effectively simulated streamflow within an acceptable range. The calibrated and validated SWAT model was subsequently employed to predict hydrological responses to climate change, land use land cover alterations, and their integrated impacts in six headwater catchments within the WSRB.

Subsequently, to assess the impacts of climate and land use land cover changes on streamflow, the 1990 to 2014 runoff model was utilized as a baseline for comparison. During this analysis, the calibrated parameters remained constant, and climate and/or land use land cover changes were incorporated. Climate data were replaced with the ensemble mean of eight CMIP6 Global Climate Models (GCMs) under four Shared Socioeconomic Pathways (SSPs): SSP1-2.6, SSP2-4.5, SSP3-7.0, and SSP5-8.5, spanning three future periods - Q2 (2026-2050), Q3 (2051-2075), and Q4 (2076-2100). The results revealed that the observed climate and land use land cover changes contributes to an increase in annual mean streamflow across all headwater catchments. However, projected climate changes projected to have a higher impact than observed land use land cover changes. Furthermore, the combined impact of climate and land use land cover changes demonstrated a more substantial increase in streamflow across all studied headwater catchments.

## 8.2 Recommendations

The findings of this research hold promising implications for the development of nature-based solutions aimed at mitigating the impacts of climate change and addressing the challenges arising from rapid population growth, which exerts considerable pressure on the natural resources within the basin/catchment. The insights gained from this analysis have the potential to inform and enhance management policies, particularly those focused on mitigating the changes in hydrological responses and their associated consequences. Based on these results, decision-makers, including land use planners, can implement effective strategies. For instance, measures to control the rapid expansion of agriculture and address land degradation in the upstream, as well as in the central parts of the basin, can be devised and executed to ensure sustainable resource use and ecosystem resilience.

Advancements in climate science and enhanced computational efficiency of climate models have contributed to significant improvements in the understanding of climate dynamics. Consequently, there is an increased capability to assess the impacts of climate change and human activities on the environment. It is imperative to conduct continuous examinations to evaluate the availability of water resources, as this is crucial for proper functioning of the environment. By regularly monitoring and assessing evolving climate scenarios, a better comprehension of the implications for water resources can be achieved, and informed decisions can be made to ensure the sustainable management of the environment.

A significant limitation of Global Climate Models (GCMs) for impact studies is their coarse spatial resolutions. To address this, spatial downscaling and bias correction of climate models are crucial following established methods. However, the absence of a standard method introduces subjectivity to these processes. Therefore, to enhance the accuracy of forecasting hydrological responses to climate change in the basin/catchment, it is imperative to assess projections from different methods, including dynamic downscaling.

Beyond focusing solely on the annual mean streamflow, it would be beneficial to consider parameters such as minimum and maximum annual flows, extreme flow events, and frequency of rainy days. Moreover, to offer more meaningful representations of future hydrological responses, it is advisable to extend the analysis to monthly and seasonal periods by considering the available information. This comprehensive approach will contribute to a better understanding of the complicated interactions between climate patterns, land use land cover changes, and hydrological dynamics in the WSRB.

While projecting future land use land cover changes using a land use dynamics model, it is crucial to acknowledge that such models may not precisely estimate actual future changes. To enhance the accuracy and relevance of these projections, it is recommended to supplement the projection models with a comprehensive development plan.This plan should consider all locally anticipated socioeconomic changes expected in the future. By integrating these aspects, the modeling process becomes more robust thereby providing a more realistic foundation for future scenarios.

River discharge/Streamflow data for the basin are spatially and temporally limited. Installing automatic gauging stations in strategic locations, coupled with skilled personnel and proper maintenance, can significantly enhance data availability and quality. Additionally, improving the distribution of meteorological stations, particularly in the central and lower basins, is crucial for future water resource assessment and planning. Establishing a publicly accessible hydroclimatic data database addresses challenges in data quality and accessibility, promoting more effective modeling and sustainable water resource management.

This study incorporated multiple models and their respective outputs, each accompanied by a certain degree of uncertainty. Consequently, it is crucial to approach the results with caution, viewing them as indicative of potential future trends rather than as precise predictions. To enhance the comprehensiveness of the study, future research should expand its scope to include variations in soil and other climate variables, along with changes in precipitation and temperature. Moreover, there is a need to delve into the impacts of climate change on socio-economic sectors reliant on water resources. This broader approach will contribute to a more holistic understanding of the complex dynamics involved in climate change.

This page is intentionally left blank.

# Bibliography


Aamir, E. and Hassan, I. (2018). Trend analysis in precipitation at individual and regional levels in Baluchistan, Pakistan. In *IOP Conference Series: Materials Science and Engineering 414*.

Abbaspour, K. C. (2015). SWAT-CUP: SWAT Calibration and Uncertainty Programs - A User Manual. Technical report, Swiss Federal Institute of Aquatic Science nad Technology, Eawag, Switzerland.

Abbaspour, K. C., Vaghefi, S. A., and Srinivasan, R. (2018). A guideline for successful calibration and uncertainty analysis for soil and water assessment: A review of papers from the 2016 international SWAT conference. *Water (Switzerland)*, 10(6).

Abbaspour, K. C., Yang, J., Maximov, I., Siber, R., Bogner, K., Mieleitner, J., Zobrist, J., and Srinivasan, R. (2007). Modelling hydrology and water quality in the pre-alpine/alpine Thur watershed using SWAT. *Journal of Hydrology*, 333(2-4):413–430.

Abburu, S. and Golla, S. B. (2015). Satellite Image Classification Methods and Techniques: A Review. *International Journal of Computer Applications*, 119(8):20–25.

Abdo, K. S., Fiseha, B. M., Rientjes, T. H. M., Gieske, A. S. M., and Haile, A. T. (2009). Assessment of climate change impacts on the hydrology of Gilgel Abay catchment in Lake Tana Basin, Ethiopia. *Hydrological Processes*, 2274(November 2008):3661–3669.

Abebe, E. and Kebede, A. (2017). Assessment of Climate Change Impacts on the Water Resources of Megech River Catchment, Abbay Basin, Ethiopia. *Open Journal of Modern Hydrology*, 07(02):141–152.

Addis, H. K., Strohmeier, S., Ziadat, F., Melaku, N. D., and Klik, A. (2016). Modeling streamflow and sediment using SWAT in ethiopian highlands. *International Journal of Agricultural and Biological Engineering*, 9(5):51–66.

Addisu, S., Selassie, Y. G., Fissha, G., and Gedif, B. (2015). Time series trend analysis of temperature and rainfall in lake Tana Sub-basin, Ethiopia. *Environ Syst Res*, 4(1).

Ademe, D., Ziatchik, B. F., Tesfaye, K., Simane, B., Alemayehu, G., and Adgo, E. (2020). Climate trends and variability at adaptation scale: Patterns and perceptions in an agricultural region of the Ethiopian Highlands. *Weather and Climate Extremes*, 29:100263.

Admassu, S. and Seid, A. H. (2006). Analysis of rainfall trend in Ethiopia. *Ethiopian Journal of Science and Technology*, 3(2):15–30.

Adu, J. T. and Kumarasamy, M. V. (2018). Assessing Non-Point Source Pollution Models : a Review. *Pol. J. Environ. Stud*, 27(5):1913–1922.

Ahmad, I., Tang, D., Wang, T., Wang, M., and Wagan, B. (2015). Precipitation trends over time using Mann-Kendall and spearman's Rho tests in swat river basin, Pakistan. *Advances in Meteorology*, 2015.

Akdeniz, H. B., Sag, N. S., and Inam, S. (2023). Analysis of land use/land cover changes and prediction of future changes with land change modeler: Case of Belek, Turkey. *Environmental Monitoring and Assessment*, 195(1):1–28.

Akinsanola, A. A., Ongoma, V., and Kooperman, G. J. (2021). Evaluation of CMIP6 models in simulating the statistics of extreme precipitation over east Africa. *Elsevier*, 136(519).

Akoko, G., Le, T. H., Gomi, T., and Kato, T. (2021). A Review of SWAT Model Application in Africa. *Water (Switzerland)*, 13(9):1313.

Alaminie, A. A., Tilahun, S. A., Legesse, S. A., Zimale, F. A., Tarkegn, G. B., and Jury, M. R. (2021). Evaluation of Past and Future Climate Trends under CMIP6 Scenarios for the UBNB ( Abay ), Ethiopia. *Water*, 13:2110.

Alemayehu, A., Maru, M., Bewket, W., and Assen, M. (2020). Spatiotemporal variability and trends in rainfall and temperature in Alwero watershed, western Ethiopia. *Environ Syst Res*, 9(1).

Alemu, Z. A. and Dioha, M. O. (2020). Climate change and trend analysis of temperature: the case of Addis Ababa, Ethiopia. *Environ Syst Res*, 9(1).

Alexandersson, H. (1986). A homogeneity test applied to precipitation data. *Journal of Climatology*, 6(6):661–675.

Alibuyog, N. R., Ella, V. B., Reyes, M. R., Srinivasan, R., Heatwole, C., and Dillaha, T. (2009). Predicting the effects of land use change on runoff and sediment yield in manupali river subwa-

tersheds using the swat model. *International Agricultural Engineering Journal*, 18(1-2):15–25.

Alifujiang, Y., Abuduwaili, J., Maihemuti, B., Emin, B., and Groll, M. (2020). Innovative trend analysis of precipitation in the Lake Issyk-Kul Basin, Kyrgyzstan. *Atmosphere*, 11(4):1–16.

Amgoth, A., Rani, H. P., and Jayakumar, K. V. (2023). Exploring LULC changes in Pakhal Lake area, Telangana, India using QGIS MOLUSCE plugin. *Spatial Information Research*, 31:429–438.

Amsalu, A., Stroosnijder, L., and de Graaff, J. (2006). Long-term dynamics in land resource use and the driving forces in the Beressa watershed, highlands of Ethiopia. *Journal of Environmental Management*, 83(4):448–459.

Aredo, M. R., Hatiye, S. D., and Pingale, S. M. (2021). Impact of land use/land cover change on stream flow in the Shaya catchment of Ethiopia using the MIKE SHE model. *Arabian Journal of Geosciences*, 14(2).

Arnold, J. G., Moriasi, D. N., Gassman, P. W., Abbaspour, K. C., White, M. J., Srinivasan, R., Santhi, C., Harmel, R. D., Van Griensven, A., Van Liew, M. W., Kannan, N., and Jha, M. K. (2012). SWAT: Model Use, Calibration, and Validation. *Transactions of the ASABE*, 55(4):1491–1508.

Arnold, J. G., Srinivasan, R., Muttiah, R. S., and Williams, J. R. (1998). Large Area Hydrologic Modeling and Assessment Part I: Model Development. *JAWRA*, 34(1):73–89.

Asfaw, A., Simane, B., Hassen, A., and Bantider, A. (2018). Variability and time series trend analysis of rainfall and temperature in northcentral Ethiopia: A case study in Woleka sub-basin. *Weather and Climate Extremes*, 19:29–41.

Awass, A. A. (2009). *Hydrological Drought Analysis-occurrence, severity, risks: the case of Wabi Shebele River Basin, Ethiopia*. PhD thesis, Universit¨at Siegen, Germany.

Awulachew, S. B., Yilma, A. D., Loulseged, M., Loiskandl, W., Ayana, M., and Alamirew, T. (2007). Water Resources and Irrigation Development in Ethiopia. Technical report, International Water Management Institute, Colombo, Sri Lanka.

Ayana, A. B., Edossa, D. C., and Kositsakulchai, E. (2012). Simulation of Sediment Yield Using SWAT Model in Fincha Watershed, Ethiopia. *Kasetsart Journal - Natural Science*, 46(2):283–297.

Ayele, H. S., Li, M. H., Tung, C. P., and Liu, T. M. (2016). Impact of climate change on runoff in the Gilgel Abbay watershed, the upper Blue Nile Basin, Ethiopia. *Water (Switzerland)*, 8(9).

Baig, M. F., Mustafa, M. R. U., Baig, I., Takaijudin, H. B., and Zeshan, M. T. (2022). Assessment of Land Use Land Cover Changes and Future Predictions Using CA-ANN Simulation for Selangor, Malaysia. *Water (Switzerland)*, 14(3).

Bayable, G., Amare, G., Alemu, G., and Gashaw, T. (2021). Spatiotemporal variability and trends of rainfall and its association with Pacific Ocean Sea surface temperature in West Harerge Zone, Eastern Ethiopia. *Environmental Systems Research*, 10(1).

Bekele-Tesemma, A. (2007). Useful trees and shrubs for Ethiopia: identification, propagation and management in 17 agro-ecological zones. Technical report, RELMA in ICRAF Project, Nairobi.

Belay Tegene (2002). Land-Cover/Land-Use Changes in the Derekolli Catchment of the South Welo Zone of Amhara Region, Ethiopia. *Eastern Africa Social Science Research Review*, 18(1):1–20.

Bentsen, M., Oliviè, D. J. L., Seland, Ø., Toniazzo, T., Gjermundsen, A., Graff, L. S., Debernard, J. B., Gupta, A. K., He, Y., Kirkevåg, A., Schwinger, J., Tjiputra, J., Aas, K. S., Bethke, I., Fan, Y., Griesfeller, J., Grini, A., Guo, C., Ilicak, M., Karset, I. H. H., Landgren, O. A., Liakka, J., Moseid, K. O., Nummelin, A., Spensberger, C., Tang, H., Zhang, Z., Heinze, C., Iversen, T., and Schulz, M. (2019). NCC NorESM2-MM model output prepared for CMIP6 CMIP Historical, ssp126; ssp245; ssp370; ssp585. v20191108. *Earth System Grid Federation*.

Berg, P., Bosshard, T., Yang, W., and Zimmermann, K. (2022). MIdASv0.2.1 - MultI-scale bias AdjuStment. *Geoscientific Model Development*, 15(15):6165–6180.

Berhane, A., Hadgu, G., Worku, W., and Abrha, B. (2020). Trends in extreme temperature and rainfall indices in the semi-arid areas of Western Tigray, Ethiopia. *Environmental Systems Research*, 9(1).

Berhanu, B., Seleshi, Y., and Melesse, A. M. (2013). SurfaceWater and Groundwater Resources of Ethiopia: Potentials and Challenges ofWater Resources Development. In Melesse, A. M., Abtew, W., and Setegn, S. G., editors, *Nile River Basin: Ecohydrological Challenges, Climate Change and Hydropolitics*, number June 2018, pages 1–718.

Betrie, G. D., Mohamed, Y. A., Van Griensven, A., Popescu, I., and Mynett, A. (2009). Modeling of soil erosion and sediment transport in the Blue Nile Basin using the Open Model Interface

Approach. In *Improved Water and Land Management in the Ethiopian Highlands: Its Impact on Downstream Stakeholders Dependent on the Blue Nile*, page 132.

Betrie, G. D., Mohamed, Y. A., Van Griensven, A., and Srinivasan, R. (2011). Sediment management modelling in the Blue Nile Basin using SWAT model. *Hydrology and Earth System Sciences*, 15(3):807–818.

Betru, T., Tolera, M., Sahle, K., and Kassa, H. (2019). Trends and drivers of land use/land cover change in Western Ethiopia. *Applied Geography*, 104(August 2018):83–93.

Beyene, A. N. (2015). Precipitation and Temperature Trend Analysis in Mekelle city, Northern Ethiopia, the Case of Illala Meteorological Station. *Journal of Earth Science and Climatic Change*, 07(01):46–52.

Birhanu, A., Masih, I., van der Zaag, P., Nyssen, J., and Cai, X. (2019). Impacts of land use and land cover changes on hydrology of the Gumara catchment, Ethiopia. *Physics and Chemistry of the Earth*, 112:165–174.

Bracmort, K. S., Arabi, M., Frankenberger, J. R., Engel, B. A., and Arnold, J. G. (2006). Modeling long-term water quality impact of structural BMPs. *Transactions of the ASABE*, 49(2):367–374.

Cannon, A. J., Sobie, S. R., and Murdock, T. Q. (2015). Bias correction of GCM precipitation by quantile mapping: How well do methods preserve changes in quantiles and extremes? *Journal of Climate*, 28(17):6938–6959.

Chaemiso, S. E., Abebe, A., and Pingale, S. M. (2016). Assessment of the impact of climate change on surface hydrological processes using SWAT: a case study of Omo-Gibe river basin, Ethiopia. *Modeling Earth Systems and Environment*, 2(4):1–15.

Chaplot, V. (2014). Impact of spatial input data resolution on hydrological and erosion modeling: Recommendations from a global assessment. *Physics and Chemistry of the Earth*, 67-69:23–35.

Chattopadhyay, S. and Edwards, D. R. (2016). Long-term trend analysis of precipitation and air temperature for Kentucky, United States. *Climate*, 4(1).

Chekol, D. A., Tischbein, B., Eggers, H., and Vlek, P. (2007). Application of SWAT for assessment of spatial distribution of water resources and analyzing impact of different land management practices on soil erosion in Upper Awash River Basin watershed. *Water Resources*, pages 110–117.

Chen, E. and Mackay, D. S. (2004). Effects of distribution-based parameter aggregation on a spatially distributed agricultural nonpoint source pollution model. *Journal of Hydrology*, 295(1-4):211–224.

Cheung, W. H., Senay, G. B., and Singh, A. (2008). Trends and spatial distribution of annual and seasonal rainfall in Ethiopia. *International Journal of Climatology*, 28:1723–1734.

Cochard, F., Loukos, H., and Noël, T. (2018). Technical Report: Bias Adjusting Climate Model Projections. Technical report.

Collaud Coen, M., Andrews, E., Bigi, A., Martucci, G., Romanens, G., Vogt, F. P., and Vuilleumier, L. (2020). Effects of the prewhitening method, the time granularity, and the time segmentation on the Mann-Kendall trend detection and the associated Sen's slope. *Atmospheric Measurement Techniques*, 13(12):6945–6964.

Congalton, R. G. (1991). A review of assessing the accuracy of classifications of remotely sensed data. *Remote Sensing of Environment*, 37(1):35–46.

Congalton, R. G. (2005). Thematic and Positional Accuracy Assessment of Digital Remotely Sensed Data. *2005 Proceedings of the Seventh Annual Forest Inventory and Analysis Symposium*, (1993):149–154.

Congedo, L. (2021). Semi-Automatic Classification Plugin: A Python tool for the download and processing of remote sensing images in QGIS. *Journal of Open Source Software*, 6(64):1–225.

Degefu, M. A., Alamirew, T., Zeleke, G., and Bewket, W. (2019). Detection of trends in hydrological extremes for Ethiopian watersheds, 1975–2010. *Regional Environmental Change*, 19(7):1923–1933.

Degefu, M. A. and Bewket, W. (2015). Trends and spatial patterns of drought incidence in the Omo-Ghibe River Basin, Ethiopia. *Geografiska Annaler, Series A: Physical Geography*, 97(2):395–414.

Degefu, M. A. and Bewket, W. (2017). Variability, trends, and teleconnections of stream flows with large-scale climate signals in the Omo-Ghibe River Basin, Ethiopia. *Environmental Monitoring and Assessment*, 189(4).

Dekkers, J. and Koomen, E. (2005). Simulations of Future Land Use or Water Management: Assessing the Suitability for Scenario-Based Modelling. In *45th congress of the European Regional Science Association*.

Descroix, L. and Amogu, O. (2012). Consequences of Land Use Changes on Hydrological Functioning. In Nayak, P., editor, *Water Resources Management and Modeling*. InTech, Rijeka, Croatia.

Devia, G. K., Ganasri, B., and Dwarakish, G. (2015). A Review on Hydrological Models. *Aquatic Procedia*, 4(Icwrcoe):1001–1007.

Dong, N., Liu, Z., Luo, M., Fang, C., and Lin, H. (2019). The Effects of Anthropogenic Land Use Changes on Climate in China Driven by Global Socioeconomic and Emission Scenarios. *Earth's Future*, 7(7):784–804.

Dwarakish, G. and Ganasri, B. (2015). Impact of land use change on hydrological systems: A review of current modeling approaches. *Cogent Geoscience*, 1(1):1115691.

EC-Earth, E.-E. C. (2019a). EC-Earth-Consortium EC-Earth3 model output prepared for CMIP6 ScenarioMIP Historical, ssp126, ssp245, ssp370, ssp585. v20200310. *Earth System Grid Federation*.

EC-Earth, E.-E. C. (2019b). EC-Earth-Consortium EC-Earth3-Veg model output prepared for CMIP6 ScenarioMIP Historical, ssp126, ssp245, ssp370, ssp585. v20200225. *Earth System Grid Federation*.

Elzopy, K. A., Chaturvedi, A. K., Chandran, K. M., Gopinath, G., Naveena, K., and Surendran, U. (2021). Trend analysis of long-term rainfall and temperature data for Ethiopia. *South African Geographical Journal*.

Engida, T. G., Nigussie, T. A., Aneseyee, A. B., and Barnabas, J. (2021). Land Use/Land Cover Change Impact on Hydrological Process in the Upper Baro Basin, Ethiopia. *Applied and Environmental Soil Science*, 2021.

Esayas, B., Simane, B., Teferi, E., Ongoma, V., and Tefera, N. (2018). Trends in extreme climate events over three agroecological zones of Southern Ethiopia. *Advances in Meteorology*, 2018.

Eshetu, M. (2020). Hydro-Climatic Variability and Trend Analysis of Modjo River Watershed , Awash River Basin of Ethiopia. *Hydrology: Current Research*, 11(2):1–8.

FAO (2016). *The state of food and agriculture: Climate Change, Agriculture and Food Security*. Rome.

Flato, G., Marotzke, J., Abiodun, B., Braconnot, P., Chou, S. C., Collins, W., Cox, P., Driouech, F., Emori, S., Eyring, V., Forest, C., Gleckler, P., Guilyardi, E., Jakob, C., Kattsov, V., Reason,

C., and Rummukainen, M. (2013). Evaluation of Climate Models. In: Climate Change 2013: The Physical Science Basis. Contribution of Working Group I to the Fifth Assess- ment Report of the Intergovernmental Panel on Climate Change [Stocker, T.F., D. Qin, G.-K. Plattner, M. Tignor, S.K. Al. Technical report.

Folle, S., Dalzell, B., Mulla, D., and Birr, A. (2007). Evaluation of Best Management Practices (BMPs) in Impaired Watersheds Using the SWAT Model. Technical report, Department of Soil, Water and Climate. University of Minnesota, Minnesota.

Foody, G. M. (2002). Status of land cover classification accuracy assessment. *Remote Sensing of Environment*, 80:105–118.

Garedew, E., Sandewall, M., Söderberg, U., and Campbell, B. M. (2009). Land-use and land-cover dynamics in the central rift valley of ethiopia. *Environmental Management*, 44(4):683–694.

Gashaw, T., Tulu, T., Argaw, M., and Worqlul, A. W. (2017). Evaluation and prediction of land use/land cover changes in the Andassa watershed, Blue Nile Basin, Ethiopia. *Environmental Systems Research*, 6(1).

Gassman, P. W., Reyes, M. R., Green, C. H., and Arnold, J. G. (2007). The Soil and Water Assessment Tool: Historical Development, Applications, and Future Research Directions. *Transactions of the ASABE*, 50(4):1211–1250.

Gauthier, T. D. (2001). Detecting trends using Spearman's rank correlation coefficient. *Environmental Forensics*, 2(4):359–362.

Gebrehiwot, T. (2013). Assessing the evidence of climate variability in the northern part of Ethiopia. *Journal of Development and Agricultural Economics*, 5(3):104–119.

Gebreyohannes, T., De Smedt, F., Walraevens, K., Gebresilassie, S., Hussien, A., Hagos, M., Amare, K., Deckers, J., and Gebrehiwot, K. (2013). Application of a spatially distributed water balance model for assessing surface water and groundwater resources in the Geba basin, Tigray, Ethiopia. *Journal of Hydrology*, 499:110–123.

Gedefaw, M., Yan, D., Wang, H., Qin, T., Girma, A., Abiyu, A., and Batsuren, D. (2018). Innovative trend analysis of annual and seasonal rainfall variability in Amhara Regional State, Ethiopia. *Atmosphere*, 9(9).

Gessesse, A. A., Melesse, A. M., Abera, F. F., and Abiy, A. Z. (2019). Modeling Hydrological Responses to Land Use Dynamics, Choke, Ethiopia. *Water Conservation Science and Engineering*, 4(4):201–212.

Getahun, Y. S. and Haj, V. L. (2015). Assessing the Impacts of Land Use-Cover Change on Hydrology of Melka Kuntrie Subbasin in Ethiopia, Using a Conceptual Hydrological Model. *Journal of Waste Water Treatment and Analysis*, 06(03).

Giorgi, F., Jones, C., and Asrar, G. (2009). Addressing climate information needs at the regional level: the CORDEX framework. *World Meteorological Organization (WMO) Bulletin*, 58:175–183.

Girma, R., Fürst, C., and Moges, A. (2022). Land use land cover change modeling by integrating artificial neural network with cellular Automata-Markov chain model in Gidabo river basin, main Ethiopian rift. *Environmental Challenges*, 6(December 2021):100419.

Goldewijk, K. K. and Ramankutty, N. (2004). Land cover change over the last three centuries due to human activities : The availability of new global data sets. *GeoJournal*, 61(4):335–344.

Gudmundsson, L. (2016). Statistical Transformations for Post-Processing Climate Model Output (qmap).

Gudmundsson, L., Bremnes, J. B., Haugen, J. E., and Engen-Skaugen, T. (2012). Technical Note: Downscaling RCM precipitation to the station scale using statistical transformations; A comparison of methods. *Hydrol. Earth Syst. Sci.*, 16:3383–3390.

Gupta, H. V., Kling, H., Yilmaz, K. K., and Martinez, G. F. (2009). Decomposition of the mean squared error and NSE performance criteria: Implications for improving hydrological modelling. *Journal of Hydrology*, 377(1-2):80–91.

Gupta, H. V., Sorooshian, S., and Yapo, P. O. (1999). Status of Automatic Calibration for Hydrologic Models: Comparison with Multilevel Expert Calibration. *J. Hydrol. Eng.*, 4(2):135–143.

Gurara, M. A., Jilo, N. B., and Tolche, A. D. (2021). Modelling climate change impact on the streamflow in the Upper Wabe Bridge watershed in Wabe Shebele River Basin, Ethiopia. *International Journal of River Basin Management*, 0(0):1–13.

Haile, A. T., Asfaw, W., Rientjes, T., and Worako, A. W. (2022). Deterioration of streamflow monitoring in Omo-Gibe basin in Ethiopia. *Hydrological Sciences Journal*, 67(7):1040–1053.

Hailemariam, S. N., Soromessa, T., and Teketay, D. (2016). Land use and land cover change in the bale mountain eco-region of Ethiopia during 1985 to 2015. *Land*, 5(4).

Hamed, K. H. (2009). Enhancing the effectiveness of prewhitening in trend analysis of hydrologic data. *Journal of Hydrology*, 368(1-4):143–155.

Hamed, K. H. and Rao, A. R. (1998). A modified Mann-Kendall trend test for autocorrelated data. *Journal of Hydrology*, 204:182–196.

Hänsel, S., Schucknecht, A., and Matschullat, J. (2016). The Modified Rainfall Anomaly Index (mRAI)—is this an alternative to the Standardised Precipitation Index (SPI) in evaluating future extreme precipitation characteristics? *Theoretical and Applied Climatology*, 123(3-4):827–844.

Harka, A. E., Jilo, N. B., and Behulu, F. (2021). Spatial-temporal rainfall trend and variability assessment in the Upper Wabe Shebelle River Basin, Ethiopia: Application of innovative trend analysis method. *Journal of Hydrology: Regional Studies*, 37:100915.

Hesse, C., Krysanova, V., Stefanova, A., Bielecka, M., and Domnin, D. A. (2015). Assessment of climate change impacts on water quantity and quality of the multi-river Vistula Lagoon catchment. *Hydrological Sciences Journal*, 60(5):890–911.

Hu, X., Huang, B., and Cherubini, F. (2019). Impacts of idealized land cover changes on climate extremes in Europe. *Ecological Indicators*, 104(August 2018):626–635.

IPCC (2001). Climate Change 2001: Synthesis Report. A Contribution of Working Groups I, II, and III to the Third Assessment Report of the Integovernmental Panel on Climate Change [Watson, R.T. and the Core Writing Team (eds.)]. Technical report, IPCC, Cambridge University Press, Cambridge, United Kingdom, and New York, NY, USA.

IPCC (2007). Climate Change 2007: Synthesis Report. Contribution of Working Groups I, II and III to the Fourth Assess- ment Report of the Intergovernmental Panel on Climate Change. Technical report, IPCC, Geneva, Switzerland.

IPCC (2014a). Climate Change 2014: Impacts, Adaptation, and Vulnerability; Part a: Global and Sectoral Aspects. Contribution of Working Group II to the Fifth Assessment Report of the Intergovernmental Panel on Climate Change. Technical report, IPCC, Cambridge University Press, Cambridge, United Kingdom and New York, NY, USA.

IPCC (2014b). Climate Change 2014: Synthesis Report. Contribution of Working Groups I, II and III to the Fifth Assessment Report of the Intergovernmental Panel on Climate Change [Core Writing Team, R.K. Pachauri and L.A. Meyer (eds.)]. Technical report, IPCC, Geneva, Switzerland.

IPCC (2014c). Mitigation of Climate Change. Contribution of Working Group III to the Fifth Assessment Report of the Intergovernmental Panel on Climate Change [Edenhofer, O., R. Pichs-Madruga, Y. Sokona, E. Farahani, S. Kadner, K. Seyboth, A. Adler, I. Baum, S. Brunner,. Technical report, IPCC, Cambridge University Press, Cambridge, United Kingdom and New York, NY, USA.

IPCC (2019). IPCC Special Report on Climate Change, Desertification, Land Degradation, Sustainable Land Management, Food Security, and Greenhouse gas fluxes in Terrestrial Ecosystems. Technical report, IPCC.

IPCC (2021a). Regional fact sheet - Africa. Technical report, IPCC.

IPCC (2021b). Summary for Policymakers. In: Climate Change 2021: The Physical Science Basis. Contribution of Working Group I to the Sixth Assessment Report of the Intergovernmental Panel on Climate Change [Masson-Delmotte, V., P. Zhai, A. Pirani, S. L. Connors, C. Péan. Technical report, Cambridge University Press. In Press.

Islam, M. Y., Nasher, N. M., Karim, K. H., and Rashid, K. J. (2023). Quantifying forest land-use changes using remote-sensing and CA-ANN model of Madhupur Sal Forests, Bangladesh. *Heliyon*, 9(5):e15617.

Jenness, J. and Wynne, J. J. (2007). Kappa analysis (kappastats.avx) extension for ArcView 3.x. Jenness Enterprises.

John, J. G., Blanton, C., McHugh, C., Radhakrishnan, A., Rand, K., Vahlenkamp, H., Wilson, C., Zadeh, N. T., Dunne, J. P., Dussin, R., Horowitz, L. W., Krasting, J. P., Lin, P., Malyshev, S., Naik, V., Ploshay, J., Shevliakova, E., Silvers, L., Stock, C., Winton, M., and Zeng, Y. (2018). NOAA-GFDL GFDL-ESM4 model output prepared for CMIP6 ScenarioMIP Historical, ssp126, ssp245, ssp370, ssp585. v20180701. *Earth System Grid Federation*.

Kafy, A. ., Naim, M. N. H., Subramanyam, G., Faisal, A. A., Ahmed, N. U., Rakib, A. A., Kona, M. A., and Sattar, G. S. (2021). Cellular Automata approach in dynamic modelling of land cover changes using RapidEye images in Dhaka, Bangladesh. *Environmental Challenges*, 4(January):100084.

Kale, S. and Sönmez, A. Y. (2019). Trend Analysis for Streamflow of Devrekani Stream (Turkey). *Review of Hydrobiology*, 12(1-2):23–37.

Kamaraj, M. and Rangarajan, S. (2022). Predicting the future land use and land cover changes for Bhavani basin, Tamil Nadu, India, using QGIS MOLUSCE plugin. *Environmental Science and Pollution Research*, 29(57):86337–86348.

Kenea, U., Adeba, D., Regasa, M. S., and Nones, M. (2021). Hydrological Responses to Land Use Land Cover Changes in the Fincha'a Watershed, Ethiopia. *Land*, 10(9):916.

Kim, C. (2016). Land Use Classification and Land Use Change Analysis Using Satellite Images in Lombok Island, Indonesia. *Forest Science and Technology*, 12(4):183–191.

Kim, U. and Kaluarachchi, J. J. (2009). Climate change impacts on water resources in the upper Blue Nile River Basin, Ethiopia. *Journal of the American Water Resources Association*, 45(6):1361–1378.

Kirsch, K. J. (2002). Predicting sediment and phosphorus loads in the rock river basin using swat. *ASAE Annual Intenational Meeting, Technical Papers: Engineering Solutions for a New Century*, 45(6):1757–1769.

Kling, H., Fuchs, M., and Paulin, M. (2012). Runoff conditions in the upper Danube basin under an ensemble of climate change scenarios. *Journal of Hydrology*, 424-425:264–277.

Knoben, W. J. M., Freer, J. E., and Woods, R. (2019). Technical note: Inherent benchmark or not? Comparing Nash-Sutcliffe and Kling-Gupta efficiency scores. *Hydrology and Earth System Sciences*, 23(10):4323–4331.

Krause, P., Boyle, D. P., and Bäse, F. (2005). Comparison of different efficiency criteria for hydrological model assessment. *Advances in Geosciences*, 5:89–97.

Lambin, E. F., Geist, H. J., and Lepers, E. (2003). Dynamics of land-use and land-cover change in tropical regions. *Annual Review of Environment and Resources*, 28:205–241.

Lee, T., Srinivasan, R., Moon, J., and Omani, N. (2011). Estimation of fresh water inflow to bays from gaged and ungaged watersheds. *Applied Engineering in Agriculture*, 27(6):917–923.

Leta, O. T., El-Kadi, A. I., Dulai, H., and Ghazal, K. A. (2016). Assessment of climate change impacts on water balance components of Heeia watershed in Hawaii. *Journal of Hydrology: Regional Studies*, 8:182–197.

Liew, M. W. V. and Garbrecht, J. (2003). Hydrologic Simulation of the Little Washita River Experimental Watershed Using SWAT. *Journal of the American Water Resources Association (JAWRA)*, 39(2):413–426.

Llano, X. C. (2022). SMByC-IDEAM. AcATaMa - QGIS plugin for Accuracy Assessment of Thematic Maps, version 22.5.

Lovato, T., Peano, D., and Butenschön, M. (2021). CMCC CMCC-ESM2 model output prepared for CMIP6 ScenarioMIP Historical, ssp126, ssp245, ssp370, ssp585. v20210126. *Earth System Grid Federation*.

Loveland, T. R. and Dwyer, J. L. (2012). Landsat: Building a strong future. *Remote Sensing of Environment*, 122(October 2000):22–29.

Lukas, P., Melesse, A. M., and Kenea, T. T. (2023). Prediction of Future Land Use/Land Cover Changes Using a Coupled CA-ANN Model in the Upper Omo–Gibe River Basin, Ethiopia. *Remote Sensing*, 15(4).

Manandhar, R., Odehi, I. O., and Ancevt, T. (2009). Improving the accuracy of land use and land cover classification of landsat data using post-classification enhancement. *Remote Sensing*, 1(3):330–344.

Mango, L. M., Melesse, A. M., McClain, M. E., Gann, D., and Setegn, S. G. (2011). Land use and climate change impacts on the hydrology of the upper Mara River Basin, Kenya: Results of a modeling study to support better resource management. *Hydrology and Earth System Sciences*, 15(7):2245–2258.

Mann, H. B. (1945). Non-Parametric Test Against Trend. *Econometrica*, 13(3):245–259.

Maraun, D. (2016). Bias Correcting Climate Change Simulations - a Critical Review. *Current Climate Change Reports*, 2:211–220.

Markos, M. G., Mihret, D. U., Teklu, E. J., and Getachew, M. G. (2018). Influence of land use and land cover changes on ecosystem services in the Bilate Alaba Sub-watershed, Southern Ethiopia. *Journal of Ecology and The Natural Environment*, 10(9):228–238.

Marshall, E. and Randhir, T. O. (2008). Spatial modeling of land cover change and watershed response using Markovian cellular automata and simulation. *Water Resources Research*, 44(4):1–11.

Memarian, H., Balasundram, S. K., Abbaspour, K. C., Talib, J. B., Boon Sung, C. T., and Sood, A. M. (2014). SWAT-based hydrological modelling of tropical land-use scenarios. *Hydrological Sciences Journal*, 59(10):1808–1829.

Merritt, W. S., Letcher, R. A., and Jakeman, A. J. (2003). A review of erosion and sediment transport models. *Environmental Modelling and Software*, 18(8-9):761–799.

Meshesha, T. W., Tripathi, S. K., and Khare, D. (2016). Analyses of land use and land cover change dynamics using GIS and remote sensing during 1984 and 2015 in the Beressa Watershed Northern Central Highland of Ethiopia. *Modeling Earth Systems and Environment*, 2(4):1–12.

Meyer, W. B. and Turner, B. L. (1992). Human Population Growth and Global Land-Use/Cover Change. *Annual Review of Ecology and Systematics*, 23(1992):39–61.

Moriasi, D. N., Gitau, M. W., Pai, N., and Daggupati, P. (2015). Hydrologic and water quality models: Performance measures and evaluation criteria. *Transactions of the ASABE*, 58(6):1763–1785.

Muleta, M. K. and Nicklow, J. W. (2005). Sensitivity and uncertainty analysis coupled with automatic calibration for a distributed watershed model. *Journal of Hydrology*, 306:127–145.

Muluneh, A. (2010). Synthesis of Research on Land Use and Land Cover. *UNU-Land Restoration Training Programme*, pages 1–39.

Näschen, K., Diekkrüger, B., Evers, M., Höllermann, B., Steinbach, S., and Thonfeld, F. (2019). The Impact of Land Use/Land Cover Change (LULCC) on Water Resources in a Tropical Catchment in Tanzania under Different Climate Change Scenarios. *Sustainability (Switzerland)*, 11(24).

Nash, J. E. and Sutcliffe, J. V. (1970). River flow forecasting through conceptual models part I - A discussion of principles. *Journal of Hydrology*, 10(3):282–290.

National Planning Commission (2016). Growth and Transformation Plan II (GTP II). Technical report, National Planning Commission, Addis Ababa.

Navarro-Racines, C., Tarapues-Montenegro, J., and Ramírez-Villegas, J. (2015). Bias-correction in the CCAFS-Climate Portal: A description of methodologies. Decision and Policy Analysis (DAPA) Research Area. Technical report, International Center for Tropical Agriculture (CIAT), Cali, Colombia.

Negewo, T. F. and Sarma, A. K. (2021). Estimation of Water Yield under Baseline and Future Climate Change Scenarios in Genale Watershed, Genale Dawa River Basin, Ethiopia, Using SWAT Model. *Journal of Hydrologic Engineering*, 26(3):1–13.

Neitsch, S., Arnold, J., Kiniry, J., and Williams, J. (2011). Soil and Water Assessment Tool Theoretical Documentation Version 2009. *Texas Water Resources Institute*, pages 1–647.

NextGIS (2017). Modules for Land Use Change Evaluation (MOLUSCE): Quick Help.

NMSA (2007). Climate Change National Adaptation Programme of Action (NAPA) of Ethiopia. Technical report, NATIONAL METEOROLOGICAL AGENCY, ADDIS ABABA ETHIOPIA.

Olofsson, P., Foody, G. M., Herold, M., Stehman, S. V., Woodcock, C. E., and Wulder, M. A. (2014). Good practices for estimating area and assessing accuracy of land change. *Remote Sensing of Environment*, 148:42–57.

O'Neill, B. C., Tebaldi, C., Van Vuuren, D. P., Eyring, V., Friedlingstein, P., Hurtt, G., Knutti, R., Kriegler, E., Lamarque, J. F., Lowe, J., Meehl, G. A., Moss, R., Riahi, K., and Sanderson, B. M. (2016). The Scenario Model Intercomparison Project (ScenarioMIP) for CMIP6. *Geoscientific Model Development*, 9(9):3461–3482.

Owuor, S. O., Butterbach-Bahl, K., Guzha, A. C., Rufino, M. C., Pelster, D. E., Díaz-Pinés, E., and Breuer, L. (2016). Groundwater recharge rates and surface runoff response to land use and land cover changes in semi-arid environments. *Ecological Processes*, 5(1).

Patakamuri, S. K. and O'Brien, N. (2021). Modified Versions of Mann Kendall and Spearman's Rho Trend Tests; Package 'modifiedmk'.

Pechlivanidis, I. G., Jackson, B. M., Mcintyre, N. R., and Wheater, H. S. (2011). Catchment scale hydrological modelling: A review of model types, calibration approaches and uncertainty analysis methods in the context of recent developments in technology and applications. *Global Nest Journal*, 13(3):193–214.

Pettitt, A. N. (1979). A Non-Parametric Approach to the Change-Point Problem. *Journal of the Royal Statistical Society. Series C (Applied Statistics)*, 28(2):126–135.

Pikounis, M., Varanou, E., Baltas, E., Dassaklis, A., and Mimikou, M. (2003). Application of the SWAT model in the Pinios river basin under different land-use scenarios. *Global NEST Journal*, 5(2):71–79.

Probst, E. and Mauser, W. (2023). Climate Change Impacts on Water Resources in the Danube River Basin: A Hydrological Modelling Study Using EURO-CORDEX Climate Scenarios. *Water (Switzerland)*, 15(1).

Refsgaard, J. (1996). Terminology, Modelling Protocol and Classification of Hydrological Model Codes. In Abbott, M. B. and Refsgaard, J. C., editors, *Distributed hydrological modelling*, chapter CHAPTER 2. Kluwer Academic Publishers, DORDRECHT / BOSTON / LONDON, volume 22 edition.

Refsgaard, J. C. (1997). Parameterisation, calibration and validation of distributed hydrological models. *Journal of Hydrology*, 198(1-4):69–97.

Refsgaard, J. C. and Henriksen, H. J. (2004). Modelling guidelines - Terminology and guiding principles. *Advances in Water Resources*, 27(1):71–82.

Reis, S. (2008). Analyzing land use/land cover changes using remote sensing and GIS in Rize, North-East Turkey. *Sensors*, 8(10):6188–6202.

Reusing, M. (2000). Change Detection of Natural High Forests in Ethiopia Using Remote Sensing and GIS Techniques. *International Archives of Photogrammetry and Remote Sensing*, 33:1253–1258.

Richards, J. A. and Jia, X. (2006). *Remote sensing digital image analysis: An introduction*. Springer-Verlag Berlin Heidelberg, 4th edition.

Rwanga, S. S. and Ndambuki, J. M. (2017). Accuracy Assessment of Land Use/Land Cover Classification Using Remote Sensing and GIS. *International Journal of Geosciences*, 08(04):611–622.

Santhi, C., Srinivasan, R., Arnold, J. G., and Williams, J. R. (2006). A modeling approach to evaluate the impacts of water quality management plans implemented in a watershed in Texas. *Environmental Modelling and Software*, 21:1141–1157.

Schuol, J., Abbaspour, K. C., Yang, H., Srinivasan, R., and Zehnder, A. J. (2008). Modeling blue and green water availability in Africa. *Water Resources Research*, 44(7):1–18.

Schupfner, M., Wieners, K.-H., Wachsmann, F., Steger, C., Bittner, M., Jungclaus, J., Früh, B., Pankatz, K., Giorgetta, M., Reick, C., Legutke, S., Esch, M., Gayler, V., Haak, H., de Vrese, P., Raddatz, T., Mauritsen, T., von Storch, J.-S., Behrens, J., Brovkin, V., Claussen, M., Crueger,

T., Fast, I., Fiedler, S., Hagemann, S., Hohenegger, C., Jahns, T., Kloster, S., Kinne, S., Lasslop, G., Kornblueh, L., Marotzke, J., Matei, D., Meraner, K., Mikolajewicz, U., Modali, K., Müller, W., Nabel, J., Notz, D., Peters-von Gehlen, K., Pincus, R., Pohlmann, H., Pongratz, J., Rast, S., Schmidt, H., Schnur, R., Schulzweida, U., Six, K., Stevens, B., Voigt, A., and Roeckner, E. (2019). DKRZ MPI-ESM1.2-HR model output prepared for CMIP6 ScenarioMIP Historical, ssp126, ssp245, ssp370, ssp585. v20190710. *Earth System Grid Federation*.

Sen, P. K. (1968). Estimates of the Regression Coefficient Based on Kendall's Tau. *Journal of the American Statistical Association*, 63(324):1379–1389.

Setegn, S. G., Rayner, D., Melesse, A. M., Dargahi, B., and Srinivasan, R. (2011a). Impact of Climate Change on the Hydroclimatology of Lake Tana Basin, Ethiopia. *Water Resources Research*, 47:1–13.

Setegn, S. G., Rayner, D., Melesse, A. M., Dargahi, B., Srinivasan, R., and Wörman, A. (2011b). Climate Change Impact on Agricultural Water Resources Variability in the Northern Highlands of Ethiopia. In *Nile River Basin*, pages 241–265. Springer Netherlands, Dordrecht.

Setegn, S. G., Srinivasan, R., and Dargahi, B. (2008). Hydrological Modelling in the Lake Tana Basin, Ethiopia Using SWAT Model. *The Open Hydrology Journal*, 2(1):49–62.

Setegn, S. G., Srinivasan, R., Dargahi, B., and Melesse, A. M. (2009). Spatial delineation of soil erosion vulnerability in the Lake Tana Basin, Ethiopia. *Hydrological Processes*, 2274.

Shawul, A. A. and Chakma, S. (2019). Spatiotemporal detection of land use/land cover change in the large basin using integrated approaches of remote sensing and GIS in the Upper Awash basin, Ethiopia. *Environmental Earth Sciences*, 78:141.

Shawul, A. A. and Chakma, S. (2020). Trend of extreme precipitation indices and analysis of long-term climate variability in the Upper Awash basin, Ethiopia. *Theoretical and Applied Climatology*, 140(1-2):635–652.

Singh, A. (2018). A Concise Review on Introduction to Hydrological Models. *Global Research and Development Journal for Engineering*, 3(10):14–19.

Sitterson, J., Knightes, C., Parmar, R., Wolfe, K., Wolfe, K., and Avant, B. (2017). An Overview of Rainfall-Runoff Model Types An Overview of Rainfall-Runoff Model Types. Technical report, U.S. Environmental Protection Agency (EPA), Athens, Georgia.

Srinivasan, R., Ramanarayanan, T., Arnold, J. G., and Bednarz, S. (1998). Large Area Hydrologic Modeling and Assessment Part II: Model Application. *JAWRA*, 34(1):91–101.

Srinivasan, R., Zhang, X., and Arnold, J. (2010). SWAT ungauged: Hydrological budget and crop yield predictions in the upper Mississippi River basin. *Transactions of the ASABE*, 53(5):1533–1546.

Stehman, S. V. and Czaplewski, R. L. (1998). Design and Analysis for Thematic Map Accuracy Assessment - an application of satellite imagery. *Remote Sensing of Environment*, 64(January):331–344.

Swarna Latha, P. and Rao, K. N. (2020). Assessment of Land Use and Land Cover Changes (1988-2020) through NDVI Analysis and Geospatial Techniques. *International Journal of Research and Review (ijrrjournal.com)*, 7(December):12.

Tadese, M. T., Kumar, L., Koech, R., and Zemadim, B. (2019). Hydro-climatic variability: A characterisation and trend study of the Awash River Basin, Ethiopia. *Hydrology*, 6(2).

Taye, M., Simane, B., Zaitchik, B. F., Selassie, Y. G., and Setegn, S. (2019). Rainfall Variability Across the Agro-Climatic Zones of a Tropical Highland: the Case of the Jema Watershed, Northwestern Ethiopia. *Environments - MDPI*, 6(11).

Taye, M. T., Dyer, E., Hirpa, F. A., and Charles, K. (2018). Climate change impact on water resources in the Awash basin, Ethiopia. *Water (Switzerland)*, 10(11):1–16.

Tekleab, S., Mohamed, Y., and Uhlenbrook, S. (2013). Hydro-climatic trends in the Abay/Upper Blue Nile basin, Ethiopia. *Physics and Chemistry of the Earth*, 61-62:32–42.

Tempfli, K., Kerle, N., Huurneman, G. C., Janssen, L. L. F., Bakker, W. H., Feringa, W., Gieske, A. S. M., Gorte, B. G. H., Grabmaier, K. A., Hecker, C. A., Horn, J. A., Huurneman, G. C., Janssen, L. L. F., Kerle, N., Meer, F. D. V. D., Parodi, G. N., Pohl, C., Reeves, C. V., Ruitenbeek, F. J. V., Schetselaar, E. M., Tempfli, K., Weir, M. J. C., Westinga, E., and Woldai, T. (2013). *Principles of Remote Sensing: An introductory textbook*. The International Institute for Geo-Information Science and Earth Observation (ITC), Enschede, The Netherlands, 4th edition.

Tesfaye, S., Raj, A. J., and Geberesamuel, G. (2014). Assessment of Climate Change Impact on the Hydrology of Geba Catchment , Northern Ethiopia. *American Journal of Environmental Engineering*, 4(2):25–31.

Teshome, A. and Zhang, J. (2019). Increase of extreme drought over Ethiopia under climate warming. *Advances in Meteorology*, 2019.

Teutschbein, C. and Seibert, J. (2012). Bias correction of regional climate model simulations for hydrological climate-change impact studies: Review and evaluation of different methods. *Journal of Hydrology*, 456-457:12–29.

Tuppad, P., Mankin, K. R. D., Lee, T., Srinivasan, R., and Arnold, J. G. (2011). Soil and Water Assessment Tool (SWAT) Hydrologic/Water Quality Model: Extended Capability and Wider Adoption. *Transactions of the ASABE*, 54:1677–1684.

van Griensven, A., Meixner, T., Grunwald, S., Bishop, T., Diluzio, M., and Srinivasan, R. (2006). A global sensitivity analysis tool for the parameters of multi-variable catchment models. *Journal of Hydrology*, 324(1-4):10–23.

Van Liew, M. W. and Veith, T. L. (2010). Guidelines for Using the Sensitivity Analysis and Auto-calibration Tools for Multi-gage or Multi-step Calibration in SWAT. pages 1–30.

van Vuuren, D. P., Edmonds, J., Kainuma, M., Riahi, K., Thomson, A., Hibbard, K., Hurtt, G. C., Kram, T., Krey, V., Lamarque, J. F., Masui, T., Meinshausen, M., Nakicenovic, N., Smith, S. J., and Rose, S. K. (2011). The representative concentration pathways: An overview. *Climatic Change*, 109(1):5–31.

Velázquez, J. A., Troin, M., and Caya, D. (2015). Hydrological Modeling of the Tampaon River in the Context of Climate Change TT - Modelación hidrológica del río Tampaón en el contexto del cambio climático. *Tecnología y ciencias del agua*, 6(5):17–30.

Volodin, E., Mortikov, E., Gritsun, A., Lykossov, V., Galin, V., Diansky, N., Gusev, A., Kostrykin, S., Iakovlev, N., Shestakova, A., and Emelina, S. (2019). INM INM-CM4-8 model output prepared for CMIP6 ScenarioMIP Historical, ssp126, ssp245, ssp370, ssp585. v20190603. *Earth System Grid Federation*.

Wagino, A. M. and Amanuel, T. W. (2021). Community Adaptation to Climate Change: Case of Gumuz People, Metekel Zone, Northwest Ethiopia. *African Handbook of Climate Change Adaptation*, pages 2339–2362.

Waidler, D., White, M., Steglich, E., Wang, S., Williams, J., Jones, C. A., and Srinivasan, R. (2009). Conservation Practice Modeling Guide for SWAT and APEX. Technical report.

WaleWorqlul, A., Taddele, Y. D., Ayana, E. K., Jeong, J., Adem, A. A., and Gerik, T. (2018). Impact of climate change on streamflow hydrology in headwater catchments of the upper Blue Nile Basin, Ethiopia. *Water (Switzerland)*, 10(2).

Wang, G., Yang, H., Wang, L., Xu, Z., and Xue, B. (2014). Using the SWAT model to assess impacts of land use changes on runoff generation in headwaters. *Hydrological Processes*, 28(3):1032–1042.

Wang, S. W., Gebru, B. M., Lamchin, M., Kayastha, R. B., and Lee, W. K. (2020). Land use and land cover change detection and prediction in the kathmandu district of nepal using remote sensing and GIS. *Sustainability (Switzerland)*, 12(9).

Wang, Y., Jiang, R., Xie, J., Zhao, Y., Yan, D., and Yang, S. (2019). Soil and Water Assessment Tool (SWAT) Model: A Systemic Review. *Journal of Coastal Research*, 93:22–30.

White, K. L. and Chaubey, I. (2005). Sensitivity analysis, calibration, and validations for a multisite and multivariable SWAT model. *Journal of the American Water Resources Association*, 41(5):1077–1089.

Williams, J. R. (1975). Sediment Routing for Agricultural Watersheds. *JAWRA Journal of the American Water Resources Association*, 11(5):965–974.

World Bank (2010). Economics of Adaptation to Climate Change: Ethiopia. Technical report, The World Bank, Washington DC, New York.

Xu, Z., Han, Y., Tam, C. Y., Yang, Z. L., and Fu, C. (2021). Bias-corrected CMIP6 global dataset for dynamical downscaling of the historical and future climate (1979–2100). *Scientific Data*, 8(1):1–11.

Yang, N., Men, B. H., and Lin, C. K. (2011). Impact analysis of climate change on water resources. *Procedia Engineering*, 24:643–648.

Yen, H., Daggupati, P., White, M. J., Srinivasan, R., Gossel, A., Wells, D., and Arnold, J. G. (2016). Application of large-scale, multi-resolution watershed modeling framework using the Hydrologic and Water Quality System (HAWQS). *Water (Switzerland)*, 8(4):1–23.

Yesuf, H. M., Assen, M., Alamirew, T., and Melesse, A. M. (2015). Modeling of sediment yield in Maybar gauged watershed using SWAT, northeast Ethiopia. *Catena*, 127:191–205.

Yin, J., He, F., Jiu Xiong, Y., and Yu Qiu, G. (2017). Effects of land use/land cover and climate changes on surface runoff in a semi-humid and semi-arid transition zone in northwest China. *Hydrology and Earth System Sciences*, 21(1):183–196.

Young, N. E., Anderson, R. S., Chignell, S. M., Vorster, A. G., Lawrence, R., and Evangelista, P. H. (2017). A survival guide to Landsat preprocessing. *Ecology*, 98(4):920–932.

Yue, S., Pilon, P., Phinney, B., and Cavadias, G. (2002). The influence of autocorrelation on the ability to detect trend in hydrological series. *Hydrological Processes*, 16(9):1807–1829.

Yue, S. and Wang, C. (2004). The Mann-Kendall Test Modified by Effective Sample Size to Detect Trend in Serially Correlated Hydrological Series. *Water Resources Management*, 18:201–218.

Yukimoto, S., Koshiro, T., Kawai, H., Oshima, N., Yoshida, K., Urakawa, S., Tsujino, H., Deushi, M., Tanaka, T., Hosaka, M., Yoshimura, H., Shindo, E., Mizuta, R., Ishii, M., Obata, A., and Adachi, Y. (2019). MRI MRI-ESM2.0 model output prepared for CMIP6 CMIP Historical, ssp126, ssp245, ssp370, ssp585. v20191108. *Earth System Grid Federation*.

Zhang, L., Nan, Z., Xu, Y., and Li, S. (2016). Hydrological impacts of land use change and climate variability in the headwater region of the Heihe River Basin, northwest China. *PLoS ONE*, 11(6):1–25.

Şen, Z. (2012). Innovative Trend Analysis Methodology. *Journal of Hydrologic Engineering*, 17(9):1042–1046.

# Appendices

Table A.1: List of meteorological stations used in each agroclimatic zones

| Agroclimatic zone | No | Station Name | Latitude | Longitude | Elevation (m) | AnnRF (mm) |
|---|---|---|---|---|---|---|
| **ACZ1: Dry Bereha (Hot-lowlands)** | 1 | Gode* | 5.92 | 43.58 | 290 | 227.2 |
| | 2 | Kelafo | 5.60 | 44.21 | 246 | 166.2 |
| **ACZ2: Dry Kolla (Lowlands)** | 3 | Bisidmo | 9.21 | 42.21 | 1379 | 679.9 |
| | 4 | Degahabour* | 8.22 | 43.56 | 1070 | 326.3 |
| | 5 | Fafem | 9.24 | 42.60 | 1450 | 596.7 |
| | 6 | Huse | 8.66 | 41.85 | 1124 | 539.0 |
| | 7 | Kebri Dehar | 6.73 | 44.27 | 505 | 289.0 |
| **ACZ5: Moist Kolla (Lowlands)** | 8 | Gololcha* | 8.26 | 40.13 | 1372 | 1047.2 |
| **ACZ3: DryWeyna Dega (Midlands)** | 9 | Babile | 9.22 | 42.32 | 1657 | 630.1 |
| | 10 | Chinaksen | 9.50 | 42.60 | 2062 | 557.4 |
| | 11 | Combolcha | 9.43 | 42.12 | 2122 | 815.2 |
| | 12 | Fedis | 9.13 | 42.08 | 1690 | 752.4 |
| | 13 | Gursum* | 9.35 | 42.40 | 1900 | 806.9 |
| | 14 | Haramaya | 9.42 | 42.04 | 2020 | 800.3 |
| | 15 | Harar | 9.31 | 42.12 | 1977 | 829.0 |
| | 16 | Jijiga | 9.35 | 42.79 | 1775 | 589.5 |
| | 17 | Keberebeya | 9.10 | 43.17 | 1738 | 381.3 |
| | 18 | Kersa | 9.45 | 41.87 | 1995 | 760.3 |
| **ACZ6: Moist Weyna Dega (Midlands)** | 19 | Bedeno | 9.12 | 41.64 | 2200 | 939.2 |
| | 20 | Bedessa* | 8.91 | 40.77 | 1703 | 1047.4 |
| | 21 | Chelenko | 9.39 | 41.56 | 2178 | 980.4 |
| | 22 | Deder | 9.32 | 41.44 | 2290 | 980.7 |
| | 23 | Delosebro | 7.25 | 40.47 | 2200 | 971.5 |
| | 24 | Gelemso | 8.81 | 40.53 | 1739 | 974.8 |
| | 25 | Hirna | 9.22 | 41.10 | 1822 | 971.6 |
| | 26 | Jara | 7.37 | 40.50 | 2044 | 1126.6 |
| | 27 | Mechara | 8.60 | 40.34 | 1780 | 1018.4 |
| **ACZ4: Dry Dega (Highlands)** | 28 | Adele | 7.75 | 39.90 | 2466 | 816.2 |
| | 29 | Indeto* | 7.57 | 39.90 | 2416 | 892.0 |
| | 30 | Hunte | 7.05 | 39.40 | 2380 | 774.9 |
| | 31 | Kulubi | 9.42 | 41.69 | 2419 | 824.0 |
| | 32 | Meraro | 7.40 | 39.25 | 2940 | 875.0 |
| | 33 | Tereta | 7.57 | 39.60 | 2350 | 777.7 |
| **ACZ7: Moist Dega (Highlands)** | 34 | Adaba | 7.02 | 39.40 | 2420 | 920.9 |
| | 35 | Arsi Robe* | 7.88 | 39.62 | 2441 | 926.0 |
| | 36 | Chole | 8.14 | 39.90 | 2700 | 1070.7 |
| | 37 | Diksis | 8.05 | 39.56 | 2724 | 1103.5 |
| | 38 | Edo Dodola | 6.98 | 39.18 | 2450 | 1211.8 |
| | 39 | Girawa | 9.13 | 41.83 | 2479 | 936.2 |
| | 40 | Gobesa | 7.63 | 39.50 | 2400 | 1240.4 |
| | 41 | Kofele | 7.07 | 38.80 | 2620 | 1002.4 |
| | 42 | Seletana | 7.40 | 39.39 | 3120 | 1127.9 |
| | 43 | Seru | 7.68 | 40.20 | 2469 | 1134.8 |
| | 44 | Sidika | 7.63 | 39.81 | 2414 | 996.6 |
| | 45 | Ticho | 7.81 | 39.52 | 2553 | 996.4 |

Table A.2: Information on downloaded satellite images

| **Image (Sensor)** | **Landsat 5 (TM)** | **Landsat 5 (TM)** | **Landsat 5 (TM)** | **Landsat 8 (OLI)** |
|---|---|---|---|---|
| Acquisition date | 1990 | 2000 | 2010 | 2020 |
| Path/Row | | | | |
| 165/054 | 19900127 | 20000107 | 20100118 | 20210217 |
| 165/055 | 19900127 | 20000107 | 20100118 | 20210217 |
| 166/054 | 19901220 | 20000114 | 20100125 | 20210224 |
| 166/055 | 19901220 | 20000114 | 20100125 | 20210224 |
| 166/056 | 19901220 | 20000114 | 20100125 | 20210224 |
| 167/053 | 19901227 | 20000105 | 20100201 | 20210215 |
| 167/054 | 19901227 | 20000105 | 20100201 | 20210215 |
| 167/055 | 19901227 | 20000105 | 20100201 | 20210215 |
| 168/054 | 19910119 | 20000112 | 20110110 | 20190116 |
| 168/055 | 19910119 | 20000112 | 20110110 | 20190116 |

Table A.3: Error matrix for 1990, 2000, 2010, and 2020 LULC in Upper and Central Wabi Shebele Basin

| Classified Image | | Reference Image | | | | | | | | | | |
|---|---|---|---|---|---|---|---|---|---|---|---|---|
| | | WtB | BtU | Forest | OpSH | DeSH | GrSS | AgRL | BaRL | Total | UA | Wi |
| 1990 | WtB | 31 | 0 | 0 | 0 | 0 | 0 | 0 | 0 | 31 | 1.00 | 0.00 |
| | BtU | 0 | 28 | 0 | 2 | 0 | 0 | 0 | 0 | 30 | 0.93 | 0.00 |
| | Forest | 0 | 0 | 42 | 0 | 1 | 1 | 0 | 0 | 44 | 0.95 | 0.02 |
| | OpSH | 0 | 0 | 1 | 414 | 11 | 2 | 1 | 11 | 440 | 0.94 | 0.66 |
| | DeSH | 0 | 0 | 1 | 2 | 97 | 1 | 0 | 0 | 101 | 0.96 | 0.11 |
| | GrSS | 0 | 0 | 0 | 3 | 0 | 60 | 0 | 0 | 63 | 0.95 | 0.05 |
| | AgRL | 0 | 0 | 2 | 8 | 1 | 0 | 103 | 0 | 114 | 0.90 | 0.14 |
| | BaRL | 0 | 0 | 0 | 0 | 0 | 1 | 0 | 36 | 37 | 0.97 | 0.01 |
| | Total | 31 | 28 | 46 | 429 | 110 | 65 | 104 | 47 | 860 | | |
| | PA | 1.00 | 1.00 | 0.91 | 0.97 | 0.88 | 0.92 | 0.99 | 0.77 | | | |
| 2000 | WtB | 31 | 0 | 0 | 0 | 0 | 0 | 0 | 0 | 31 | 1.00 | 0.00 |
| | BtU | 0 | 28 | 0 | 1 | 0 | 0 | 1 | 0 | 30 | 0.93 | 0.00 |
| | Forest | 0 | 0 | 38 | 0 | 0 | 0 | 0 | 0 | 38 | 1.00 | 0.01 |
| | OpSH | 0 | 0 | 0 | 439 | 8 | 2 | 2 | 5 | 456 | 0.96 | 0.69 |
| | DeSH | 0 | 0 | 1 | 9 | 69 | 0 | 0 | 0 | 79 | 0.87 | 0.08 |
| | GrSS | 0 | 0 | 0 | 3 | 0 | 50 | 0 | 0 | 53 | 0.94 | 0.04 |
| | AgRL | 0 | 0 | 1 | 6 | 0 | 1 | 126 | 0 | 134 | 0.94 | 0.17 |
| | BaRL | 0 | 0 | 0 | 2 | 0 | 0 | 0 | 37 | 39 | 0.95 | 0.01 |
| | Total | 31 | 28 | 40 | 460 | 77 | 53 | 129 | 42 | 860 | | |
| | PA | 1.00 | 1.00 | 0.95 | 0.95 | 0.90 | 0.94 | 0.98 | 0.88 | | | |
| 2010 | WtB | 30 | 0 | 0 | 0 | 0 | 0 | 0 | 0 | 30 | 1.00 | 0.00 |
| | BtU | 0 | 26 | 0 | 0 | 0 | 1 | 3 | 0 | 30 | 0.87 | 0.00 |
| | Forest | 0 | 0 | 34 | 2 | 0 | 0 | 0 | 0 | 36 | 0.94 | 0.01 |
| | OpSH | 0 | 0 | 0 | 424 | 5 | 4 | 1 | 4 | 438 | 0.97 | 0.66 |
| | DeSH | 0 | 0 | 0 | 9 | 53 | 0 | 1 | 0 | 63 | 0.84 | 0.05 |
| | GrSS | 0 | 0 | 0 | 6 | 1 | 30 | 0 | 0 | 37 | 0.81 | 0.01 |
| | AgRL | 0 | 0 | 0 | 20 | 0 | 2 | 162 | 0 | 184 | 0.88 | 0.25 |
| | BaRL | 0 | 0 | 0 | 0 | 0 | 0 | 0 | 40 | 40 | 1.00 | 0.02 |
| | Total | 30 | 26 | 34 | 461 | 59 | 37 | 167 | 44 | 858 | | |
| | PA | 1.00 | 1.00 | 1.00 | 0.92 | 0.90 | 0.81 | 0.97 | 0.91 | | | |
| 2020 | WtB | 31 | 0 | 0 | 0 | 0 | 0 | 0 | 0 | 31 | 1.00 | 0.00 |
| | BtU | 0 | 29 | 0 | 0 | 0 | 0 | 2 | 0 | 31 | 0.94 | 0.00 |
| | Forest | 0 | 0 | 32 | 0 | 2 | 0 | 1 | 0 | 35 | 0.91 | 0.01 |
| | OpSH | 0 | 0 | 1 | 408 | 4 | 1 | 6 | 8 | 428 | 0.95 | 0.64 |
| | DeSH | 0 | 0 | 0 | 1 | 53 | 0 | 1 | 0 | 55 | 0.96 | 0.04 |
| | GrSS | 0 | 0 | 0 | 5 | 0 | 32 | 1 | 0 | 38 | 0.84 | 0.01 |
| | AgRL | 0 | 0 | 0 | 14 | 4 | 2 | 177 | 0 | 197 | 0.90 | 0.27 |
| | BaRL | 0 | 0 | 0 | 1 | 0 | 0 | 1 | 42 | 44 | 0.95 | 0.02 |
| | Total | 31 | 29 | 33 | 429 | 63 | 35 | 189 | 50 | 859 | | |
| | PA | 1.00 | 1.00 | 0.97 | 0.95 | 0.84 | 0.91 | 0.94 | 0.84 | | | |

Table A.4: Sensitivity analysis results of streamflow component of SWAT

| **Errer** | | | | **Furuna** | | | | **Harero** | | | |
|---|---|---|---|---|---|---|---|---|---|---|---|
| Rank | Parameter Name | t-Stat | P-Value | Rank | Parameter Name | t-Stat | P-Value | Rank | Parameter Name | t-Stat | P-Value |
| *1* | *R__CN2.mgt* | *-41.84* | *0.00* | *1* | *V__GW_DELAY.gw* | *-24.93* | *0.00* | *1* | *R__CN2.mgt* | *28.10* | *0.00* |
| *2* | *V__ESCO.hru* | *-2.41* | *0.02* | *2* | *R__CN2.mgt* | *23.20* | *0.00* | *2* | *V__GW_REVAP.gw* | *-15.19* | *0.00* |
| *3* | *V__GW_DELAY.gw* | *-1.36* | *0.17* | *3* | *V__GW_REVAP.gw* | *-11.78* | *0.00* | *3* | *V__GWQMN.gw* | *-10.31* | *0.00* |
| *4* | *R__SOL_BD(..).sol* | *1.11* | *0.27* | *4* | *V__ESCO.hru* | *10.42* | *0.00* | *4* | *V__ESCO.hru* | *9.33* | *0.00* |
| *5* | *V__REVAPMN.gw* | *-0.78* | *0.44* | *5* | *V__GWQMN.gw* | *-7.92* | *0.00* | *5* | *V__REVAPMN.gw* | *8.16* | *0.00* |
| 6 | R__SOL_K(..).sol | -0.73 | 0.46 | 6 | R__SOL_BD(..).sol | 7.87 | 0.00 | 6 | R__SOL_BD(..).sol | 7.84 | 0.00 |
| 7 | R__CH_K2.rte | 0.54 | 0.59 | 7 | V__REVAPMN.gw | 5.70 | 0.00 | 7 | V__GW_DELAY.gw | -4.72 | 0.00 |
| 8 | V__ALPHA_BNK.rte | 0.32 | 0.75 | 8 | V__ALPHA_BF.gw | 4.21 | 0.00 | 8 | V__ALPHA_BF.gw | 3.42 | 0.00 |
| 9 | V__GW_REVAP.gw | -0.28 | 0.78 | 9 | R__SOL_AWC(..).sol | -2.57 | 0.01 | 9 | R__SOL_AWC(..).sol | -3.24 | 0.00 |
| 10 | V__EPCO.bsn | -0.21 | 0.83 | 10 | R__SOL_K(..).sol | 1.86 | 0.06 | 10 | V__ALPHA_BNK.rte | 1.93 | 0.05 |
| 11 | V__GWQMN.gw | 0.17 | 0.86 | 11 | V__ALPHA_BNK.rte | 1.80 | 0.07 | 11 | R__SOL_K(..).sol | 1.79 | 0.07 |
| 12 | R__SOL_AWC(..).sol | -0.15 | 0.88 | 12 | V__SURLAG.bsn | 1.22 | 0.22 | 12 | R__CH_N2.rte | -1.41 | 0.16 |
| 13 | R__OV_N.hru | -0.11 | 0.91 | 13 | R__CH_N2.rte | -0.95 | 0.34 | 13 | R__OV_N.hru | -0.81 | 0.42 |
| 14 | R__CH_N2.rte | 0.07 | 0.94 | 14 | R__OV_N.hru | -0.35 | 0.73 | 14 | V__EPCO.bsn | -0.67 | 0.50 |
| 15 | V__SURLAG.bsn | 0.03 | 0.98 | 15 | R__CH_K2.rte | 0.19 | 0.85 | 15 | V__SURLAG.bsn | 0.05 | 0.96 |
| 16 | V__ALPHA_BF.gw | -0.03 | 0.98 | 16 | V__EPCO.bsn | 0.18 | 0.86 | 16 | R__CH_K2.rte | 0.03 | 0.98 |
| **Maribo** | | | | **Robe** | | | | **Wabi@Bridge** | | | |
| *1* | *R__CN2.mgt* | *42.25* | *0.00* | *1* | *R__CN2.mgt* | *-25.51* | *0.00* | *1* | *R__CN2.mgt* | *-20.72* | *0.00* |
| *2* | *V__GW_DELAY.gw* | *-32.07* | *0.00* | *2* | *V__GW_DELAY.gw* | *-1.51* | *0.13* | *2* | *V__ESCO.hru* | *-2.68* | *0.01* |
| *3* | *V__GW_REVAP.gw* | *-12.89* | *0.00* | *3* | *R__SOL_AWC(..).sol* | *-1.25* | *0.21* | *3* | *V__GW_REVAP.gw* | *-1.71* | *0.09* |
| *4* | *V__ESCO.hru* | *9.58* | *0.00* | *4* | *V__GW_REVAP.gw* | *-1.19* | *0.24* | *4* | *V__GW_DELAY.gw* | *1.64* | *0.10* |
| *5* | *V__GWQMN.gw* | *-8.12* | *0.00* | *5* | *V__ESCO.hru* | *-0.94* | *0.35* | *5* | *R__SOL_BD(..).sol* | *1.41* | *0.16* |
| 6 | V__REVAPMN.gw | 5.92 | 0.00 | 6 | R__SOL_K(..).sol | -0.93 | 0.35 | 6 | V__ALPHA_BNK.rte | 1.25 | 0.21 |
| 7 | V__ALPHA_BF.gw | 4.91 | 0.00 | 7 | R__SOL_BD(..).sol | -0.66 | 0.51 | 7 | V__EPCO.bsn | -1.08 | 0.28 |
| 8 | R__SOL_AWC (..).sol | -4.41 | 0.00 | 8 | V__GWQMN.gw | -0.60 | 0.55 | 8 | R__OV_N.hru | -0.77 | 0.44 |
| 9 | R__SOL_BD (..).sol | 4.13 | 0.00 | 9 | R__CH_K2.rte | 0.53 | 0.60 | 9 | R__CH_K2.rte | 0.74 | 0.46 |
| 10 | V__ALPHA_BNK.rte | 1.88 | 0.06 | 10 | V__EPCO.bsn | -0.53 | 0.60 | 10 | R__SOL_K(..).sol | -0.68 | 0.49 |
| 11 | V__SURLAG.bsn | 1.56 | 0.12 | 11 | V__ALPHA_BNK.rte | 0.48 | 0.63 | 11 | R__SOL_AWC(..).sol | 0.55 | 0.58 |
| 12 | R__CH_N2.rte | -1.06 | 0.29 | 12 | R__OV_N.hru | -0.43 | 0.67 | 12 | V__GWQMN.gw | -0.47 | 0.64 |
| 13 | R__SOL_K (..).sol | 0.94 | 0.35 | 13 | V__SURLAG.bsn | 0.12 | 0.90 | 13 | V__SURLAG.bsn | 0.28 | 0.78 |
| 14 | R__OV_N.hru | -0.43 | 0.67 | 14 | R__CH_N2.rte | 0.07 | 0.95 | 14 | V__REVAPMN.gw | -0.20 | 0.84 |
| 15 | V__EPCO.bsn | 0.29 | 0.77 | 15 | V__REVAPMN.gw | -0.07 | 0.95 | 15 | V__ALPHA_BF.gw | -0.20 | 0.84 |
| 16 | R__CH_K2.rte | -0.04 | 0.97 | 16 | V__ALPHA_BF.gw | 0.07 | 0.95 | 16 | R__CH_N2.rte | 0.16 | 0.88 |